A microfluidic study of the physical and chemical mechanisms induced by CO2 injection in deep saline aquifers

Mahdi Mansouri-Boroujeni

UNIVERSITÉ D'ORLÉANS

ÉCOLE DOCTORALE
Énergie, Matériaux, Sciences de la Terre et de l'Univers
Institut des Sciences de la Terre d'Orléans (ISTO)

THÈSE présentée par :

Mahdi Mansouri-Boroujeni

Soutenue le : **12 Mai 2022**

Pour obtenir le grade de : **Docteur de l'Université d'Orléans**
Discipline/ Spécialité : Sciences de l'Univers

A microfluidic study of the physical and chemical mechanisms induced by CO_2 injection in deep saline aquifers

THÈSE dirigée par :

Mr. AZAROUAL Mohamed	Directeur adjoint ISTO-HDR, Université d'Orléans, Directeur de thèse
Ms. ROMAN Sophie	Maitre de conférences, Université d'Orléans, Co-directrice de thèse

RAPPORTEURS :

Mr. MARRE Samuel	Directeur de recherche, CNRS, ICMCB, Bordeaux
Mr. RAOOF Amir	Ass. Prof. Utrecht University (Pays Bas)

JURY :

Mr. MAZELLIER Nicolas	Maitre de conférences HDR, Université d'Orléans, Président du jury
Mr. GOLFIER Fabrice	Maitre de conférences HDR, Université de Lorraine
Ms. MIQUEU Christelle	Maitre de conférences HDR,Université de Pau et des Pays de l'Adour
Ms. LUQUOT Linda	Chargée de recherche CNRS HDR, Géosciences Montpellier

Resumé

Le captage et le stockage du carbone s'inscrivent dans un plan à long terme visant à ralentir et limiter de manière optimale le réchauffement climatique en réduisant le CO_2 atmosphérique, le gaz à effet de serre le plus émis. La séquestration du CO_2 dans des réservoirs géologiques est une méthode d'atténuation fiable, bien que complexe. Diverses méthodes de stockage telles que l'utilisation du CO_2 pour les procédés EOR (Enhanced Oil Recovery, récupération assistée du pétrole), le stockage dans des réservoirs pétroliers épuisés, le stockage dans des aquifères salins profonds, etc. sont proposées, parmi lesquelles les aquifères salins ont la capacité de stockage la plus élevée. Lors de la séquestration du supercritique CO_2 dans un réservoir géologique, différents processus ont lieu, d'abord l'injection du CO_2 dans un puits, le déplacement immiscible et miscible du CO_2 et du fluide initialement présent dans les pores du réservoir, ainsi que le transport réactif incluant la dissolution, les précipitations et les changements pétrophysiques. Ces processus s'étendent de l'échelle des pores (nm-µm) à l'échelle de Darcy (mètre) et à l'échelle du réservoir (kilomètre). L'efficacité et l'intégrité de la séquestration du CO_2 dépendent du couplage entre tous ces processus et définissent la capacité de stockage du réservoir. Ainsi, une compréhension approfondie de chaque processus et de leur interaction est cruciale pour la gestion des réservoirs et l'évaluation de la sécurité du stockage.

Les écoulements multiphasiques immiscibles dans les milieux poreux sont omniprésents et d'une importance capitale dans la séquestration du CO_2 en aquifères salins. En raison de la plus faible viscosité du fluide injecté (CO_2) par rapport au fluide déplacé (saumure), le déplacement est considéré comme défavorable car le front a tendance à devenir instable. Cette instabilité entraîne un front de déplacement ramifié, ce qui a un impact surl'efficacité du déplacement et la propagation du fluide dans le système aux échelles de réservoir, de Darcy et de pores, affectant ainsi la capacité de stockage., par conséquent, la capacité de stockage. Les instabilités se propagent à travers le milieux poreux selon les caractéristiques de ce dernier (mouillabilité, distribution de taille des pores, connectivité des pores, etc.), des propriétés du fluide (viscosité, densité, tension interfaciale, etc.) et des conditions d'écoulement, créant ainsi différents régimes d'écoulement et une efficacité de déplacement et une distribution de la saturation différentes. Les déplacements diphasiques en milieux poreux

sont classés en trois régimes d'écoulement distincts (régime stable, régime visqueux et régime capillaire) en fonction des caractéristiques des fluides et de l'écoulement, caractérisés par des paramètres sans dimension, le nombre capillaire Ca (rapport entre les forces visqueuses et la tension de surface) et le rapport de mobilité M (rapport entre la viscosité des fluides).

L'écoulement diphasique est composé d'une série d'invasions de pores qui définit le comportement global du front de déplacement pour chaque régime d'écoulement. Il est établi qu'en conséquence de la dynamique complexe d'invasion des pores, le mouvement du front dans les milieux poreux, dans des conditions spécifiques, est composé d'invasions intermittentes plutôt que d'un déplacement du front en continu. L'étude et la compréhension des mécanismes d'invasion des pores sont essentiels pour prédire le comportement global du front dans différentes conditions. De plus, cela contribue à révéler le rôle des forces à petite échelle, qui ne sont pas prises en compte dans la formulation de Darcy (par exemple, les forces capillaires, les forces cinétiques et les contraintes de cisaillement entre les phases). En outre, une étude systématique à l'échelle des pores précisera dans quelles conditions ces forces doivent être prises en compte dans les équations pour capturer avec précision les processus de transport clés dans les milieux poreux. Malgré les progrès récents des outils de simulation numérique à l'échelle des pores leur capacité prédictive n'est pas toujours au point. Jusqu'à présent, presque aucun des modèles existants ne peut prédire de manière précise les processus de déplacement à l'échelle des pores dans les milieux poreux, en particulier lorsque les forces capillaires sont dominantes.

En plus de la physique du déplacement dans les milieux poreux, les transferts de masse et de chaleur entre les phases lors de la séquestration du CO_2 sont critiques. Le CO_2 se dissout dans la phase aqueuse et forme de l'acide carbonique, entraînant une réduction du pH de l'aquifère. En réduisant le pH, les minéraux tels que les carbonates vont se dissoudre dans la phase aqueuse sous forme d'ions mobiles et vont réagir avec d'autres ions pour précipiter sous forme de nouveaux minéraux en raison des nouvelles conditions thermodynamiques. En effet, cet échange d'ions aux interfaces (minéral-aquifère et aquifère-CO_2) joue un rôle essentiel dans le comportement du système et peut contrôler la cinétique du processus de dissolution et de précipitation. Ces dissolutions et précipitations modifient les propriétés pétrophysiques des milieux poreux (telles que la forme des pores, la porosité, la connectivité des pores et les perméabilités absolues et relatives). En outre, l'altération chimique du milieu poreux modifie les propriétés physicochimiques de surface et les conditions de mouillabilité qui, à leur tour, modifient les conditions d'écoulement. Par ailleurs, l'évolution du débit peut modifier le temps de séjour des réactifs, puis les conditions de transfert de masse et de réaction. Le couplage des réactions et de l'écoulement des fluides forme un système dynamique qui varie en permanence. L'échelle des pores est adaptée pour

étudier les mécanismes chimiques et physiques de base induits lors de la séquestration du CO_2 et explorer le couplage entre eux.

Cette thèsevise à étudier les mécanismes physiques et chimiques impliqués dans la séquestration du CO_2 dans les aquifères salins profonds à l'échelle des pores. A cet égard, dans cette recherche, nous poursuivons principalement deux objectifs ;

- Comprendre les mécanismes d'invasion des pores pour chaque régime d'écoulement lors du déplacement diphasique immiscible dans les milieux poreux, pour quantifier le rôle des phénomènes à l'échelle des pores impliqués sur le comportement du front et la dynamique interfaciale qui affectent le stockage du CO_2.

- Étudier la cinétique de dissolution de la calcite en présence d'ions sulfate et suivre l'altération physique et chimique des milieux poreux en raison des mécanismes à l'échelle des pores, quantifier l'effet des impuretés sur le stockage du CO_2 et l'évolution de la surface réactive dans les réservoirs carbonatés.

Les micromodèles sont des milieux poreux artificiels confinés entre deux substrats, nous permettant de caractériser et d'observer directement dans le système. En effet, les micromodèles permettent de contrôler avec précision les conditions expérimentales telles que la taille des pores, la géométrie et la rugosité de surface, la composition des fluides et les conditions d'écoulement. Cela permet de recréer des conditions similaires à celles des milieux poreux naturels et d'étudier les phénomènes de déplacement de manière détaillée et reproductible.

Les micromodèles sont également très utiles pour étudier les interactions fluide-minéral et fluide-roche dans les milieux poreux. Les réactions de dissolution et de précipitation qui se produisent lors de la séquestration du CO_2 peuvent être étudiées en utilisant des micromodèles avec des minéraux spécifiques et en contrôlant les conditions de pH et de concentration en ions dans les fluides. Les micromodèles sont également utilisés pour étudier les effets des processus de précipitation sur les propriétés de transport des fluides dans les milieux poreux.

Grâce à notre montage expérimental, à l'aide d'un microscope couplé à une caméra haute résolution, nous sommes capables de capturer des séquences d'images à différentes étapes du processus de drainage (lorsque la phase non-mouillante déplace la phase mouillante) dans le dispositif microfluidique. Les expériences ont été réalisées dans des conditions de laboratoire standard ($25°C$ et $1\,bar$). La pression entre l'entrée et la sortie du micromodèle est contrôlée (de 30 mbar à 110 mbar) pour obtenir différents débits. Pour obtenir une large gamme de rapports de viscosité, différentes paires de fluides ont été sélectionnées pour reproduire la condition de déplacement instable de la séquestration du CO_2 dans les environnements souterrains ($-2 < \log M < -1$ et

, $logCa < -3$). Pour se concentrer sur les mécanismes de transport fondamentaux et distinguer l'effet des instabilités interfaciales sur le déplacement du front et la perturbation des fluides, la géométrie étudiée est un doublet de pores avec des capillaires sinusoïdaux, représentative d'une succession de pores et de constrictions en milieux poreux. Les micromodèles sont moulés en PDMS (un élastomère de silicone). En parallèle, nous avons développé un modèle théorique général basé sur la moyenne volumique des équations de Navier-Stokes pour un volume élémentaire représentatif (VER) qui prend en compte les forces d'inertie, visqueuses et capillaires et nous permet d'évaluer les processus d'invasion prédits pour le modèle de doublet de pores pour une large gamme. De valeurs Ca et M.

Nous avons identifié et caractérisé les régimes d'écoulement classiques de déplacement non miscible en milieu poreux. Les expériences réalisées nous permettent de capturer les mécanismes fondamentaux d'invasion des pores pour chaque régime d'écoulement spécifique et ont mis en évidence le rôle des forces visqueuses, capillaires et d'inertie sur le comportement de l'interface et la dynamique d'invasion des pores. Des différences significatives ont été observées entre les régimes d'écoulement visqueux et capillaires dans le comportement du front, la dynamique de l'interface et les mécanismes d'invasion des pores. En régime d'écoulement visqueux ($\log Ca > -1,4$), lorsque les forces visqueuses sont dominantes, les pores sont envahis simultanément avec un front stable avec un déplacement continu de l'interface, et il ne s'arrête à aucun moment au seuil du pores en raison de sa vitesse et de ses forces d'impulsion. Pendant ce temps, l'interface ne trouve pas assez de temps pour s'étendre sur toute la surface des pores, et du fluide mouillant résiduel reste aux courbures de l'espace des pores. Pour le régime d'écoulement capillaire ($\log Ca < -2,8$), les forces capillaires sont dominantes et le pore dans lequel l'interface atteint la pression seuil d'invasion sera envahi. Dans ces conditions, les sauts de Haines sont le mécanisme d'invasion des pores privilégié. L'interface se dilate latéralement lors de l'invasion des pores et déplace toutes la phase mouillante, à l'exception des écoulement de coins et des films de mouillage. A chaque invasion, l'interface dans le capillaire adjacent montre un mouvement de va-et-vient à la constriction dû aux forces d'inertie et à la capillarité. Les résultats de PIV (Vélocimétrie par Images de Particules) à l'intérieur des pores confirment les observations d'oscillation d'interface au niveau de la constriction. Le régime d'écoulement « croisé » présente un comportement mixte entre le régime apillaire et visqueux. Pour ce régime, les deux canaux sont envahis ; cependant, ils ne participeront pas de la même manière au déplacement. Le mécanisme d'invasion pore par pore reste le principal mécanisme d'invasion. Le modèle numérique développé est capable de capturer les principaux mécanismes d'invasion des pores et de montrer des comportements du front similaires pour tous les régimes d'écoulement testés. Les résultats du modèle sont utilisés pour prédire

les transitions entre les régimes d'écoulements en termes de diagramme de phase $\log Ca - \log M$ au-delà des domaines explorés expérimentalement.

Dans les pores envahis, des fluides mouillants résiduels ont été observés. La phase mouillante résiduelle est collectée dans les coins des canaux et vraisemblablement sous la forme d'un mince film liquide sur les surfaces pour le régime d'écoulement capillaire. En appliquant la technique micro-PIV et en mesurant le profil de vitesse des fluides de coin, il a été révélé qu'il existe un comportement dynamique dans les fluides de coin, tandis que l'interface semble immobile dans la constriction du pore avant l'invasion des pores par les sauts de Haines. Un flux continu des coins vers le corps de fluide existe pendant cette période d'attente. Ce débit a un effet essentiel sur le temps pour atteindre la pression de seuil capillaire, et donc sur le temps pendant entre l'invasion de la constriction et le saut de Haines. Un modèle basé sur l'équation d'écoulement de coin et de drainage de mousse est développé. Les résultats numériques montrent une grande ressemblance avec les mesures micro-PIV, et expliquent la dynamique des écoulements de coin liés aux sauts de Haines.

Un effort pour capturer les mécanismes chimiques induits par l'introduction d'une phase non mouillante miscible dans un système de calcite est fait. Ce système ressemble à la séquestration du CO_2 dans les réservoirs carbonatés. À cet égard, une nouvelle méthode de conception et de préparation de micromodèles silicium-verre est proposée, qui permet de mettre la phase injectée (mélange de CO_2 et SO_2, comme impureté gazeuse à haut risque) en contact direct avec la phase aqueuse. Des minéraux de calcite à l'échelle du micron sont cultivés à la surface de la micropuce pour avoir une micropuce avec une composition contrôlée et une géométrie bien définie qui imite les formations de carbonate. En couplant un microscope avec la spectroscopie Raman confocale, l'évolution de la composition de la phase aqueuse, de la surface réactive et de la cinétique de dissolution de la calcite et de la précipitation du gypse peut être surveillée et caractérisée. Grâce à ce dispositif expérimental nous sommes en mesure d'étudier l' évolution de la phase aqueuse résiduelle et piégée lors de la séquestration du CO_2 et quantifier différents mécanismes de stockage. Les principaux mécanismes géochimiques sont étudiés à l'aide de simulations réalisées avec le logiciel PHREEQC, qui montrent une dissolution intense de la calcite lorsque le SO_2 existe dans le système par rapport au cas du CO_2 pur. De plus, une précipitation de gypse est observée à l'entrée du système, ce qui peut entraîner un blocage des voies d'écoulement.

En conclusion, cette étude s'est attachée à étudier les mécanismes physiques et chimiques à la micro-échelle induits par le stockage du CO_2 dans les aquifères salins. Nos résultats indiquent que l'interaction entre les phases et les couplages physico-chimiques sont entièrement différents à mesure qu'on s'éloigne du puits d'injection, car le régime d'écoulement passe d'un régime visqueux à un régime capillaire. Loin du puits, la vitesse lente du CO_2 et l'interaction solide-liquide s sont les principaux

mécanismes en jeu. Nos résultats indiquent clairement que les forces d'inertie affectent la dynamique interfaciale aux régimes d'écoulement capillaire et croisé. En outre, cela peut augmenter le risque de digitations capillaires dans les roches de couverture et accélérer les altérations de la mouillabilité, entraînant une diminution du piégeage capillaire et une réduction de la sécurité de stockage du réservoir. De plus, nos observations suggèrent que la capacité de stockage de CO_2 pour lerégime d'écoulement croisé est plus élevée que pour les autres régimes d'écoulement en raison de la saturation résiduelle la plus faible (efficacité de déplacement la plus élevée, indiquée dans la littérature). En outre, ce résultat remet en question la notion selon laquelle les forces d'inertie sont négligeables lors de la mise à l'échelle. Une autre découverte importante qui ressort de cette étude est que les écoulements de coin ont un rôle de contrôle dans la dynamique des écoulements aux faibles débits et des sauts de Haines. Ces résultats appuient l'idée que bien que l'écoulement soit dominé par les forces capillaires, il existe une région derrière le front où le drainage lent des films de coins contrôle la dynamique. Les résultats rapportés ici jettent un nouvel éclairage sur le déplacement dans un régime d'écoulement capillaire que les modèles de transport actuels ne parviennent pas à prédire de manière précise. Maintenant que nous avons une compréhension fondamentale des mécanismes à l'échelle des pores, l'utilisation d'un système poreux plus complexe nous rapprochera d'une estimation plus précise de la capacité de stockage.

Il reste encore de nombreuses questions auxquelles il faut répondre. Ici, nous mentionnons quelques suggestions sur la façon dont la recherche future peut être orientée.

- Le rôle de la géométrie des pores sur le comportement des fluides et la transition des régimes d'écoulement doit être étudié.

- Bien que le modèle ait été en mesure de prédire le comportement global du front et la dynamique de l'interface, il montre toujours une limitation dans la correspondance précise avec les expériences en termes de résolution temporelle. Comme nous l'avons observé expérimentalement, il existe certains phénomènes à petite échelle tels que le glissement visqueux et le couplage à l'interface fluide-fluide ou l'écoulement de coin que nous négligeons lors de la dérivation du modèle. Le couplage visqueux entre les phases et la prise en compte de la dynamique des écoulements de coin amélioreront la prédictivité du modèle.

- Ici, une géométrie homogène des pores est utilisée. Cependant, pour comprendre les milieux poreux naturels, la prise en compte de l'hétérogénéité de la taille, de la forme et de la connectivité des pores met en lumière le rôle de l'hétérogénéité des milieux poreux dans les voies d'écoulement préférentielles.

- Bien que l'effet des forces d'inertie soit mis en évidence ici, une étude approfondie sur l'inclusion des forces d'inertie dans des modèles à grande échelle (échelle continue) ou des simulations de réseaux de pores est nécessaire.

- Bien sûr, l'effet de la composition de la phase aqueuse, de la pression du réservoir, de la température, etc., est important pour améliorer notre compréhension des mécanismes chimiques à l'échelle des pores dans un réservoir géologique naturel et surmonter les simplifications et hypothèses que nous avons faites. Néanmoins, un facteur crucial encore peu exploré dans les expériences de microfluidique est l'effet de gravité. Avec une nouvelle configuration, on apportera de nouvelles informations sur l'effet des instabilités chimio-hydrodynamiques induites par la gravité sur la réactivité du système et les modèles de précipitation de dissolution.

Abstract

CO_2 sequestration in geological reservoirs is a reliable mitigation method to reduce atmospheric CO_2, albeit challenging, involving multiphase reactive flow processes. CO_2 is captured from the power plants' atmosphere, purified, transported, and injected in deep geological reservoirs covered with an impermeable caprock that prevents leakage to the atmosphere. The success of secure and permanent storage of CO_2 in subsurface formations depends mainly on our understanding of physical and chemical mechanisms induced by CO_2 sequestration. The distribution of CO_2 and the displacement patterns are fluid, rock, and flow properties functions. Fluid displacement is composed of a series of pore invasions that build up the overall front behavior. However, the link between pore invasion mechanisms and global front behavior is not clear. Moreover, the injected CO_2 reacts with the brine and disturbs the prevailing thermodynamic equilibrium. CO_2 dissolution triggers a chain of reactions resulting in alteration of petrophysical and physicochemical porous media by induced dissolution and precipitation kinetics. So far, the definition of pore-scale parameters describing the induced mechanisms is lacking for understanding mineral trapping. The two main objectives of this Ph.D. are (i) to address triggered pore invasion mechanisms at each flow regime to quantify the role of pore-scale phenomena on the front behavior and interfacial dynamics, (ii) to investigate the kinetics of calcite dissolution, the evolution of the reactive surface area and to monitor porous media alteration, to quantify the effect of SO_2 impurities on the CO_2 storage.

We use micromodels, i.e., a transparent replica of porous media network made in synthetic materials. The experimental setup consists of a microscope coupled with a high-resolution camera to visualize flow and reaction processes at the pore-scale. We developed a general theoretical model based on Navier-Stokes volume averaging that considers inertia, viscous, and capillary forces and allows us to evaluate the predicted invasion processes.

We conducted a series of drainage experiments (a non-wetting fluid displacing a wetting fluid) for various flow rates, fluid pairs, and wettability conditions. We identified the classical flow regimes of immiscible displacement and captured fundamental pore invasion mechanisms and their interface dynamics. The viscous flow regime is characterized by pores that are invaded simultaneously with a continuous interface

displacement due to viscous forces dominancy and inertia effects. We observed that threshold capillary pressure defines the invasion condition at the capillary flow regime. At this condition, Haines jumps (i.e., sudden interface movement at a pore throat) are the primary pore invasion mechanism. The interface expands laterally, and only corner wetting fluid and films are retained in drained pores. The crossover flow regime is characterized by pore by pore invasion and a front showing a mixed capillary and viscous flow regime behavior. The results of our model agree with the experiment results. Besides, we explored a large range of conditions numerically to predict flow regime transitions.

We investigated the dynamics of waiting times (when the interface is pinned at a pore throat before Haines jump) and corner flows for the capillary flow regime. Our results suggest a continuous flow in the body of the wetting fluid during pinning. It is observed the dynamics of the corner flow have an important effect on reaching the invasion threshold pressure and on the definition of waiting times. By theoretical developments, we are able to predict the waiting time and corner flow velocity.

Finally, a novel silicon-glass micromodels preparation method and design are proposed to study reactive transport. Micron-scale calcite minerals are grown in a micromodel resembling carbonate rocks. Raman spectroscopy results help monitor and characterize the evolution of the aqueous phase composition, reactive surface area, and kinetics of reactions. Experimental results and main geochemical mechanisms are compared with simulations performed with PHREEQC (a geochemical modeling software). This study highlighted the relationship between pore-scale mechanisms and the front dynamics. In addition, the presented experimental setup paves the way for an accurate study of kinetic parameters and minerals nucleation. The results obtained during this Ph.D. will serve to optimize the process of CO_2 sequestration in geological reservoirs.

Acknowledgements

I express my deepest gratitude toward my supervisors, Prof. Mohamed Azaroual and Dr. Sophie Roman for their trust and support during these years. They always were there to help and guide me toward our goals. They always brought kind suggestions to the table during our helpful discussions. I am most grateful to them for their interest in new ideas that I suggested and their support for pursuing them. It was a pleasure to work side by side with them, and I learned a lot from them.

A special thanks to Dr. Cyprien Soulaine for his advice and help through the theoretical developments. He always had new ideas for improvement and was kindly willing to help. He is undoubtedly an asset to the group.

I would like to also thank all people from the porous media group who brought up exciting discussions during my presentations in our weekly seminars and the people whom I referred to for their advice. I want to thank Dr. Aneta Slodczyk for her irreplaceable efforts in the Nanomicrolab. I appreciate the effort of people from the workshop, Remi Champallier, Fredric Savoie, Remy Planckaert, and Ferly Clodomar, for their help in the lab. I also would like to thank Marie-France Rouillier, who has always been an asset to me.

I want to thank our collaborators from GREMI, Dr. Mukesh Kulsreshath, Dr. Arnaud Stolz, Dr. Remi Dussart, and Philippe Lefaucheux, for showing me the lithography process and their helpful discussion on the fabrication improvement. A special thanks to Jack Nos, who assisted me in preparing and developing our silicone molds.

I express my warmest gratitude toward my parents, Parvin and Jafar Agha, my sister Soude, my brother-in-law Sam and my nephew Aria, who always have supported me from the beginning to the end. You have always been there for me and motivated me to continue. There is no word in any language to describe what you did for me and to show my appreciation toward you.

A very special thanks to Shakiba, who was always there supporting me, and for being a reason to continue. I most certainly can not thank you enough. I will never forget and hope there will be a day that I can make it up to you.

I want to thank my friends who have always been a source of comfort for me and encouraged me through my Ph.D. Thank you, Amir, Armin, Alale, Ali, Alirez, Hasan, Majid, Parisa, Mohamad, Federica, and Javad for your support.

List of Figures

List of Tables

Contents

Preface

Over the past 50 years, the average global temperature has increased at the fastest rate in recorded history; this global warming is attributed to the increased atmospheric concentration of greenhouse gases. Among those, CO_2 is the most abundant one, and humanity is contributing to its increasing rate at a high pace. For example, only in 2019, approximately 39 GT of CO_2 was released into the atmosphere due to human industrial activities (18 GT more than Earth's natural elimination ability). This CO_2 overproduction is considered as the main factor in global warming. Carbon dioxide removal (CDR) is a long-term plan for atmospheric CO_2 reduction to slow down and optimally limit global warming. CO_2 sequestration in deep saline aquifers has been considered as a reliable method for CO_2 mitigation. The process involves capturing the CO_2 from power plants atmosphere, its separation and purification from other gases, transportation to the sequestration site, and injection to deep geological reservoirs. In this method, CO_2 is injected in the supercritical form in deep saline aquifers to be trapped either in the form of mineralization, dissolution in the brine, or structural entrapment (under the cap-rock or capillary trapping). Several complex mass transport, thermodynamics, and kinetics of interactions and reactions are activated during these trapping mechanisms. Fluid flow, solute transport, mineral dissolution, and mineral precipitation combine within the mechanical framework of the porous medium, scaling from millimeters to kilometers and form a complex structure [40]. Still, the exact physical and chemical mechanisms involved in underground CO_2 storage and their scaling are not fully understood.

This work is funded by BRGM (Bureau de recherches géologiques et minières) under the 2nd issue of the COP BRGM project, "to engage in the energy transition", and is accomplished at ISTO (Institut des Sciences de la Terre d'Orléans), CNRS, in the porous media group under the thematic BRGM funding of Carbon dioxide capture and storage in deep geological reservoirs as a promising mitigation method. More precisely, this work addresses multiphase reactive flows in porous media by studying the physical and chemical mechanisms induced by CO_2 injection in deep saline aquifers and couplings between phenomena at different scales under various flow rates, wetting, and salinity conditions. The Ph.D. project is based on a multi-scale strategy using microfluidics experiments and GLoC (Geological Lab on a Chip)

concept. Experiments were mainly performed in the microfluidics lab, at ISTO. In the framework of collaboration, cleanroom facilities of GREMI (Groupe de Recherches sur l'Energétique des Milieux Ionisés) were used for microfluidic device fabrication and development.

Fluid movement in porous media is ubiquitous inside the nature of many processes of environment and industry. Enhanced oil recovery, carbon capture and sequestration, groundwater contamination, nano-particle deposition, and drug deliveries are examples of fields that porous media properties and related phenomena can play a notable role in the performance of the system [44]. For single-phase flow, usually, Darcy's equation, which can be obtained by averaging the Navier-Stokes equation over porous media for low flow rate, is being used. The Darcy equation is extended to multiphase flow using the concept of relative permeability for each phase. In this framework, relative permeability for each phase is only considered as a function of the saturation of the phase, and saturation of each phase is a function of pressure in the porous media, following saturation-capillary pressure ($S - P_c$) curves (see Fig. 1a and Fig. 1b respectively). In most large-scale studies of two-phase flow, these macroscopic rules are adopted, as it is explained in Dullien [35]. By consideration of saturation-relative permeability relation for an immiscible incompressible displacement, Buckley-Leverett propose an equation describing the displacement along the porous media with respect to time [25]. However, later core studies were not entirely explained by this theory since a sharp front, and piston-like displacement was not observed for many flow conditions, showing the assumptions of macroscopic laws are not always valid [10]. This is due to the fact that several factors such as viscosity, density, flow rate, porous media structural properties (e.g., pore size distribution, spatial relation, and pore shape), interface properties (e.g., dynamic and static contact angle and interfacial tension) affect the multiphase transport inside porous media and provoke front instabilities and induce fingering in the flow patterns; properties, which are not considered in the extended Darcy law for describing the two-phase flow. In this extension of the Darcy approach, it is assumed that small-scale phenomena have no or negligible effects on overall displacement. For example, it assumes the shear stress exerted on the interface has no effect on the displacement. That is to say, in general, it does not take non-equilibrium and inertial effects into account due to the assumption of low flow rate in porous media [95, 33, 151, 149]. Front instabilities lead to a reduction in the efficiency of the displacement by leaving some fluid behind as fluid clusters that reduce CO_2 storage capacity of the reservoir. To ensure a promising storage capacity, we have to obtain a better understanding of multiphase flow in porous media and have additional insights into the microscopic and macroscopic phenomena and mechanisms happening in porous media.

The study of immiscible displacement involves several mechanisms ranging from

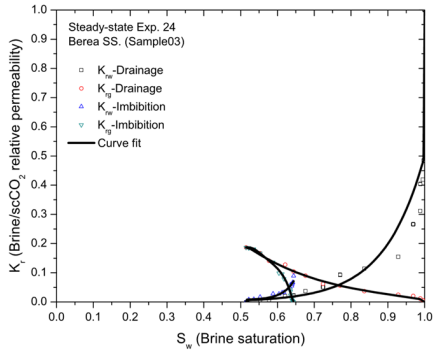

(a) $K_r - S_w$

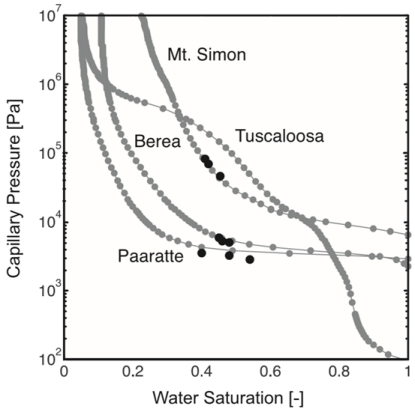

(b) $P_c - S_w$

Figure 1: (a) Experimental data for relative permeability with respect to saturation ($K_r - S_w$) for CO_2 and brine system, taken from [2]. (b) Experimental curves of pressure ($P_c - S_w$) for CO_2 and brine for different geological samples, from [68].

short to long distances that are coupled and affect each other in different time scales. In addition, the overall behavior of small-scale phenomena builds the front behavior and, by controlling over front behavior, they dictate the overall flow behavior. However, pore-scale phenomena are not fully understood. As an example, for a vast domain of fluid flow, it is well established that fluid invades porous media in the form of a series of abrupt jumps, known as Haines jumps[53]. However, the dynamics and length, and time scale of the phenomena are not fully understood.

In addition to the physical behavior of flow in porous media, coupling the physics of flow with kinetics of geochemical reactions in reactive flow through porous media (both single-phase and multiphase) leads to emergent phenomena that continuously change the transport properties of porous media. For example, in supercritical CO_2 sequestration, by the dissolution of CO_2 in the aqueous phase, acid ions are produced in a chain of reactions, then the produced ions are transported to minerals surfaces (e.g., calcites), and can react with the minerals. These reactions form the dissolution of minerals and releases ions that can react to other present chemical components and precipitate new minerals in the porous media. This coupling between flow and reactions that leads to alteration of porous media properties (porosity, permeability, etc.) is not thoroughly understood, and further studies are required.

Microfluidic devices provide the opportunity to study fluid transport in porous media by mimicking properties of natural porous media using a micro-scale artificial structure ($10^{-6} - 10^{-3} m$). These devices are used to conduct experiments with high-resolution analysis [44, 138]. There have been great improvements in fabrication techniques and design systems of microfluidics devices, and nowadays, there are vast methods and materials to fabricate microfluidics chips compatible with the

understudy system. Considering these properties and advantages, micromodels are an excellent choice for studying the fluid flow and reactions in porous media at a micro-scale.

The objective of this thesis is to study the underlying physics and chemistry of two-phase flow in porous media at the pore-scale, using well-controlled simple geometries for microfluidic experiments. This Ph.D. thesis has been conducted as follows: design of two-phase flow experiments, data acquisition for various flow rates and fluid properties, development of a theoretical foundation, design of reactive flow microfluidic experiments, data acquisition for various salinities, and pHs. This document is organized into seven chapters. In the first chapter, the state-of-the-art of physics of multiphase flow and reactive flow behavior in porous media is presented. In the second chapter, the experimental methodology and setup are introduced. The third chapter contains the fundamental two-phase flow theoretical developments. The fourth chapter goes through the experimental results of fluid front behavior and discusses the physics of multiphase flow in porous media. Chapter five concerns the role of corner flows in slow drainage in porous media. In chapter six, we present the developed methodology for studying reactive transport and discuss the effect of impurities on the reactive behavior of sequestration in carbonate reservoirs. We close the manuscript by summarizing and concluding this work in chapter seven.

Chapter 1

Introduction

Multiphase flow is ubiquitous in many natural and industrial processes such as Enhanced Oil Recovery (EOR), CO_2 sequestration, colloid transport, etc. In the process of CO_2 sequestration, one fluid phase displaces another in a porous media. Flow properties and fluid configuration in porous media vary from one to another based on the various displacing-displaced fluid properties (e.g., viscosity, wettability, interfacial tension, etc.), porous media properties (such as pore and throat size distribution, pore shape, connectivity, etc.), and porous media heterogeneity. Based on the relative affinity of the porous media surface to the displacing and displaced fluid, displacement processes are divided into two categories, "drainage" and "imbibition". Drainage takes place when the invading fluid displaces the wetting fluid (the fluid that has more affinity to the surface). Imbibition is defined as the opposite of drainage when the wetting fluid invades the porous media initially saturated with the non-wetting fluid.

At the continuum scale, an extension of Darcy's law for multiphase flow is used to describe the flow. Eq. (1.1) represents the one dimensional form of this extension for phase i, where $u_i, k_{ri}, \mu_i, P_i, K_{abs}$ and x represent respectively velocity , relative permeability, viscosity, pressure of phase i, absolute permeability and coordination axis representative of direction and length. K_{abs} is defined as the permeability of the porous media when it is fully saturated with the wetting fluid,

$$u_i = \frac{k_{ri} K_{abs}}{\mu_i} \frac{\delta P_i}{\delta x}. \tag{1.1}$$

For each saturation, the relative permeability is defined as the ratio of the measured permeability for each phase and the absolute permeability ($k_r = \frac{K_i}{K_{abs}}$). At first, a unique relation between relative permeability and saturation was imagined. However, the first signs of the inadequacy of this consideration appears by observing hysteresis effects, resulting in different permeability values for imbibition and drainage conditions for a given saturation. This is due to different flow paths adopted during each process, which also leads to irreducible nonwetting saturation after the imbibition. This non-

uniqueness of $k_r - S$ curves questions the Darcy equation application for multiphase flow at different flow conditions. Besides, the the Darcy equation is achieved by assuming steady-state or very stable displacement. In contrast, displacement processes can violate these conditions as is experimentally observed in core-scale ([10]) or in micro-scale using microfluidics ([142]), which is performing experiments in a 2-D replica of porous media. Based on core-scale experiments, Aryana and Kovscek [10] suggested that improvements in our physical understanding of multiphase flow is needed for a better assessment of unstable displacement.

Moreover, in CO_2 sequestration, the injected CO_2 dissolves into the brine and starts a chain of reaction, ranging from dissolution of reservoirs minerals to precipitation of new minerals. The change in the equilibrium condition and mineralogy of the system leads to deformation of pore structure and physicochemical properties alterations. Porous media evolves in different forms depending on the system geochemical properties (solid and fluid) and flow conditions. Understanding porosity evolution in porous media as a result of mineral reactions and its impact on fluid and solute transport is critical since it is a crucial component in the long-term behavior of underground storage systems [99]. The exact correlation between porous media petrophysical alterations, governing kinetic reactions, and flow conditions is yet to be discovered.

To better understand the main goals of this research, this chapter provides the state-of-the-art of facing challenges in the subsurface immiscible displacement process. Additionally, the specific methodology adopted to meet our goals is necessary to be discussed in comparison with available assets to have a clear view of how we tackle objectives. For this purpose, this chapter is organized as follows: first, the concept of multiphase flow is introduced and reviewed under two major parts: physics of flow, which focuses on the physics of transport either in single pores or highly connected porous media and reactive flow with a focus on the evolution of the porous media during reactive transport, both physically and chemically. Then, a short review of numerical models applicable to fluid displacement in porous media is presented. Next, the available experimental methods are shortly reviewed. Finally, the objectives of this research are presented.

1.1 Multiphase flow in porous media: state-of-the-art

One important challenge is to predict fluid behavior during unsteady-state multiphase flow. It was first presented in the work of Buckley et al. [25] that by considering the multiphase Darcy equation and applying the mass balance equation for a porous media during a two-phase displacement process, one can find a relation between

saturation and flow fraction (f) as a function of time and position, Eq. (1.2). ,

$$(\frac{dS_w}{dt})_x = -\frac{q_t}{A\Phi}(\frac{df_w}{dx}), \tag{1.2}$$

where $S_w, t, q_t, A, \Phi, f_w$ and x are respectively water saturation, time, total flow rate, flow area, porosity, water flow fraction ($f_w = \frac{q_w}{q_t}$) and distance. One important result of such a formulation is the stable displacement, displayed as the sharp saturation change at the front, see Fig. 1.1a which presents the saturation profiles and front movement in a displacement process for different injection volumes. However, experiments proved that several factors such as large viscosity difference between invading and resident fluids (large $\Delta\mu$), large density difference ($\Delta\rho$), heterogeneities in porous media, etc. leads to instabilities [10]. Especially when the viscosity of the invading phase is smaller than the resident fluid, the displacement process is prone to instabilities at the front. The saturation profile and the front position are different for each viscosity ratio. The lower the viscosity of invading fluid compared to the resident fluid, the higher the instabilities. This deviation with the Darcy equation is due to the violations of Darcy assumptions; the Darcy equation assumes stable and steady-state flow in porous media. That is to say, inertia effects are ignored in Darcy's assumptions. However, depending on the flow condition, inertia can be decisive for the front behavior during displacement processes. Viscous coupling is another phenomenon that is ignored in the Darcy equation. Rose [110] mentions that when viscous coupling happens in porous media Darcy equation is not applicable. These factors can cause front instability and affect the fluid flow. Additionally, Hassanizadeh and Gray [54] discussed some inherent inconsistencies in the application of the multiphase Darcy equation to describe fluid flow in porous media.

The efficiency of fluid displacement at a large scale is tied with the fluid behavior at the interface in porous media. Front instabilities affect the efficiency over a large span, from very low to very high efficient displacements. It is critical to know what factors dictate fluid front behavior to be able to have control of the displacement of the fluid inside porous media.

Two dimensionless numbers are commonly used to indicate the balance between active forces in porous media and multiphase transport. Viscosity ratio, which is a comparison of mobility of displacing and displaced phase, is defined as the ratio of the viscosity of displacing fluid (for drainage, non-wetting fluid, μ_{nw}) to the viscosity of displaced fluid (for drainage, wetting fluid, μ_w) $M = \frac{\mu_{nw}}{\mu_w}$. The capillary number is the other practical dimensionless number in multiphase flow. It is defined as the ratio of viscous forces and capillary forces $Ca = \frac{u_{nw}\mu_{nw}}{\sigma_{nw}\cos\theta}$. Where, u_{nw} is the non-wetting fluid velocity, σ_{nw} is the interfacial tension of the phases, and θ is the contact angle. These numbers are useful indications to describe different flow conditions and flow regimes

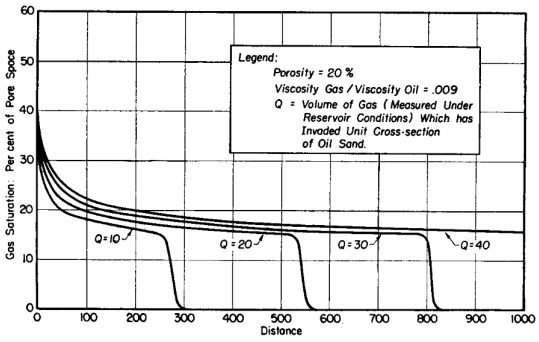

(a)

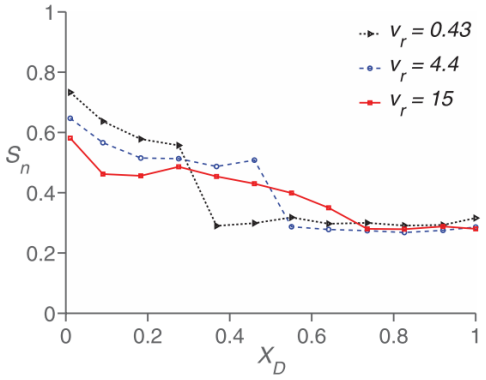

(b)

Figure 1.1: (a) Saturation history of oil-bearing sand under gas displacement, presenting the sharp front during unsteady-state flow, taken from Buckley et al. [25] (b) One-dimensional saturation profile for experiments with different viscosity ratios ($V_r = \frac{\mu_{resident}}{\mu_{invading}}$) for the time of 0.21 pore volume injection of invading phase, taken from Aryana and Kovscek [10]. It is depicted that by increasing the defined viscosity ratio the front instability has increased and the displacement saturation profile has deviated from the predicted profile of Buckley-Leverett equation.

[72].

In this section, we focus on drainage and, then, on imbibition displacement by presenting the basic flow regimes and invasion mechanisms for each flow condition. Next, we focus on interface instabilities and one important pore-scale mechanism for drainage, known as Haines jumps. Then, this section is closed by presenting underrated phenomena during the imbibition process known as precursor flow.

1.1.1 Front instability: drainage

Effect of flow regime and fluid properties

The study of fluid transport in porous media using micromodels goes back to the work of Lenormand et al. [73]. In this study, they explained the fluid behavior in terms of porous media characteristics, capillary pressure, and basic mechanisms, such as snap-off [1], etc., happening during multiphase transport in porous media. They also tried to attribute obtained pressure difference profiles for drainage and imbibition to these presented mechanisms. In the later work of Lenormand et al. [72] series of numerical simulations in comparison with experiments in etched micromodels were used for observing the effect of fluid and transport properties on mechanisms of transport. They used Ca and M as indicators for classifying various flow and fluid parameters. This characterizing methodology allowed them to sort their results in different flow

[1] Snap-off happens when the wetting fluid accumulates at a drained pore throat because of capillary forces and bridges across the throat. More information and details are be found in Rossen [112].

regime categories as the stable front, viscous fingering, and capillary fingering, both in experiments and simulations. The front is almost flat in stable flows, and none of or a tiny amount of displaced fluid is left behind. In the capillary flow regime, fluids are left behind in the form of small or large bodies, interface displaces fluid in all directions, including lateral and even backward movements, and loops in flow patterns or trapping a large cluster of displaced fluid are observed. On the other hand, the interface in viscous fingering is mostly oriented toward the outlet by making long narrow fingerings, and almost no loop is observed. Consequently, a tree shape flow pattern is indicative of this mechanism. The result of Lenormand et al. [72] work is presented in Fig. 1.2 and Fig. 1.3.

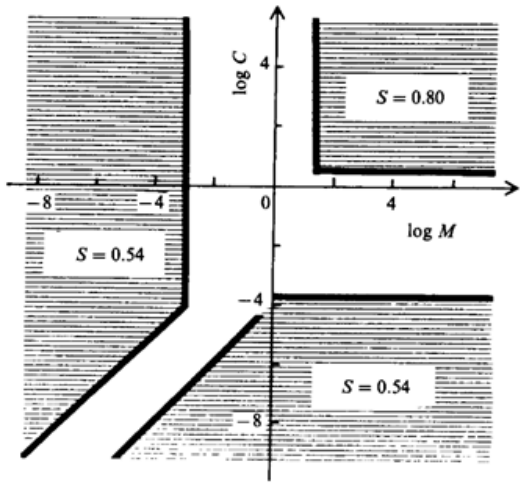

Figure 1.2: Diagram of different flow regimes based on Ca and M in logarithmic axis, from Lenormand et al. [72].

The same results were observed by later Zhang et al. [152] when they conducted series of immiscible fluid displacements to measure the impact of viscous and capillary forces on the stability of the displacement and fluid saturation distributions in a homogeneous micromodel device. The final saturation, fluid and interface distributions, and the global pattern in porous media were used as primary factors for flow regime definitions. Also, they defined some regions as crossover regions between stable and capillary fingering mechanisms and between viscous and capillary fingering mechanisms. In an experimental study of transitions in crossover region for supercritical CO_2-water drainage in a homogeneous porous media, Wang et al. [142] investigated three different flow regimes. The overall behavior of the invading fluid saturation in these three regions is presented in Fig. 1.4. They report that for low flow rates, while the capillary fingering is the dominant flow regime, the saturation of supercritical CO_2 increases a bit as the flow rate increases. On the other hand, at high flow rates (viscous fingering regime), by increasing the flow rate, the amount

of CO_2 saturation remains almost constant. It is worth mentioning that they found crossover flow regime has a lower saturation of supercritical CO_2 comparing to two other regimes. The differences in saturation, as is reported in Fig. 1.3, is primarily because of the change in the flow path and interface movement.

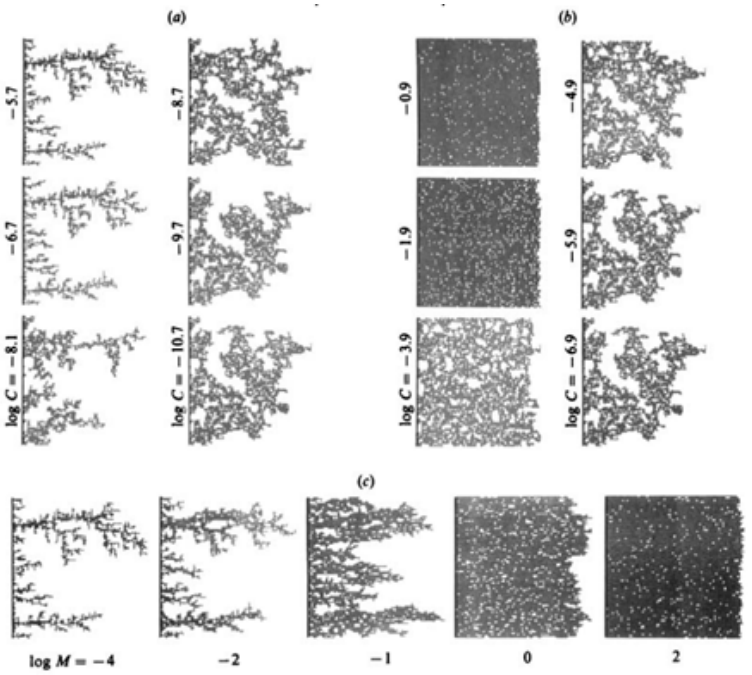

Figure 1.3: Result of the simulations of Lenormand et al. [72]. a) at constant $\log M = -4.7$ (from capillary fingering toward viscous fingering flow regime by increasing the Ca), b) at constant $\log M = 1.9$ (from capillary fingering flow regime toward stable displacement by increasing Ca), c) at constant $\log Ca = 0$ (moving from viscous flow regime toward stable flow by increasing the viscosity ratio M).

Zhang et al. [152] realized that, at viscous flow regime, although multi-branch fingering exists, after breakthrough (when the invading fluid reaches the outlet of the system), only one of these branches continues conducting the fluid, the preferential flow path. Conversely, at capillary flow regime, the flow will spread laterally over the micromodel and, after breakthrough, all the channels participate in fluid transport until the end of the experiment. In Singh et al. [115] the increase in residual saturation is linked with the effect of preferential flow paths and the interface ramification. This demonstrates how the flow regime and, as a result, the phase distribution can change the preferential flow paths and overall flow properties.

Haines jumps

Based on the work of Haines [53], it is unshakable that the drainage process and interface movement in porous media is composed of a series of abrupt jumps, known as Haines jumps. These jumps are associated with inertial effects, and sudden pressure

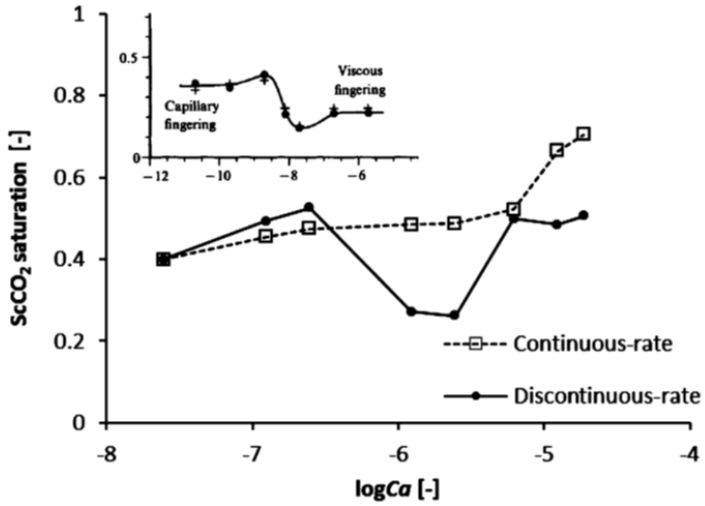

Figure 1.4: CO_2 saturation vs capillary number in discontinuous-rate and continuous flow experiments. For discontinuous-rate experiment, the micromodel is saturated with water and then injection is started with favorable rate until it gets to quasi-static condition. For the continuous-rate experiments, experiments are started with the lowest flow rate and as soon as reaching the quasi-static condition, the flow rate is increased and kept constant until it reaches quasi-static condition again. Results of discontinuous experiments are in agreement with work of Lenormand et al. [72] as presented in top left corner of the graph (taken from Wang et al. [142]).

fluctuations [77, 3] for fluid transport, see Fig. 1.5. It is suggested that these inertia effects rule the invasion mechanisms thoroughly, and change invasion dynamics [41, 84]. The change in invasion patterns results in different residual saturations, flow paths, and large-scale behavior. Singh et al. [115] report based on experimental observations that the main reason for the ramified front and residual saturation is the preferential paths that fluid takes as a result of Haines jumps in slow drainages. They found a relationship between the frequency of Haines jumps and the residual saturation, based on governing Haines jumps probability function and comparing it with the residual saturation data. On the other hand, Moebius and Or [84] investigated the effect of inertial dynamics on the flow patterns and reported that inertial forces are not able to change the invasion patterns and residual saturations. Still, the role of momentum forces on the front is not well understood and needs to be investigated.

Understanding Haines jumps plays a crucial role in understanding the interface transfer and, in general, multiphase flow in porous media. Nevertheless, this interfacial process dynamics and origin are not thoroughly understood.

By comparing the interface velocity and average fluid velocity, measurements show that the interface velocity is different from the mean flow velocity. In the work of Roman et al. [107], the interface velocity is reported to be 2-3 orders of magnitude greater than the mean velocity in terms of Reynolds number. In the study of Moebius and Or [83], the interface velocity reaches up to 50 times the mean velocity due to the

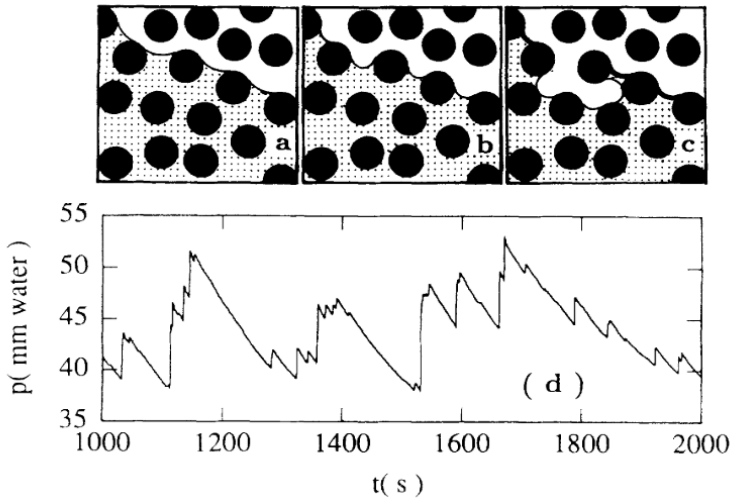

Figure 1.5: (a)-(c) Invasion of air into a glass-beads pack saturated with water. The interface first reforms before the invasion and after invasion finds a new configuration adjusting a lower capillary pressure. (d) water pressure as a function of time, taken from Måløy et al. [77]

Haines jumps at the interface, happening at throats. It requires a more elaborate study and characterization to understand the dynamics of Haines jumps.

By using micro-PIV[2] technique in research of Roman et al. [107], sudden movements far from the interface in the body of the defending fluid, and some pressure oscillations, velocity changes and perturbations in areas near the interface were observed. They relate these movements to the abrupt displacement of the interface during Haines jumps and as proof of long-range effects of this phenomenon on streamlines. The same results were reported by Blois et al. [18]; they observed that the interface disturbs the fluid velocity pattern in resident fluid before it reaches the measurement point. As a result, although the porous media is still saturated with the defending fluid, fluid flow does not occur with the same pattern as it had in steady-state single-phase flow. In some cases, the velocity field is more intense at pore bodies rather than pore throats, contradictory to what usually is the expected pattern for single-phase flows[18]. Armstrong et al. [9], report a certain pressure gradient in porous media over which flow occurs due to interfacial instabilities. It was concluded that fluid acts in a pressure gradient field on the microscopic scale, which changes instantly and continuously and does not follow the overall macroscopic pressure gradients. In other words, capillarity is a nonlocal process involving capillary pressure difference that spans over several pores over the porous media geometry. In addition, flow instabilities such as Haines jumps have a significant impact on the pressure field, and its effects may propagate downstream and upstream [18]. This

[2]Particle Image Velocimetry, a more detailed definition of this technique is presented in Section 1.4.1 and also in Chapter 2.

demonstrates the effect of mechanisms at the microscale on the preferential flow paths of the fluid and connectivity of side pores in terms of decisive effects on flow patterns. In other words, these phenomena emphasize the importance of taking into account the local mechanisms related to the drainage processes and macroscopic effects linked with the topology of the nonwetting fluid[107].

Moebius and Or [83], in their studies of the dynamics of drainage at pore-scale, report very distinguishable pressure burst in pressure records. These pressure fluctuations are attributed to fluid jumps, which show interfacial relaxations by capillary, viscous, gravity, and inertia forces. They report Haines jumps as the main pore invasion mechanism at low withdrawal rates and mention that interfacial jumps and pressure bursts tend to be separated and clearly distinguishable from pore to pore. For higher flow rates, however, jumps start to interfere with each other to the point that they turn into avalanche-like invasions, in which several pores are being invaded at the same time. These results agree with the model they present, and they suggest that the amplitude of these pressure fluctuations is a function of the dimension of the pore throat, its interaction with adjacent pores, and components such as roughness. This is critical to point out that interfaces at different pores are connected to each other [83, 8] and are able to affect the other interface dynamics and, as a result, invasion pattern. Keeping in mind the aforementioned parameters, further studies are required to elucidate the role of these factors.

The state-of-the-art shows the critical role of Haines jumps in multiphase flow in porous media. It seems that these jumps shape the displacement and interface and have an undeniable effect on the porous media flow regime and near interface flow behavior. Nevertheless, these jumps dynamics and time, length scale, and affecting factors are not clear. To investigate the origin and consequences of Haines's jump, we focus on pore-scale mechanisms in this study.

Porous media morphology: side pores effect

In this section, we present studies dedicated to the dynamics of Haines jumps and their connection with the fluid dynamics and interface movements in adjacent pores.

Armstrong et al. [9], studied the transient dynamics of Haines jumps and reported velocity of the interface at the pore for different flow rates, see Fig. 1.6. Based on their simulation results, they suggest the velocity of jumps are not dependent on the flow rate (Fig. 1.6) as it was suggested in their previous work [8]. Additionally, they propose a direct correlation between viscosity of non-wetting phase and time scale of the event and an inverse correlation, and an inverse relation between interfacial tension and time scale of Haines jump. In other words, the duration of the pore invasion increases by increasing the viscosity or decreasing interfacial tension.

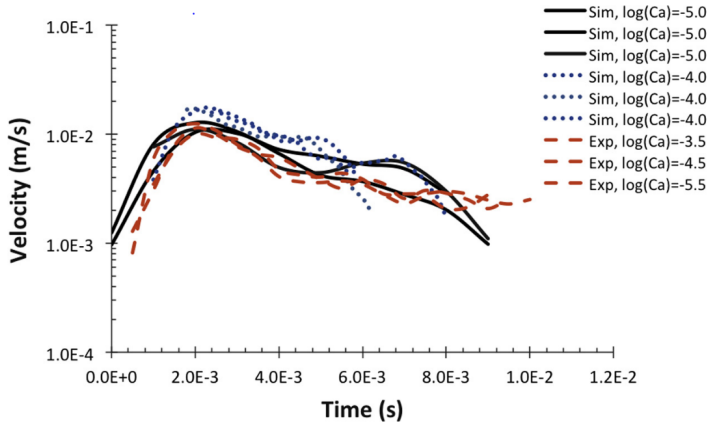

Figure 1.6: Independency of interfacial jumps with imposed flow rate [9].

Armstrong and Berg [8] report that the dynamics of Haines jumps is also a function of the morphology of porous media and the configuration of the interface. It was observed that fluid volumes in throats provide a part of drainage volume. When a pore is drained, some adjacent necks were imbibed to supply the fluid volume in the drained pore. It was observed that there is a direct relationship between the maximum interface speed and the ratio of throats volumes near the invaded pore to the volume of the pore. The more the ratio was, the faster the jumps were. In addition, when invading fluid was invading two similar pores simultaneously, the pore with more throats around dominated the invasion and inhibited other invasions from happening. Furthermore, studies of dynamics of interface jumps show that the front speed varies during the drainage process of pores [8]. In the beginning, the speed reaches a maximum and then decreases to an approximately constant value. Calculations of power-law coefficient for the displacement of the interface at different stages of the invasion of a single pore (i.e., distance versus time) reveals different flow regime before and after the maximum velocity of the interface during jumps. This difference in power-law coefficient is attributed to the difference in driving forces of each of identified flow regimes. Prior to reaching the maximum velocity, capillary forces[3], and the topology of porous media have a great impact on the displacement behavior of the interface.

One noticeable result is that Ca is not always a proper indicative for multiphase flow in porous media as Armstrong et al. [9] found different interfacial dynamics for the same capillary number by manipulation of fluid viscosity and interfacial tension (increasing and decreasing respectively), see Fig. 1.7. Additionally, Ca does not

[3]The pressure difference between the interface at adjacent pores and at the invading interface. It is worth mentioning that in the work of Armstrong and Berg [8], the Young-Laplace equation is used to calculate the capillary pressure. More details and information on the Young-Laplace equation are presented in Appendix A.1.

consider the morphology of porous media; hence, it is susceptible to fail to predict interface behavior for different morphologies and fluid distributions.

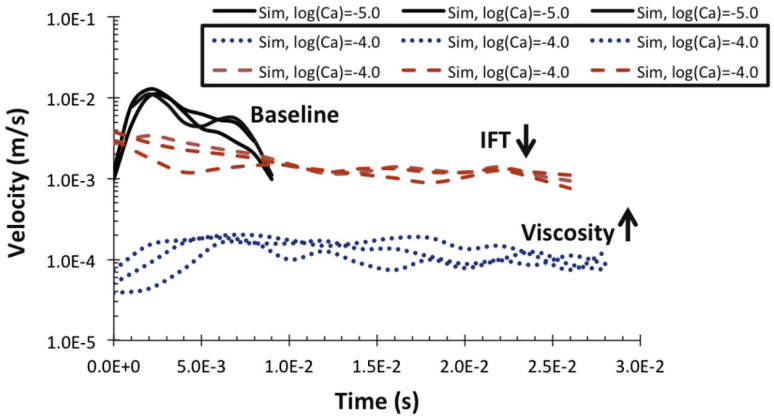

Figure 1.7: The front velocity with respect to time for different capillary numbers. First, the velocity calculations are performed for $\log Ca = -5$, then by alteration of interfacial tension and viscosity, decreasing and increasing respectively, front velocity at $\log Ca = -4$ is calculated [9].

Based on the behavior of the interface at irregular capillaries during pinning-jumping behavior of interface in the study of Moebius and Or [83], as a result of the relaxation of active forces, jump in one channel resulted in retreating and oscillation of interface in the other channel. These oscillations are normally related to inertia forces. Very clear interface oscillation and pressure burst are observed for low withdrawal rates both experimentally and numerically, Fig. 1.8; in higher flow rates, however, jumps started to happen more frequently and to interfere with each other until they were not distinguishable. The amplitude of these pressure fluctuations is a function of the dimension of the pore throat, and its interaction with adjacent pores. It is worth mentioning that the effect of pore shape and corners are not considered here.

1.1.2 Front instability: imbibition

The surface forces are at the heart of all the fluid and front dynamics that result in distinct displacement processes in porous media. For the ultimate goal of harnessing porous media, understanding these forces and how they control the front and fluid movement is critical. For this purpose and to cast a new light on surface phenomena and transport in porous media, the imbibition condition plays a significant role besides the drainage state. Additionally, imbibition is an important part of natural and engineering processes. It is also worth keeping in mind that recent studies, presented later in this chapter, show that even in drainage conditions, invasion of wetting fluid is happening in certain places due to inter-connectivity of the interface, which is discussed in the last section [8].

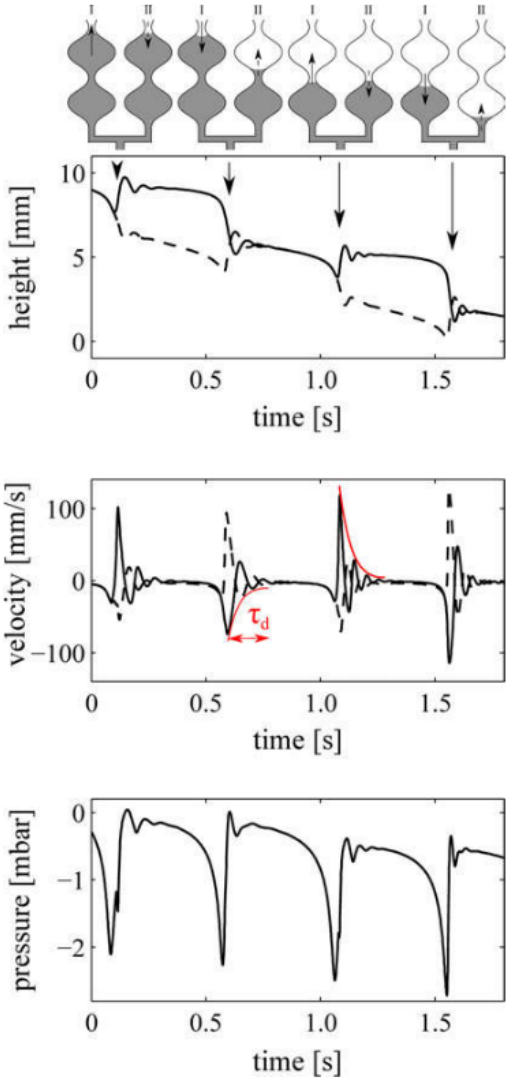

Figure 1.8: Interface position, velocity and pressure records, respectively from top to bottom, for a double sinusoidal channel [83]. Pining-jumping behavior and oscillation at interface is clear based on the sudden change of interface position, drastic changes in velocity and pressure records and oscillation interface position plot and alteration of velocity sign.

Zhao et al. [154], studied a variety of wettability conditions ranging from strongly wet to strongly non-wet surfaces, and three capillary numbers were used during a viscosity unfavorable condition, i.e. $M < 1$, to investigate the influence of wettability on the displacement front. Different flow patterns and displacement mechanisms were observed similar to the presented flow patterns in the drainage condition. In fact, various imbibition flow regimes are categorized based on their propagation pattern through the porous media in the work of Lenormand [71] in terms of an imbibition flow phase diagram. Additionally, Lenormand [71] pronounce the role of film and corner flows on the fluid imbibition, fluid accumulation, and pore occupation.

In the work of Zhao et al. [154], it was observed that by increasing the affinity of the

surface to draining fluid, before some limit, the efficiency of displacement increases; however, by improving the wettability of the imbibing fluid after the mentioned limit, the efficiency drops and the invading fluid saturation reduces drastically. Fluid in this regime covers the surface of channels by thin films, known as precursor film, and defending fluid remains at the center of the channel. The other noticeable finding of this paper is that by increasing Ca, the fluid saturation and, as a result, the displacement efficiency reduces. In the wetting condition, i.e., imbibition, wetting fluid tends to flow from corners of porous media, and a large portion of defending fluid remains in pore space. Fig. 1.9 is a summary of mentioned results. These results are in agreement with observations of Lenormand [71] on precursor films.

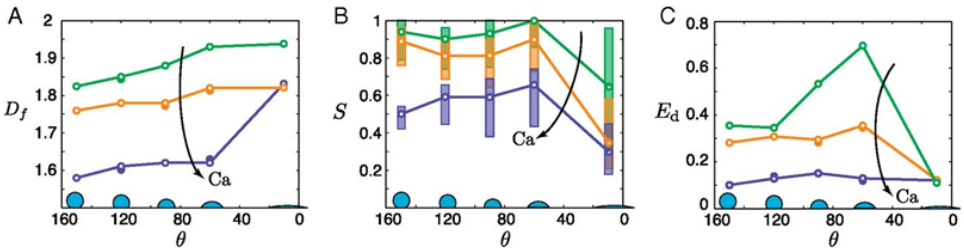

Figure 1.9: Results for a vast range of wettability and different capillary number (D_f is fractal dimension, S invading fluid saturation, E_d displacement efficiency and θ is the contact angle) [154].

Tanino et al. [131], used a crushed marble pack with low wettability to study displacement mechanisms for three flow conditions indicated with three Ca. It is observed that the saturation at the end-point is not a function of flow rate for their experiments, although it is already mentioned that many factors as wettability, roughness, etc., affect the results. On the other hand, the saturation of the wetting fluid in porous media was in inverse relation with the capillary number for early injection times. In other words, the lower the flow rate is, the higher the wetting phase saturation will be inside the column. This is attributed to the prominence of precursor films at low flow rates and their transition to piston-like displacement mechanisms by changing the flow rate. Nevertheless, this phenomenon length scale and involved parameters remain a question. As it is noticeable in Fig. 1.10, for low capillary numbers, the precursor film is the dominant mechanism of invasion for early times of experiments and fluid covers the surface of the porous media all the way from the inlet to the outlet.

Some studies focused on the phase distributions and flow paths during the imbibition process. In the work of Blois et al. [18], after performing a series of imbibition experiments, besides the trapped non-wetting phase, some wetting phase parts were found to be stagnant with zero velocity vectors. It demonstrates that these parts of the wetting phase do not participate in the main flow, affecting overall permeability and pore connectivity. This phenomenon results in some preferential flow paths referred

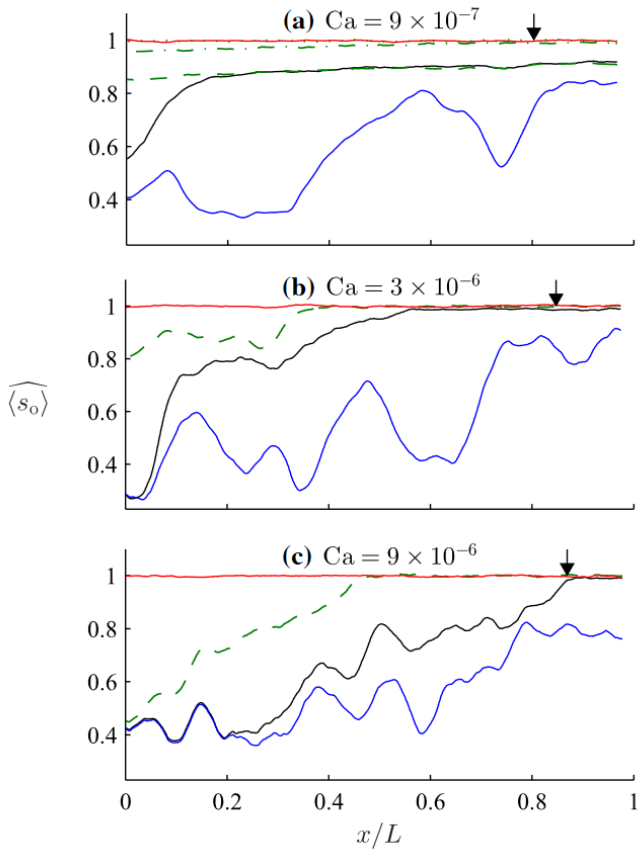

Figure 1.10: Instantaneous, width-averaged oil saturation as a function of distance along the packed bed at the beginning of water injection (red), at water breakthrough (black), and 200 s after breakthrough (blue) at Ca=9×10-7 (a), 3×10-6 (b), and 9×10-6 (c). Depicted lines correspond to intermediate times t-tb=-200.6 (a green dotted), -121.2 (a green dashed-dotted), -30.0 (a green dashed), and -3.9 s (c green dashed), respectively. [131].

to as channeling. These channelings vary in time (sudden flow direction deviation, etc.) because of competition of viscous dissipations and elastic energy accumulated via capillary forces.

These studies illustrate that the fluid front can be further ahead of the apparent front in the form of corner flows and precursor films. There is still a lot to know on this subject, such as how far this film moves, what can affect its thickness, how they operate in the context of porous media and overall flow regimes, and what their role is in imbibing a pore in porous media.

In this section, Darcy-scale multiphase displacement is presented. Then, it is mentioned that in several conditions, Darcy's assumptions are not valid, and displacements deviate from Darcy's prediction, e.g., when inertia forces or viscous couplings are comparable to other active forces. These conditions lead to different front instabilities that must be studied in pore-scale. These instabilities are categorized, and different

properties of them are defined. After, Haines jumps are introduced as one of the main pore invasion mechanisms that are associated with inertia effects and can disturb flow patterns and be decisive on flow and front behavior. Later, the dynamics of Haines jumps, the effect of these jumps on fluid and interface behavior in adjacent pores, and its effect on fluid configuration based on porous media morphology are presented. Next, the effect of wettability on the flow regime and front behavior is discussed, and precursor flows are mentioned as an important factor in the fluid configuration in porous media in imbibition conditions. Here we studied how the physics of porous media and flow can change the transport in porous media. The following section focuses on the coupling between transport and reactions in the porous media and how it will modify the flow patterns and porous media.

1.2 Reactive transport in porous media during the CO_2 sequestration process

Reactive transport in porous media is a key process in both industrial and natural applications, such as erosion due to acid rain, porous media reactors in chemical engineering, subsurface mineral dissolution, and precipitation caused by acid injection in EOR processes and CO_2 sequestration. Mass transfer between the solid and liquid phase leads to porous media physical and chemical properties alteration, leading to rock petrophysical and physicochemical properties alterations, such as porosity and absolute and relative permeability. The physics of these alterations are mostly due to the change of pore shape, connectivity, and pore size distributions [99]. These alterations are a result of various complex couplings of small-scale processes taking place in porous media. In the process of CO_2 sequestration, porous media pattern and transport properties dictate the displacement main flow paths and fluid configurations. The geochemical properties of porous media indicate in-place minerals and their interaction with adjacent phases. Keeping these in mind, fluid-fluid interface interactions add more complexities to the process, see Fig. 1.11 [125].

Fig. 1.11 is an abstract presentation of the interaction between different phases at pore scale (at fluid-fluid and fluid-solid interfaces). Injected CO_2 dissolves into the aqueous phase and forms carbonic acid. Carbonic acid dissociates to bicarbonate ion and proton according to Eq. (1.3) and Eq. (1.4). As a result, pH reduces in the aquifer. These ions, either by diffusion or advection, are transported through porous media, and if they get in contact with minerals that are susceptible to dissolution in low pH, e.g., calcite, the solid phase of porous media dissolves into the aqueous phase. These ions react with other present ions (either released by dissolution or already existing in the equilibrium state) and result in precipitation of secondary minerals [125, 121].

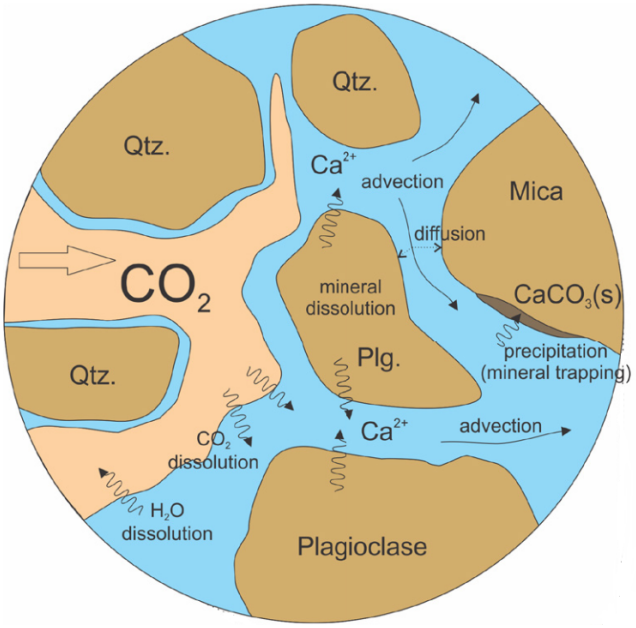

Figure 1.11: A pore-scale schematic of physical and chemical processes during CO_2 sequestration [125].

These dissolutions and precipitations change the transport properties of the porous medium.

$$CO_2 + H_2O \rightleftharpoons H_2CO_3 \tag{1.3}$$

$$H_2CO_3 \longrightarrow HCO_3^- + H^+ \tag{1.4}$$

The transportation of ions plays a significant role in this interplay between phases. Hence, the dominancy of each type of transportation results in different interactions of fluid and solid phases and, as a result, different alterations of porous media. For example, at low flow rates, the characteristic time scale of reactions is lower than the ion transportation time scale. The transported ions, therefore, are consumed as soon as they enter the media and form a compact dissolution [121]. On the other hand, when the flow rate increases and the transport time scale is comparable or lower than the reaction time scale, different dissolution patterns appear in porous media, as are described and presented in Soulaine et al. [121].

Two dimensionless numbers are defined to indicate transport and reaction conditions in porous media. Pe, Peclet number, is the ratio of mass transport rate by advection to transport rate by diffusion,

$$Pe = \frac{vl}{D}, \tag{1.5}$$

where v, l and D represent velocity, characteristic length scale and diffusion coefficient

respectively. Second Damköhler number, Da_{II}, is defined as the ratio of reaction rate and diffusive mass transfer rate at fluid/solid interface. It is defined as

$$\frac{rl'}{D}, \tag{1.6}$$

where r, l' and D respectively represent reaction rate constant, characteristic length and diffusion coefficient.

For studying reactive flow in porous media and emergent behaviors, the pore scale is critical since it contains the framework that smaller-scale (nano and molecular scale) phenomena happen [125] while keeping the coupling between different mechanisms. Moreover, it provides the chance to study reaction-induced porosity, permeability, and the system reactivity changes. Micromodels are ideal tools to study flow and porous media behavior at pore-scale, given that it provides us the perfect control on porous media geometry and mineral distribution in addition to the ability of direct monitoring of the system. Furthermore, in this method, we control the chemical system and pore environment. Later in this chapter, we present the state-of-the-art of pore-scale reactive flow study and the ability of micromodels to capture different stages and mechanisms for a deeper understanding of the coupling between flow dynamics and kinetics of the reaction.

The first quantitative measurements of ramified patterns produced by reactive flow through porous media is found in the work of Daccord and Lenormand [29]. They address fractal properties of dissolution patterns and present different dissolution patterns for different flow and boundary conditions. Fig. 1.12 shows different dissolution patterns of their work. Later, they presented a model to predict the cumulative deformation of dissolution structure for a limited case, [28].

Daccord et al. [30] studied the dissolution patterns with a focus on the impact of transportation mechanisms and reaction types. They defined three different regimes and categorized them in a $Pe-Ki$ phase diagram, where K_i is the kinetic dimensionless number and is defined as $Ki = PeDa$. They defined three major regimes.

Convection-limited condition is defined as a condition in which convection is very low with respect to reaction, and reaction kinetics are limited by injection rate. They mention that typically this regime results in compact dissolution patterns. Mass transport-limited is defined when convection rate and reaction rate constants are high, so the reaction is limited by the mass transportation to the interface. Normally, dissolution occurs as dissolved channels known as wormholes, similar to viscous fingering in a shape-oriented point of view. Dissolution is surface reaction-limited when a high convection rate couples with a low reaction rate. Daccord et al. [30] mention that a surface reaction-limited regime leads to a uniform dissolution. See

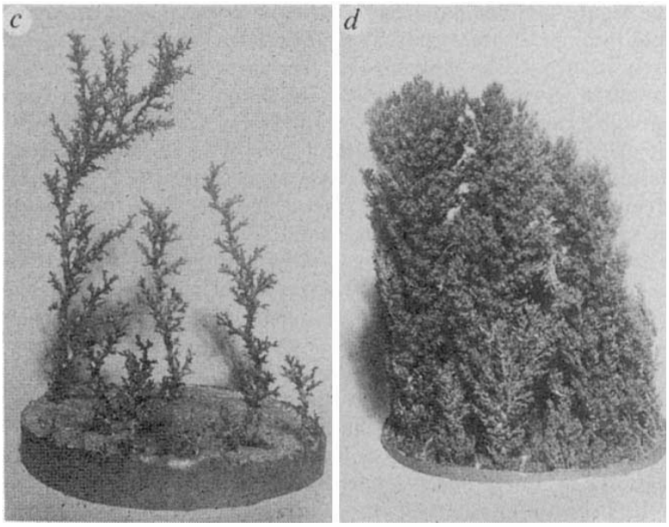

Figure 1.12: Dissolution patterns based on different flow rates, Daccord and Lenormand [29].

Fig. 1.13, where dissolution patterns are presented as a phase diagram.

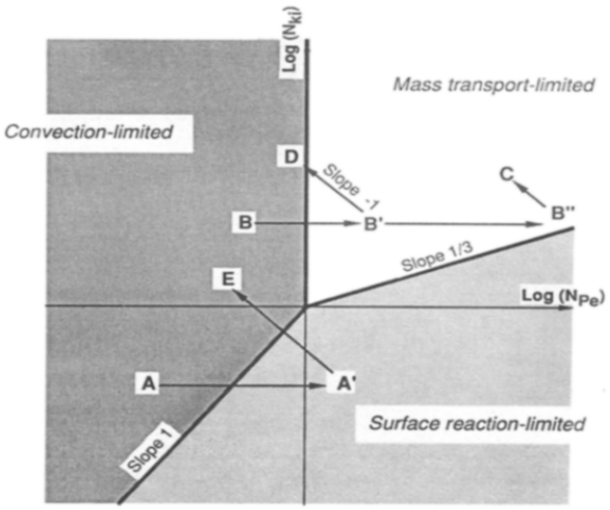

Figure 1.13: The presented behavior diagram by Daccord et al. [30] for dissolution patterns in porous media based on Pe and Ki.

Later works focused on the effect of transport and reactivity on the whormholing and dissolution patterns [42, 46, 128]. In the work of Golfier et al. [46], a Darcy-scale model to quantitatively describe the coupling between fluid flow and reaction was presented. They categorized resulting dissolution patterns into five categories, face dissolution, conical wormhole, dominant wormhole, ramified wormhole, and uniform dissolution. It was confirmed later in the work of Soulaine et al. [121]. Results were presented both in $Pe-Ki$ and $Pe-Da$ phase diagrams, see Fig. 1.14.

A very stable front is observed in facial (or compact) dissolution. In this domain, solvents or acids are transported only by diffusion to the solid surface. As a result,

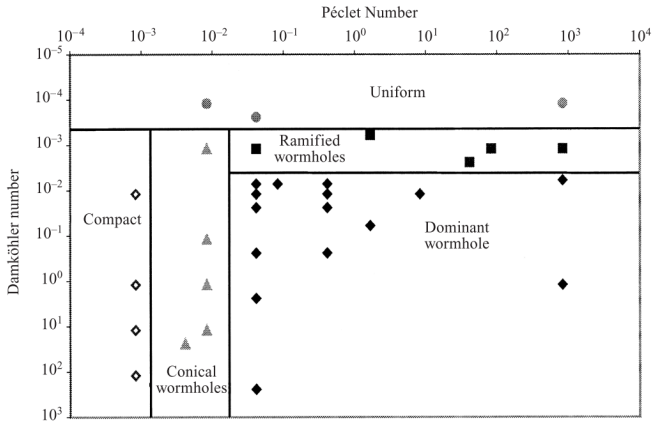

Figure 1.14: Dissolution patterns phase diagram based on the results of Golfier et al. [46].

concentration is homogeneous at the cross-sections to the flow Fig. 1.15(b). Conical wormholes are representative of the condition that the dissolution is mainly diffusion-dominated, but convections are effective as well. For this reason, fluid flow drags the dissolution front toward the main stream and makes a conical pattern Fig. 1.15(c). For a dominant wormhole, the transportation of chemical components to the matrix happens mostly by advection. The dissolution, therefore, follows the higher velocity domains, and since the diffusion is weak in comparison with advection, dissolution is limited to the surrounding matrix Fig. 1.15(d). When the advection is the dominant transport mechanism, fluid flow forms multiple dissolution pathways and ramified wormholes Fig. 1.15(e). When the characteristic timescale of reaction is more than transportation time, the solvent is transported to the whole porous media (by diffusion or advection), and all the porous media is affected the same and results in a homogeneous dissolution all around the porous media Fig. 1.15(f).

Most researchers adopted $Pe - Da$ to present their results in dissolution phase diagrams. Szymczak and Ladd [128], studied the dissolution of fractures using a lattice Boltzmann method coupled with a stochastic solver to account for fluid flow and solute transport, respectively. They studied the effect of porous media geometry, flow rate, and dissolution rate to obtain the optimal condition for wormholing. The presented phase diagram was in agreement with previous works. Besides, the effect of constant flow rate and constant pressure drop were investigated, and results show a more intense erosion for constant flow rate conditions.

In the work of Soulaine et al. [121], a micro-continuum approach was used for studying mineral dissolution from a pore-scale point of view. They found that both grain shape and flow pattern change during different flow and reaction conditions.

The effect of reaction rates and transport mechanism on porous media evolution and wormholing resulted in 5 different categories of dissolution that were in agreement

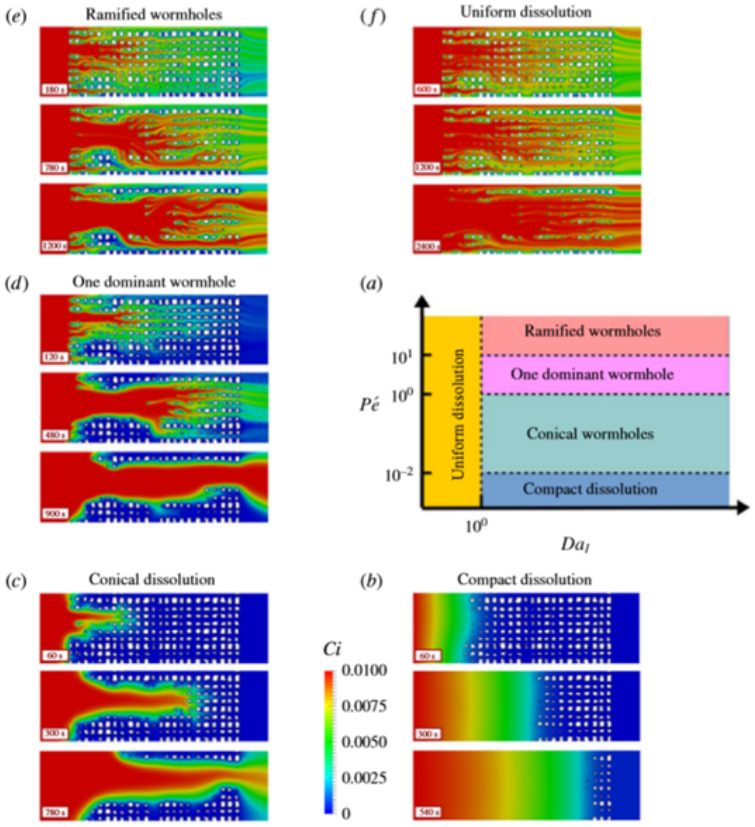

Figure 1.15: Different dissolution patterns based on Pe and Da [121].

with previous works. However, the transitions between different patterns were not the same. At low Da, the dissolution led into uniform dissolution. For higher Da, based on the Pe, the following flow regimes were observed from low to high Pe correspondingly: compact dissolution, conical wormholes, one dominant wormhole, and ramified wormholes, see the phase diagram in Fig. 1.15 and compare with Fig. 1.14.

Later, in Soulaine et al. [122], they extended their work to two-phase dissolution, where CO_2 bubbles are created during the dissolution process of calcite. They showed that the gas phase limits the transportation of the acid in the porous domain and prevents the emergence of wormholes, and limits the average dissolution rate, see Fig. 1.16.

In general, the emergence of non-soluble products as a result of mineral dissolution alters the storage, flow, and reactivity properties of porous media. One of the most important and frequent examples of this alteration is the precipitation of secondary minerals in the porous media and its effect on porosity. These dissolution and precipitation processes are results of complex coupling between physical and chemical processes. By dissolution and precipitation in porous media, the physics and chemistry properties of flow are altered, resulting in different dissolution and precipitation patterns. Understanding the relationship between precipitation (porosity changes) and flow properties (permeability) alteration plays an important role in better

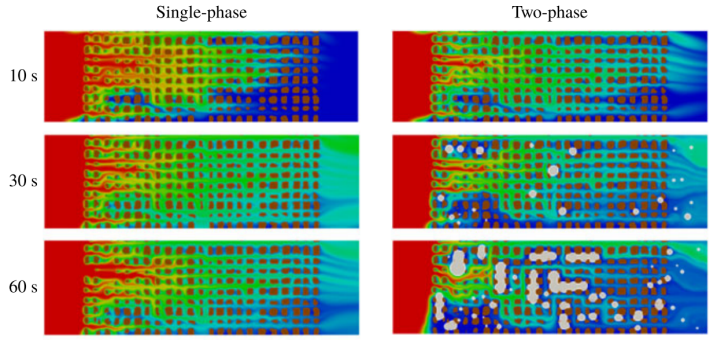

Figure 1.16: Comparison of single- and multiphase dissolution. Undissolved produced CO_2 appears as bubble form on the mineral surface and changes the flow patterns; by growing in size, bubbles might detach and move through the porous media or block some paths [122].

understanding the system.

For predicting the relation between porosity and permeability, Kozeny-Carman equation is a well-established semi-empirical equation, Equation (1.7). Where k, ϕ, τ, and s represent permeability, porosity, tortuosity, and specific surface area, respectively. By considering the validity of this equation, few works have developed empirical equations to predict the permeability of porous media after alteration by mineral precipitation. Xie et al. [147], and Poonoosamy et al. [101], simplified the relation between primary and secondary permeability using Eq. (1.8) and Eq. (1.9) respectively;

$$k = \frac{\phi^3}{\tau(1-\phi)^2 s^2}, \tag{1.7}$$

$$k = k_0(1-\phi_0/1-\phi)^2(\frac{\phi}{\phi_0})^3, \tag{1.8}$$

$$k = k_0(\frac{\phi}{\phi_0})^3, \tag{1.9}$$

where k, k_0, ϕ, and ϕ_0 represent secondary and primary permeability and porosity, respectively.

These equations are not extendable to all conditions and porous media since the calculated amount for any change in porosity does not take into account the variation of pore geometry, connectivity, pore and throat size distribution, and main flow paths in porous media. As a result, it is important to have information on the conditions affecting nucleation and precipitation of minerals on the solid surface and mineral dissolution conditions to estimate the pore alteration rate for different pore properties.

One important factor is the pore size dependency of the precipitation process in porous media. There is a diverse discussion on this topic. Borgia et al. [22] consider no precipitation pore size dependency in their model for salt precipitation during thermal energy recovery using CO_2. Emmanuel et al. [37], observed quartz precipitation in

smaller pores is inhibited due to interfacial energy of small pores, which increase solubility. Hedges and Whitelam [55], predicts theoretically that the smaller pores are preferential pores for precipitation. This controversy on pore size dependency of precipitation in porous media arises from the fact that several other factors such as precipitation composition, solution condition, and flow condition in porous media affect the precipitation in different systems [124].

1.2.1 Carbonate systems and CO_2 sequestration

One important system for CO_2 sequestration process is carbonate minerals (calcite and dolomite) rich system. The plausible dissolution and precipitations during the sequestration process in these systems can significantly impact the process and are necessary to be studied. Dissolution of carbonates during CO_2 sequestration has a great impact on reservoir porosity, and permeability [125]. CO_2 dissolution in aqueous phase and proton and bicarbonate ion formation as a result of chain reactions Eq. (1.3) and Eq. (1.4) lowers the pH.

By reducing pH in the aqueous phase, the balance of the chemical system moves toward reducing carbonate formation in the aquifer. In addition, by dissolution of more CO_2 in the aqueous phase and as a result reduction of pH ($pH = 4-5$ [24]), carbonates dissolve and form carbonate ions.

$$\underset{\text{Calcite}}{CaCO_{3(s)}} + H^{+}_{(aq)} \longrightarrow Ca^{2+}_{(aq)} + HCO_3^{-}{}_{(aq)} \tag{1.10}$$

$$\underset{\text{Dolomite}}{CaMg(CO_3)_{2(s)}} + 2\,H^{+}_{(aq)} \longrightarrow Ca^{2+}_{(aq)} + Mg^{2+}_{(aq)} + 2\,HCO_3^{-}{}_{(aq)} \tag{1.11}$$

By exposure of the products to sulfate ions (produced by dissolution of other minerals or dissolution of SO_2), gypsum is produced.

$$Ca^{2+} + SO_4^{2-} + 2\,H_2O \longrightarrow CaSO_4 \cdot 2\,H_2O \tag{1.12}$$

Precipitation of gypsum changes the carbon capture capacity of the aquifer, reduce the permeability of the porous media and flow patterns, resulting in different dissolution and wormholing patterns. Besides, by covering the carbonate minerals surfaces, leads to reduction of reactive surface area of the porous media.

Although kinetics of carbonate dissolution and precipitation are studied before, to the best of our knowledge, the dynamics of these phenomena coupled with fluid flow in porous media is not studied and well understood at pore scale. Moreover, the kinetics of mineral dissolution and precipitation is fundamentally dependent on

kinetic parameters such as the available reactive surface area [127, 56]. So far, the definition of pore-scale parameters describing the induced mechanisms is lacking for understanding mineralogy alterations. In this research we aim to quantify dynamics of evolution of carbonate system resulting from dissolution and gypsum nucleation using microfluidics, resembling CO_2 sequestration with SO_2 impurities.

As presented, pore-scale is an important study scale for either the physics of multiphase flow or the study of reactive flows. These studies could be performed experimentally or using numerical methods. The following section presents a short review of the available numerical models for simulation of fluid transport and reaction at the pore scale.

1.3 Numerical methods for pore-scale simulations

On large scales, single-phase simulations are based on the idea that properties of the subsurface media are constant over the representative elementary volume (REV) and structural details can be averaged [80]. The REV properties are extensively used in large-scale simulations of multiphase phase flow in subsurface media, taking the relative permeability concept as an example. However, due to the complex behavior of porous media at different flow conditions, including the hysteresis behavior of porous media, it can not be simulated by saturation-relative permeability relations that are derived for a REV of the reservoir.

Pore-scale simulations are essential, as the large-scale behavior of displacement is closely related to pore-scale behavior. Additionally, it is easier to have control on boundary conditions, the geometry of porous media, and fluid and porous media properties in simulations in comparison to experiments [80]. Considering pore-scale physical and chemical processes, including the interfacial behavior, demands a very fine resolution. Having existing computational limitations in mind, two types of pore-scale simulations exist. One type sacrifices having a larger under-study domain for having the high resolution of the porous media geometry (such as Boltzman method, particle method, and grid-based direct numerical simulations). The other category compromises the fine resolution of porous media geometry over consideration of a larger domain of porous media by assuming the porous media as a network of pores connected with channels (Pore network modelings) [125]. One other approach is micro-continuum approach, where continuum-scale concepts are combined with the pore-scale process modelings [125].

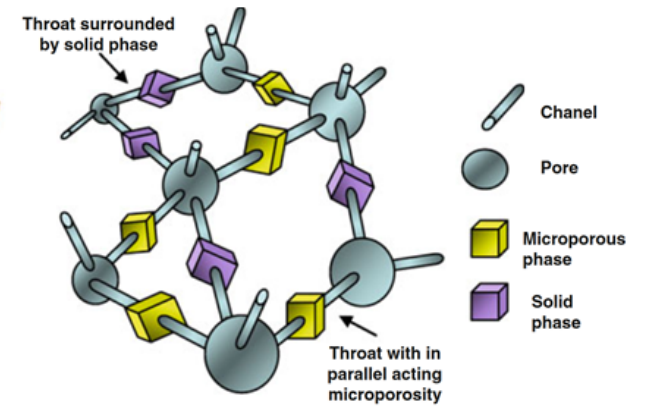

Figure 1.17: Description of pore network model porous media representation, considering throats and micro-porosity in connection with macro-porosity (from [15]).

1.3.1 Pore network modeling

In pore network modeling, porous media is considered as a network of pore volumes connected by channels or pore throats [39] (see, Fig. 1.17). For each channel and each pore, mass fluxes are calculated, and mass balance equations are solved, Eq. (1.13). In Eq. (1.13), the mass balance for the i^{th} pore is considered as the sum of the mass flux from all the connected pore volumes j (q_{ij}),

$$\sum_j q_{ij} = \sum_j G_{ij}(P_i - P_j), \tag{1.13}$$

where P_i, P_j, G_{ij} are respectively pressures at i^{th} and j^{th} pore and the conductivity of the channel between pore i and j, as an example G_{ij} for a cylindrical channel is considered as $G_{ij} = \frac{\pi r_{ij}^4}{8\mu L_{ij}}$ where r_{ij} and L_{ij} are radius and length of channel respectively.

For obtaining an accurate representative pore network, the structure of porous media can be extracted from 3D images of porous media. Normally, skeletonization technique is used to extract the pore network, see Fig. 1.18.

1.3.2 Lattice Boltzmann

An alternative approach for CFD[4] simulations instead of directly solving the Navier-Stokes was introduced by the invention of the lattice gas methods [140]. These

[4]Computational Fluid Dynamics

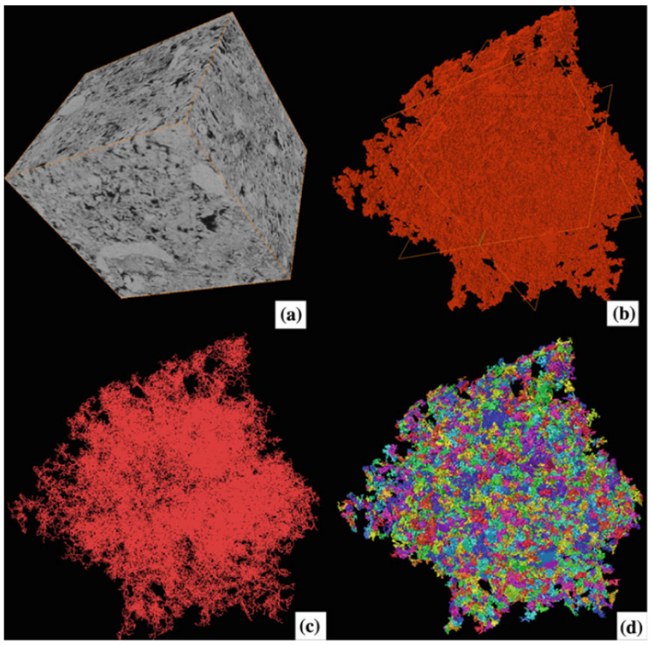

Figure 1.18: Extraction of the equivalent macro-pore network illustrated on the reservoir sample Original 1000 × 1000 × 1000 voxel grey level image (a), binary image of the resolved pore space (b), skeleton extracted from the binary image (c), and partitioned macro-pore space (d) (from Bauer et al. [15]).

methods allowed particles to move on a discrete lattice and local collisions conserved mass and momentum. However, the lattice gas methods had several drawbacks consisting mainly of their noisy nature. Then, a particles density distribution was considered instead of discrete particles, which eliminated the noisiness of the method and allowed for a more general collision operator. The Lattice-Boltzmann (LB) method has the advantage of describing non-equilibrium dynamics, especially in fluid flow applications involving interfacial dynamics and complex boundaries [125].

1.3.3 Particle method

In particle methods, fluids are discretized considering particles that occupy a certain position and carry an intensive physical property (e.g., mass). Particles are tracked in time as they move at the pore space. Continuous variables (e.g., density) are represented as the superposition of kernel functions centered on a set of discrete particle points. The smooth particle hydrodynamics method (SPH), moving particle method (MPS), Dissipative particle dynamics (DPD), and Cracking particles method (CPM) are examples of particle method modeling.

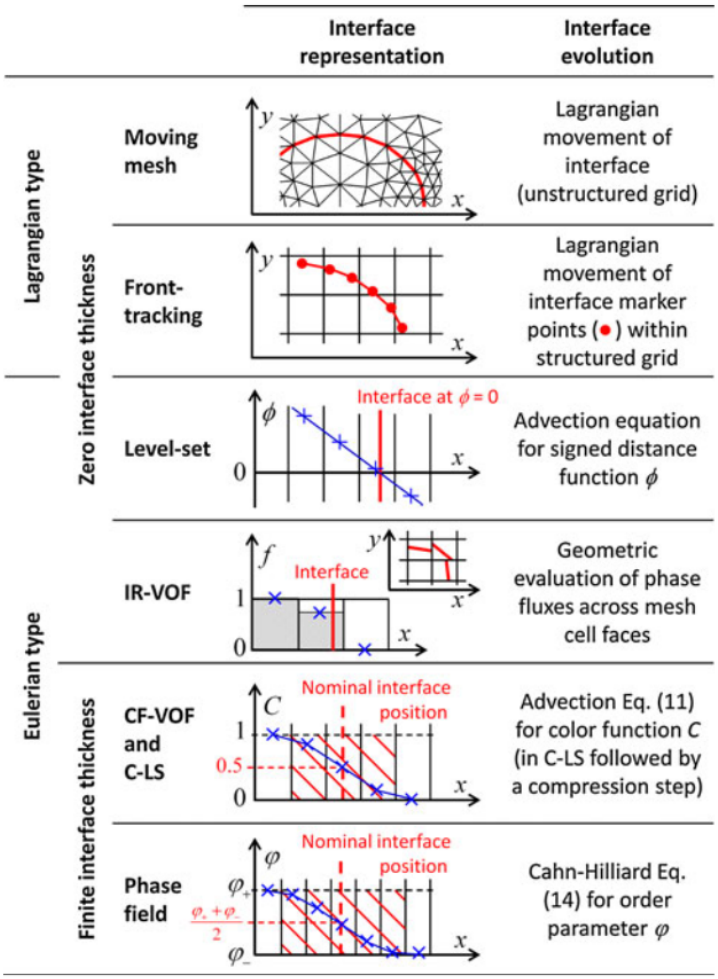

Figure 1.19: Different direct numerical simulation methods and theire consideration of interface (either as zero interface thickness or finite interface thickness), from Wörner [146].

1.3.4 Direct numerical simulation

Direct numerical simulations (DNS) follow the conventional discretization of continuum-scale equations (finite volume, finite differences, and finite element) and meshing for flow and transport (e.g., the Navier-Stokes equation). However, capturing the evolution of the interface is a challenge in this method, and specific methodologies are employed to capture the interface in the defined resolution of the discretized equations. Volume-of-fluid method for multiphase processes and embedded boundary methods for mineral-fluid interfaces are examples of direct numerical simulation methods, see Fig. 1.19.

Despite all the computational improvements and developed numerical methods in these years, numerical modeling is still confined to a specific range of flow, and it fails to simulate the flow at very low Ca (lower than 10^{-5}). That is to say, new experiments are necessary to explore the physics of flow, especially at low Ca, to extract

flow mechanisms and provide new data for modeling the displacement behavior. The following section presents a short review of the experimental method and available characterization methods.

1.4 Experimental method: microfluidics

The characteristics of porous media (such as absolute permeability) are directly and closely related to porous system properties (e.g., pore and throat size distribution, connectivity, and spatial relation of pores and throats). In natural porous media, the complex connectivity of the pores, irregularity of pore and throat shape, and the complexity and heterogeneity of composed materials complicate understanding the relationship between the involved parameters. Additionally, although X-ray computational tomography (CT) has improved in terms of resolution and real-time characterization in recent years, it still lacks capturing the dynamics of small-scale fast mechanisms of invasions. Despite great improvements in computational fluid dynamics (CFD) techniques, it is still challenging to accurately model the dynamics of the interface of two immiscible fluids in the pore space at low Ca. Accurate measurements of multiphase flow in porous media are required to bring insight into the physics of the problem and to compare the results of multiphase pore-scale simulators. For this purpose, several experimental techniques for the fabrication of porous media and characterization of flow properties are developed. Among these methods, microfluidics has drawn significant attention as a promising tool and an excellent asset for studying porous media flow at pore-scale. Coupled with a high-resolution monitoring system, microfluidics has shown a great potential to capture mechanisms involved in displacement processes. Especially when the displacement concerns very fast dynamics [8, 83]. Besides, microfluidics allows us to meticulously design the geometry of the artificial porous media that enables us to reduce the complexity of studying natural samples. Furthermore, by recent advancements in fabricating methods and post-modification of microfluidic devices, it is possible to replicate natural porous media by growing minerals inside the device [141]. One other advantage of microfluidic systems is the direct observation and in-situ characterization of the porous system with optical and spectroscopy methods. By this setting, one is able to observe the transport in the porous media and, by using spectroscopy methods, is able to monitor existing chemical components in the porous system. This section presents several fabrication and characterization methods for microfluidics set-up for pore-scale studies.

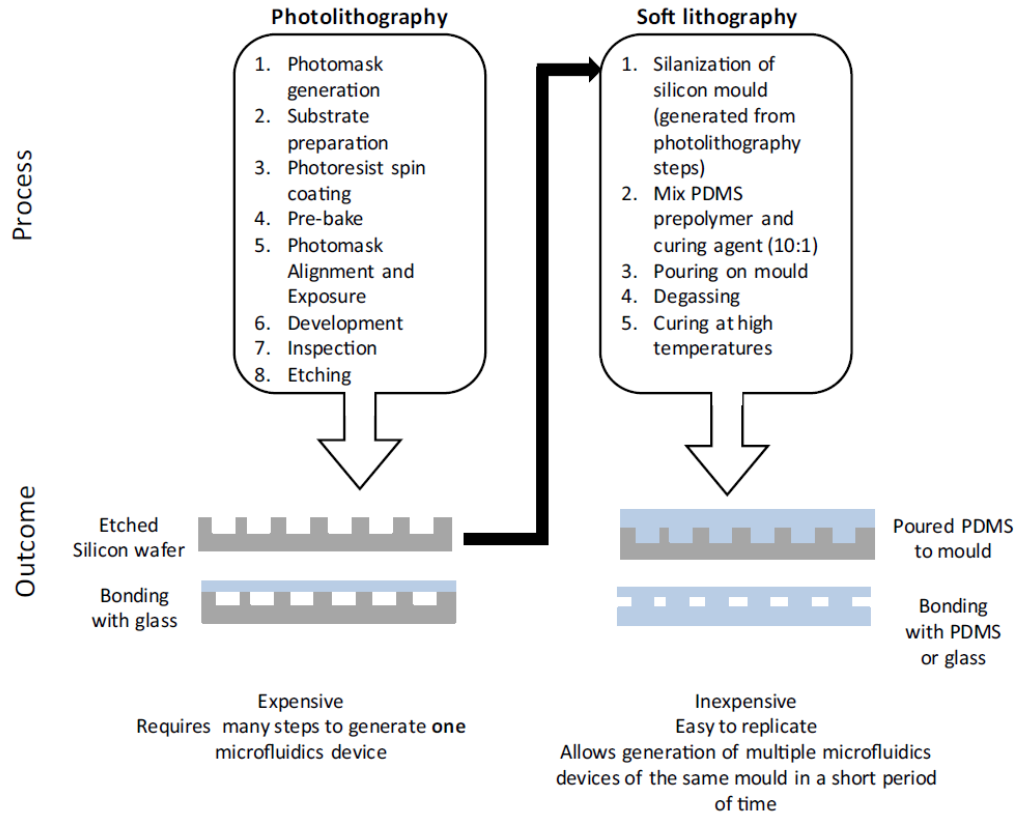

Figure 1.20: Schematic process of photolithography and soft lithography [44].

1.4.1 Fabrication methods

Based on which material is used to fabricate microfluidic chips, the chips are divided into two different groups. First, a group of microfluidic chips made of geo-material substances; second, a group of chips composed of polymers, silicon, etc., generally, no geo-material is used to build them.

There are different methods and procedures for fabricating a microfluidic chip in each category. There are two major methods to fabricate microfluidic chips based on fabrication process types: photolithography and soft lithography. These methods are presented schematically in Fig. 1.20.

Synthetic micromodels

Silicon, glass, and polymers are three major materials that are used for microfluidics devices fabrication. Among them, silicon is the first material that has been used for this mean, but some drawbacks of silicon, such as opaque nature, convinced researchers to find substitute ways for microfluidics chips fabrication in respect to their research and needs [44, 47, 52].

Silicon wafer The process of microfabrication using silicon is considered as three major parts: photolithography, deposition of thin-film, and etching and bonding. Photolithography is the process of making photomasks and transferring the desired patterns on the photomask to the previously photoresist-coated substrate using ultra-violet (UV) light[126]. The thin-film deposition step is the process that a thin layer of materials such as silicon dioxide or silicon nitride is placed on the surface of a silicon wafer using methods such as physical vapor deposition (PVD) or chemical vapor deposition (CVD). Etching and bonding are the last steps in the preparation of silicon wafers: it is possible to etch silicon substrate by employing wet etching (by chemical solutions) or dry etching (plasma), e.g., reactive ion etching (RIE), deep RIV (DRIE) and cryogenic etching. In the end, for microfluidics devices closure, a cover is placed on top of the channels and bonded to the silicon wafer. Based on materials, different bonding methods can be applied, e.g., fusion bonding and anodic bonding [59, 74].

Glass Glass is another material that is used as both wafer and cover of the microfluidics devices. Glass enables us direct visualization over the system. It is possible to put the glass through a photolithography process. Chemical etching and laser are applicable for the etching of the glass material [44]. one drawback of glass micromodel that goes under wet etching process is non-vertical walls, so the profile of channel are in trapeze form.

Polymer Polymers are of other materials that are used for the fabrication of microfluidics devices. The procedure based on soft lithography is fully explained in [62]. At the first step, a negative image of the pattern is generated on a silicon wafer, see Fig. 1.20. After that, the polymer is poured on the master mold and is placed in an oven. The next step is to remove the reticulated polymer from the master mold and seal the projected patterns by bonding a polymer or glass layer. There are various methods for bonding the sealing layer to the channels-containing polymer, but one of the most frequently used ones is the plasma method [43, 60, 62]. This method is much quicker and low-cost in comparison to silicon and glass etching, although the preparation of the master mold takes time, and expenses are relatively high at first. One of the most famous polymers for microfluidic purposes is PDMS[5], a type of elastomer, which is very common in microfluidics, for it is friendly for normal laboratory conditions and is non-toxic.

[5]Poly-Di-Methyl-Siloxane, for more detailed information, see Chapter 2

Geo-material-based microfluidics

This method, recently, has attracted the attention of researchers working on microfluidics in works related to hydrology and, in general, geosciences. The main reason for using this method is to have a more realistic view of what happens in real porous media. In addition, it is possible to study phenomena such as mixed wettability. This is important because the surface forces and surface properties can profoundly affect the flow in such small pores.

There are different techniques for using geo-materials as microfluidics devices. One technique is laser-etched rock substrate. It was at first introduced by Porter et al. [102]. They used this method to have a more realistic view of the flow properties by considering reservoir conditions and rock properties. Also, Song et al. [119] used a calcite rock to make a micromodel chip using wet etching directly.

Another method is to functionalize the surface of silicon, glass, and polymer microfluidic devices by coating its surface with the desired material. For example, coating the micromodel surface with clay minerals can simulate sandstone porous media. Another method is to put small sliced pieces of minerals between layers of polymers. Details of these methods can be found in [6, 120].

In this section, different fabrication methods are reviewed. Based on the experimental methodology and the understudy system, different quantities are of importance and must be measured to describe the system. In the following section, different characterization methods are presented.

1.4.2 Characterization methods

In the microscale studies of fluid flow, both quantitative and qualitative data can reveal the mechanisms of fluid flow inside pores. For example, when the displacement of two immiscible fluids is considered, the average saturation of phases and the shape of flow paths can be a sign of dominant forces in pores or at least give an insight into the overall performance and efficiency of the displacement. In addition to that, some information such as the dynamic contact angle and the front velocity are obtained easily by visualization of the porous media and give us some quantitative data on the flow characteristics. These data help us to detect the reason for preferential paths for the fluids, mechanisms of trapping, boundary layers, etc. Also, in reactive flows, for measurement and observation of porous media's physics alteration, following porous media properties through the system, obtaining data on chemical composition for new models, and comparing with numerical simulations, several methods based on the sample type, scale of the study, etc. are developed. In the following section, we aim to quickly present some of the most frequent and innovative methods that are able to perform characterization at pore-scale experiments.

Optical observation One of the most common ways of visualization of the fluid transport inside microfluidic devices is using a microscope coupled with a camera. In this manner, information such as the saturation of phases, etc., are obtained using image processing techniques. Another strength of this method is the ability to measure the contact angle, interfacial curvature, and interface area. In addition, using high-speed cameras, this method is able to record fast events happening in porous media by focusing on a specific area in the porous media [62, 83]. There are two major setup types. The first one is when the light source is beneath the microfluidic chip (the opposite side of the camera), and light beams transmit through the chip, and details are transferred to the camera. The other one is when the light source is on the same side of the camera. In this method, the light reflects from the surface and gets to the camera. Optical imaging is one of the most feasible methods for reactive transport in porous media that does not need complicated instruments and facilities. A thin section of the under-study sample or a designed microchip is imaged under the microscope. Based on the obtained images, it is possible to dynamically follow the geometry changes as a result of dissolution or precipitation throughout the experiment. For example, Soulaine et al. [121], observed the dissolution of calcite mineral using HCl acid. Optical observations, however, are applicable to limited pore size, and pores in a nanometer scale are not quantified during observations on couples of microns wide.

Confocal microscopy Confocal microscopy is a precise 3D imaging technique. This method is used for relatively slow flow rates. The idea is to take consecutive pictures from the different depths of the object and make a 3D picture of that. This method tracks the particle patterns inside a flow and finds the flow velocity field (refer to micro-PIV section). In addition, this method is used to study the thickness and other properties of the film over the solid surface. Basic information and resources can be found in [44, 61, 150].

2D backscattered electron microscopy This method was first introduced by Peters [96] and is based on the backscattered mode of scanning electron microscopy technique for mapping porosity and mineral distribution at the pore scale. This combination of mineral characterization and porosity mapping makes this method a powerful tool to measure the accessible reactive surface area.

X-ray micro-CT X-ray computed microtomography is a technique composed of an X-ray source, object, and detector that measures the transmitted or emerging X-ray intensity off the sample. Based on these data that normally are gathered in 2D radiographs, a spatially resolved 3D image containing both physics and chemistry of sample is obtained by stacking the data together [125]. This method works best at

a micro-scale. However, nano-scale resolution is achievable by reduction of sample investigation volume. Imaging in this technique is time-consuming. As a result, this technique is not perfect for highly transient stages of CO_2 sequestration.

FIB-SEM Focused Ion Beam-Scanning Electron Microscopy is a high-resolution tomography technique. This technique has a resolution in nano-scales. Hence, this method is applicable to determine porosity, considering nano-pores. The same as XCMT, this FIB-SEM is not capable of capturing high transient phenomena during displacement processes.

Raman spectroscopy Raman spectroscopy is a non-destructive method based on analyses of scattered light off the sample as a result of emission of a high-intensity light on the sample molecules. Based on the wavelength of the scattered light, the chemical composition of the sample is detectable. High-intensity laser light is emitted on a molecule, and the scattered light is analyzed. Most of the scattered light lies in the same wavelength as the emitted laser (this portion is called Rayleight scatter); however, a small portion of it has a different wavelength, which depends on the chemical structure. Each chemical bond has its own wavelength and is distinguished by intensity picks, which are collected after emission. This method, coupled with microfluidics, is able to provide information on the chemical composition of the sample at pore-scales. This shows how solid chemicals dissolve in other phases, what is the exact mass transfer coefficients between phases, how precipitations form, and what path do chemicals choose [50, 63, 117, 104].

Microscopic particle image velocimetry (Micro-PIV) This method aims to add very small particles to the fluid and use an intense light source to capture images of them in sequent times and measure the fluid velocity field by analyzing images. The time difference between two sequential images is used to track particles as time passes. It enables us to find the velocity vector of particles by dividing the position changes over time. The position changes of particles are found by cross-correlation of interrogation windows (IW). There are a couple of factors that affect micro-PIV results and are considered for designing the system. First of all, it is important that the light source be in such a manner that particles are clearly distinguished from other parts of the fluid and intense enough that the camera be able to capture the image in a relatively short time so that particles are not shaded. Second, particles should not disturb the flow, so the size of particles should be small enough to move, accelerate and deaccelerate with the flow and not block the pore throats and also not be affected by Brownian motions. Its density, also, must be compatible with the fluid and not sediment during the flow. Besides, the particles should not interact chemically with the solid phase or the liquid

phase. This factor restricts the implication of some particle types, especially when the fluid is a strong solvent such as supercritical CO2. In recent years, this method has evolved and has been used in different research fields, such as carbon dioxide capture and storage. In following papers, a more detailed review and application methods and aforementioned considerations of micro-PIV are found [64, 81, 107].

1.5 Summary and objectives

In this chapter we presented state of the art in fluid flow and reactive transport in porous media and established pore scale as the right scale for studying transport in porous media. First, we presented different displacement patterns and decisive factors for different flow behaviors. Then, Haines jumps was presented as one of the most important invasion mechanisms among presented different invasion mechanisms. Later, some characteristics of these interfacial instabilities, such as pressure bursts, pinning and jumping, connectivity of the interface through porous media, etc., was discussed and importance of the study of the dynamics of this phenomena was pointed out. Then, the effect of surface forces and wettability on drainage and imbibition was discussed and corner flow and precursor flow were presented as two important phenomena that are able to affect fluid distribution and recovery factor. In the next section, basics of reactive flow was presented. Then, the state of the art of different chemical dissolution fingering patterns were shortly reviewed and the importance of mass transport and kinetics of the reaction beside involved mechanisms were highlighted. Additionally, the effect of precipitation on alteration of porous media and as a result on porosity, permeability, flow patterns and reactivity was explained and reactive system of carbonate-gypsum was presented as the desired system for the study. Finally, micro-scale study of the system by using the microfluidics experimental method and a confocal Raman spectroscopy for chemical characterization, was considered as the ideal configuration for studying dynamics of porous media alteration (physically and chemically) and its effect on the reactive transport through the system. In the last section, an update and a brief review on the different microfluidic chips and characterization methods for fluid flow study in micromodels were presented.

This study is conducted to investigate the physical and chemical mechanism involved in CO_2 sequestration in deep aquifers at the pore-scales using microfluidic devices. In this regard, in this research, we seek mainly two aims:

- To address triggered pore invasion mechanisms at each flow regime during two-phase immiscible displacement in porous media to quantify the role of involved pore-scale phenomena on the front behavior.

1. Microfluidics will be adopted as the experimental method, and the porous media geometry will be designed to study the displacement process at a well-defined geometry.
2. A set of experiments of immiscible drainage for different flow rates, fluid pairs, and wettability conditions will be conducted.
3. Experimental results for dynamics of pore invasions based on interface dynamics and micro-PIV results will be extracted.
4. A model capable of capturing interface dynamics by considering main active forces on the interface will be developed and compared to the experimental results.
5. The impact of the residual wetting phase on interface dynamics will be studied by investigation of corner flows dynamics. A numerical model will assist us in evaluating our results.

- To investigate the kinetics of calcite dissolution, the evolution of the reactive surface area, and to monitor porous media alteration, to quantify the effect of SO_2 impurities on the CO_2 storage.

  1. Microfluidics will be adopted as the experimental methodology, and a microchip is designed and developed to simulate the sequestration process.
  2. Calcite minerals are grown in the microfluidic system to mimic a carbonate rock system.
  3. Experiments will be designed to study calcite dissolution and gypsum precipitations for different gas compositions. A confocal Raman spectroscopy will be used to probe the system chemical compositions and obtain a 3D map of dissolution precipitation processes in our microfluidics chip.
  4. By compiling the obtained data from dissolution and precipitation of minerals, a model for the kinetics of the porous media alteration and the available reactive surface will be developed.
  5. PHREEQC (a geochemical software) will assist us in the validation and comparison of the results.

Chapter 2

Materials and methods

In previous chapter, microfluidic devices were reviewed as a cheap, accurate and favorable tool for pore-scale studies of flow and transport in porous media, see Section 1.4. In this chapter we present the experimental framework and methods we use to obtain data for answering raised questions in studying physics of subsurface multiphase flow and geochemical interactions of the porous system. First, we present our micromodel in terms of patterns and preparation method and procedure, then a description of experimental set up and materials and experimental protocol is presented. After, we provide a description of techniques that were used for data acquisition in our experiments. Finally, calculations of frequently used dimensionless numbers in following chapters is presented.

2.1 Experimental methodology and setup

2.1.1 Micromodel patterns

Using microfluidic techniques, we are able to design the morphology of the porous system. Various works have investigated different porous settings from 2D replicas of real rocks [107] to simplified homogeneous systems [18]. In most of the studies, pores are vastly connected through a pore network system, making it almost impossible to associate observed front disturbance to a specific invasion, due to the non-locality of events. In other words, the connectivity of pores rises the chance of interference by a phenomenon happening at large number of pores, which adds limitation to distinguish between understudy phenomena and disturbing effects. Since in this research the focus is to determine and extract the effect of pore scale phenomena on the interface and the front behavior at other pores, the geometry designs were kept as minimal as possible to be able to separate individual effects.

The first design is based on the conceptual illustration of successive pores and

throats in porous media as pore doublet model with two sinusoidal capillaries, Fig. 2.1. The theory behind two phase flow in such models is presented in the Chapter 3. Throats and pores were considered 40 and 160 μm wide and a depth of 40 μm was assigned to the whole micromodel. The schematic of the channels is presented in Fig. 2.1. The designed porous media is connected to the inlet and outlet with two capillaries of 1 cm long from each side.

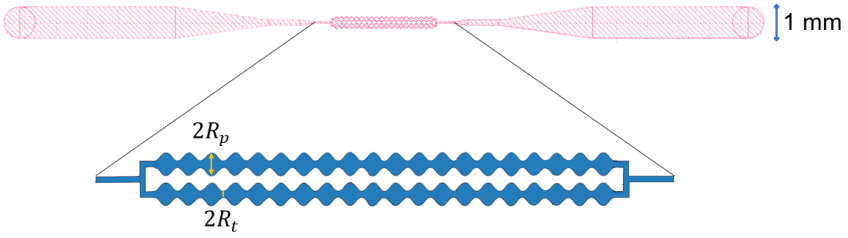

Figure 2.1: Patterns of microfluidic capillaries are presented schematically. The dimensions and aspect ratio of presented pattern are considered as 80 μm and 20 μm respectively for R_p and R_t.

One other microchip is designed to produce a microfluidics system that resembles the CO_2 sequestration in carbonate reservoirs. An effort toward capturing the chemical mechanisms induced by introducing a miscible non-wetting phase to a calcite system is made. In this regard, a novel design of a silicon-glass microchip is proposed to put the gaseous phase in direct contact with the aqueous phase. The designed geometry is made of homogeneously distributed 40 μm circular pillars and 2.5 mm capillaries to transport chemicals, see Fig. 2.2. More details on the design and properties of the porous media is found in Chapter 6.

2.1.2 Master mold preparation

Nowadays, there is a wide variety of choices for fabricating microfluidic chips. Various methods and materials have been developed and are available, ranging from silicon-glass, polymer-based, geo-material-based, etc. One major method to obtain the porous media network as a chip is to use a type of transparent polymer known as PDMS (Poly-Di-Methyl-Siloxane). PDMS is a type of viscoelastic silicon-based organic polymer. It is safe and easy to work in a normal laboratory environment (i.e., it is nontoxic, nonflammable, and inert), and it does not need any complicated facility and clean rooms to prepare. In addition, and most importantly, the geometries are very well controlled on these devices. Another advantage of this method is the ease of replicability in addition to the financial privilege. A detailed review of micromodel types is presented in Karadimitriou and Hassanizadeh [61].

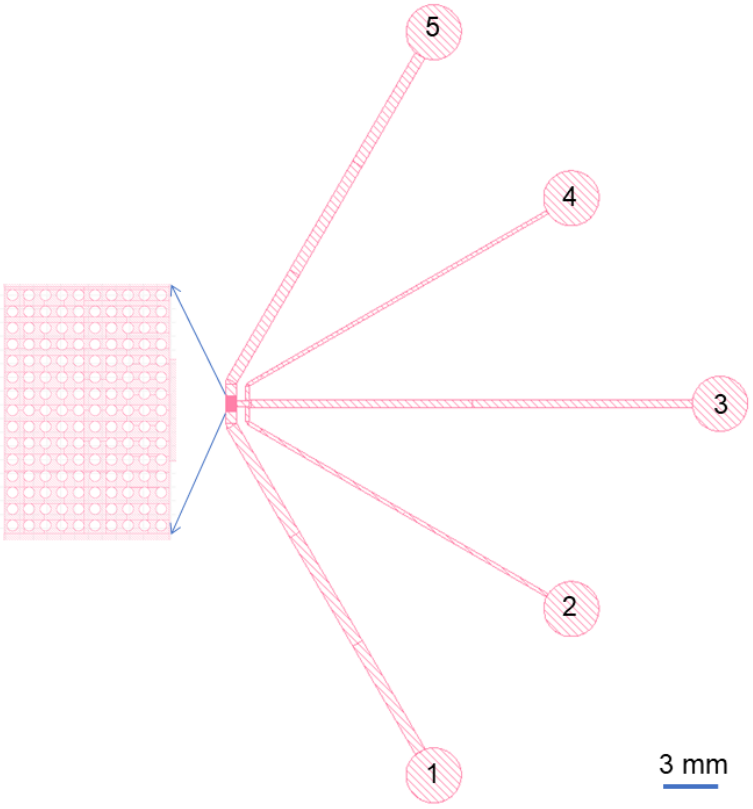

Figure 2.2: A schematic representation of the microchip pattern for studying reactive transport. The porous media is composed of homogeneously distributed circular posts.

For our experiments, PDMS microchips are used as our primary method. For the preparation of chips, a silicon wafer serves as a mold (the process of master mold preparation and soft lithography is presented in Fig. 2.4 and Section 2.1.3, Fig. 2.5). For master mold preparation, two methods and protocols are mainly adopted that we explain here. Master molds were prepared in the cleanroom facility of GREMI (Groupe de Recherches sur l'Energétique des Milieux Ionisés). Here, we mainly summarize the workflow of each method. The detailed protocol is found in Appendix A.

- A silicon substrate is used through the photolithography process for microfabrication. A layer of photoresist is distributed homogeneously on the surface of the silicon wafer. Then, the wafer is placed on a hot plate to perform the soft baking. For the next step, the patterns are transferred to the wafer by a precise exposure of the photoresist layer to ultraviolet light through the mask. The wafer is immersed in a developer bath to remove the exposed photoresists. Then, the wafer goes through a plasma cryogenic etching process. A high-resolution control on the geometry of the patterns along with extremely vertical walls are

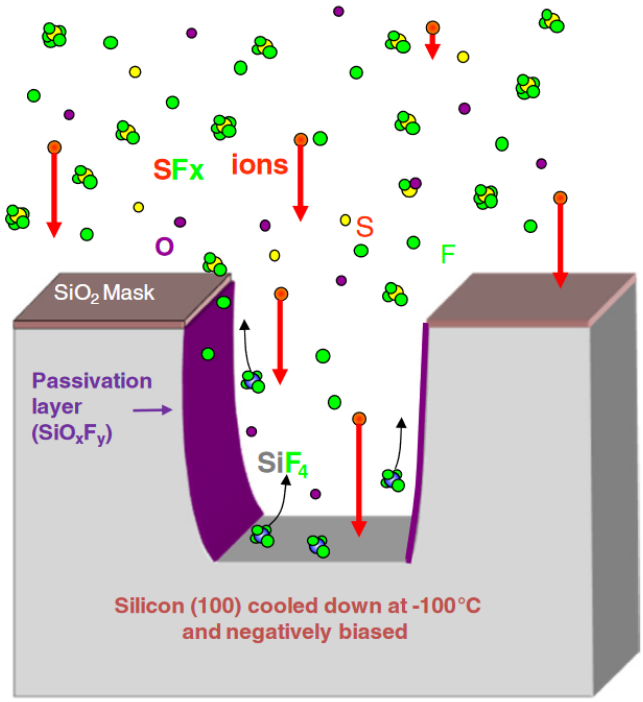

Figure 2.3: Scheme of cryogenic etching method, taken from Dussart et al. [36].

obtained sing a ICP reactor (inductively coupled plasma, ALCATEL). This process removes layers of the wafer at areas that are not covered with photoresist (see Fig. 2.3). The channels remain on the wafer to be used as the master mold for PDMS soft lithography. More detailed steps of the process and more details on cryogenic etching are presented in Appendix A.2 and [1, 36].

- The second method that is used for microfabrication is employing SU-8-2025 photoresist in the fabrication process. In this process, the photoresist remains as patterns and obstacles on the wafer for soft lithography. The photoresist spreads homogeneously on the wafer, and the thickness is adjusted by controlling spin-coating speed (Fig. 2.4a-b). After, the wafer follows a soft baking process (Fig. 2.4c) and, then, it is exposed to UV light (Fig. 2.4d) and a post-exposure baking is followed (Fig. 2.4e). Then, the patterns are developed by immersing the wafer in SU-8 developer (1-methoxy-2-propanol acetate, MICROCHEM), Fig. 2.4f, and finally rinsing with water. In the end, the non-exposed parts of the photoresist on the wafer are removed, and the SU-8 on the designed porous media remains. Then, the surface is coated with a hydrophobic layer (PFOCTS, Merck, Sigma-Aldrich) to facilitate the PDMS molding, Section 2.1.3. The obtained wafer is ready to be used as a master mold for the preparation of PDMS micromodels (Fig. 2.4g). The details of the master mold preparation protocol using SU-8 is provided in Appendix A.3.

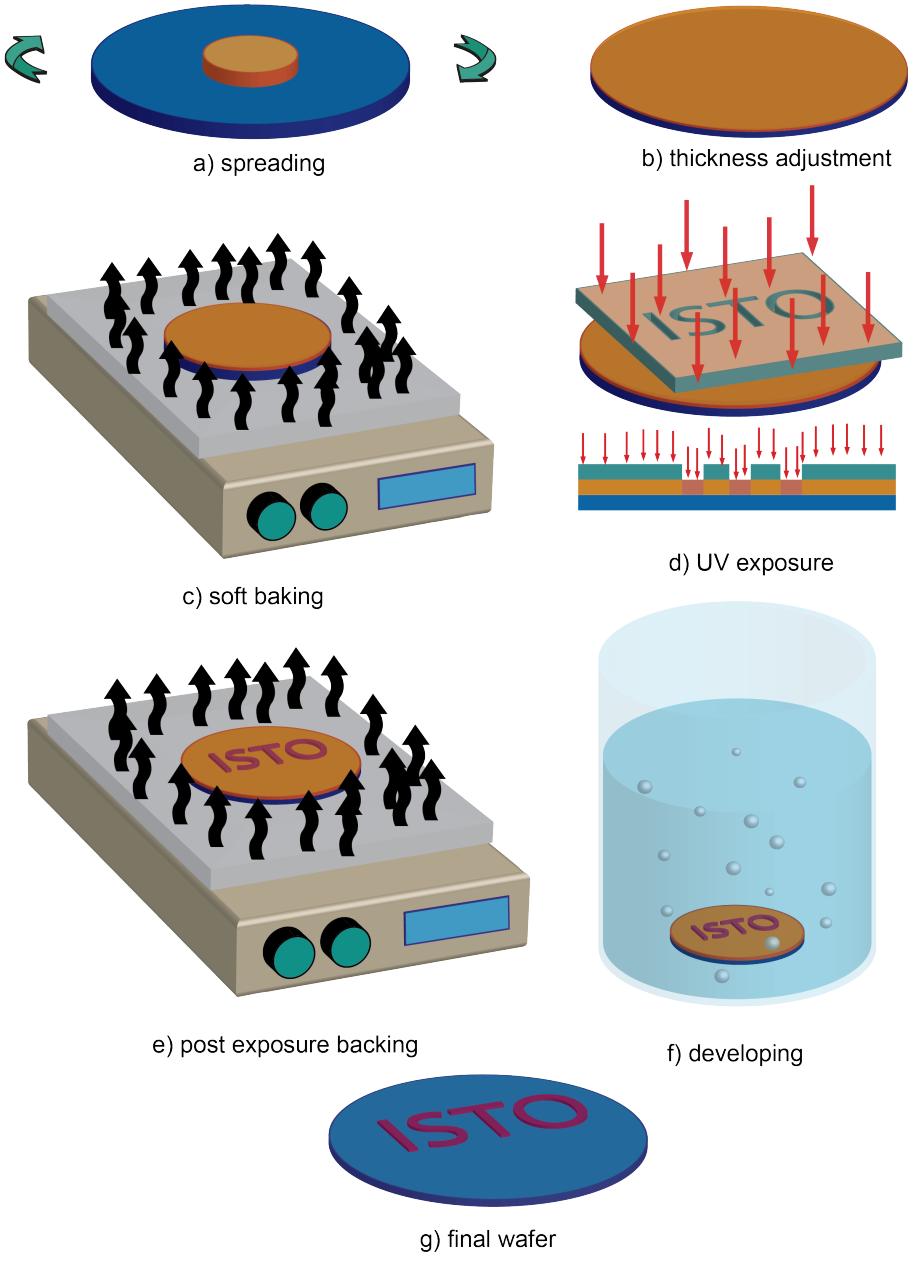

Figure 2.4: Schematic of SU-8 master mold microfabrication.

In what follows, the process of PDMS replication and preparation of microchips for experiments are explained. Before that, it is important to keep in mind that with all the benefits of PDMS soft lithography, PDMS is permeable to gases. Hence, since our geochemical system contains a toxic gaseous phase, a silicon-glass microchip is considered there. The process of silicon substrate etching remains similar to what is explained here. However, microfluidic chip preparation follows a different flow that is explained in details in Section 6.2.2.

2.1.3 Preparation of micromodels

In the beginning, it is necessary to polymerize liquid PDMS elastomer using the curing agent. Monomers are completely mixed with the activating agent following the workflow of Roman et al. [106]. Pouring liquid PDMS on the mold surface is preceded by cleaning the mold with isopropanol (IPA) and water. Then the polymer on top of the mold rests to complete the reticulation process, Fig. 2.5a. The warmer the resting environment is, the faster the reticulation process will be. Then, the PDMS layer is ripped off the mold. After, the injection points are drilled precisely using a biopsy puncher in the inlet and outlet channels. As the final stage, the porous media pattern on the PDMS layer is closed by covering the surface with a smooth slab of PDMS by activating the PDMS surface using a plasma treatment and attaching it to the other layer (Fig. 2.5b-c).

2.1.4 Surface treatment

It is noteworthy to keep in mind that PDMS is a hydrophobic material in its nature. Nevertheless, heterogeneous wettability of PDMS has been reported in previous works [62]. Wettability is a crucial parameter for two-phase flow processes. Thus, a good control of the wettability of our microfluidic devices is needed. There are methods to modify the PDMS surface properties to make it homogeneously hydrophilic or hydrophobic. In what follows, the methods that have been used in this research are presented.

Plasma treatment

PDMS surface is susceptible to change properties with plasma treatment. In the work of Tan et al. [130], it is proposed that the surface contact angle of PDMS is a function of the duration of oxygen plasma treatment, plasma properties, preservation environment after the treatment, and duration of exposure to the lab environment.

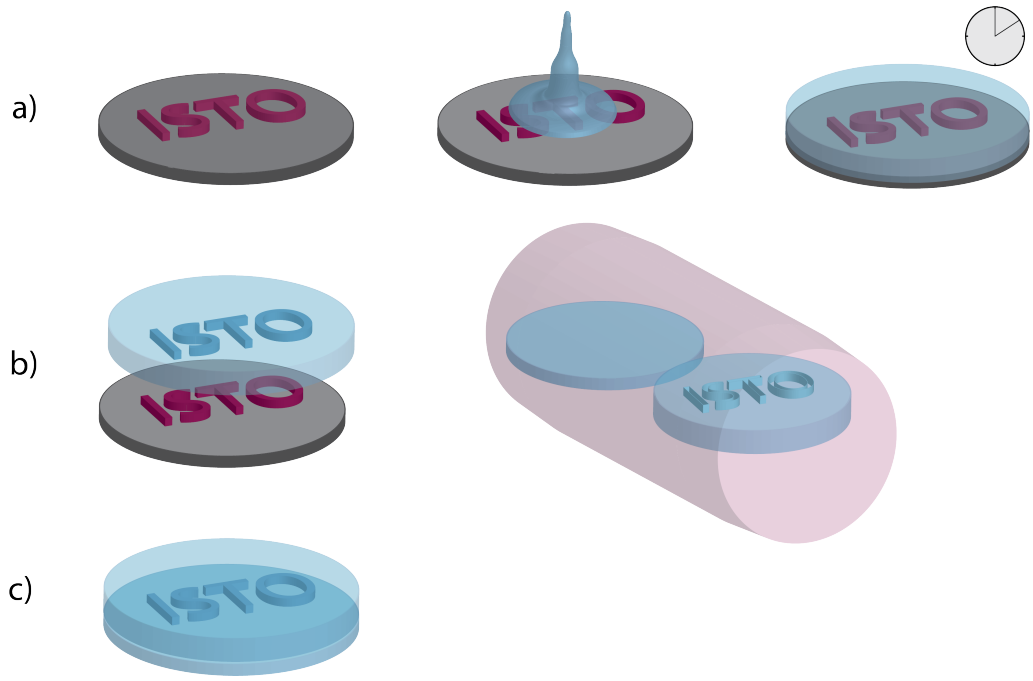

Figure 2.5: A schematic view of PDMS soft lithography process. The PDMS is poured on geometries of a clean wafer and rest in oven to reticulate at 65° *C* for two hours (a). The PDMS layer containing geometries and the covering layer are plasma treated for 40 seconds (b). Two layers are bonded after plasma treatment and are placed on a hot plate at 100° *C* for 5 minutes (c).

In addition, they mention that the duration of plasma treatment may affect the PDMS surface's roughness. The results of Tan et al. [130] are presented in Fig. 2.6. Results show that the contact angle after 5 minutes of plasma treatment stabilizes between 50°-60° and this contact angle is preserved for several weeks if the PDMS is kept in deionized water (DI water).

For validation and certifying the contact angle after plasma treatment of our micromodels, a series of contact angle tests are conducted to measure contact angle dynamics with time. Layers of smooth surface PDMS are treated in a plasma chamber for 5 and 6 minutes. Then contact angles are measured using KRÜSS ADVANCE drop shape analyzer at different time stages using a sessile drop method. The results are presented in Fig. 2.7.

After plasma treatment, the initially measured contact angle is approximately 15°. As time passes, the contact angle increases gradually. After almost 4 hours in contact with air, the contact angle stabilizes at a constant value of 45°. Fig. 2.8 shows some frames of contact angle measurement for different droplets at different times.

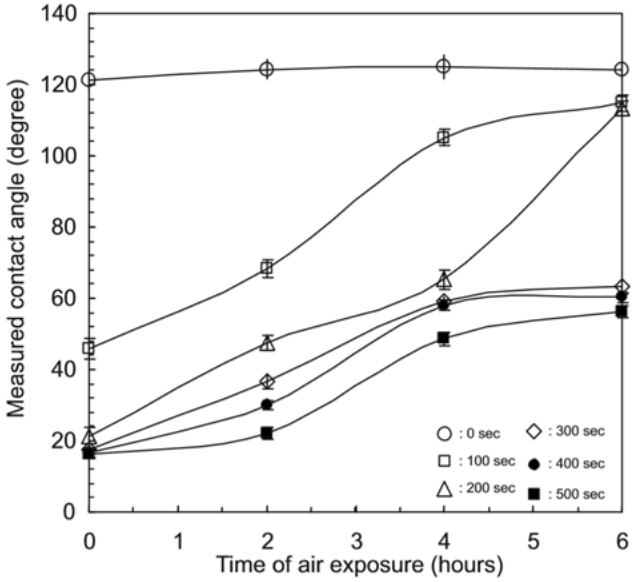

Figure 2.6: Reported water-air contact angles for an oxygen plasma treated PDMS microfluidic device for various treatment duration versus time of exposure to air, taken from Tan et al. [130].

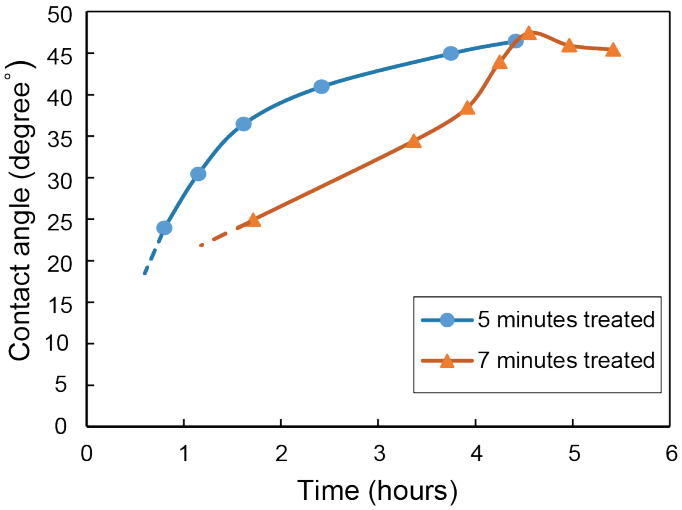

Figure 2.7: Experimental results of contact angle measurements of plasma treated PDMS with respect to exposure time to air for two different plasma treatment durations.

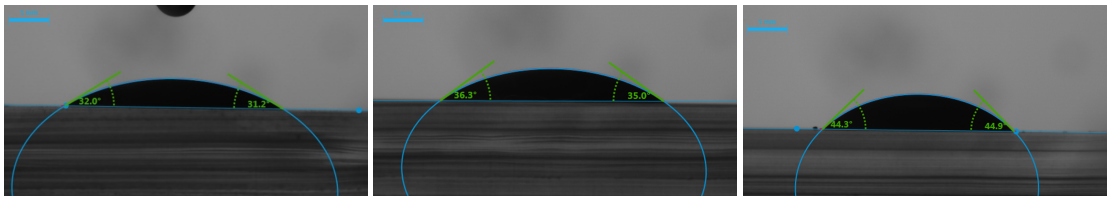

Figure 2.8: Contact angle measurements for Oxygen plasma treated PDMS layer at different time stages. The measured contact angle from left to right is respectively 31.6°, 34.65° and 43.6°.

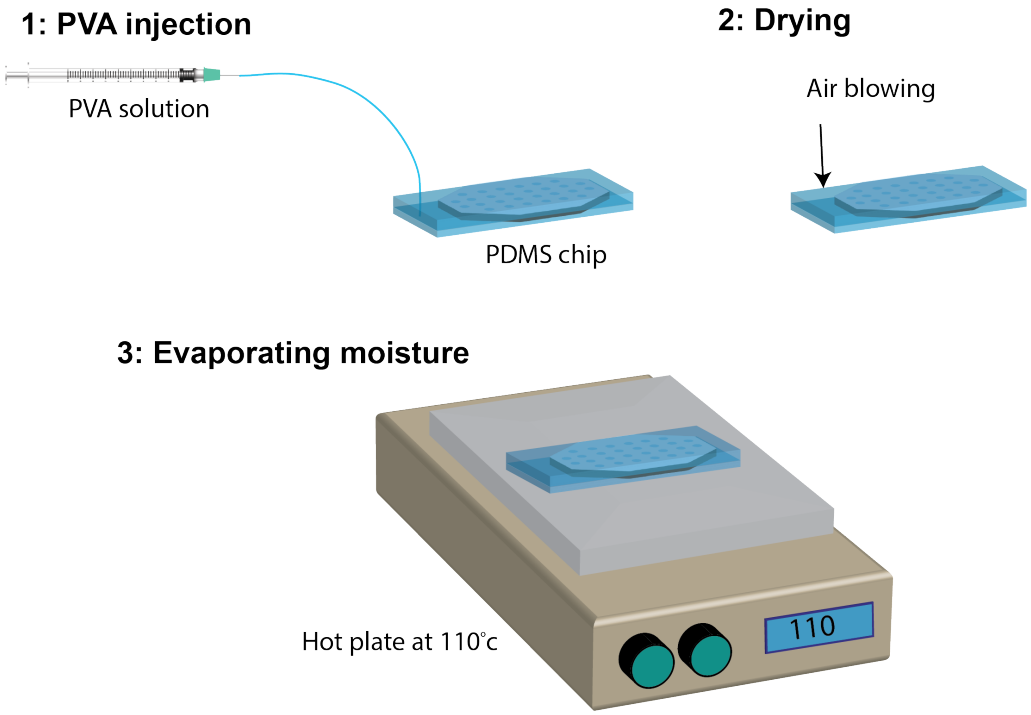

Figure 2.9: The schematic of the PVA deposition process in a PDMS microfluidics chip.

PVA deposition

Trantidou et al. [137] presented a method to modify the PDMS surface by the deposition of PVA (polyvinyl alcohol). By this method, a homogeneous long-lasting hydrophilic PDMS surface is obtained. First, a homogeneous solution of PVA in water must be prepared. To fully dissolve PVA, initially, it is added to DI-water (1 $wt\%$) at room temperature. The solution is stirred for 40 minutes. Then, the temperature is increased to 100°C while the stirring continues for another 40 minutes. Finally, the temperature decreases to 65°C and the solution is left to stir overnight. The next day, to compensate for any water losses due to evaporation overnight, water was added to the solution to keep it at 1 $wt\%$. Then, PDMS microchips are placed in the plasma chamber for 5 minutes, and PVA solution is injected inside the porous media right away. The solution rests in the microchip for 10 minutes at room temperature. Then, it is completely removed by blowing air. Finally, chips are heated for 15 minutes on a hot plate at 100°C. Fig. 2.9 summarizes the PVA deposition process in a schematic representation. The air-water contact angle is measured to be 18° after treatment with PVA and it keeps the same value for the first day. More information on durability of the treatment are found in Trantidou et al. [137].

Silane deposition

Karadimitriou et al. [62] developed a novel procedure to change PDMS wettability to a

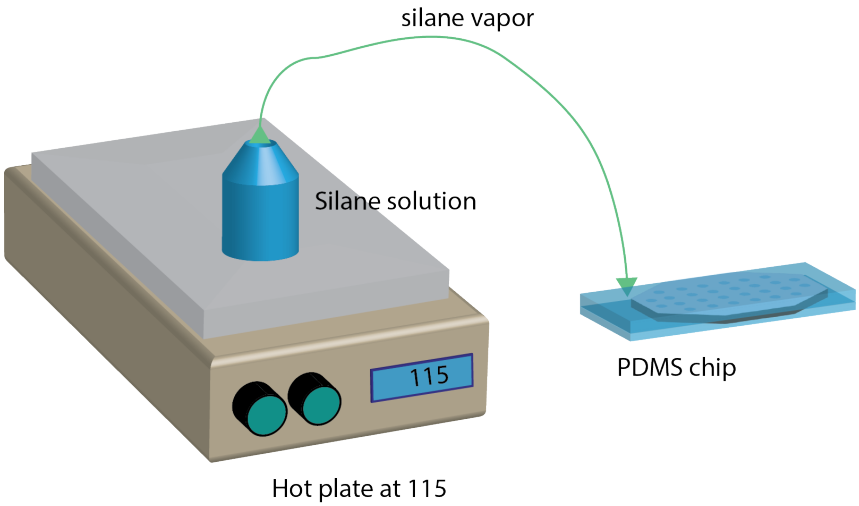

Figure 2.10: Injection of TCP silane in a PDMS microfluidic chips to make it uniformly hydrophobic.

uniform hydrophobic surface. In this process the TCP silane, Trichloro(1H,1H,2H,2H perfluorooctyl), is dissolved in ethanol with 0.018 $\frac{v_s}{v_e}$ volume ratio. Then, the solution is filtered using a 0.45 μm pore size Millex filter. After, the filtered solution is poured into a flask and is heated to 115°C. The vapors are conducted into the microfluidic chip for half an hour, Fig. 2.10. Finally, the chip is placed in an oven to dry. Karadimitriou et al. [62] report a contact angle of 4° for water-fluorinert and we measured the value of 33° between water-glycerol ($\frac{60}{40}$ $\frac{v}{v}$) and silicone oil 100 cSt.

2.1.5 Experimental setup

The experimental setup is presented in Fig. 2.11. for visualization of the system, an upright microscope (Nikon, Eclipse) is synced with a camera (Andor Neo, sCMOS 5.50 Megapixel, up to 500 f/s) and a Metal Halide lamp is used as the light source. our setup is also equipped with a Raman spectroscopy system for monitoring chemical composition. Two different systems of fluid injections are used, a syringe pump (Harvard Apparatus Pump 11 Elite) for constant flow rate experiments and a pressure controller (OB1 MK3+, Elveflow microfluidics flow controller, with a pressure range of 0 to 8 bar) for having constant pressure difference between inlet and outlet of micromodel.

2.1.6 Experimental workflow

All the experiments are conducted at room temperature. The aqueous phase is seeded with micro-particles (Polybead Carboxylate Microsphere 1 μm diameter, Polysciences) at approximately 0.06% volume concentration to visualize fluid movements during

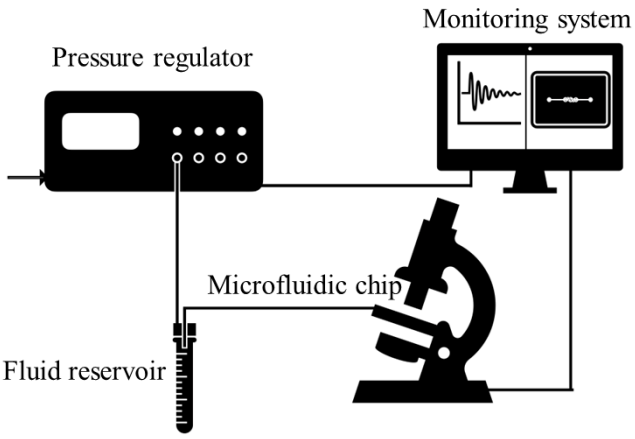

Figure 2.11: The schematic of experimental setup, including pressure regulator, monitoring system, fluid reservoir and microfluidic chip.

experiments. The density and surface properties of these particles are chosen to minimize deposition and aggregation in our micromodels. Usually, the interface between gases and liquids is sharp enough; however, liquid-liquid interfaces are difficult to differentiate. A royal blue dye (PME, Royal blue food color) is added to the aqueous phase to ease distinguishing phases. Before each experiment, for each choice of fluid pairs, micromodels are treated with one of the mentioned methods to modify the PDMS wettability so that it is always a drainage condition with an unfavorable mobility ratio ($M < 1$). In the drainage experiment, the micromodel is filled with the wetting fluid. Then the nonwetting phase is injected into the micromodel to displace the occupying phase. Meanwhile, image sequences of the flow process are recorded with different magnification and frame rates.

2.2 Data acquisition methodology

For the experiment, we mostly extracted three types of data from the recorded image sequence, interface dynamics, fluid body dynamics, and residual corner fluid dynamics. In each type, a workflow is considered, which is presented in the following sections.

2.2.1 Interface dynamics

The first data set of our interest is the displacement, dynamics of the interface, and saturation data during experiments. A MATLAB® code is developed using the image processing toolbox to analyze images. In the beginning, images are turned to grayscale

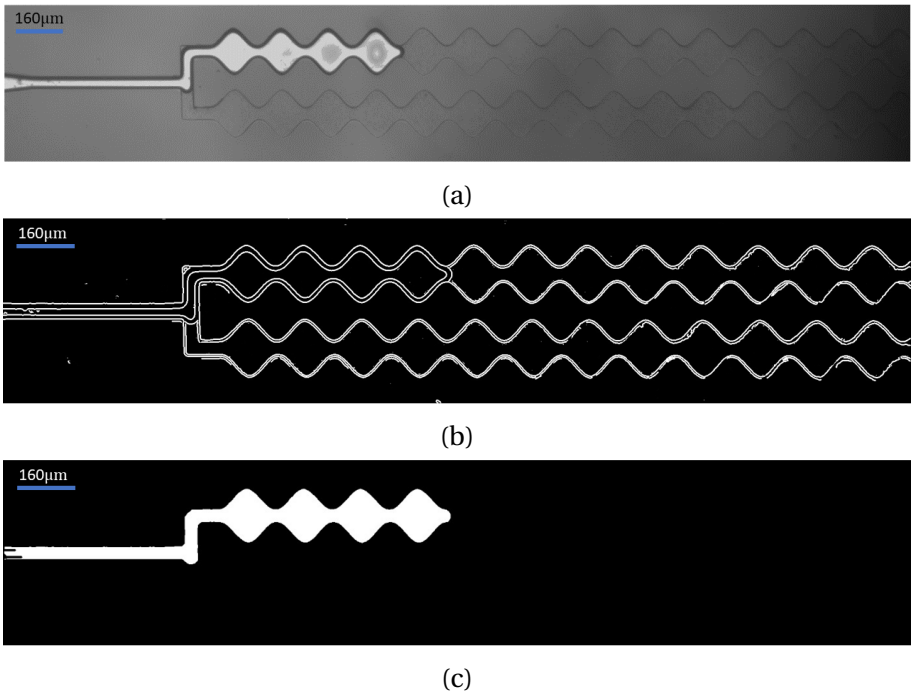

Figure 2.12: Process of extraction of invading phase out of images. From top to bottom, (a) captured image, (b) edges detection and (c) extracted invading phase are presented.

images and a pixel-wise adaptive Wiener correction filter is applied to each image, Fig. 2.12a. Then, the edge detection technique is employed to detect channels' outer boundaries and the interface, Fig. 2.12b. By using image filling techniques, the interface of invading fluid (including fluid-fluid and fluid-solid interface) is detected, Fig. 2.12c. In this step, measurement of front position (measured as the distance between inlet or outlet of the geometry from the interface), saturation (measured by calculation of the ratio of the surface area occupied by invading phase and the surface area of capillaries), and interface surface area are feasible.

2.2.2 Fluid body

PIV is a widely used technique that provides information about velocity fields and streamlines in fluids. In this method, the fluid is seeded with particles. Then, sequential images of moving fluid are taken. After that, captured images are divided into several interrogation windows. Each interrogation window contains particles that have made a pattern. PIV benefits from a cross-correlation technique to find the position of each pattern in the next image of the image sequence. The displacement between two interrogation windows containing the same pattern is considered fluid movement. Velocity vectors, then, are calculated by dividing displacement by the time difference between images. Fig. 2.13 illustrates the described process.

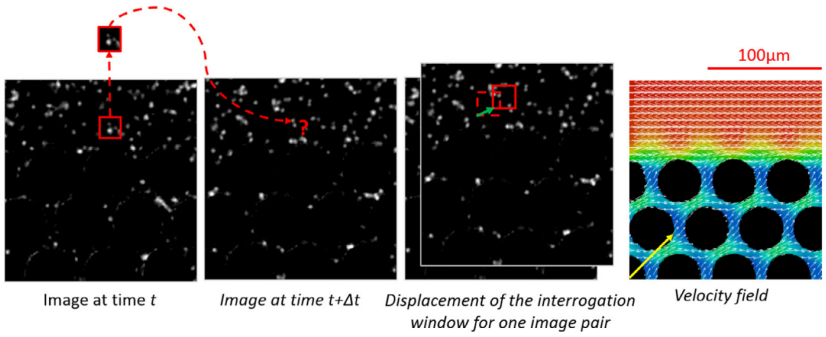

Figure 2.13: PIV process at a glance; interrogation windows, their transform between two adjacent images in image sequence, calculation of displacement and velocity and an example of final results, taken from Roman et al. [107].

Particle concentration is critical to be high enough to cover the practical resolution of streamlines and velocity field while avoiding any change in fluid properties by filling the fluid with a high concentration of particles [5]. Typically, in standard PIV, laser illuminations with fluorescent particles are used to blackout everything other than particles. Roman et al. [107] used a normal microscopy illumination to obtain the image sequences of the porous media and perform PIV. As is described by Roman et al. [107], because of the shallow depth of the porous media and small focal depth of the microscope, the focal plane of the objective is considered equivalent to the depth of the micromodel; hence, PIV measurements are applicable in this configuration. For this purpose, an image processing sequence precedes PIV analysis to remove the background out of the images.

Image processing for micro-PIV technique has several steps in common with the process for interface detection and tracking (discussed processes in Section 2.2.1). For the next steps, we follow the work of Roman et al. [107] to prepare images for performing PIV. To be able to separate the foreground from the background of the images, binarization and morphological techniques are applied on a time-averaged image to detect the edges of channels and correspondingly distinguish the grain texture from pores. By subtraction the background from each image, only the particles in channels remain. By adjusting the histogram of the resulting images, particles that are highly out of focus are removed from images.

Imaging frequency is an important factor of the captured image sequence. The time interval between images should be large enough to capture displacement of the patterns within two sequential images and low enough to prevent extreme distortion of patterns from one image to another. As a result, the time interval between shooting

times depends on how fast the fluid moves, which is a function of imposed flow rate and the timescale of the understudy phenomenon. For micro-PIV calculations, the maximum displacement should be around three-particle diameters as a thumb rule, as is explained in the work of Roman et al. [107].

In this research, the PIVlab toolkit of MATLAB® is used for the PIV analysis. It provides us with pre-and post-processing of images and PIV results. Details of the functionality of PIVlab are described in Thielicke and Stamhuis [135]. Direct Fourier transform correlation with multiple passes and deforming windows algorithm is used to cross-correlate the image data. Three different sizes of interrogation windows are used to obtain the velocity fields. This method helps to reduce noise in calculations and increases the resolution of results [107]. The smallest window size must be considered so that it contains at least three particles. Then, a step size of two times longer was considered for enlarging the interrogation window area for each iteration. PIVlab starts with the biggest interrogation window size. The bigger the window is, the higher the signal-to-noise ratio, but the lower the vector resolution of results is obtained. Then, iteratively, it moves to lower window size for the next pass. The settings were so that windows in each timestep overlapped previous windows by half. As a post-processing step, outlier data are filtered from the results at the final stage, and a local median filter is applied to the results. For steady-state conditions, since micro-PIV measurements usually are deprived of having high particle image density, the results were averaged for each 50 image pair. For unsteady flows, it depends on the time scale of the instability and perturbations. The work of Roman et al. [107] provides details on micro PIV for unstable flows.

2.3 Characteristic numbers and measurements

In the following chapters, when we refer to viscosity ratio (M) and capillary number (Ca), they are calculated in terms of Eqs. (2.1) to (2.3), otherwise it will be pointed out.

In general M is defined as

$$M = \frac{\mu_{invading}}{\mu_{defending}}, \tag{2.1}$$

for drainage, it reads

$$M = \frac{\mu_{nw}}{\mu_{w}}, \tag{2.2}$$

and the Ca is

$$Ca = \frac{\mu_{w} v_{interface}}{\sigma \cos\theta}, \tag{2.3}$$

where μ_w, μ_{nw}, $v_{interface}$, σ and θ are viscosity of wetting fluid, viscosity of non-wetting fluid, velocity of interface, interfacial tension and contact angle respectively.

The velocity of interface has been calculated mainly in two ways:

- First method is based on the average interface movement in the inlet channel. In this method, the interface position in the inlet channel is recorded at each time step. The mean value of interface displacement, based on the interface position data, is considered for calculation of mean front velocity and flow rate. Fig. 2.14 shows a schematic of velocity measurement in the inlet channel.

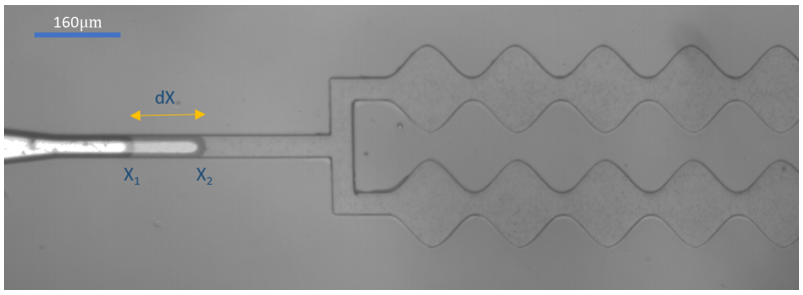

Figure 2.14: Measurement of interface velocity in inlet channel.

- In the second method, the average front speed in porous media is calculated to indicate the in situ velocities in porous media. In this method, the mean interface position in porous media is recorded at each time step. Then, the interface velocity is calculated by fitting a straight line to interface positions through experiment time. Fig. 2.15 presents an example of the curve fitting to mean interface position data to measure the mean velocity of interface based on the slope of the line.

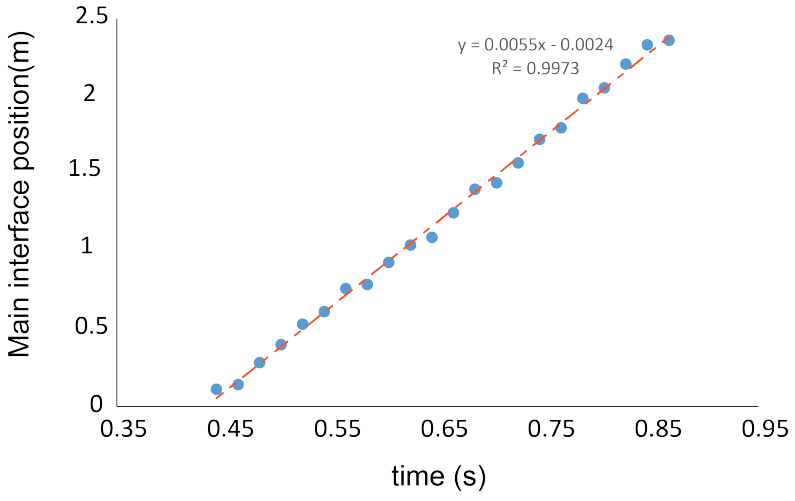

Figure 2.15: An example of mean interface position in porous media and fitted linear equation for obtaining interface velocity (for example $v = 0.005\, m.s^{-1}$).

In this chapter, we have summarized our experimental methodology and our microfluidics system. We noted our porous media properties, microchip preparation process, experimental condition, and data acquisition techniques. In the following chapters, if any specific technical data is required, it will be explained.

Chapter 3

Pore doublet model: theoretical development

3.1 Introduction

A pore doublet is a simplified consideration of a porous media, consisted of a pore splitting in two capillaries that join again after a distance, Fig. 3.1. It is representative of the pore space between rock grains in geological porous media. Although it is a very simplified replication of the porous media, it still captures the essence of the transport and interface displacement in the porous media, and results can be extended to larger scales. Pore doublet was originally proposed to explain oil entrapment mechanisms during water flooding and the fluid distribution during immiscible displacement in porous networks [16, 86, 111]. Pore doublet models are theoretical tools to investigate the fundamental mechanisms of two-phase flow in porous media [16, 26, 86, 4, 111] and enable a direct comparison with experiments. Theoretical consideration of the dynamics of front behavior in pore doublet geometries has been investigated, accounting for viscous and capillary forces [86, 111, 26, 143]. Al-Housseiny et al. [4] modeled the preferential flow paths in smoothly varying rectangular cross-section capillaries. Moebius and Or [83] implemented the effect of inertia forces on the interface behavior in their model and were able to predict interfacial perturbations as a result of momentum forces.

In this chapter we aim at developing a generalized dynamic model for studying the front behavior in a pore doublet system. In this regard, the theory behind fluid displacement with a pore-scale perspective is introduced. First, a theory based on the Navier-Stokes volume averaging technique for multi-phase flow is developed and tested. Then, the theory is non-dimensionalized for a general form of pore-doublet system. A the end, the developed model is applied to a system of consecutive pores and throats to study different displacement behaviors and mechanisms involved in

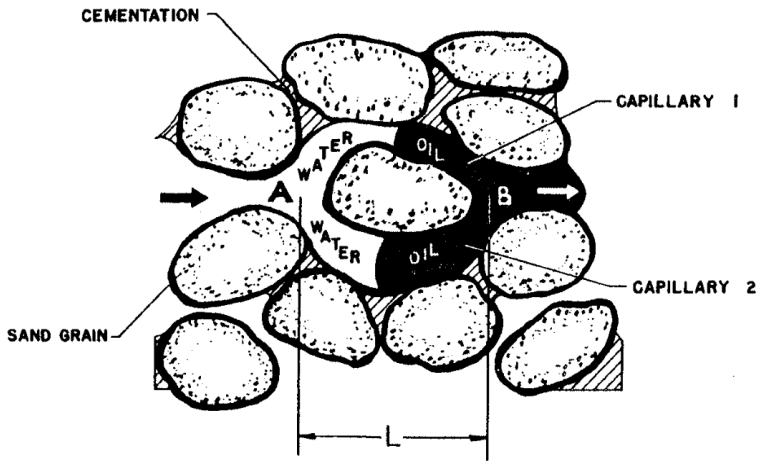

Figure 3.1: One of the first descriptions of pore doublet model as a representative of porous media, taken from Moore et al. [86].

multi-phase displacement in geological porous media.

3.2 Volume averaging

To investigate the fluid displacement through the pores and throat network of a porous system, we begin with the consideration of the microscopic momentum equation for the flow of an incompressible fluid. In its general form, it is written as

$$\rho\left[\frac{\partial v}{\partial t}+\nabla.(vv)\right]=-\nabla p+\mu\nabla^2 v+\rho g, \tag{3.1}$$

where ρ, v, t, p and g respectively denote density, velocity, time, pressure and gravity constant. The volume-averaged form of a property such as f is defined as

$$\langle f\rangle=\frac{1}{\Delta V}\int_{\Delta V} f\,dV. \tag{3.2}$$

The property f at each point is decomposed into its individual average ($\langle f\rangle$) and its deviation from the average value f', which reads as

$$f=\langle f\rangle+f', \tag{3.3}$$

according to Gray [48]. A volume average technique is applied on the momentum equation, Eq. (3.1), for the REV considering a no-slip condition at fluid-solid interface ($v=0$ at S_{f-s}) and assuming the velocity is a function of position and time at entrance

and outflow boundaries ($v = \mathbf{F}(r,t)$ at S_{f-e}). It reads as

$$\rho\left[\frac{\partial\langle v\rangle}{\partial t} + \nabla.\langle vv\rangle\right] = -\nabla\langle p\rangle + \mu\nabla^2\langle v\rangle - \nabla.\left(\rho\langle v'v'\rangle\right) + \rho g - \frac{\mu\langle v\rangle}{K} - \frac{c_f\rho|\langle v\rangle|\langle v\rangle}{\sqrt{K}}, \quad (3.4)$$

where K and c_f are known as permeability and Forchheimer coefficient respectively.

Knowing $\langle f'\rangle = 0$, by taking a thin cross-section of the porous media as the volume element, for a Newtonian fluid with a laminar-unidirectional flow Eq. (3.4) transforms into

$$\rho\left[\frac{d\bar{v}(x)}{dt}\right] = -\frac{\partial\bar{p}}{\partial x} - \mu\frac{\bar{v}(x)}{K(x)}. \quad (3.5)$$

Noting that the cross-section averaged value for property f is denoted as $\bar{f}$, Eq. (3.5) represents a cross-section averaged 1D equation, describing fluid transport for the position x in the channel. Now that we have the upscaled behavior of the fluid along the channel, we aim to specify the displacement behavior for the whole channel length.

3.3 Displacement in a channel

Here we attempt to find the momentum equation for the fluids inside a channel. In the beginning, we note that in this text, the displacing and displaced phases are identified by superscript (1) and (2), respectively. The position of the interface between displacing and displaced fluids in channels i and ii is denoted h_i and h_{ii}, respectively. Therefore, the velocity of the meniscus in each channel is $\dot{h}_i = \frac{dh_i}{dt}$ and $\dot{h}_{ii} = \frac{dh_{ii}}{dt}$.

3.3.1 System definition

Considering a two-phase displacement in a channel with the interface position h, the momentum balance for the invading phase is the integration of cross section-averaged momentum equation (Eq. (3.5)) along the channel,

$$\rho^{(1)}\left[\int_0^h \frac{d\bar{v}(x)}{dt}\,dx\right] = \int_0^h -\frac{\partial\bar{p}^{(1)}}{\partial x}\,dx - \mu^{(1)}\int_0^h \frac{\bar{v}(x)}{K(x)}\,dx,$$

which can be rearranged as

$$\rho^{(1)}\left[\frac{d\int_0^h \bar{v}(x)\,dx}{dt}\right] = -\Delta\bar{p}^{(1)} - \mu^{(1)}\int_0^h \frac{\bar{v}(x)}{K(x)}\,dx. \quad (3.6)$$

Similarly, for the displaced phase, we have

$$\rho^{(2)}\left[\frac{d\int_h^{L-h}\bar{v}(x)\,dx}{dt}\right]=-\Delta\bar{p}^{(2)}-\mu^{(2)}\int_h^{L-h}\frac{\bar{v}(x)}{K(x)}\,dx. \tag{3.7}$$

In Eq. (3.6) and Eq. (3.7) some terms can be simplified for our configuration. In what follows, we will address the calculation of pressure drop for each phase.

3.3.2 Displacing phase

Let us consider that the flow rate is constant along the channel; hence, the flow rate is related to the interface velocity as $A(h)\dot{h}$. Then the terms $\int_0^h \bar{v}(x)\,dx$ and $\mu^{(1)}\int_0^h \frac{\bar{v}(x)}{K(x)}\,dx$ are calculated as

$$\int_0^h \bar{v}\,dx = Q\int_0^h \frac{1}{A(x)}\,dx = A(h)\dot{h}\int_0^h \frac{1}{A(x)}\,dx. \tag{3.8}$$

and

$$\int_0^h \frac{\bar{v}}{K(x)}\,dx = Q\int_0^h \frac{1}{A(x)K(x)}\,dx = A(h)\dot{h}\int_0^h \frac{1}{A(x)K(x)}\,dx. \tag{3.9}$$

3.3.3 Displaced phase

With the same assumptions applied to displacing fluid, for the displaced phase, occupying from the interface to the end of the channel (L), one can write:

$$\int_h^L \bar{v}(x)\,dx = A(h)\dot{h}\int_h^L \frac{1}{A(x)}\,dx, \tag{3.10}$$

and

$$\int_h^L \frac{\bar{v}(x)}{K(x)}\,dx = A(h)\dot{h}\int_h^L \frac{1}{A(x)K(x)}\,dx. \tag{3.11}$$

Now that we have all assets to calculate the momentum balance for each phase as a function of interface position and channel shape and properties, we apply this formulation for a simple case of a pore doublet with two rectangular capillaries.

3.3.4 Capillaries with rectangular cross section

In this section, first, we apply the developed momentum balance equation for a channel during displacement. Then, the formulation is scaled for a pore doublet. Finally, the mass balance over the system is considered to find the governing equation for the front displacement.

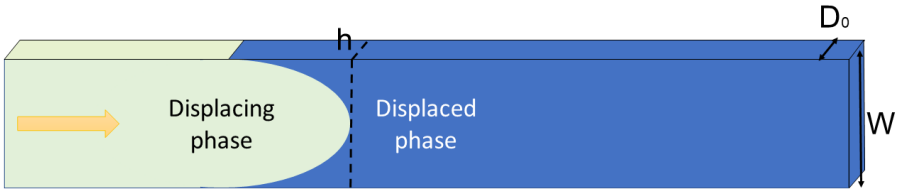

Figure 3.2: Top-view schematics of the flow in a rectangular channel, showing the descriptive parameters, h, D_0, and W respectively corresponding to interface position, channel depth, and channel width.

The pressure drop over a channel

Assuming a channel with constant rectangular cross-section, $A(x) = cte$, we aim to calculate the momentum balance over the channel. The non-wetting phase displaces the wetting phase, Fig. 3.2. For the displacing phase, the terms $\int_0^h \bar{v}(x)\,dx$ and $\mu^{(1)}\int_0^h \frac{\bar{v}(x)}{K(x)}\,dx$, in Eq. (3.6) are written as:

$$\int_0^h \bar{v}(x)\,dx = A(h)\dot{h}\int_0^h \frac{1}{A(x)}\,dx = \dot{h}h, \tag{3.12}$$

and

$$\int_0^h \frac{\bar{v}(x)}{K(x)}\,dx = A(h)\dot{h}\int_0^h \frac{1}{A(x)K(x)}\,dx = \frac{\dot{h}h}{K}. \tag{3.13}$$

The permeability of a rectangular channel is approximated from the work of Al-Housseiny et al. [4] by,

$$K = \left(\frac{D_0^2}{12}\right)\left(1 - 6\left(\frac{2}{\pi}\right)^5 \frac{D_0}{W}\right), \tag{3.14}$$

while D_0 and W denote channel depth and width; note that this expression is only valid for $D_0/(W) < 1$. It is obtained from the first term of the Fourier series solution for the velocity profile of a viscous flow in a rectangular channel [4]. Combining Eq. (3.6), Eq. (3.12), and Eq. (3.13) leads to

$$\rho^{(1)}\left[\frac{d}{dt}(h\dot{h})\right] = -\Delta p^{(1)} - \mu^{(1)}\frac{h\dot{h}}{K}. \tag{3.15}$$

Thus, it is concluded that the momentum balance for the invading phase reads as

$$\rho^{(1)}\left[h\ddot{h} + \dot{h}^2\right] = -\Delta p^{(1)} - \mu^{(1)}\frac{h\dot{h}}{K}. \tag{3.16}$$

Similarly, to calculate momentum balance for the displaced phase as Eq. (3.7), $\int_h^L \bar{v}(x)\,dx$ and $\int_h^L \frac{\bar{v}(x)}{K(x)}\,dx$ are computed for a rectangular cross-section as follows,

$$\int_h^L \bar{v}(x)\,dx = A(h)\dot{h}\int_h^L \frac{1}{A(x)}\,dx = \dot{h}(L-h), \tag{3.17}$$

and

$$\int_h^L \frac{\bar{v}(x)}{K(x)}\,dx = A(h)\dot{h}\int_h^L \frac{1}{A(x)K(x)}\,dx = \frac{\dot{h}(L-h)}{K}. \tag{3.18}$$

Inserting these values into Eq. (3.7), leads to,

$$\rho^{(2)}\left[\frac{\partial}{\partial t}(L-h)\dot{h}\right] = -\Delta p^{(2)} - \mu^{(2)}\frac{(L-h)\dot{h}}{K}, \tag{3.19}$$

that is rewritten as

$$\rho^{(2)}\left[(L-h)\ddot{h} - \dot{h}^2\right] = -\Delta p^{(2)} - \mu^{(2)}\frac{(L-h)\dot{h}}{K_{th}}. \tag{3.20}$$

The momentum balance over the whole channel is the sum of momentum balances of current phases. Hence, the overall momentum balance for the presented system is the sum of Eq. (3.16) and Eq. (3.20),

$$\rho^{(1)}\left[h\ddot{h} + \dot{h}^2\right] + \rho^{(2)}\left[(L-h)\ddot{h} - \dot{h}^2\right] = -\Delta p^{(1)} - \mu^{(1)}\frac{h\dot{h}}{K} - \Delta p^{(2)} - \mu^{(2)}\frac{(L-h)\dot{h}}{K}. \tag{3.21}$$

The pressure drop over the displacing and displaced phases are respectively

$$\Delta p^{(1)} = p_h^{(1)} - p_0^{(1)}, \tag{3.22}$$

and

$$\Delta p^{(2)} = p_L^{(2)} - p_h^{(2)}. \tag{3.23}$$

Sum of pressure drop over displacing and displaced phase $(-(\Delta p^{(1)} + \Delta p^{(2)}))$ that appears in Eq. (3.21) can be rearranged as

$$-\left[(p_h^{(1)} - p_i^{(1)}) + (p_L^{(2)} - p_h^{(2)})\right] = -\left[(p_L^{(2)} - p_i^{(1)}) + (p_h^{(1)} - p_h^{(2)})\right]. \tag{3.24}$$

The term, $(p_h^{(1)} - p_h^{(2)})$ in drainage condition is capillary pressure and $(p_L^{(2)} - p_i^{(1)})$ is the overall pressure drop over a channel. Hence, Eq. (3.21) is rearranged as

$$\rho^{(1)}\left[h\ddot{h} + \dot{h}^2\right] + \rho^{(2)}\left[(L-h)\ddot{h} - \dot{h}^2\right] = -\mu^{(1)}\frac{h\dot{h}}{K} - \mu^{(2)}\frac{(L-h)\dot{h}}{K} - \Delta p^{(overall)} - p_c\,. \tag{3.25}$$

In general, the pressure drop over each channel in a pore doublet system is written as

$$\Delta p_a^{(overall)} = -\rho_a^{(1)}\left[h_a\ddot{h}_a + \dot{h_a}^2\right] - \rho_a^{(2)}\left[(L-h_a)\ddot{h}_a - \dot{h_a}^2\right] - \mu_a^{(1)}\frac{h_a\dot{h}_a}{K_a} - \mu_a^{(2)}\frac{(L-h_a)\dot{h}_a}{K_a} - p_{ca} \text{ with } a = i, ii. \tag{3.26}$$

The capillary pressure is estimated for a rectangular cross-section by the Young-

Laplace equation. Assuming the interface shapes as a semi-circle in curvature planes, the radius of the curvature at location h will be half of the channel width (W) and depth (D_0). Thus the capillary pressure is written as

$$p_c = \sigma\kappa, \tag{3.27}$$

where $\kappa = \left(\frac{2}{D_0} + \frac{2}{W}\right)\cos(\theta)$, and θ denotes the contact angle.

Capillaries are connected at the inlet and outlet in a pore doublet system. The pressure at the inlet and outlet of a pore doublet configuration is assumed to be equal to the inlet, and outlet pressure of each channel [26]. Thus, the pressure drop over the two connected capillaries is equal in pore doublet. By equality of Eq. (3.26) for two capillaries and rearranging, the momentum balance over the pore doublet system reads as

$$\begin{aligned}[\rho^{(1)}h_i + \rho^{(2)}(L-h_i)]\ddot{h_i} + [-\rho^{(1)}h_{ii} - \rho^{(2)}(L-h_{ii})]\ddot{h_{ii}} = \\ (-\rho^{(1)} + \rho^{(2)})\dot{h_i}^2 - (\rho^{(1)} + \rho^{(2)})\dot{h_{ii}}^2 - \mu^{(1)}\frac{h_i\dot{h_i}}{K} + \mu^{(1)}\frac{h_{ii}\dot{h}_{ii}}{K} \\ - \mu^{(2)}\frac{(L-h_i)\dot{h}_i}{K} + \mu^{(2)}\frac{(L-h_{ii})\dot{h}_{ii}}{K} - p_{ci} + p_{cii}.\end{aligned} \tag{3.28}$$

Mass balance

Now that we have the momentum balance over the pore doublet, it is essential to note that the mass flow rate Q injected at the inlet is conserved throughout the system. Assuming that both phases are incompressible, the sum of the mass flow rates Q_a (with $a = i, ii$) in each channel is equal to the mass flow rate, Q, at the pore doublet inlet – also called the total mass flow rate. We have,

$$Q_i + Q_{ii} = Q. \tag{3.29}$$

For our configuration, it will be

$$W_i D_0 \dot{h_i} + W_{ii} D_0 \dot{h_{ii}} = Q. \tag{3.30}$$

Numerical solution

Momentum and mass balance equations lead to a system of second-order nonlinear ordinary differential equations. The numerical solution of Eq. (3.31) describes dynam-

ics of interface and interface velocity.

$$\begin{bmatrix} 1 & 0 & 0 & 0 \\ 0 & 1 & 0 & 0 \\ W_i & W_{ii} & 0 & 0 \\ 0 & 0 & \rho^{(1)}h_i + \rho^{(2)}(L-h_i) & -\rho^{(1)}h_{ii} - \rho^{(2)}(L-h_{ii}) \end{bmatrix} \frac{d}{dt} \begin{bmatrix} h_i \\ h_{ii} \\ \dot{h_i} \\ \dot{h_{ii}} \end{bmatrix} = \begin{bmatrix} \dot{h_i} \\ \dot{h_{ii}} \\ \frac{Q}{D_0} \\ A \end{bmatrix} \tag{3.31}$$

Where A is defined as:

$$A = (-\rho^{(1)} + \rho^{(2)})\dot{h_i}^2 - (-\rho^{(1)} + \rho^{(2)})\dot{h_{ii}}^2 - \mu^{(1)}\frac{h_i\dot{h}_i}{K_{th}} + \mu^{(1)}\frac{h_{ii}\dot{h}_{ii}}{K_{th}} - \mu^{(2)}\frac{(L-h_i)\dot{h}_i}{K_{th}} + \mu^{(2)}\frac{(L-h_{ii})\dot{h}_{ii}}{K_{th}} - p_{ci} + p_{cii}. \tag{3.32}$$

Dimensionless equations

To generalize the equation and to avoid scale dependency, equations are non-dimensionalized using series of reference and characteristic values, $t_c, \Pi, K_c, h_c, \kappa_c, A_c$ and r_c respectively for, time, pressure, permeability, length, interface curvature, surface area and radius.The viscosity and density ratio are respectively defined as following,

$$M = \frac{\mu^{(1)}}{\mu^{(2)}}, \quad \Gamma = \frac{\rho^{(1)}}{\rho^{(2)}}.$$

We start with mass conservation, Eq. (3.29), to find the dimensionless form of the equation. By non-dimensionalizing parameters, one can write

$$\frac{\bar{A}h_c}{t_c Q}\left(A^*(h_i)\dot{h}_i^* + A^*(h_{ii})\dot{h}_{ii}^*\right) = 1, \tag{3.33}$$

which by defining $t_c = \frac{A_c h_c}{Q}$ transforms to

$$A^*(h_i)\dot{h}_i^* + A^*(h_{ii})\dot{h}_{ii}^* = 1. \tag{3.34}$$

Considering Eq. (3.26), the dimensionless form of the overall pressure drop after some manipulation is

$$\Delta p_a^{*(overall)} = -\frac{\rho^{(2)}h_c^2}{\Pi {t_c}^2}\left[\Gamma\left[h_a^*\ddot{h}_a^* + \dot{h}^*{}_a^2\right] + \left[(h_c^* - h_a^*)\ddot{h}_a^* - \dot{h}_a^{*2}\right]\right] - \frac{\mu^{(2)}h_c^2}{\Pi t_c K_c}\left[M\frac{h_a^*\dot{h}_a^*}{K_a^*} - \frac{(h_c^* - h_a^*)\dot{h}_a^*}{K_a^*}\right] - \frac{\sigma\kappa_c}{\Pi}\left(\kappa_a^*\right) \text{ with } a = i, ii. \tag{3.35}$$

By defining the viscous pressure drop for the characteristic length of a porous media with characteristic permeability, due to imposed flow rate as the characteristic pres-

sure, $\Pi = \frac{\mu^{(2)} h_c Q}{A_c K_c}$, and the definition of t_c, the dimensionless pressure drop is written as

$$\Delta p_a^{*(overall)} = -\frac{\rho^{(2)} Q K_c}{\mu^{(2)} h_c \bar{A}} \left[\Gamma \left[h_a^* \ddot{h}_a^* + \dot{h}_a^{*2} \right] + \left[(1-h_a^*) \ddot{h}_a^* - \dot{h}_a^{*2} \right] \right] - \left[M \frac{h_a^* \dot{h}_a^*}{K_a^*} - \frac{(1-h_a^*)\dot{h}_a^*}{K_a^*} \right] - \frac{\sigma \kappa_c K_c \bar{A}}{\mu^{(2)} h_c Q} \left(\kappa_a^* \right) \text{ with } a = i, ii. \quad (3.36)$$

By definition, the Ca (capillary number) is the ratio of viscous pressure drop and capillary pressure, and Re (Reynolds number) is the ratio of momentum forces to viscous forces; hence, one can define the characteristic capillary number

$$Ca_c = \frac{\mu^{(2)} h_c Q}{\sigma \cos(\theta) \kappa_c K_c \bar{A}}, \quad (3.37)$$

and

$$Re_c = \frac{\rho^{(2)} Q K_c}{\mu^{(2)} h_c \bar{A}}. \quad (3.38)$$

As a result, the final dimensionless form of the pressure drop over a channel in a rectangular cross-section will be

$$\Delta p_a^{*(overall)} = -Re_c \left[\Gamma \left[h_a^* \ddot{h}_a^* + \dot{h}_a^{*2} \right] + \left[(1-h_a^*) \ddot{h}_a^* - \dot{h}_a^{*2} \right] \right] - \left[M \frac{h_a^* \dot{h}_a^*}{K_a^*} - \frac{(1-h_a^*)\dot{h}_a^*}{K_a^*} \right] - Ca_c^{-1} \left(\kappa_a^* \right) \text{ with } a = i, ii. \quad (3.39)$$

By setting equality between the pressure drop over both capillaries, the final form of the equation for the pore doublet will be:

$$Re_c \left[\Gamma h_i^* + (1-h_i^*) \right] \ddot{h}_i^* + \left[-\Gamma h_{ii}^* - (1-h_{ii}^*) \right] \ddot{h}_{ii}^* = Re_c(-\Gamma+1)\dot{h}_i^{*2} - Re_c(-\Gamma+1)\dot{h}_{ii}^{*2} - M\frac{h_i^* \dot{h}^*{}_i}{K^*} + M\frac{h_{ii}^* \dot{h}^*{}_{ii}}{K^*} - \frac{(1-h_i^*)\dot{h}^*{}_i}{K^*} + \frac{(1-h_{ii}^*)\dot{h}^*{}_{ii}}{K^*} - Ca_c^{-1}\left(\kappa_i^*\right) + Ca_c^{-1}\left(\kappa_{ii}^*\right). \quad (3.40)$$

Similar to Section 3.3.4, momentum and mass balance over the pore doublet will lead to a system of second-order differential equations as follows,

$$\begin{bmatrix} 1 & 0 & 0 & 0 \\ 0 & 1 & 0 & 0 \\ (DW)_i^* & (DW)_{ii}^* & 0 & 0 \\ 0 & 0 & Re_c[\Gamma h_i^* + (1-h_i^*)] & Re_c[-\Gamma h_{ii}^* - (1-h_{ii}^*)] \end{bmatrix} \frac{d}{dt^*} \begin{bmatrix} h_i^* \\ h_{ii}^* \\ \dot{h}_i^* \\ \dot{h}_{ii}^* \end{bmatrix} = \begin{bmatrix} \dot{h}_i^* \\ \dot{h}_{ii}^* \\ 1 \\ \alpha \end{bmatrix}, \quad (3.41)$$

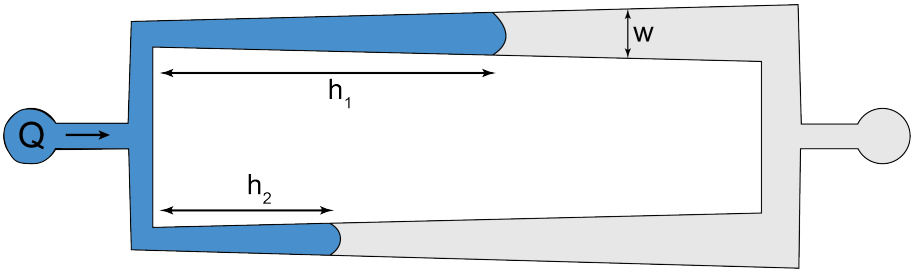

Figure 3.3: A schematic of the doublet geometry for rectangular channels that increase linearly in width in direction of flow, $w(x) = w_0 + \alpha x$. Modified from Al-Housseiny et al. [4].

where α is

$$\alpha = Re_c(-\Gamma+1)\dot{h}_i^{*2} - Re_c(-\Gamma+1)\dot{h}_{ii}^{*2} - M\frac{h_i^*\dot{h}^*{}_i}{K_i^*} + M\frac{h_{ii}^*\dot{h}^*{}_{ii}}{K_{ii}^*} - \frac{(1-h_i^*)\dot{h}^*{}_i}{K_i^*} + \frac{(1-h_{ii}^*)\dot{h}^*{}_{ii}}{K_{ii}^*} - Ca_c^{-1}\left(\kappa_i^*\right) + Ca_c^{-1}\left(\kappa_{ii}^*\right).$$

Interplay between viscous and capillary forces

Here we study a system similar to what Al-Housseiny et al. [4] studied to compare with our model results. Al-Housseiny et al. [4] used a pore doublet with a pore size that increases in the flow direction, $w(x) = w_0 + \alpha x$, where the gradient $\alpha \ll 1$, see Fig. 3.3. Here, a constant flow rate is applied to the system, and the interface is tracked until breakthrough with a $\dot{h}^* > 0$ constraint. A small size difference, 1%, is considered between capillaries as a perturbation that grows depending on the system's parameters. Results are reported in Fig. 3.4 for different flow rates.

Presented results are in agreement with data reported in Al-Housseiny et al. [4]. It is observed that in low Ca_c, since the surface forces are dominant, the lower capillary force that acts on the wider channel, and its higher conductivity prompts instability in displacement front, Fig. 3.4a. At this condition, the front makes a preferential flow path for fluid transport, Fig. 3.4c. However, at higher Ca_c viscous forces stabilize the displacement. A transient behavior is observed at flow rates ranging in between, Fig. 3.4b.

In what follows, we generalize the formulation for pore doublet geometry. The equations are non-dimensionalized, and the developed model is applied to an undulated pore doublet system that follows the geometry used in our experiments in Chapter 4.

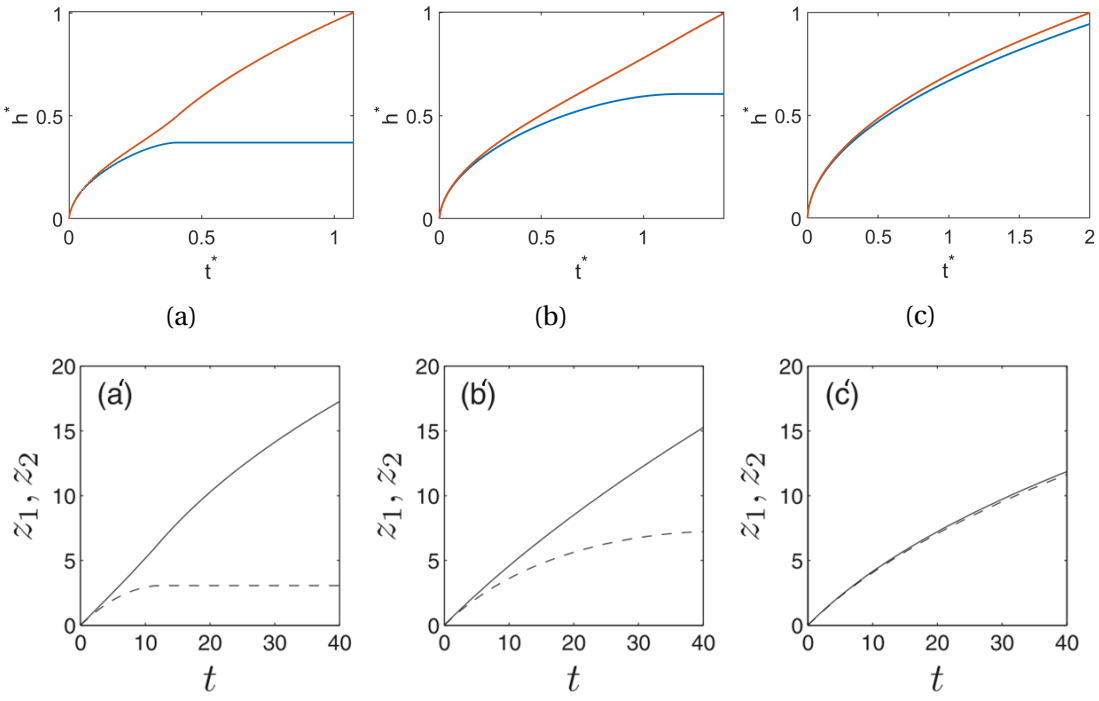

Figure 3.4: Front behavior at different flow conditions (Ca_c). Data corresponds to (a) $\log Ca_c = -3.31$, (b) $\log Ca_c = -3.11$, and $\log Ca_c = -2.82$ conditions with $\theta = 0$ and $log\, M = 1.69$, when the dimension increasing rate is $\alpha = 0.05$. The data reported in red corresponds to the interface position in wider channel. Data from Al-Housseiny et al. [4] is reported here as (a'),(b), and (c') correspond to $\log Ca = -2.24$, $\log Ca = -2.19$, and $\log Ca = -2$ respectively, with $\log M = 1$.

3.4 General format

The general format of the pressure drop over a displacing and displaced phase is presented in Eq. (3.6) and Eq. (3.7). It is applicable to any given channel satisfying our assumptions, see Fig. 3.5. In what follows, we will develop a general dimensionless format for pressure drop and the dynamics of the interface for a displacement in a pore doublet system.

3.4.1 Pressure drop over a channel

The pressure drop over a channel is the sum of the pressure drop of the displacing, displaced phase and the capillary pressure. With the same analogy as Section 3.3.2 and Section 3.3.3 one can write

$$\rho^{(1)}\left[\frac{d\left(A(h)\dot{h}\int_0^h \frac{1}{A(x)}\,dx\right)}{dt}\right] = -\Delta\bar{p}^{(1)} - \mu^{(1)}A(h)\dot{h}\int_0^h \frac{1}{A(x)K(x)}\,dx, \tag{3.42}$$

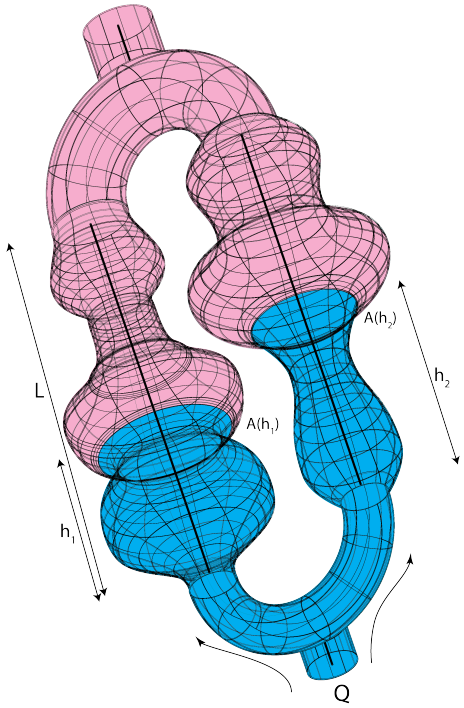

Figure 3.5: A schematic representation of a general pore doublet geometry. A constant flow rate of Q is injected to the system. L, h and $A(h)$ respectively represent total length of the pore doublet, invaded length in each channel and the cross-section area of the channel as a function of the position.

and

$$\rho^{(2)}\left[\frac{d\left(A(h)\dot{h}\int_h^L \frac{1}{A(x)}\,dx\right)}{dt}\right] = -\Delta\bar{p}^{(2)} - \mu^{(2)}A(h)\dot{h}\int_h^L \frac{1}{A(x)K(x)}\,dx, \tag{3.43}$$

where A and K are a function of position in the channel, Fig. 3.5. As a result, the total pressure drop over a channel with some rearrangement and manipulation will be

$$\Delta\bar{p}^{overall} = -\rho^{(2)}\frac{d}{dt}\left(\left(A(h)\dot{h}\right)\Theta(h)\right) - \mu^{(2)}A(h)\dot{h}\Phi(h) - \sigma\kappa(h), \tag{3.44}$$

where

$$\Theta(h) = \Gamma\int_0^h \frac{1}{A(x)}\,dx + \int_h^L \frac{1}{A(x)}\,dx,$$

and

$$\Phi(h) = M\int_0^h \frac{1}{A(x)K(x)}\,dx + \int_h^L \frac{1}{A(x)K(x)}\,dx.$$

By non-dimensionalizing the equation, we find

$$\Delta\bar{p}_a^{*(overall)} = -Re_c\frac{d}{dt^*}\left(A_a^*(h_a^*)\dot{h}_a^*\Theta^*(h_a^*)\right) - A_a^*(h_a^*)\dot{h}_a^*\Phi^*(h_a^*) - Ca_c^{-1}\kappa^*(h_a^*), \tag{3.45}$$

where,

$$\Theta^*(h_a^*) = \Gamma \int_0^{h_a^*} \frac{1}{A_a^*(x)}\, dx + \int_{h_a^*}^{L^*} \frac{1}{A_a^*(x)}\, dx,$$

and

$$\Phi^*(h_a^*) = M \int_0^{h_a^*} \frac{1}{A_a^*(x) K_a^*(x)}\, dx + \int_{h_a^*}^{L^*} \frac{1}{A_a^*(x) K_a^*(x)}\, dx,$$

with $a = i, ii$. Fig. 3.6 represents Φ and Θ functions for the interface with distance h^* from the inlet. The mass balance for this system reads

$$A^*(h_i)\dot{h}_i^* + A^*(h_{ii})\dot{h}_{ii}^* = 1. \tag{3.46}$$

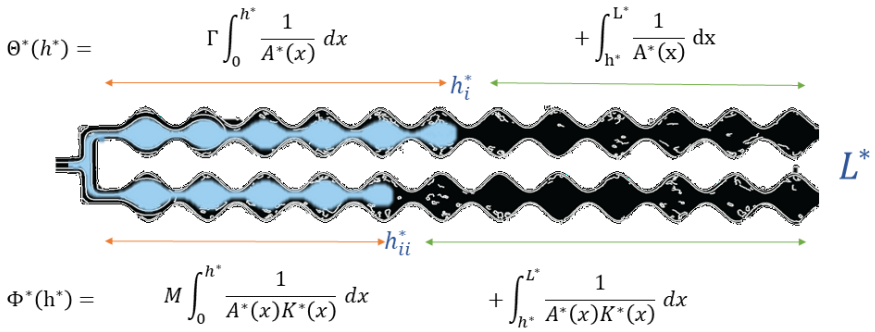

Figure 3.6: A schematic representing the Φ and Θ functions for a displacement over a pore doublet system.

3.4.2 Displacement in a pore doublet

Now that we have extended the pressure drop for a single channel, we apply it to a pore doublet model. For a pore doublet system with any given pore geometry, one can write

$$Re_c \frac{d}{dt^*}\left(A^*(h_i^*)\dot{h}_i^*\Theta^*(h_i^*) - A^*(h_{ii}^*)\dot{h}_{ii}^*\Theta^*(h_{ii}^*)\right) = \\ -A^*(h_i^*)\dot{h}_i^*\Phi^*(h_i^*) + A^*(h_{ii}^*)\dot{h}_{ii}^*\Phi^*(h_{ii}^*) - Ca_c^{-1}\left(\kappa^*(h_i^*) - \kappa^*(h_{ii}^*)\right). \tag{3.47}$$

$\Theta^*(h^*)$ and $\Phi^*(h^*)$ must be computed for each system.

Here we have developed a generalized dimensionless equation to describe interface dynamics by taking viscous, capillary, and momentum forces into account. We observe that mobility ratio and capillary number, which most previous studies have used as an indicator of flow conditions, appear as an inherent part of the displacement equation. Additionally, in this definition of the capillary number, the pore shape is considered as well, which will help the validity and comparability of Ca_c over a vast

range of porous media. Other terms regarding the inertia forces, which have been neglected in multiphase Darcy-based formulations, appear in this formulation and will improve predicatively of the model for fast dynamics.

3.5 Sinusoidal pore-throat geometry

Now that we have a general form of the pore doublet equation, we apply the presented model to a system corresponding to our microfluidic experiments. Considering each channel in the pore doublet model as a succession of pores and throats. The geometry of pores and throats are defined as a function of distance from the inlet, (h), using a sinusoidal function as follows,

$$r(h) = \frac{r_p + r_{th}}{2} - \frac{r_p - r_{th}}{2} \cos\left(\frac{2\pi h}{H}\right), \tag{3.48}$$

where r_p and r_{th} are the pore and throat radius, and H is the pore length, Fig. 3.7. Let us consider the pore profile to be rectangular because of the etching process in micromodel preparation. Therefore, if D_0 is the micromodel depth, then the cross-section area is,

$$A(h) = 2r(h)D_0, \tag{3.49}$$

the curvature of the interface at each position is

$$\kappa = \left(\frac{2}{D_0} + \frac{1}{r(h)}\right)\cos(\theta), \tag{3.50}$$

and the permeability of a rectangular channel is approximated by,

$$K(h) = \left(\frac{D_0^2}{12}\right)\left(1 - 3\left(\frac{2}{\pi}\right)^5\left(\frac{D_0}{r(h)}\right)\right). \tag{3.51}$$

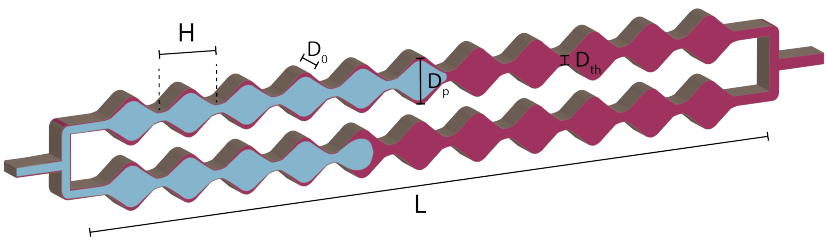

Figure 3.7: Schematic of a pore doublet with sinusoidal pore-throat morphology and rectangular cross-section capillaries.

It is possible to solve the Eq. (3.47) and Eq. (3.46) fully numerically for each system. However, for a defined geometry as ours, the $\Theta^*(h^*)$, $\Phi^*(h^*)$ and $\frac{d}{dt^*}\left(A^*(h^*)\dot{h}^*\Theta^*(h^*)\right)$ functions have an analytical solution as is presented in Appendix A.4. This reduces the

computational effort substantially and enables us to reconfigure the system to a first-order ODE set with mass matrix, which is solved using built-in functions of MATLAB®.

3.6 Summary and conclusions

In this chapter a volume averaging technique is applied to a pore doublet system to predict the front behavior and interface dynamics in a two-phase flow displacement. We propose a general dynamic pore doublet model and make the foundation to systematically study the front instabilities and pore invasion dynamics based on characteristic dimensionless numbers, Ca_c, M, Re and Γ. This sheds light on why these dimensionless numbers are a prominent indicator to categorize and predict front instabilities. In the next chapter, we seek the study of interface dynamics and pore invasion mechanisms using precise microfluidic experiments and the developed model.

Chapter 4

Pore invasion interface dynamics and front behavior in a pore doublet

4.1 Introduction

Multiphase transport in porous media is ubiquitous during the CO_2 sequestration process, where supercritical CO_2 displaces formation brine through pores and throats of porous media. The achieved storage capacity is tied with fluid displacement behavior, which is a function of fluid properties (viscosity, density, interfacial tension, etc.), porous media properties (affinity of porous surface to one fluid, i.e., wettability, pore and throat size, pore connectivity, etc.) and flow conditions [97]. Due to the low viscosity ratio between displacing and displaced fluid, CO_2 sequestration displacement is considered unfavorable, as it is prone to leave some of the displaced fluid behind by developing a ramified displacement front as it was first noted by Saffman and Taylor [113]; this is a central factor in displacement efficiency and consequently storage capacity. In the multiphase Darcy equation, the flow is only considered a saturation function. However, depending on the flow condition and pore and fluid properties, in different configurations, the displacement process shows distinct flow patterns in an unsaturated porous media, which dictate the transport properties and the storage capacity at a later stage. One of the earliest works, Lenormand et al. [72], distinguished different flow patterns and categorized them in three flow regimes based on two important active forces during the drainage process, presented as the ratio between viscous and capillary forces (Ca) and viscosity ratio (M), see Fig. 1.2. In addition, as a consequence of complex pore invasion dynamics, the macroscopic apparent steady advancing front in porous media during the displacement process is known to be built of a series of discrete pore invasion events [53, 83]. Recent studies have demonstrated that inertial forces, which are traditionally neglected in multiphase Darcy extension, are not always negligible [83, 8]. Additionally, the

development and application of novel techniques such as micro-PIV have improved our understanding of sub-pore-scale phenomena, and fluid streamlines revealed different viscous dissipation mechanisms [107, 108]. Due to strict assumptions on the interface equilibrium and stable displacement and some inherent inconsistencies in the traditional description of two-phase flow [54, 49], the development of front instabilities casts a shadow of doubt on the prediction of immiscible displacement using relative permeabilities [51, 97, 49, 54].

In order to capture the instabilities and invasions mechanisms, which are a result of small-scale phenomena, pore-scale is a prominent scale of study and characterization. Several pore invasion mechanisms have been presented and were distinguished in experimental and numerical works [73, 14, 115]. Although shreds of evidence of the important effect of these pore invasion mechanisms on the flow pattern and front displacement can be found in litterateurs ([31]), the focused study of the flow regimes and embedded pore invasion mechanisms remained limited.

Using microfluidic techniques, we are able to design the morphology of the porous system. Various works have investigated different porous settings, from 2D replicas of real rocks [107] to simplified homogeneous systems [18]. In most of the studies, pores are vastly connected through a pore network system, making it almost impossible to associate observed front disturbance to a specific invasion due to the non-locality of events. In other words, the connectivity of pores increases the chance of interference by a phenomenon happening at many other pores, adding a limitation to distinguish between understudy phenomena and disturbing effects. Since in this research, the focus is to determine and extract the effect of pore scale phenomena on the interface and front behavior at other pores, the geometry designs were kept as minimal as possible to be able to separate individual effects.

Experimental studies of invasion dynamics for slow displacements show that interface moves through the porous media by pinning at constrictions followed by an abrupt movement of the interface associated with pressure bursts, named after the work of Haines [53] as Haines jumps [83]. These jumps are associated with inertial effects and are proposed to rule the invasion mechanisms and change invasion patterns [41]. Velocimetry of these jumps showed that the interface velocity can reach up to 50 times the mean interface velocity [83, 107]. Sudden pressure and velocity fluctuation and associated inertial movement of the interface are accompanied by relaxation and retraction of the interface inside pores, showing non-locality of capillary effects [8]. These small-scale phenomena add to the complexity of displacement prediction and bring up the question of whether it affects global fluid displacement. Singh et al. [115]

reported a direct relation between ramification of the front and frequency of Haines jumps. Moebius and Or [84] report the alteration of displacement pattern and the change in invaded pores' size distributions as a result of the inertial effect of Haines jumps in their simulations. Roman et al. [107] and Blois et al. [18] reported downstream perturbations and flow fluctuations during two-phase displacement process, showing local pressure gradients. Despite significant contributions in studying displacement behavior, the majority of the experimental works have focused on the overall macroscopic behavior of the interface, and there is no conclusive understanding of the pore-scale invasion for precisely defined pore geometry. Additionally, most of the previous works were performed at highly connected pore network systems, making it almost impossible to associate observed front disturbance to a specific invasion due to the non-locality of events. In this regard, a study of pore invasions at a single-pore scale seems the main step because small-scale phenomena such as interface deformation and contact-line pining are captured during the displacement process. Using microfluidics, we are able to design minimal porous media to study invasions at a single pore-scale and side pore effects in detail.

This chapter aims to investigate experimentally and numerically pore-scale dynamics, key pore invasion mechanisms, and their contribution in defining global front behavior at different flow regimes using a well-defined microfluidic system. First, we describe the applied experimental and characterization methodology. Then, the different active pore invasion mechanisms for various flow conditions in porous media are then studied at pore-scale. The developed dynamic model in Chapter 3 is adapted to the experimental system, and results are compared. Then, the results will be discussed in terms of the Lenormand phase diagram [72] and estimated front behavior. Finally, experimental and numerical results on dynamics of interface displacement and the inter-connectivity of the interface at porous media at different pores (i.e., alteration in dynamics and position of the interface at one pore is able to change the dynamics of the interface at other pores) are presented.

the results of this chapter and Chapter 3 are published in AWR and are accessible here.

4.2 Experimental methodology

In this section, we present our experimental method, setup, and measurement techniques along with investigated fluid pairs.

A cutting-edge microfluidic system is set up to perform direct, fast, and high-resolution monitoring of fluid-fluid displacement. Details of the experimental setup are found in Section 2.1.5. A microfluidic chip with a well-defined geometry representing a succession of pores and throats with a sinusoidal pore doublet model is considered our porous media. A schematic representation of the considered porous media is presented in Fig. 3.7, and details of the designed geometry are given in Table 4.1. Each pore has a length of H, pore radius of r_p, throat radius of r_t, and depth of D_0, which remain constant all over the porous media. A plasma cryogenic etching method [36] is adopted to prepare high-resolution silicon molds. Chips are prepared by using PDMS soft lithography [62] (see Section 2.1.3) and were sealed using a flat PDMS slab by using plasma treatment for 40 to 50 seconds. Then, microfluidic devices were placed on the hot plate for 10 minutes at $100^{\circ}C$ to fix the bonding.

PDMS has heterogeneous wettability properties and needs surface treatment to obtain full hydrophilic or hydrophobic conditions. For more details on different surface treatments and reported contact angles, see Section 2.1.4. To obtain a wide range of viscosity ratios, various fluid pairs were selected according to Table 4.2 to replicate the unfavorable displacement condition of CO_2 sequestration in subsurface environments ($-2 < log\,M < 0$ and $log\,Ca < -3$). A KRÜSS ADVANCE drop shape analyzer from BRGM is used to measure interfacial tension between different fluid pairs.

Drainage experiments are performed by applying a high precision control on micromodels' inlet and outlet pressure. Different flow rates (ranging from 2.79×10^{-14} to 1.32×10^{-11} $(m^3 s^{-1})$) resulted from various applied pressure gradients (ranging from 30 $mbar$ to 110 $mbar$), which are corresponding to various capillary numbers, Ca, ranging from $\log Ca = -5.85$ to $\log Ca = -3.4$ with classical definition of Ca introduced in Section 2.3, for overall 65 experiment. To be consistent with the defined Ca_c in Eq. (3.37), which also takes pore shape characteristics into account, reported capillary numbers for experiments will be according to Ca_c, ranging from $\log Ca = -3.92$ to

Table 4.1: Aspects of the designed porous geometry.

Pore size ($2 \times r_p$)	Throat size ($2 \times r_{th}$)	Depth (D_0)	Pore length (H)
$160\,\mu m$	$40\,\mu m$	$40\,\mu m$	$160\,\mu m$

Table 4.2: Presentation of the fluid pairs which were used for displacement experiments.

Fluid pairs	Displacing phase	Displaced phase	log M	contact angle	Interfacial tension
1	air	DI-water	-1.7	30	72.86
2	DI-water-glycerol ($\frac{60}{40}\ \frac{v}{v}$)	silicone oil 100 cSt	-1.3	30	44.87
3	silicone oil 5 cSt	DI-water-glycerol ($\frac{40}{60}\ \frac{v}{v}$)	-0.53	60	39.34

$\log Ca = -0.75$.

Experiments were captured as image sequences containing different stages of the drainage process. Image processing of the resulting image sequences provides data on dynamics of drainage process, residual saturations, interface dynamics, etc. By tracking the interface, the position and velocity of the interface in the porous media are measured using a set of self-developed image processing codes in MATLAB®. More details of the steps of this process is available in Section 2.2.1. Micro-PIV technique was used to obtain velocity fields in the body of the defending fluid (seeded aqueous phase) to observe the effect of front instabilities in adjacent pores. Particles were separated from the background using a code adapted from the workflow of Roman et al. [107]. The final images were fed to PIV-lab [134], a user friendly MATLAB extension for performing PIV (for more information of micro-PIV protocol see Section 2.2.2 and refer to Roman et al. [107]).

We developed a dynamic multiphase pore doublet model based on applying volume averaging techniques on Navier-Stokes equation in Chapter 3. Then, to be consistent with our microfluidic chips geometry, the model was applied on a pore doublet with sinusoidal pores and throats geometry and rectangular cross-section normal to the channel direction. Data on porous media dimensions are noted in Table 4.1.

This study considers two identical capillaries, and the mentioned porous media aspects were kept constant throughout the whole geometry. A small surface area difference is imposed between capillaries to account for plausible minimal heterogeneities in the system (channel 2 is 1% wider than the other). A constant flow rate boundary condition is applied to the system, leading to a second-order nonlinear ordinary differential equations (ODE) system. It is possible to solve the equations fully numerically for each system. However, for a defined geometry as ours, the $\Theta^*(h^*)$, $\Phi^*(h^*)$ and $\frac{d}{dt^*}\left(A^*(h^*)\dot{h^*}\Theta^*(h^*)\right)$ functions have an analytical solution as is presented

respectively in Appendix A.4. It substantially reduces the computational load and reconfigures the system to a first-order ODE set with mass matrix, which was solved using built-in functions of MATLAB®.

In the following sections, first, the results of experiments on front behavior with a focus on the invasion mechanism will be presented. Then, the numerical model is adapted to the experiments, and simulation results are discussed compared to experiments. Then, the results are applied to predict the flow regimes in terms of Ca_c and M as a Lenormand phase diagram.

4.3 Front behavior: invasion mechanisms

Studying fluid displacement in a well-defined porous media under different flow conditions sheds light on different pore invasion mechanisms involved in each flow condition during the drainage process. The pressure gradient displaces fluids and interfaces through porous media. For a single-phase flow, viscous dissipation controls the fluid flow. However, in multiphase flows, when the interface reaches the smaller constrictions, i.e., throats, capillary forces increase and become comparable with viscous forces ([73, 83]) and are able to change the flow condition. This interplay between different forces triggers different pore invasion mechanisms that we believe are able to control the overall flow patterns in porous media. In this regard, we perform several drainage experiments with different flow rates leading to different flow regimes. In each flow regime, we characterize the pore invasion dynamics and mechanisms to shed light on the effect of active forces on pore invasion and, accordingly, front behavior.

4.3.1 Experimental pore-scale observations on pore invasion mechanisms

The fluid-fluid interface of displaced and displacing phases is tracked throughout experiments. In our experiments, depending on the ratio of viscous to capillary forces indicated by Ca_c, different flow regimes are observed for various viscosity ratios, M, based on the front behavior and interface movement in the porous media (Fig. 4.1, Fig. 4.6 and Fig. 4.3). These regimes are described in the following sections. Generally, the more dominant the viscous forces are, the more probable it is that both capillaries are invaded.

At the viscous flow regime, corresponding to the higher flow rates ($log\, Ca_c > -1.4$), invading phase is able to enter both channels simultaneously and displace the water inside the porous medium with almost no restriction in the interface displacement.

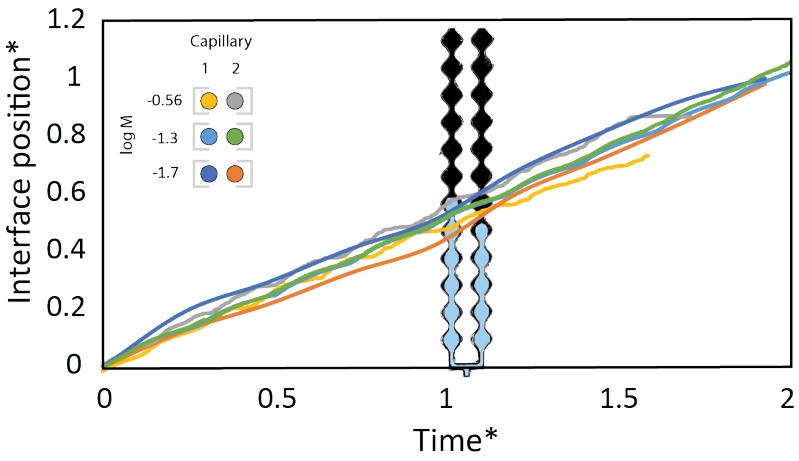

Figure 4.1: Position of the interface during drainage displacement process for various fluid pairs ($log\,(M, Ca_c) = (-1.7, -0.78), (-1.3, -1.4)$ and $(-0.56, -1.2)$) at viscous flow regime ($log\,Ca_c > -1.4$). Distances are measured from the inlet of the porous media geometry for each channel. Interface moves through pores and throats of capillaries similar but independent of each other and almost independent of the position in porous media.

Interface tends to maintain the same speed in both capillaries (see the parallel superimposed displacement lines in Fig. 4.1). The viscous forces are dominant at this regime ([72]) and overcome the entry pressure in both channels and start to displace the fluid inside. Despite the minor differences in pore dimensions between two capillaries, which cause different capillary forces and, as a result, different restrictions in fluid flow in each channel, flow maintains a movement with the same speed at the interface in both capillaries. In other words, both capillaries contribute similarly to the overall flow rate. In this flow condition, the increase in absolute capillary forces at porous media constrictions (pore throats) does not affect or has minor influence on the interface movement and fluid withdrawal, see the uniformity and smoothness of interface movement through porous media in Fig. 4.1. These characteristics are similar to how fluid and interface transport in viscous fingering flow regime, see Fig. 1.2.

The front displacement through porous media can be depicted by spatiotemporal graphs Fig. 4.2. The interface position is displayed in the geometry of the porous media. Time in this type of graph is presented with a color transition. Each instant corresponds to a specific time, which is noted in the color bar. Hence, the dynamics of the interface passage through capillaries is exhibited as the color transition in the porous system. Here, Fig. 4.2, time is the dimensionless time that was defined in Chapter 3. The color transition in the viscous flow regime is continuous and diffusive, indicating continuous displacement through capillaries. All aforementioned descriptions of viscous displacement in the pore doublet system are summarized graphically in Fig. 4.2.

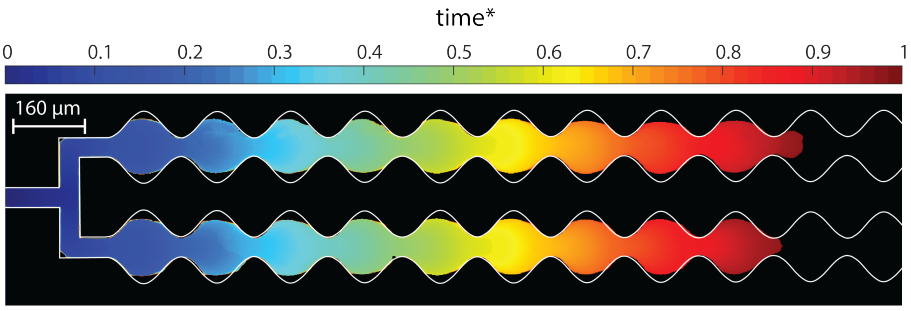

Figure 4.2: Spatiotemporal graph of the interface position in pore doublet geometry at viscous flow regime. In this graph the interface position at each time is correlated with a color as indicated by the color bar and the image show progression of the interface with respect to time. Continuous invasions are clearly shown by a sort of diffusive color change.

By reduction of flow rate, for lower Ca ($logCa_c < -2.8$), corresponding to the capillary flow regime, the invading phase enters one of the capillaries while a continuous slow movement of the interface is observed in the inlet channels. As the interface reaches the pore space, it moves by a sudden jump to the next constriction. This suppresses the interface movement in the inlet channel of the lagging meniscus; the interface will move backward until it reaches the point that capillary pressure equilibrates with the leading interface. As a result, the invasion only takes place at one of the capillaries. In this flow condition, the pore invasion mechanism is by sudden interfacial instability and burst into the draining pore by a sudden decrease of local capillary pressure, i.e., Haines jumps. Haines jumps of the interface are evident in Fig. 4.3 by sharp changes in interface position. The interface jumps into the next pore and drains the fluid until it reaches the next throat; Fig. 4.4 summarizes the invasion process. The invasion process consists of a series of interface pinning at throats followed by Haines jumps. For this flow regime, capillary forces are dominant; thus, when the interface reaches the pore throats, capillary forces define the entry pressure needed to invade the next pore. Consequently, the interface is pinned at the throat before it reaches the entry pressure. Surface forces dominate the invasion patterns, and interface invades pores with lower invasion pressure thresholds. This dominancy of the capillary forces is the reason that interface does not reach both capillaries at the beginning of the experiments. The interface invades the slightly larger channel. The difference may develop during the etching process or during ripping off the PDMS.

The pinning-jumping behavior of the interface at capillary flow regime and the preferential flow path is depicted in Fig. 4.5, where the spatiotemporal representation of the front displacement is depicted. Sharp color transitions between pores indicate the discontinuous interface displacement in the porous media. In other words, it

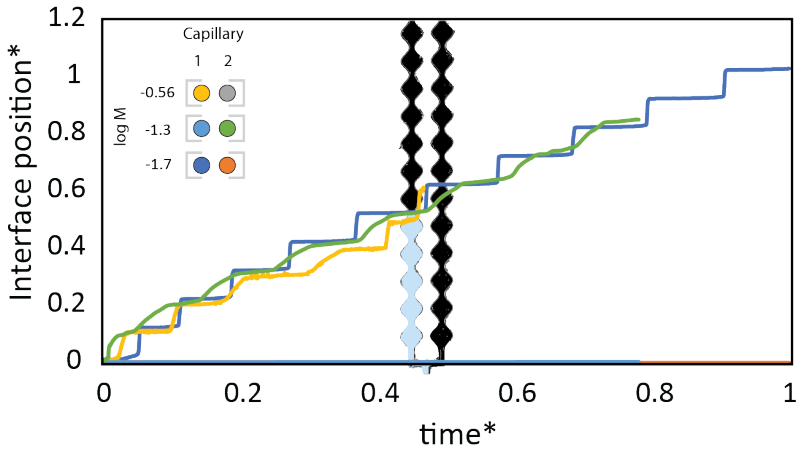

Figure 4.3: Position of the interface during drainage pore invasion process at capillary flow regime for different fluid pairs ($log(M, Ca_c) = (-1.7, -3.97), (-1.3, -2.82)$ and $(-0.56, -3.47)$). The interface invades the next pore by an interface burst into the pore until it reached the next throat at porous media. Pore invasions take place completely separately with a constant timing between each jump.

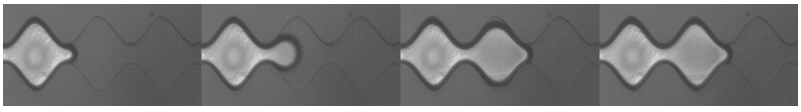

Figure 4.4: Dynamics of the interface during drainage pore invasion process at ($\log Ca = -5.5$). The interface invades the next pore by an interface burst until it reached the next constriction at porous media. Images are $0.014s$ delayed.

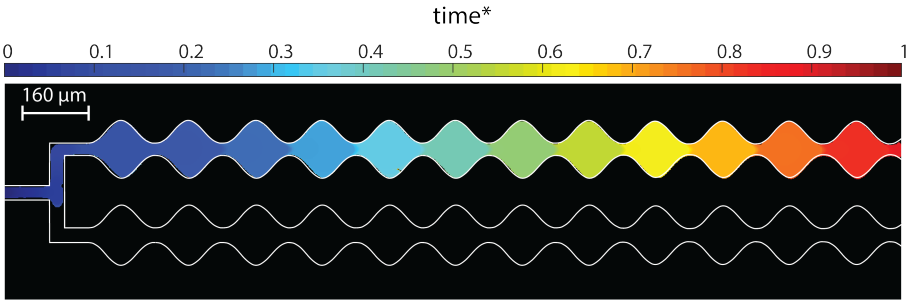

Figure 4.5: Spatiotemporal graph of the interface position in pore doublet geometry at capillary flow regime. Distinct pore invasion events are clearly shown by sudden changes of the color.

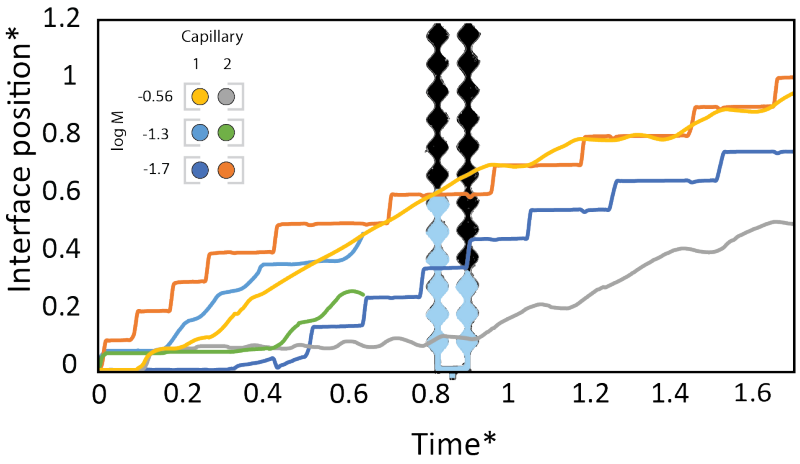

Figure 4.6: Position of the interface during drainage displacement process for different fluid pairs ($log\,(M, Ca_c) = (-1.7, -2.3), (-1.3, -2.77)$ and $(-0.56, -2.3)$) at the crossover flow regime ($\log Ca = -4.5$). The interface shows different displacement in each channel. Porous media is drained pore by pore with sudden interface movements and geometry and dimension of porous media becomes important. Additionally the effect of pore invasion is noticeable on the interface displacement in adjacent channel.

indicates that there have been periods that the interface has not moved while time has been passing. Additionally, the fact that each pore is filled with a single color shows how fast the dynamics of pore invasion are at the capillary flow regime.

A transition from capillary to viscous flow regime is observed when the flow rate is neither low enough that capillary forces fully control the displacement nor high enough that they are negligible. At mid-range flow rates in porous media ($-2.8 < \log Ca_c < -1.4$), corresponding to the crossover regime, different invasion patterns and invasion mechanisms were observed. The interface is able to enter both capillaries, but not necessarily simultaneously, see Fig. 4.6. Each channel is drained at a different rate, and there is a position difference between fronts at capillaries which varies with time (note the non-parallel position-time trajectory of the interface at two capillaries in Fig. 4.6).

The flow rate is not high enough that the front invades two capillaries at the same

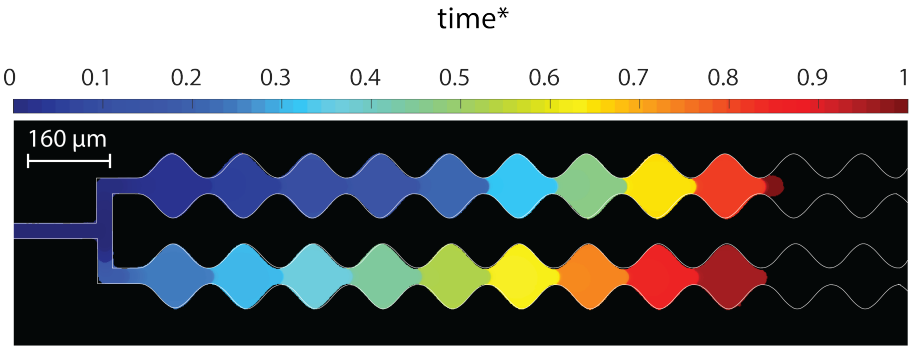

Figure 4.7: Spatiotemporal graph of the interface position in pore doublet geometry at crossover flow regime.

time; hence, the pore invasion mechanism tends to be pore by pore invasion. Haines jumps remain one of the main pore invasion mechanisms. However, the waiting time, the time that interface is pinned at a constriction, varies with the flow rate and for each pore, Fig. 4.6. The higher the flow rate, the lower the waiting time is. In this flow regime, the balance between capillary forces, inertia, and viscous forces is critical; not only it determine in which channel the invasion happens, but also it indicates timing between these jumps. An example of invasion patterns at crossover flow regimes is presented in Fig. 4.7. Random pore invasions are distinguishable in this graph.

Based on the work of Wang et al. [142], it is expected to see invasion in both capillaries for viscous flow regime, as they report multiple single-branch invasions along the flow direction. However, here we elucidate the stable front dynamics under the effect of viscous and momentum forces. At capillary flow regime, the ramified front has been reported, and it has been related to the frequency of Haines jumps in porous media [115]. Here we define Haines jumps as the primary invasion mechanism at capillary flow regime and bring insight to the dynamics of appearance of ramifications at front. Additionally, based on the presented dynamics, the results indicate that quasi-static pore-network modeling may lead to inaccurate results since the invasion in one channel is suppressed by invasion in adjacent pores due to non-locality of capillary pressure, although two capillaries were identical. By crossing over the capillary regime toward higher flow rates, homogeneous invasion dynamics were expected due to the homogeneity of the porous media. Nevertheless, local force balances determine local instabilities and invasions frequency. This is in agreement with the results of Berg et al. [17] where it is mentioned that drainage is more constrained by the entry pressure despite pore size and geometry. When the front reaches constrictions in the capillaries, capillary forces arise, and the potential energy in the form of local pressure difference should excess the dictated throat minimum energy required as entrance pressure to invade the next pore. The throat that has lower entry pressure or the interface that

reaches the required pressure earlier will be invaded prior to the other. In some cases, inertia forces change the force balance toward invasion by providing additional energy in the form of the initial speed and momentum of the interface, which leads to the shorter required time for invasion and sequential pore invasions (see Section 4.4). It is worth mentioning that it is plausible as well that an invasion in one channel delays invasion in adjacent channel [84].

We have presented the experimental results for various flow rates and categorized them into three flow regimes. In each flow regime, observed pore invasion mechanisms are presented. In the next section, we present the results of the double sinusoidal channel model, and the results will be discussed and compared with experimental data.

4.3.2 Double sinusoidal channel model

This section is dedicated to the results of applying the presented model to a pore doublet that mimics our experimental porous system and flow conditions. Various simulations with various flow rates for various fluid pairs have been performed. Here we compare our experiments with simulations analogous to our experimental condition in terms of front behavior and invasion patterns.

4.3.3 Comparison of model with experimental results

The front behavior trend and invasion patterns are analogous in numerical and experimental results. Different flow regimes are observed, and each flow regime is related to its pore invasion mechanism and interface dynamics. Meniscus dynamics in simulations match the overall front behavior in experiments.

At higher flow rates corresponding to the viscous dominated flow regime, Fig. 4.8, the interface is able to invade both capillaries. Although a small surface area difference between capillaries gives an advantage to the second channel for the interface movement, the interface shows almost identical displacement behavior in both capillaries with no pinning behavior of the interface at throats. One noticeable point is the acceleration and deceleration of the interface when it reaches and passes pore throats, Fig. 4.8. This is observed clearly in simulations but is less pronounced in experiments, Fig. 4.1. This is due to the fact that, in the model, it is assumed that while the interface moves through the channel, it drains all the fluid behind it. In experiments, however, at high flow rates, the interface does not displace all the fluid inside a pore, and a portion of the wetting fluid remains at pore curvatures, corners, and walls as wetting films.

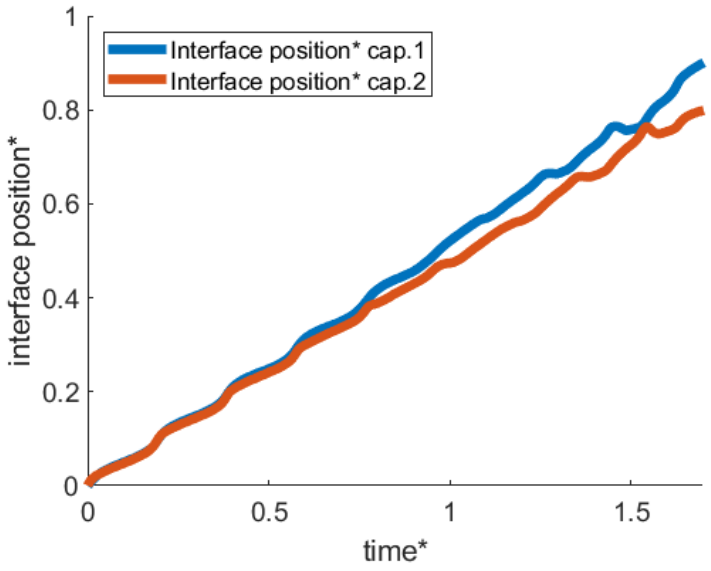

Figure 4.8: Interface tracking through drainage process simulated using the presented model. Pore and throat dimensions are analogous to the experimental design (r_p = 80μm and r_t = 20μm) as well as fluid properties. Time and the interface position are reported in dimensionless values and the graph is representative of simulation results for $log\, M = -1.7$ and $log\, Ca_c = -0.27$.

The fact that some fluids are left behind in pores reduces the cross-section available for the non-wetting fluid. It results in fewerfewer accelerations and deceleration while the fluid movies through the porous media. A snapshot of an invaded pore for viscous flow regime is available in Fig. 4.9, where the remaining wetting phase is evident at curvatures of the pore. Additionally, the remaining wetting phase increases the viscous dissipation at the interface due to momentum transfer from invading phase to residual defending phase as is reported in Roman et al. [108]. This contrasts with multiphase Darcy assumptions, where the interface is considered to be at equilibrium condition, and no energy dissipation is taken into account at the interface between two fluids.

By reducing the flow rate to the capillary-dominated regime, the invasion takes place only in the second channel with the wider channel. As presented in the previous section, at low capillary numbers, the dominance of capillary forces increases and pores and constrictions size have a major role on flow and invasion patterns as it is directly correlated to capillary pressure in our model. Observations for capillary flow regime confirm these results, where at capillary flow regimes, the probable dimension difference conducts the fluid only in one of the capillaries (Fig. 4.3). The pinning and jumping behavior of the interface is the dominant invasion mechanism for the capillary flow regime in simulations. Interface in both capillaries advances into the tightest constriction. However, interface in the wider channel invades the throat with Haines jumps mechanism and, as a result, a simultaneous retreat of the interface in

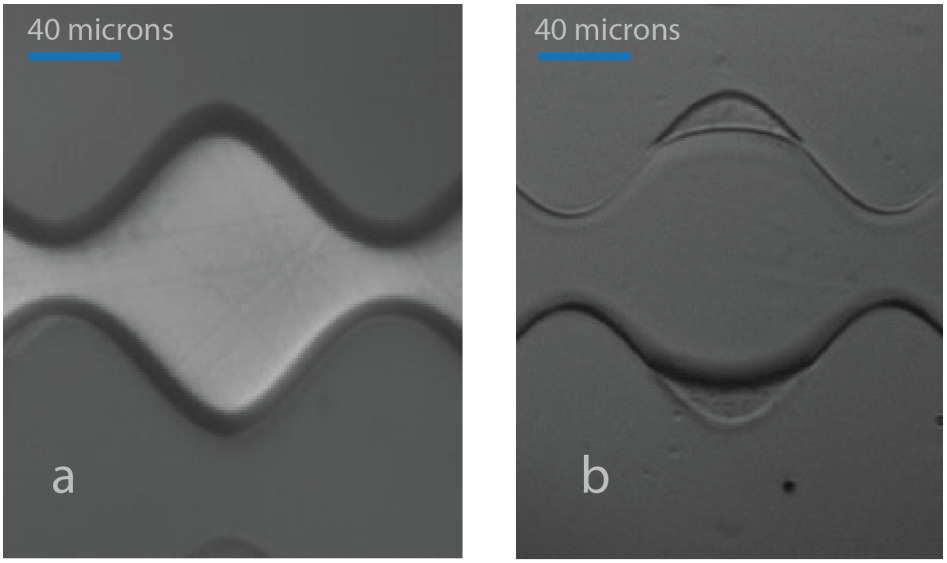

Figure 4.9: Images of an invaded pore at different flow regimes. (a) Invaded pore at capillary flow regime, $logCa_c = -3$ (related to the experiment with fluid pair 1, see Table 4.2). Most of the wetting phase has been displaced and only a portion of it remains at corners. (b) $logCa_c = -1.27$ and fluid pair 3, on the contrary, although the displacing phase has invaded the pore, still a portion of wetting phase remains at curvatures of the pore.

the connected channel, Fig. 4.11. It is worth mentioning that these retractions and reconfiguration of fluids in porous media are not captured in pore-network models, [19]. This synced retraction of the interface at secondary channel was observed in experiments as well (experiments related to capillary flow regime); however, it was not captured in the graph (Fig. 4.3), as the retraction was happening in the inlet channel and out of our focused porous media frame.

In simulations, during the waiting time, the interface creeps slowly toward the tightest part of the porous media; in experiments, nevertheless, the interface keeps its position with no movement in the channel direction. We believe that this is due to the assumption that pores are fully drained in the model and the effect of dynamics of corner and film flow during experiments for this flow regime.

At crossover flow regimes, the interface is able to invade both capillaries at pores near the inlet. Nevertheless, as invading phase saturation increases, viscous forces share in momentum balance decreases, and capillary and momentum forces will control the preferential flow path. That is why at next pore throats, the interface does not invade both capillaries due to higher capillary forces at channel 1, see Fig. 4.11. At this condition, pinning and jumping start to become one of the involved mechanisms of pore invasion. This mixed behavior between pinning and jumping and invasion in both capillaries was observed in experiments as well (Fig. 4.6) when the

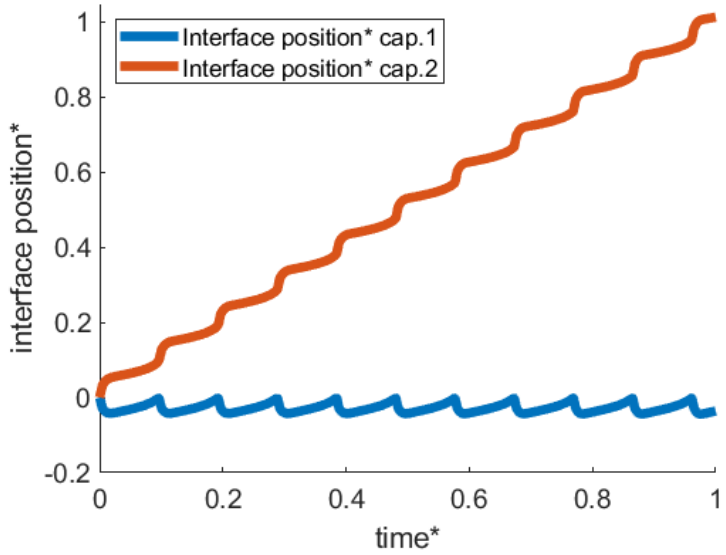

Figure 4.10: The simulation results for $log\,M = -1.7$ and $log\,Ca_c = -2.87$ flow condition. Haines jumps appear as the dominant pore invasion mechanism as the capillary forces become the most dominant force in the transport process. Interfaces at both capillaries are connected and invasion in one channel affects the interface position in the connected channel.

interface remains at one throat while the interface at the adjacent channel continues the invasion. However, in experiments, we observe that one pinned interface at a throat may start the invasion again and the interface at the other channel pins at a throat. We believe this is due to the difference in entry pressure between pores due to existing sub-pore factors, which define the threshold pressure. This represents the growing role of the pore and throat dimension in the invasion process as they define capillary forces.

Retraction of the pinned meniscus was observed in this flow regime as well. Pore invasion happens as Haines jumps in one channel, while the interface in the other channel retreats and returns to the throat, as shown by small peaks on the interface position curve numerically and experimentally (see Fig. 4.11 and Fig. 4.6). further discussion follows in Section 4.4

In this section, different pore invasion mechanisms at different flow conditions were observed both experimentally and numerically. It is observed at the viscous flow regime, viscous forces are the dominant forces, and pore invasions happen almost at the same speed as front displacements. On the other hand, at the crossover region and capillary flow regime, it seems that the geometry and dimension of pores play a great role in the definition of properties of pore invasions. Haines jumps are the most important pore invasion mechanism in these flow conditions and show an inter-

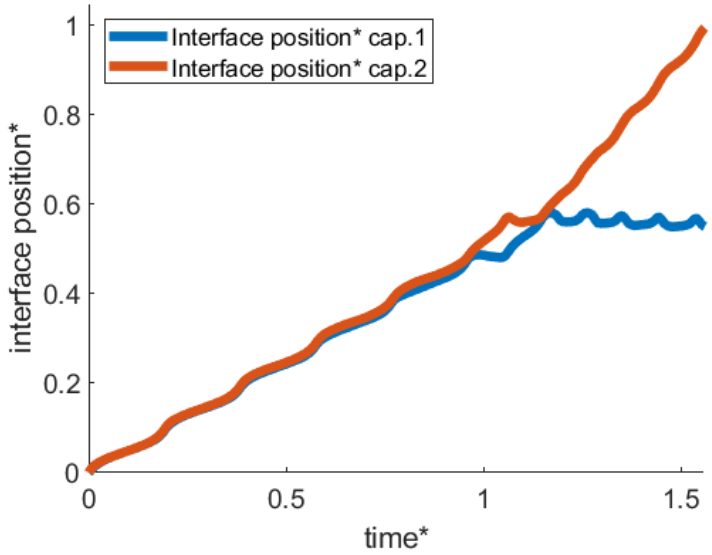

Figure 4.11: Simulation results $log\,M = -1.7$ and $log\,Ca_c = -0.56$ corresponding to crossover flow regime. The results show different invasion mechanisms based on the competition between active forces. Distinct and rapid pore invasions start to become one of the pore invasion mechanisms.

connected behavior during the invasion process. To obtain more realistic data from the model, the model must consider corner flows and viscous slippage between phases. This is a part of future work. The next section presents the dynamics of pore invasions in our microfluidic system.

4.3.4 Prediction of flow phase diagram

Now that we have detailed experimental observations and simulation results, in this section, we discuss our findings in terms of the prediction of the front behavior and the flow regime.

Characterization of the front behavior at different flow conditions and categorizing them into different flow regimes in a Ca and M $log-log$ Cartesian coordinate was first proposed by Lenormand et al. [72] and has been known as Lenormand's phase diagram. As presented in Section 4.2 and Section 4.3.2, immiscible displacement for various fluid pairs and at vast flow conditions were performed experimentally and numerically. In all the explored conditions, regardless of the tested viscosity ratio, interfaces positions in capillaries start to diverge from each other by decreasing Ca_c and moving from viscous flow regime to crossover flow regime. This divergence continues until the capillary preferential flow path takes over the front behavior that is the onset of the capillary flow regime. Experimental results and simulation predictions

of the front behavior are presented in a $log - log$ Cartesian coordinate of characteristics capillary number (Ca_c) and viscosity ratio M, see Fig. 4.12. Resulted diagram and the transition from different flow regimes are in line with previous research [72, 152]. Similar results are observed in our experiments in comparison to simulations; however, there is a difference in transition onsets between different flow regimes. Overall, predictions of numerical simulations for the transition of flow regimes are higher in terms of Ca_c for each fluid pair. The difference goes to the assumptions that were made during the model development and experimental characterization. The model assumes that the flow is unidirectional, with negligible momentum transfer at the liquid-liquid interface and the meniscus at each instance invades the whole channel cross-section. In reality, however, fluid moves with converging and diverging streamlines through pores and throats with additional viscous dissipation. Besides, it is experimentally observed that a layer of wetting phase remains near walls and corners, and it has been observed that a viscous coupling may develop between displacing and displaced phases by momentum transfer through the interface [108]. These facts, along with the existence of corner and film flow and integrated energy dissipation in their dynamics, especially at capillary flow regime, shortens the capillary forces' ability to dominate the fluid displacement. Additionally, since the invaded surface area is smaller than the pore's cross-section, see Fig. 4.9, by knowing the Ca_c and $\bar{A}$ are inversely related by definition, Eq. (3.37), the actual Ca_c is higher than what is measured in experiments. In addition, the permeability equation applied, Eq. (3.14), is developed for equilibrium condition and constant channel cross-sections; however, this assumption is not entirely valid here. We speculate that all aforementioned phenomena play a role in the small difference that exists between the model and experimental predictions and the time scale of the events.

The data from the experimental prediction of transition between different flow regimes of the work of Zhang et al. [152] is included in the Fig. 4.12. The transitions are in line and compatible with the $\log(Ca_c) - \log(M)$ system that we have proposed. It is worth mentioning that the definition of the flow regimes and the transition between them is based on the macroscopic front behavior and fingering formats in a highly connected pore system. While in our system, we differentiate between flow regimes based on the pore-scale behavior of the invasion patterns. This can explain the small difference in the margin of transition between these two experimental data sets.

It is worth mentioning that based on what Eq. (3.47) predicts, momentum forces play a role in interface dynamics during displacement. To the best of our knowledge, and based on all the performed experiments and simulations, inertia forces do not seem to have a profound effect on the overall front behavior and definition of ruling flow regime that is in line with findings of Moebius and Or [84]. Nevertheless, there is

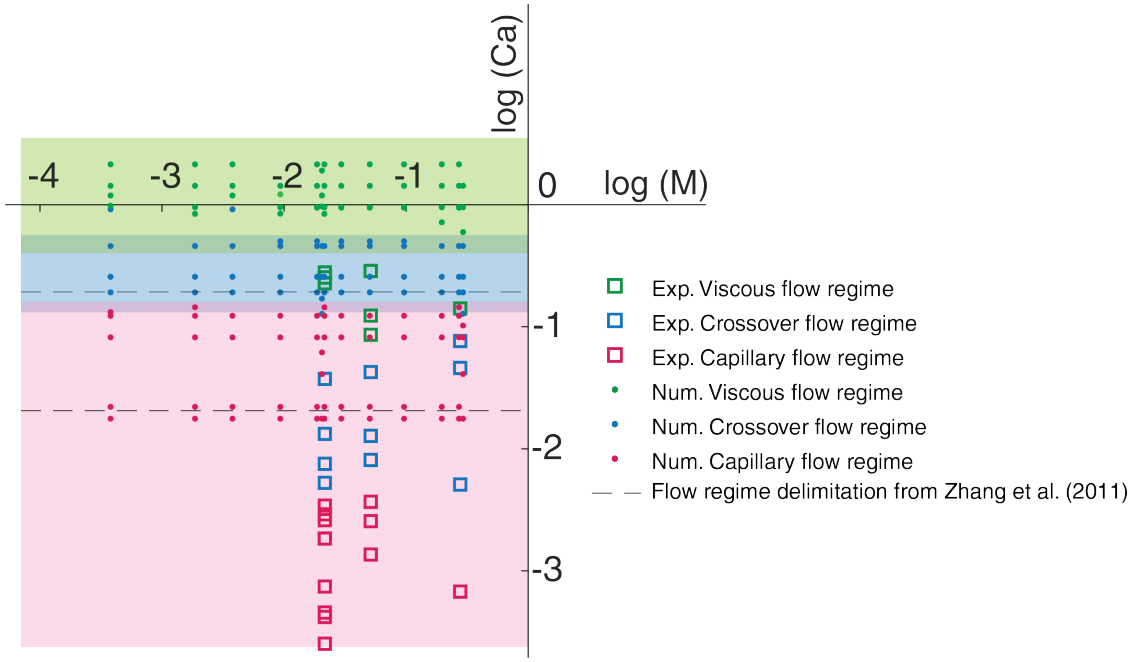

Figure 4.12: The phase diagram in $\log(Ca_c) - \log(M)$ coordinate based on simulation results along with our experimental results and results of Zhang et al. [152]

an essential need for their consideration when it goes to the interface dynamics during pore invasions, as is discussed in the next section.

4.4 Pore invasion dynamics

This section focuses on meniscus dynamics for slow drainage conditions (i.e., capillary and cross-over flow regime) when Haines jumps is the dominant pore invasion mechanism. We apply the micro-PIV technique to follow the fluid motion and get more insights into the capillarity effect.

4.4.1 Influence of Haines jumps on flow dynamics in neighbouring pores

To better understand the inter-connectivity of drainage processes at connected capillaries and invasion dynamics at pore-scale, the study of the interface velocity elucidates the magnitude and correlation between pore invasion mechanisms and interfacial dynamics. The data on front velocity shows that in the flow regimes that pinning and jumping mechanism plays as the pore invasion mechanism, drastic changes in the front velocity exist for each jump (Fig. 4.14 and Fig. 4.15); in contrast, for viscous flow regime, front maintains almost constant velocity, see Fig. 4.13. By comparison of mean front velocity in porous media (for more explanation refer to Section 2.3)

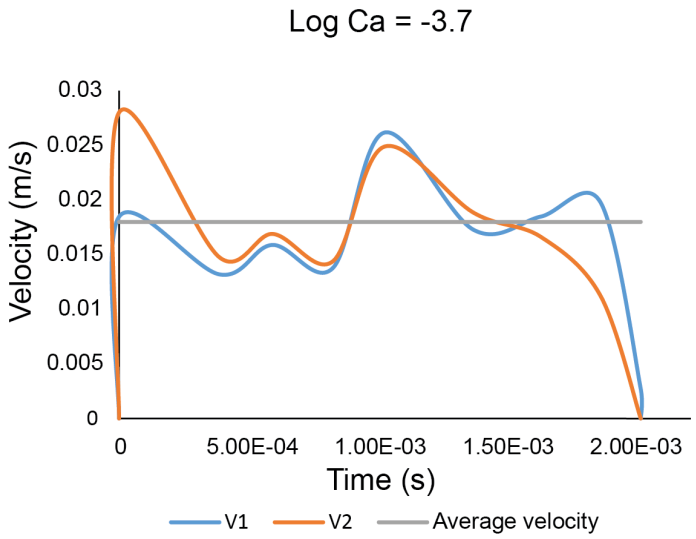

Figure 4.13: Interfacial velocities during the drainage process for viscous dominated flow regime corresponding to $\log Ca = -3.7$. The mean interface velocity corresponding to the flow rate is at the same range as the measured velocities.

with the front velocity for different flow rates, it is evident that by increasing flow rate (and as a result mean front velocity), the local front velocities approach the mean flow velocity, concluding that resisting forces (such as capillary forces) and constrictions have a minor effect on the front movement in this flow regime. Whereas, there is an enormous difference between mean and local front velocities at capillary flow regimes, where Haines jumps are the main pore invasion mechanism. The front velocity in this condition reaches up to 80 times larger amounts than the mean values. These sharp changes in the velocity, and accordingly pressure as is presented by Morrow [87] and measured by Moebius and Or [83], are as a result of accumulation of energy at the interface at constrictions and sudden release of it.

Velocity data clearly reveals the interface connectivity at pore invasions with the Haines jumps mechanism. For any jump at one of the capillaries, the velocity profile of the adjacent channel shows a response. Right after the jump, the velocity profile shows a sudden change to negative amounts followed by a drastic change to positive velocity and then decrease to zero, see Fig. 4.14b. This corresponds to the retraction and advance of the interface and invading phase at the secondary channel. A closer observation of the effect of Haines jumps on the interface behavior at the connected channel reveals that interface moves toward the smallest part of the constriction as the capillary pressure increases right before the invasion [107, 83, 84, 8]; almost instantaneously by invasion at the adjacent channel, the interface faces a reduction of capillary pressure. The interface in the adjacent channel relaxes and retreats suddenly into the pore, Fig. 4.16a, which is related to the sudden change of velocity

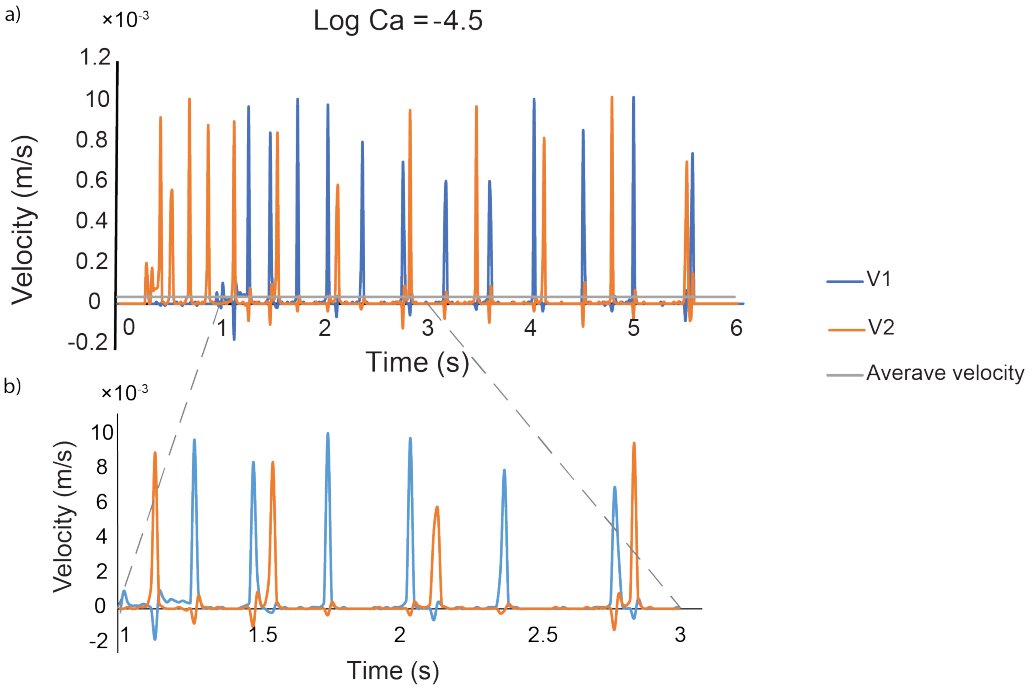

Figure 4.14: (a) Velocity measurements related crossover regions at $\log Ca = -4.5$. The drastic change in velocity corresponding to Haines jumps is evident for both capillaries. There is a noticeable difference between the mean interface velocity calculated from the flow rate and the measured velocities. (b) Measured interfacial velocities for $\log Ca = -4.5$ between times $2s$ and $3s$. Each pore invasion results in simultaneous negative velocities (corresponding to retraction of the interface) in the adjacent channel followed by a positive velocity peak as the interface advances toward the constriction.

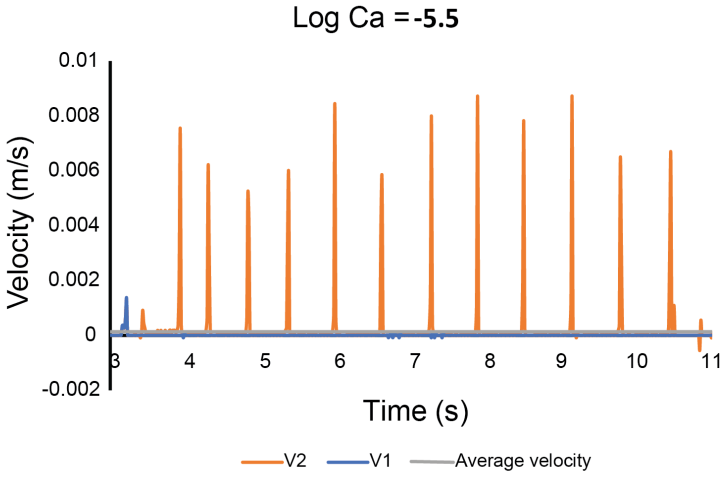

Figure 4.15: Measured velocity of interface at capillary dominated flow regime. The dramatic velocity changes as a result of Haines jumps is evident. Pore invasions are happening completely separated from each other on a periodic basis.

values to negative values. Then, the interface advances toward the throat again and rests there until capillary pressure at one of these capillaries passes the entrance pressure of the constriction, this part of the movement of the interface corresponds to the sudden change of sign of velocity toward positive values and then decreasing to zero. See Fig. 4.16b that shows the interface position at the first channel while the second channel is being invaded with sudden jumps. This is in agreement with the experimental observation of Moebius and Or [83]. This is observed for all pore invasions with the same flow regime despite the distance interfaces had from each other in our system (for some cases, interfaces were more than ten pores apart).

Armstrong and Berg [8] report when a pore invasion by Haines jumps takes place, the interface in the adjacent throats steps back until it reaches a pore body and finds equilibrium in capillary pressure with the invaded pore. By extending this result to our experiments, we expect interface retract to the widest parts of pore geometry. On the contrary, the retraction of the interface never reached wide pore bodies; it is always limited to the pore throats vicinity. This difference between different observations of the interface dynamics might be explained by higher dominancy of capillary forces in the design of Armstrong and Berg [8], due to the smaller cross-section of their constrictions (around 24 times). In addition, in Armstrong and Berg [8], throats are long constant cross-section rectangular capillaries ($13\,\mu m$), leading to retraction of the interface to the pore body as the only way to obtain lower capillary pressure, causing a larger contribution to invasion process. The same retraction of interface phenomena in the secondary channel is expected in the study of Morrow [87] by considering two parallel capillaries; one is considered as a succession of pores and throats and the other as a smooth channel with decreasing diameter toward the outlet (Fig. 4.17). According to Morrow [87] the magnitude of pressure changes due to front instabilities and pore invasions are directly related to the system's ability to transport fluid. For example, their results expect a higher volume of fluid displacement (retraction) in the secondary channel when no flow condition is allowed out of the system during the jump period. In a system similar to ours, when hypothetically no fluid is withdrawn from the system during pore invasion, and saturation remains constant, a considerable pressure difference in the side pore is expected due to geometrically induced capillary pressure change. Nevertheless, lower pressure variation is expected when the system can deplete a large portion of the invaded volume. Besides, as already established by the model developed in this paper, and previous works [84], the viscous dissipation and inertia of phases influence the attenuation of interface fluctuation and the distance retracted by the interface. This is in agreement with our observations (Fig. 4.16) and justifies the lower range of fluid retraction observed in experiments of Moebius and Or [83]. Although, their results show velocity alteration in the same order as jumps

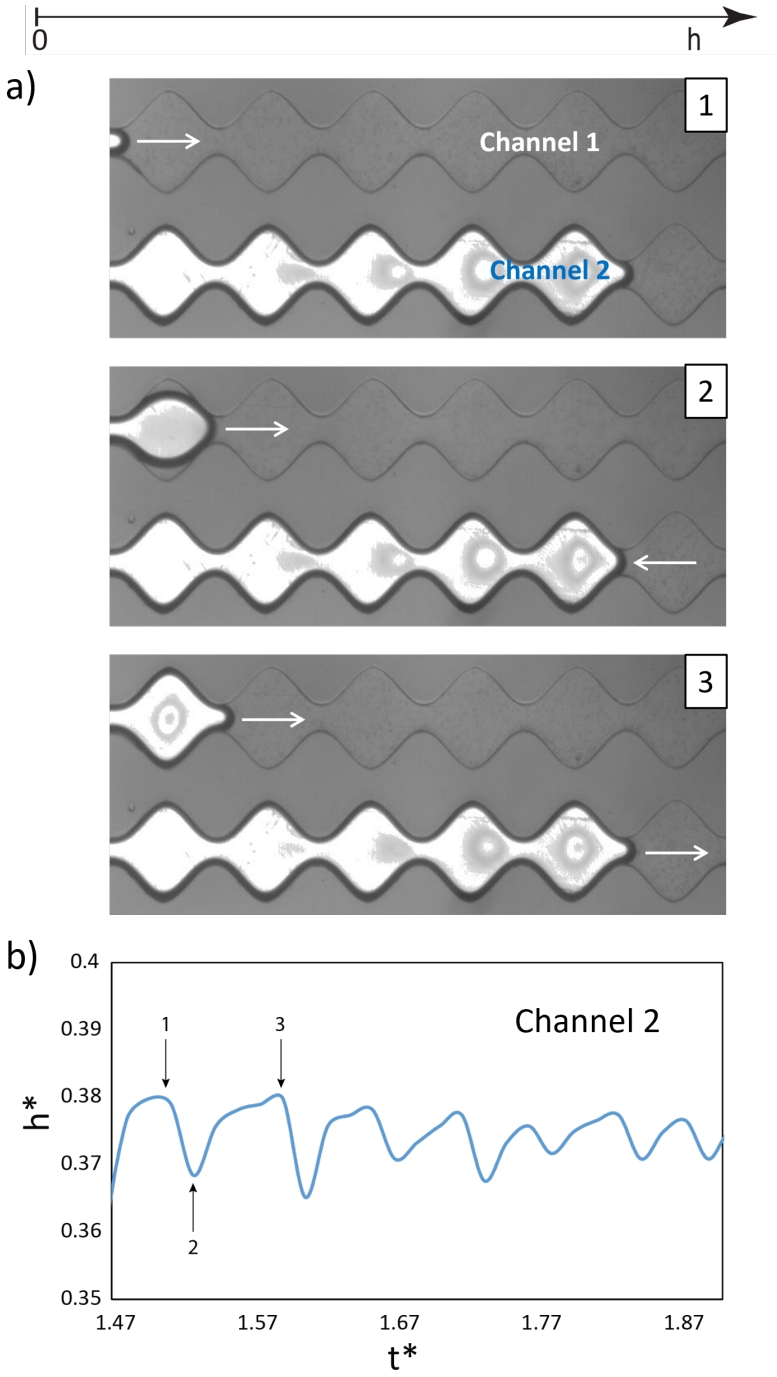

Figure 4.16: (a)Snapshots of the back and forth movement of the interface at a pore throat in channel 2 while the interface is advancing in channel 1. (b)Measurement of the dimensionless position of the interface in channel 2 as a function of the dimensionless time. Each oscillation of the interface at the pore throat in channel 2 is synced with a Haines jumps in channel 1. With $log\,Ca_c = -2.08$ and $log\,M = -1.7$, corresponding to cross-over flow regime.

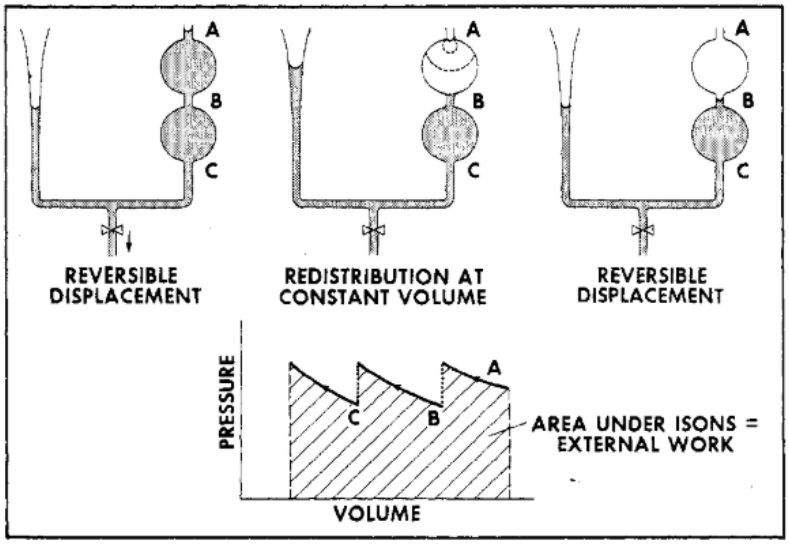

Figure 4.17: The geometry presented by Morrow [87] as an explanation of the effect of Haines jumps on the pressure and fluid displacement in side pores (capillaries).

velocity at the primary channel (see Fig. 1.8), whereas our experiments suggest lower magnitudes for velocities at secondary channel. This is mainly related to the perfect circular cross-section of their porous media design for simulations that do not take corners and viscous and surface energy dissipation into account. Additionally, their result is not conclusive whether this interfacial oscillation is a result of interfacial relaxation and is limited to the area near the interface or it penetrates through the body of the fluid. In this work, we are able to reveal the fluid dynamics behind it by micro-PIV analysis. It gives us insight into how capillarity and local pressure gradients develop complex interface dynamics.

Micro-PIV results confirm the front velocity profile and assure interface retraction due to jumps is not just an interface relaxation around the interface but is related to fluid transport in connected capillaries. Micro-PIV measurements are performed during pore invasion by Haines jumps at three different points in the body of the seeded wetting fluid, following the protocol presented in Section 2.2.2 and Roman et al. [107] (see Fig. 4.18, micro-PIV is performed for 3^{rd} and 9^{th} pores and at the throat between 5^{th} and 6^{th} pores). We observe that for each jump during pore invasion, the fluid in the adjacent channel is disturbed and shows an oscillating movement, i.e., first retreating, then advancing, see Fig. 4.19 and Fig. 4.20. While, when the invasion is in the same channel, the fluid shows a sudden forward movement. The micro-PIV data in this graph represents the flow disturbance for different pores concerning the pore invasions occurring in adjacent pores. This back and forth movement is repetitive through the porous media and maintains the same behavior from far to near pores. Velocity data are reported until corresponding pores are invaded, first pore 3 and then the throat between pores 5-6 are invaded in Fig. 4.20. Presented data are consistent

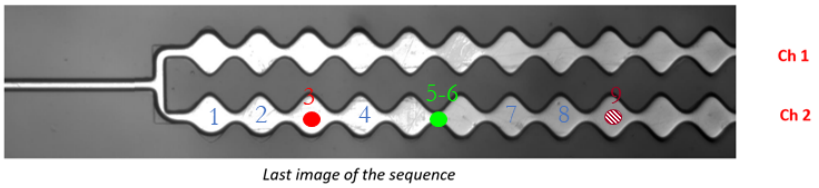

Figure 4.18: Number indications of pores in porous media for the last image of the image sequence for $\log Ca = -3.8$ experiment.

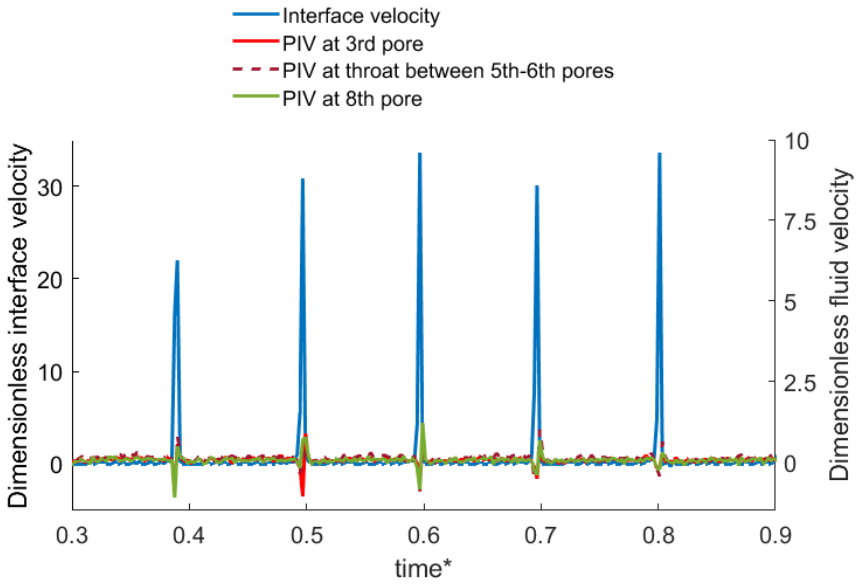

Figure 4.19: Micro-PIV measurements related to capillary dominated flow regime in presence of interface velocity for $\log Ca = -5.5$. The velocity changes due to Haines jumps at the side channel is evident (a). Micro-PIV results between time $3.5s$ and $6.5s$. The effect of Haines jumps at side channel is presented without interference with invasions at the same channel. The reciprocal movement that was observed for interface tracking results is confirmed (b).

with the interfacial velocity data reported before (compare Fig. 4.14b and Fig. 4.20a). Besides, Fig. 4.19 evidences that, at capillary flow regime, reaching velocities several times the average front velocity is not exclusive to the invading interface, and fluids at adjacent capillaries can surpass the front velocity or even retreat with that velocity. In this flow regime, as pore invasions are separated, the effect of invasions in capillaries are not interfering, and the effect of each jump is clearly observable, see Fig. 4.19.

The downstream disturbance of the fluid has been previously reported in the work of Blois et al. [18] and Roman et al. [107]. They were able to measure fluid velocity field in pores near the place that invasion took place, and disturbance of fluid flow due to pore invasions was quantified using the micro-PIV technique. However, in non of these works, the effect of jumps on the flow distribution is distinguished from

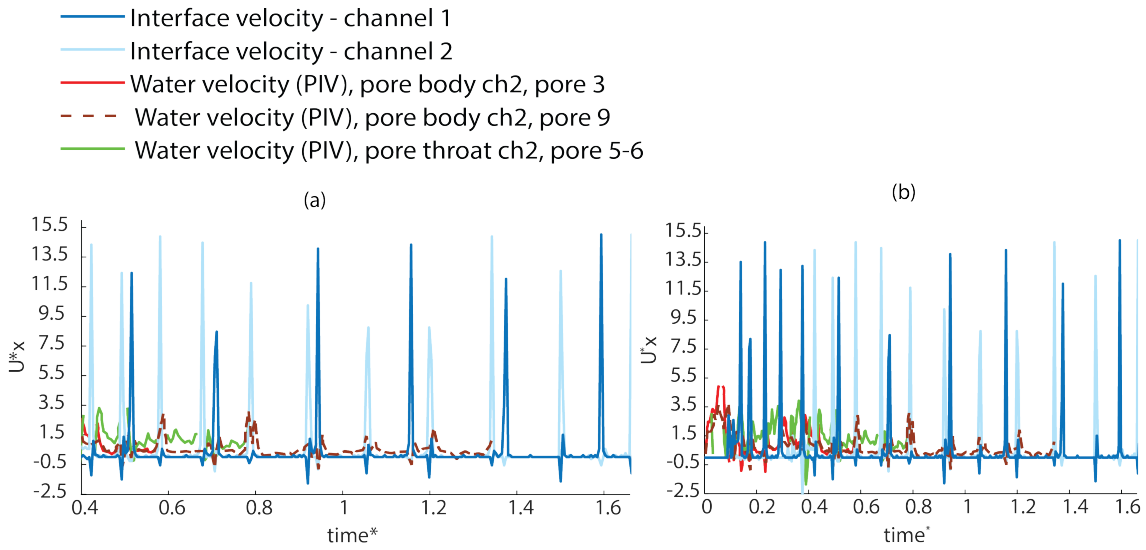

Figure 4.20: Micro-PIV results, at 3^{rd} and 9^{th} pores and at the throat between 5^{th} and 6^{th} pores (color coded in Fig. 4.18), and interface velocities at capillaries for $\log Ca = -4.5$. Micro-PIV results are available until the corresponding pore is invaded. Results show fluid disturbance at body of the fluid for Haines jumps pore invasions in both capillaries. The reciprocal movement of the fluid is evident for jumps in the side channel (a). A highly disturbed flow pattern is observed at initial times as the combined effect of invasions in side channel, invasion in same channel and the inlet effect (b).

the rest of the pore-scale phenomena based on the highly interconnected porous media patterns they use, leading to uncertainty in linking an observed disturbance to an exact interfacial dynamic. That is to say, the highly disturbed flow near the interface ([107]) and local flow dynamics due to invasions ([18]) suggest the extensive effect of fast dynamics of pore invasion on the flow patterns in the wetting fluid. Our findings are in line with the observed perturbations and back and forth movements of particles in the wetting fluid in the work of Roman et al. [107], attributed to local pressure gradients that develop in front of the interface. Although, these pore invasion dynamics are not directly correlated with the Haines jumps dynamics. Here, the data clearly correlates the fluctuations inside pores to the interface instabilities and states that it is able to propagate through the system even more than ten pores apart from the invasion. Additionally, here we provide new data on the effect of Haines jumps on the reconfiguration of adjacent interfaces in relation to the induced flow through porous media. This direct observation of interface dynamics is in contrast with multiphase Darcy's equation assumption that when a pathway is established, no dynamics will be dedicated to the interface, and it is considered fixed [123].

In this section, we have studied the effect of flow regime on the waiting time between pore invasion events. It is mentioned that waiting time is almost constant at a capillary-dominated flow regime because our geometry is homogeneous. On the

contrary, waiting time varies from pore to pore at the crossover region. Later, we discussed dynamics of pore invasion in comparison to the mean front velocity, and it was observed that when Haines jumps are the main pore invasion mechanisms, the local front velocity is very different from the mean front velocity and consists of a series of discrete drastic changes of interface velocity. The invasion mechanisms changed by increasing the flow rate, and local velocities converged toward the mean front velocity. Finally, the effect of Haines jumps on the interface and body of the fluid in the adjacent pores was studied, using interface tracking and micro-PIV technique. It was observed that with each pore invasion, the interface and body of the fluid in the connected channel follow a back and forth movement. At capillary flow regime, pore invasions are fully distinguished from each other, as shown by the interface tracking data and micro-PIV results. Increasing the flow rate and moving to the crossover flow regime leads to more frequent pore invasions. This causes interference between the dynamics of pore invasions in both capillaries. Keeping in mind the interface's connectivity between both capillaries, invasion in one channel might provoke or delay invasion in adjacent capillaries and cause different pore invasion dynamics from pore to pore. In the next section, we will cover the effect of the transition from the capillary to the crossover flow regime on the dynamics of the pore invasion.

4.4.2 Pinning time at throats and front behavior

By defining waiting time as the delay between two subsequent pore invasions, it is distinguishable that the higher the flow rate, the lower the waiting times are. By normalizing the measured values using the mean invasion time for a single pore in each flow regime, we are able to compare different experiments, see (Fig. 4.21). The mean value for normalized waiting times is 1 for all flow regimes. Values lower than 1 show that the corresponding pore has been invaded faster than the reference invasion time, and values higher than 1 show that it took longer to invade the pore. For capillary flow regime (low Ca_c), the waiting time for each pore invasion through porous media is constant as shown in the histogram graph, Fig. 4.21(standard deviation (σ) of 0.2 for capillary flow regime). It goes along with the fact that our porous media is homogeneous and pore space is similar through porous media. However, at higher flow rates, crossover flow regime, waiting times are not constant through the pore invasion process. This is reflected by a wider range of waiting time and higher deviation from the mean value for crossover regime, see Fig. 4.21 (σ = 0.5 for crossover region). That is to say, the waiting time for some pores approaches zero, while a longer waiting time is observed before some invasions. This is attributed to the interaction between the different active forces in the invasion process and inter-pore interactions. Especially, interfacial and inertial relaxations occurring after pore

invasions are able to encourage or prevent pore invasion [83]. The acceleration and the initial velocity provided by a pore invasion may initiate a successive pore invasion (normalized waiting time of < 1), while an interface retraction at the side pore may extend the required waiting time [84] or inhibit an invasion [8]. This inertial effect was reflected in the work of Moebius and Or [84] through having a broader velocity range (both higher and smaller values) in comparison with when inertia was ignored. Additionally, fluid configuration and distribution differ from case to case, and various level differences in capillaries exist that can change the interaction of side pores. This is worth keeping in mind that by increasing the flow rate and reaching the viscous flow regime, the waiting time tends to converge toward zero and reduce in variations, as the pinning mechanism is vanishing. Additionally, the first pore invasions are under the inlet effect, especially at capillary dominated flow regime, and the first waiting times are normally lower than the mean values (highlighted with a dotted vertical line). By not considering the first two pores in each experiment, to eliminate the inlet effect, we find the capillary flow regime's data to be more smooth ($\sigma = 0.18$), and crossover region is more dispersed ($\sigma = 0.52$).

These results are consistent with experimental observations of Moebius and Or [83] (in mm-scale inside glass beads porous media), where for capillary flow regimes, individual pore invasions take place, while at higher flow rates, the invasions are disturbed, and avalanche-like pore invasion is observed, while some pores follow pinning-jumping behavior at the interface. Additionally, they report the disturbance of distinct pinning and jumping behavior in their simulations for higher flow rates. These provide evidence of the effect of side-pores in damping or assisting invasion at this flow regime as is reported in Moebius and Or [83] and Armstrong and Berg [8]. Armstrong and Berg [8] witnessed that in pore invasions happening simultaneously in porous media, the most dominant invasion is able to damp the other invasion at the neighbor pore.

4.5 Conclusions

Competition between capillary and viscous forces results in different flow regimes in porous media. Each flow regime is attributed to different pore invasion mechanisms that, based on their characteristics, can control the front behavior. At the viscous flow regime, pores are invaded consecutively with almost no restriction at porous media constrictions as a result of the high ratio between viscous and capillary forces. High viscous force and high momentum energy (inertia) of the moving fluid result in the tendency of flow to move in a straight direction, i.e., the direction of flow. Crossover flow regime happens where viscous and capillary forces are comparable in quantity. In

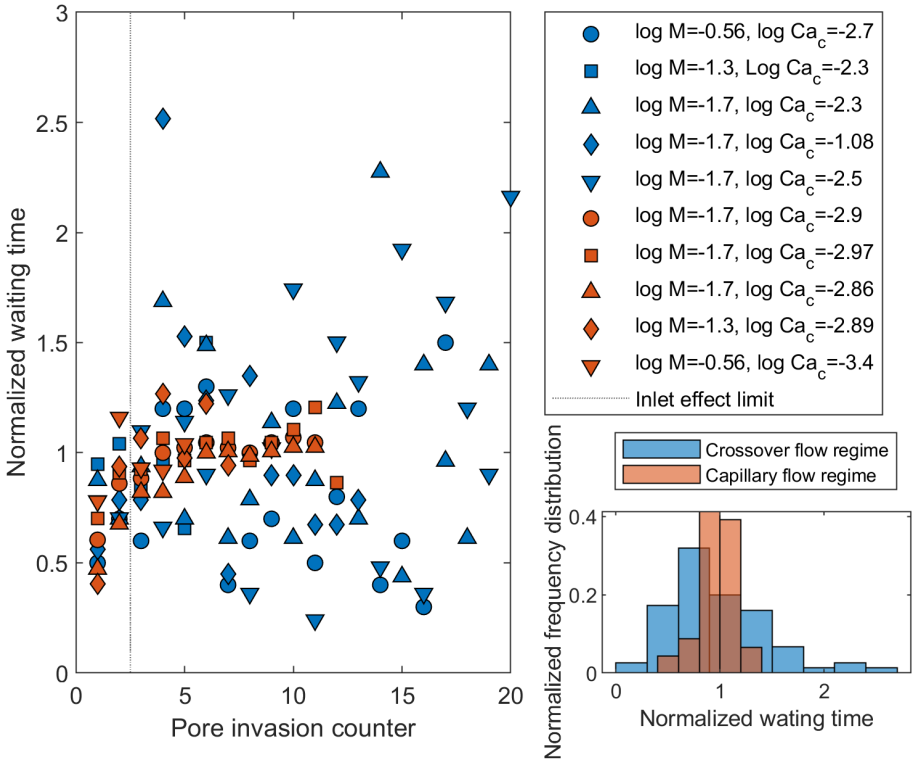

Figure 4.21: Measured waiting times for various flow conditions presented by different M and Ca_c. Waiting time values are normalized with the mean value of the time that interface needs to invade one pore in each flow condition. By increasing the flow rate and increasing the effect of viscous and inertia forces, the waiting time spreads over a wide range as a result of different cooperation between active forces and interfacial effects from side channel. First pore invasions are normally affected by the inlet and have lower waiting time in comparison to the mean value. This has been specified using a vertical dotted line.

this flow regime, the mixed behavior and pore invasions between viscous and capillary flow regimes are evident. Pores are invaded mostly on pore by pore bases, and Haines jumps start to be an important mechanism. At capillary flow regime, Haines jumps are the most important pore invasion mechanism. As capillary forces dominate this flow regime, the front invades the constriction with lower entrance capillary pressure. In this regard, lateral movement of the front and backward flow is possible, which are characteristics of the capillary flow regime. Additionally, different displacement behavior and fluid retention at pore level for different flow regimes shed new light on the understanding of the variation of parameters such as critical water content and pore-scale residual saturations in other studies. The reported retention of wetting layer on porous media walls, corners, and curvatures at viscous flow regime reflects as a higher critical water content at larger scales [58]. On the other hand, for the capillary flow regime, the remaining wetting phase placed in the corners explains the lower reported critical water content in other studies and the distribution of fluids behind the front [58].

We were able to apply the presented model for double sinusoidal channel for micro-scale porous media. Results are consistent with experimental results. However, the residual wetting layer and film on the porous media walls and corners at all flow conditions demonstrate the need for modification to the model.

When viscous forces are not the dominant forces (crossover and capillary flow regimes), the interface dynamics at one channel is able to alter the position of the interface in side pores. Results of micro-PIV show that the influence of reconfiguration of the interface is not restricted to the near interface areas. Micro-PIV results show that the body of the fluid oscillates (moves backward and forward) as a result of decreasing capillary pressure and retraction of interface and then increasing the capillary pressure and advancing of the interface to the constriction.

The study of interface dynamics shows that the velocity of the interface at capillaries deviates from the mean flow velocity at the porous media, from viscous to capillary flow regime. At the viscous flow regime, the mean flow velocity is equal to the interface velocity. Nevertheless, by adopting Haines jumps as an invasion mechanism, the mean front velocity deviates from the interface velocity at each channel. Flow in this condition is characterized by impulsive peaks of velocity changes that are up to 80 times higher than mean flow velocity.

4.5.1 Perspective

This chapter has been mainly about the behavior of interface for drainage process in double sinusoidal capillaries for drainage conditions. Many ideas and experiments exist to be explored. In this work, some assumptions and simplifications have been

made to be addressed in future research. There are some ideas that I would have liked to try and dig deeper.

- In this chapter, the interface behavior in a double channel was observed; however, having different geometry, such as multi-branches or inter-connected capillaries, will provide information on the length-scale of side-pore effects and momentum role in different invasion mechanisms.
- Pore shape and morphology is one important factor in dynamics of pore invasions, interface burst and defines when other phenomena such as snap-off will take over the invasion patterns. Various pore shapes and pore connectivities remain to be studied.
- Simulations can be extended to two dimensions and be tested with microfluidics experiments. Additionally, it remains to be improved by including the fluid-fluid viscous slippage effect and the corner flow dynamics.

Chapter 5

Controlling role of corner flow dynamics at capillary dominated flow conditions

5.1 Introduction

In the previous chapter, dynamics of pore invasions for various flow conditions were discussed. Different pore invasion mechanisms are attributed to each flow regime. When the capillary forces are dominant, at very low capillary numbers, rapid interfacial bursts, known as Haines jumps, are the principal active pore invasion mechanism [53, 8]. Recent studies show that invasion in this flow regime consists of a series of intermittent interfacial jumps accompanied with interface pinning, known as waiting times [83]. Although this mechanism has been known for a while and studied in previous works [83, 8], the interface dynamics and the nature of waiting times remain unrevealed.

In multiphase systems, a portion of the resident fluid remains behind the front in the form of fluid ganglia or in rock curvature and crevices [58]. In general, invasion of a non-wetting phase in a channel that initially is saturated with wetting phase is integrated with retention of the wetting fluid on the walls [132, 27]. Fairbrother and Stubbs [38] and Taylor [132] studied the fluid flow and front dynamics in a tube at different capillary numbers. Bretherton [23] correlated the thickness of the fluid film with the Ca in a circular tube and Aussillous and Quéré [11] experimentally validated results and followed up to higher Ca by developing a theory for deposited film on cylindrical walls. Wong et al. [145] and Magnini and Matar [76] extended deposition of liquid films for a square channel by theoretical developments and a series of numerical simulations respectively.

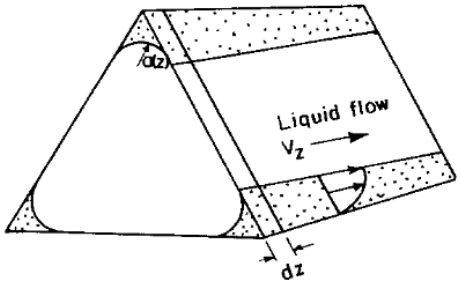

Figure 5.1: A 3D representation of the residual wetting fluid at corners and the flow along them, taken from Ransohoff and Radke [103].

The remained wetting phase is able to flow and move through occupied surface area. This flow in residual fluid on the solid surface is specifically important in various industrial and environmental applications such as foam generation [66, 85], Enhanced oil recovery (phase entrapment in porous media, snap-off mechanism and smart water), and CO_2 sequestration. In a circular cross-section channel, i.e. no edges, the wetting phase is distributed as wetting films or layers. However, in an angular cross-section tube, characteristic of geological porous media, the residual wetting phase is mainly stored at corners [76], and corner flow highly contributes to the residual wetting phase dynamics [103], see Fig. 5.1. Fluid flow through non-circular paths has been investigation in previous studies [70, 103, 67]. Recent studies of displacement through porous media have shown that the dynamics of the retained fluid in the invaded zone contribute to the drainage process through irregular pathways along the corners or fluid films over the porous media surface [88, 57, 58].

In this chapter, we aim to study the dynamics behind the waiting times in Haines jumps pore invasion mechanism and to quantify the role of corner flows in definition of pore invasion dynamics using a well-defined porous media. We apply microfluidics and corner flow theories to have a better understanding of corner flow contribution in drainage process. In what follows, first the experimental methodology is presented. Then, we go through the governing equations behind corner flows and non-dimensionalize the equations. Next, the experimental results on dynamics of residual wetting phase during waiting time are presented and compared to simulations. Finally, experimental results on corner flow dynamics during the pore invasion is presented.

5.2 Experimental methodology

In this section, we present the experimental setup, experimental conditions and explain the acquisition techniques.

The experimental setup presented in Chapter 2 is used for this study. A PDMS micro-chips with an undulated pore doublet geometry is used for drainage experiments (see Section 2.1.3, Fig. 3.7 and Table 4.1 for further details). Experiments have been performed at room pressure and temperature and flow is accurately controlled by precisely defining the inlet and outlet pressure, ranging from 40 to 70 $mbar$ corresponding to $logCa < -4.8$. PDMS wettability is altered to water-wet using plasma treatments ($\theta \leq 30°$). Experiments are performed at drainage condition where air displaces the water through the porous media. To be able to perform PIV, the aqueous phase is seeded with micro-particles (Polybead Carboxylate Microsphere 1μm diameter).

During the invasion of porous media by the non-wetting phase in an angular channel, a layer of the wetting fluid remains at corners of capillaries as a result of wettability effects. For each interfacial curvature, the corner residual wetting phase spreads laterally over the solid wall, Fig. 5.2a. The higher the curvature of the interface at the corner is, the lower the spreading over the walls will be, see Fig. 5.2b. Considering the schematic presentation of a corner with half angle of $\frac{\alpha}{2}$, water-solid contact line of l_{sw}, contact angle of θ and corresponding to capillary curvature of R, see Fig. 5.2a, one can use sine rule and write:

$$\frac{R}{\sin\frac{\alpha}{2}} = \frac{l_{sw}}{\cos\frac{\alpha}{2}+\theta}. \tag{5.1}$$

Measuring this water-solid contact line (l_{sw}) provides an indicator for the actual fluid thickness at corners and the amount of the residual corner fluids. In the acquired image sequences from experiments, this layer is observed by darker areas at corners of the porous media geometry. These dark areas are the top view of the corner fluids; more precisely, this band is the spreading length of the corner wetting fluid over the walls, or l_{sw} in Fig. 5.2b. By following the image processing protocol presented in Section 2.2.1, the outer boundary of porous media geometry and the inner boundary of the corner fluid profile can be obtained as pictured in Fig. 5.3. The water-solid contact line of the corner fluid for each point is obtained by measuring the distance between the inner and outer boundary of the corner layer, normal to the porous media geometry, Fig. 5.4.

PIV technique is applied to study the fluid velocity and streamlines in the body of the wetting phase. Micro-PIV technique is performed by following the protocol

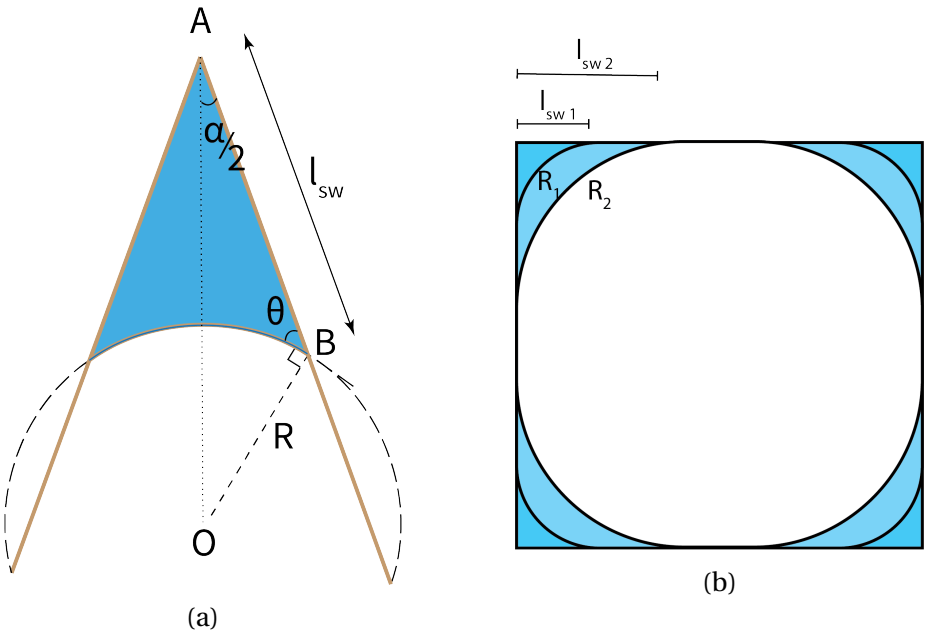

Figure 5.2: (a) Schematic presentation of wetting fluid confined at a corner of porous media geometry with half angle of $\frac{\alpha}{2}$, contact angle θ, solid-water contact line l_{sw} and interfacial curvature R. (b) A schematic of residual corner wetting fluid in our micromodel at different capillary pressures with the visible lateral spread.

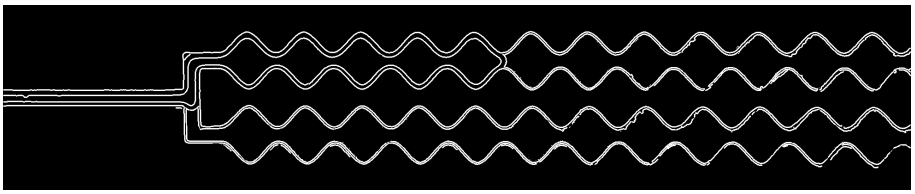

Figure 5.3: The obtained image by applying image processing techniques to detect boundaries of corner liquid.

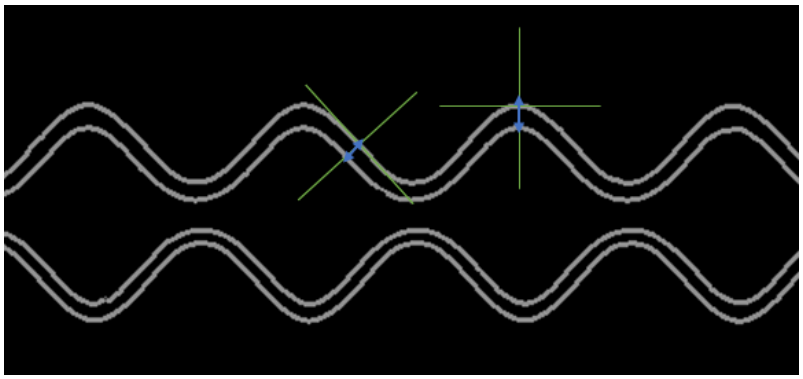

Figure 5.4: Apparent corner width measurement by measuring the distance between inner and outer boundary normal to the geometry of the porous media.

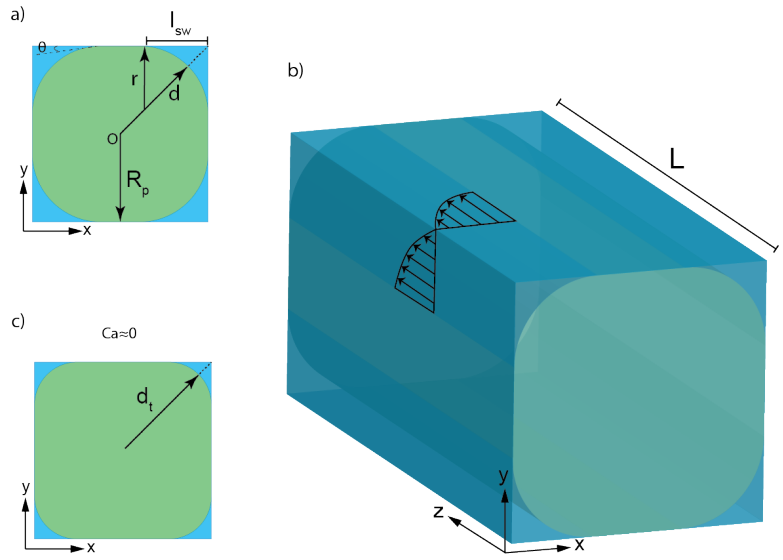

Figure 5.5: A schematic of the retained wetting phase in a square capillary.

presented in Section 2.2.2. PIVlab is used to perform PIV measurements [135, 134].

In the following sections, first the theories behind corner flows are presented. Then, the experimental data on residual wetting phase behavior at different flow regimes are discussed. Next, experimental results on the corner dynamics and fluid velocimetry results using micro-PIV technique are presented and the results are compared with experiments. Finally, we look at the corner flow dynamics during fast pore invasion by Haines jumps.

5.3 Governing equations

In this section, the theory behind corner flows is discussed. Equations are non-dimensionalized and are applied to our system configuration. Finally, results of residual wetting fluid are presented .

5.3.1 Flow equation

Two-phase flow in capillaries has been studied in previous works [103, 11, 145]. For a channel with a non-circular cross-section, the non-wetting phase occupies the center and wetting fluid saturates corners, as is depicted in Fig. 5.5a-b. In this phase configuration, the wetting phase flows along the corners. Assuming the channel is horizontal and it is slim enough that gravitational effects are negligible [70], we can study the flow through one corner and extend it to the rest with similar properties[103].

The momentum balance equation is written as

$$\rho\left[\frac{\partial v}{\partial t}+v.\nabla v\right]=-\nabla p+\mu\nabla^2 v, \tag{5.2}$$

where v, t, μ and p are respectively fluid velocity vector, time, viscosity and pressure. Assuming the flow is slow and steady state condition results in reduction of inertia and time dependent terms in Navier-Stokes equation [70]. Considering unidirectional laminar flow and assuming the pressure difference along the corner is constant over the flow cross-section ($x-y$ plan) implies that the corner velocity field is only a function of the position in the cross-section plan ($u_z(x,y)$). It brings us to

$$-\frac{\partial p}{\partial z}+\mu\left(\frac{\partial^2}{\partial^2 x}+\frac{\partial^2}{\partial^2 y}\right)u=0, \tag{5.3}$$

where u is the flow velocity in z direction, along the channel, Fig. 5.5b. Ransohoff and Radke [103] solved for velocity profiles for different geometries by considering a no-slip boundary condition at solid-liquid surface and momentum balance between wetting and non-wetting phases by considering a shear stress. Legait [70] proposed

$$\bar{u}_{z,t}=\frac{r^2}{\beta\mu}\frac{\partial p}{\partial z}, \tag{5.4}$$

where $\bar{u}_{z,t}$ is the averaged fluid velocity through the corner calculated by dividing the flow rate by the wetting phase cross-section area, r is the radius of the interface and β is the dimensionless flow resistance coefficient defined by Ransohoff and Radke [103]. β depends on the corner geometry, contact angle and roundness factor of the corner. It is worth mentioning that β remains independent of the absolute size of the corner.

Here we assume that the stress exerted on the interface by non-wetting fluid is negligible as it was proposed by Zhou et al. [155]. β values for different corner half-angles and contact angles for no-stress boundary condition at fluid-fluid interface is reported in Ransohoff and Radke [103]. Values for a square channel ($\alpha=\pi/4$, where α is the half angle of the corner, Fig. 5.2a) and different contact angles at no-stress boundary condition are given in Table 5.1. The resistance to flow increases by an increase in the contact angle. It is readily explained by the fact that for a constant curvature radius, when the contact angle increases, the interface is driven further into the corner resulting in smaller cross-section, which decreases the ability to flow, see Fig. 5.6.

The flow rate (q) according to the velocity definition will be

$$q=-\frac{Ar^2}{\beta\mu}\frac{\partial p}{\partial z}, \tag{5.5}$$

Table 5.1: β values for different contact angles for a right angle corner ($\alpha = \frac{\pi}{4}$).

Contact angle	0	$\frac{\pi}{36}$	$\frac{\pi}{18}$	$\frac{\pi}{9}$	$\frac{\pi}{6}$	$\frac{\pi}{5}$
β	93.93	93.99	100.2	139.0	290.7	698.2

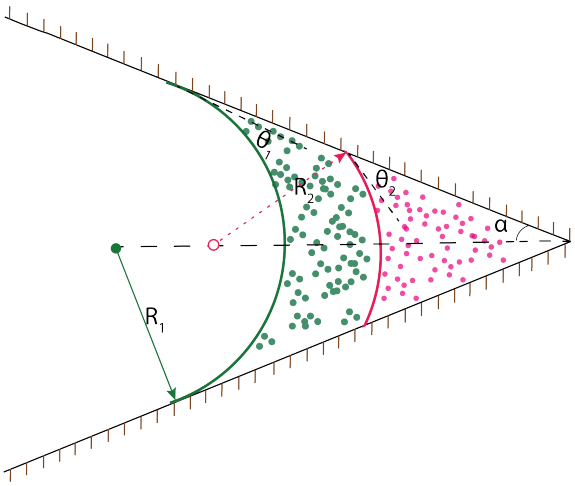

Figure 5.6: The corner wetting phase cross-section for constant interfacial curvature ($R_1 = R_2$) and different contact angles. The cross-section decreases by increasing contact angle ($\theta_2 > \theta_1$) resulting in an increase in dimensionless resistance factor, see Table 5.1

where A is cross section of the corner fluid along z. The cross-section area of the corner flow is related to the interface radius, r, and the corner angle, α. In its general form, it reads as

$$A = Cr^2, \tag{5.6}$$

where C is a coefficient depending on contact angle and corner half-angle. For a right angle corner and a contact angle θ, the coefficient is

$$C = \frac{\cos\theta\cos\left(\frac{\pi}{4}+\theta\right)}{\sin\frac{\pi}{4}} - \left(\frac{\pi}{4}-\theta\right), \text{ [34]}.$$

Hence, the final form of the flow rate equation is defined as follows

$$q = -\frac{Cr^4}{\beta\mu}\frac{\partial p}{\partial z}. \tag{5.7}$$

The capillary pressure by definition is the difference between the non-wetting and wetting phases pressures,

$$p_c = p_{nw} - p_w.$$

As a result, changes in capillary pressure corresponds to changes in the non-wetting

and wetting phase pressure changes,

$$dp_c = dp_{nw} - dp_w.$$

Assuming the pressure changes in the non-wetting phase (gas phase) is negligible, the pressure changes in the wetting phase pressure is negatively correlated to the capillary pressure changes,

$$dp_c = -dp_w. \tag{5.8}$$

Hence, by combining Eq. (5.8), Eq. (5.13) and Eq. (5.7) one writes

$$q = \frac{C}{\beta\mu} r^4 \frac{\partial p_c}{\partial z}. \tag{5.9}$$

5.3.2 Mass balance

The continuity equation of the system can be written in terms of cross section of the corner occupied by wetting phase, since it is assumed that the wetting fluid is incompressible,

$$\frac{\partial A}{\partial t} + \frac{\partial uA}{\partial z} = 0. \tag{5.10}$$

It describes the accumulation in corners, with respect to the fluid velocity. The term uA describes volumetric flow rate, q, and the equation can be rearranged as

$$\frac{\partial A}{\partial t} + \frac{\partial q}{\partial z} = 0. \tag{5.11}$$

By combining Eq. (5.11), Eq. (5.9) and Eq. (5.8) leads into curvature radius evaluation equation as a function of time and position;

$$\frac{C\partial r^2}{\partial t} + \frac{\partial}{\partial z}\left(\frac{C}{\beta\mu} r^4 \frac{\partial p_c}{\partial r}\frac{\partial r}{\partial z}\right) = 0. \tag{5.12}$$

Assuming a straight channel, the curvature of the interface in the direction of the channel is infinitely small; the capillary pressure by Young-Laplace equation will be

$$p_c = \frac{\sigma}{r}, \tag{5.13}$$

where σ is the interfacial tension. Hence, Eq. (5.12) is transformed to

$$\frac{\partial r}{\partial t} = \frac{\sigma}{2\beta\mu} r \frac{\partial^2 r}{\partial z^2} + \frac{\sigma}{\beta\mu}\left(\frac{\partial r}{\partial z}\right)^2. \tag{5.14}$$

Eq. (5.14) represents the evolution of the radius of the curvature of the arc meniscus along the channel with respect to time. This evolution is a function of viscosity of the fluid, interfacial tension, geometrical resistance and contact angle, which are included in β.

5.3.3 Non-dimensionalized equations

To have a general understanding of the corner flow behaviors, we propose a generalized and dimensionless formulation. By choosing channel half width, R_p (see Fig. 5.5a-b), channel length, L, and time $t_c = \frac{2\beta\mu L^2}{\sigma R_p}$ as the characteristic values respectively for radius and position and time, Eq. (5.14) is easily read as

$$\frac{\partial r^*}{\partial t^*} = r^* \frac{\partial^2 r^*}{\partial z^{2*}} + 2\left(\frac{\partial r^*}{\partial z^*}\right)^2, \tag{5.15}$$

where r^*, z^* and t^* are dimensionless radius, position and time. This characteristic time incorporate the effect of corner geometry effects, the length of the corner and fluid properties on the drainage time scale [67].

5.3.4 Numerical results

A self-developed code in MATLAB® is developed to solve the Eq. (5.15). The evolution of the curvature radius along the corner is studied with respect to time. A uniform initial condition is applied over the total length of the corner. It corresponds to the condition that the wetting fluid occupies the whole corner, when r is equivalent to d and $l_{sw} = R_p$, Fig. 5.5a. It is assumed that the corner fluid represents the arc meniscus in an invaded pore and the tip meniscus has reached a constriction to invade, simillar to the condition illustrated in Fig. 5.11. At capillary flow regime, invasion occurs only when the interface reaches the threshold capillary pressure defined by the constriction. Wong et al. [145] predicts that when Ca is very low ($Ca \approx 0$), the diagonal distance of the capillary origin to the deposited corner layer, d, in a square channel will be $d_t = 1.2 \times R_p$, see Fig. 5.5. In this regard, at one end of the corner, a Dirichlet boundary condition with a corner radius corresponding to invasion entry pressure of the constriction, predicted from Wang et al. [142], is exerted. At the other end, a Neumann boundary condition, $\frac{\partial r^*}{\partial z^*} = 0$, is applied. With this setting, we calculate the rate of corner radius changes in response to a pressure difference along the corner as a result of reconfiguration of phases at the throat. The mean radius of the curvature over the length of channel is reported in Fig. 5.7. The radius decreases with faster rate at the beginning, since the flow rate is directly correlated with the radius. The higher the corner fluid radius is, the higher the flow rate will be. Accordingly at later stages, lower

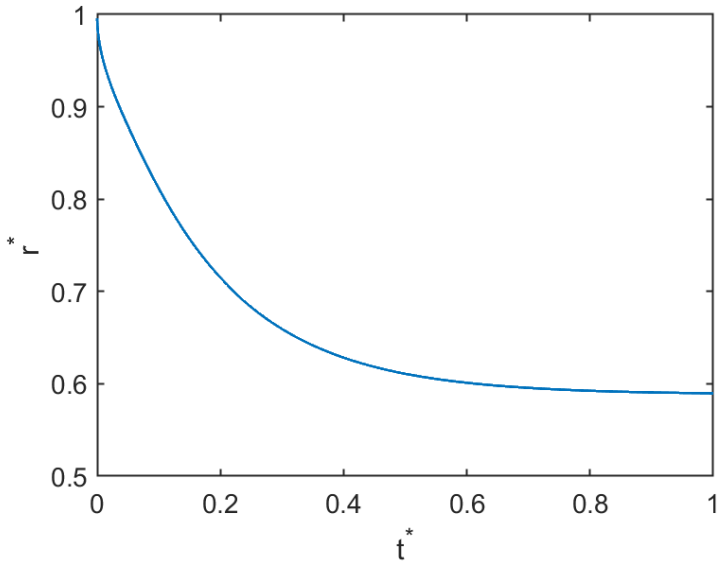

Figure 5.7: The mean dimensionless radius of arc meniscus along the corner with respect to dimensionless time.

radius corresponds to lower flow rate (depletion rate) and respectively lower radius reduction rate.

5.4 Experimental results

5.4.1 Fluid distribution at invaded pores for different flow regimes

While the interface is invading the porous media, the trace of invasion will be different at different flow regimes. This is due to different mechanisms that cast for pore invasion. Various fluid configurations and phase distributions occur at macroscopic and microscopic scales.

Our geometry consists of a series of pores and throats. In viscous flow regime, as the interface is invading the pore space, by passing the throat, it enters a wider area. Interface maintains the movement in the longitudinal direction, while it begins to expand laterally due to wider space. Since the longitudinal velocity in this flow regime is normally higher than the lateral expansion, and the interface invades throats with no pinning behavior, a layer of wetting phase remains at curvatures of pores, see Fig. 5.8. In other words, curvatures of porous media act as pockets and retain a portion of wetting phase, which may interact with the invading phase at later stage [108]. This retention of wetting phase at high flow rates is projected in finding of other studies as an increase in the critical water content of the porous media [58, 90].

Considering the range of the capillary numbers that we face in our experiments for

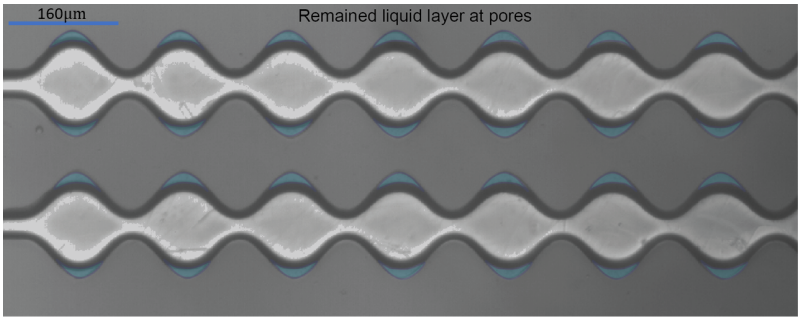

Figure 5.8: Remained liquid layer in the curvature of pores (specified with light blue) in drainage displacement with $\log Ca = -3.5$.

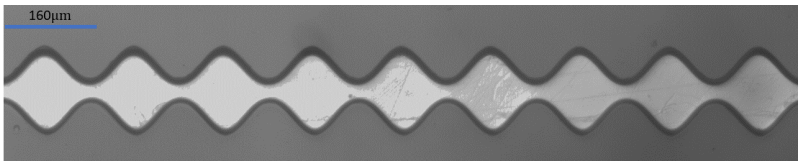

Figure 5.9: Remained wetting phase in corners at capillary flow regime, $log\, Ca = -6.24$.

the capillary flow regime, we are well below the presented threshold by Magnini and Matar [76], i.e., $Ca < 0.05$, that below which wetting phase mostly deposes in corners. In line with this prediction, residual wetting phase layers were only observed at corners (see Fig. 5.9). In this case after pore invasion, interface reached the next throat and meanwhile expanding laterally. However, in this flow regime, interface does not invade the next throat spontaneously. At capillary flow regime, as it is discussed in details in Chapter 4, capillary forces are dominant and the prerequisite of a pore invasion is that tip meniscus reaches the threshold pressure of the constriction. When the interface reaches a constriction that the threshold capillary pressure is higher than the current pressure difference, the interface waits there until the pressure surpasses the threshold. At this condition, the arc meniscus (the interface between invading and resident fluid at corners) has to cope with this condition by changing curvature, described by Young-Laplace equation. Fig. 5.2b presents the schematic profile of wetting fluid at corners of porous media after invasion for different interfacial radius corresponding to different capillary pressure.

Here, we verify the calculated values of l_{sw} predicted in Eq. (5.1) by comparing to experiments. We consider the limit presented by Wong et al. [145] and apply this theory to our experiments at very low Ca ($Ca \approx 0$), when the front is pinning at a constriction at invaded throats that our cross section is square (Table 4.1), and it is far from the tip meniscus. We can estimate the interfacial curvature radius to be $22.4\mu m$ based on theory. Using Eq. (5.1) we can relate the measured water-solid line (l_{sw}) to curvature of the interface at corners. By applying this formulation to the calculated amount of $22.4\,\mu m$ for interfacial curvature radius, we expect $8.2\,\mu m$ from the top view. From

the corresponding experiment we obtain the mean value of $l_{sw} \approx 9\,\mu m$ ($7.8 < l_{sw} < 10.4\,\mu m$) which is in good agreement with the calculated value. This variation with theory can rise from the resolution of our imaging system, that is $\approx 1.3\,\frac{\mu m}{pixel}$, and one pixel error results in a micron difference. Additionally, defining the exact boundary of the corner fluid has some limitations using optical instruments. It is worth mentioning that the applied theory is developed for a long straight square channel, while we have approximated that it is true for throats of our geometry. Not only the cross-section is not constantly square all over the channel, but also the effect of converging and diverging walls causes deviation from these results regarding Young-Laplace equation. Besides, the error margin for the measured contact angle of the system may result in a small divergence from the theoretical prediction.

Now that we are able to relate the water-solid contact line of the corner liquid from the top view of our microfluidic system to the amount of residual wetting phase, the connection between the waiting time at capillary flow regime and residual corner fluids is studied. We know that the interface pins at throats during waiting time and suddenly the meniscus invades the next pore. It still remains undiscovered whether there is any dynamics behind these waiting times. First, we will study the dynamics of near interface corner fluids before each pore invasion at the capillary flow regime by studying the changes in the profile of the corner fluid. Then, using micro-PIV technique, we will explore whether there is any dynamics in the body of the wetting fluid while the interface is statically pinned at the throat. By this mean we also discover whether there is any exchange between invaded pores and saturated porous media through corners.

5.4.2 Corner flow dynamics during waiting time

Residual wetting fluid at corners of a porous media are most of the time considered to be involved in slow processes of unsaturated zone drainage ([58, 88]) and a systematic experimental study of their dynamics in porous media remain limited. Here we claim that corner fluids are dynamic and play a role in fast dynamics of pore invasions and near front fluid configuration.

Experimental results suggest that the corner fluids reduce to a minimum amount before pore invasion. When a pore is invaded by Haines jumps mechanism, the interface moves to the next constriction. After reaching to the next constriction, the capillary pressure over the interface increases to reach the entrance pressure of the constriction. Considering the interface at the constriction with corner residual fluids corresponding to the current capillary pressure, for advancing into the constriction,

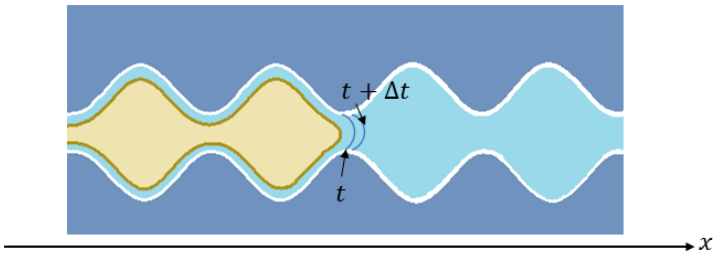

Figure 5.10: A schematic representative of the configuration of phases, interface and corner fluids before pore is invaded with Haines jumps. The interface position at Δt time difference after the jumps is presented in comparison of the interface position right before the jump.

the capillary pressure should increase. In this condition, one can write:

$$\begin{cases} P^{t}_{c(throat)} < P^{t+\Delta t}_{c(throat)} \\ P_c = P_{nw} - P_w \\ P_{nw} = cte. \end{cases} \tag{5.16}$$

This equation results into:

$$P^{t+\Delta t}_{w(throat)} < P^{t}_{w(throat)}. \tag{5.17}$$

Considering an infinitesimally time step, at a distance $\Delta x < 0$ from the throat, Fig. 5.10, by considering no change in the corner wetting fluid, and the non-wetting phase pressure remains constant, one can derive:

$$P^{t+\Delta t}_{c(throat+\Delta x)} = P^{t}_{c(throat+\Delta x)} = P^{t}_{c(throat)}$$

As a result one can conclude:

$$P^{t+\Delta t}_{w(throat+\Delta x)} = P^{t}_{w(throat)}, \tag{5.18}$$

which results in:

$$P^{t+\Delta t}_{w(throat)} < P^{t+\Delta t}_{w(throat+\Delta x)}. \tag{5.19}$$

The Eq. (5.19) confirms a flow from the corner wetting phase to the body of the fluid as a result of an increase in capillary pressure leading to the thinning of the residual corner wetting phase. This corresponds to very low flow rates, during the waiting time when the Haines jumps mechanism is active. At this condition, the dynamic of corner drainage can control the dynamics of the interface invasion into

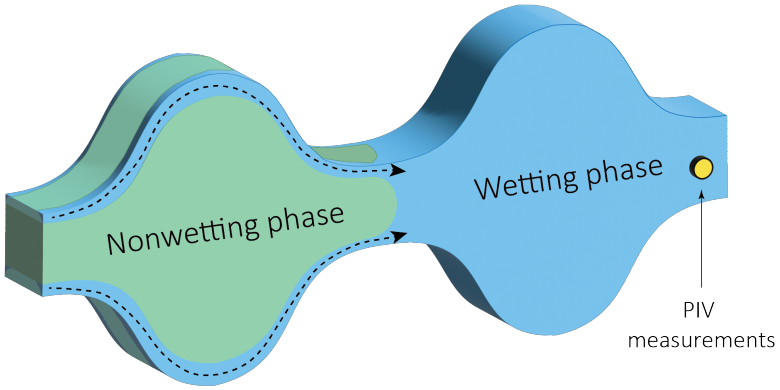

Figure 5.11: A graphical representation of the corner flows and the frame that micro-PIV has been performed in.

the constriction. It suggests that, due to the existing pseudo-equilibrium condition, increasing of the capillary pressure at tip meniscus and moving to tightest parts of the pore throat is bonded with drainage of the wetting fluid through corner flows. This flow through corners plays an important role in the determination of waiting time and the apparently steady condition that interface hold for a while before it moves to the throat and drains next pore with Haines jumps mechanism, see Fig. 4.15, Fig. 4.16.

Now that we have observed evidences of existence of corner flows during waiting times, micro-PIV measurements will help us to quantify them. In what follows, we present the micro-PIV results in the body of the wetting fluid during the waiting time.

Micro-PIV is performed for the seeded wetting fluid while the interface is pinned at a throat. A schematic of the system is depicted in Fig. 5.11. Measurements are performed from the time that interface reaches the constriction and stops, until it passes the threshold capillary pressure and invades the next pore.

Fluid flow through corners is demonstrated with micro-PIV results, see Fig. 5.12a. The body of the wetting fluid maintains flow during the time that interface is waiting at the constriction and does not advance. Fig. 5.12a shows the average flow velocity in the body of the fluid while interface rests at the throat. It is evident that fluid is still being drained from capillaries and there is a continuous flow to the body of the fluid. At the time that interface reaches the constriction, a thicker layer of fluid is left behind at edges of the porous media geometry. As a result, a higher gradient exist for fluid flow. This is represented in form of higher speed of streamlines in the fluid body, as is presented in micro-PIV results for initial times, presented in Fig. 5.12b.

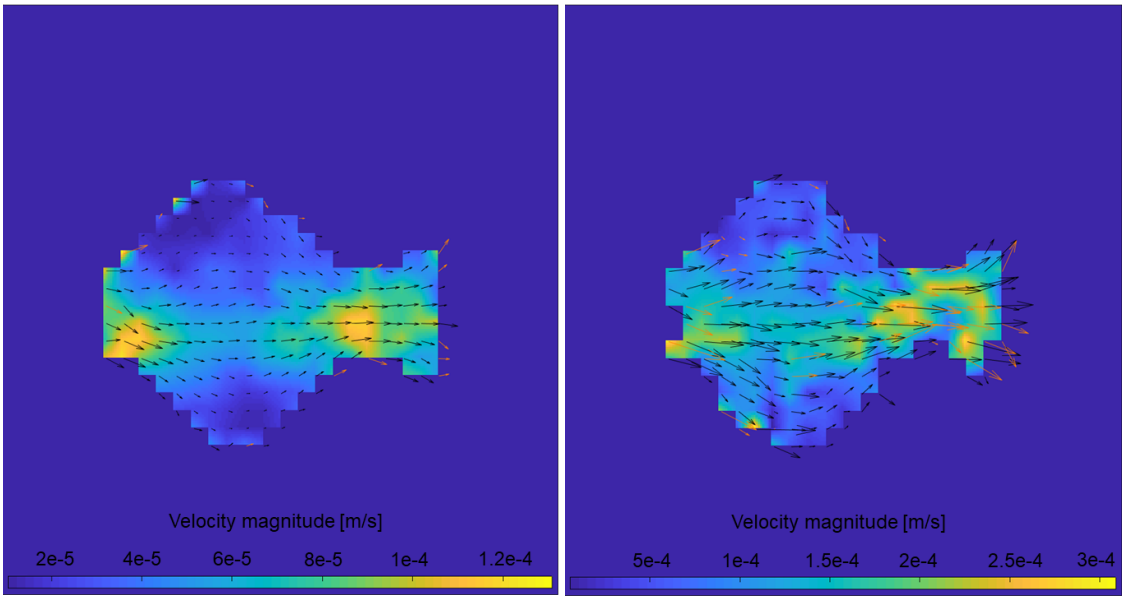

(a) Average (b) t_0

Figure 5.12: (a) Micro-PIV velocity vectors measured by averaging over the period that interface is pinned at the pore throat. Results show that there is a continuous flow from corners to the body of defending fluid. (b) Micro-PIV results for initial times of arrival of the interface at throat that a thicker layer of wetting fluid has remained on the walls and at corners and results in higher gradients for fluid flow, and accordingly higher velocities.

Comparison of the developed model with experiments

According to Eq. (5.11) and Eq. (5.6), one is able to calculate the fluid velocity by numerical integration over the corner cross-section area changes over the channel length. In the assumed condition that the corners are drained across the tip meniscus into the body of the wetting fluid during the waiting time, PIV measurements are able to give us insight into the experimental fluid velocity. Here we present micro-PIV results at the closest throat to the interface, see Fig. 5.11. Fluid velocity and time are normalized with the initial measured velocity and duration of waiting time.

Experimental results confirm that the corners are drained faster at the beginning, and their velocity converges to zero later, see Fig. 5.13. At the initial conditions, the corner fluid occupies a higher cross-section of the corner, resulting in a higher conductivity of corners. Additionally, as the time passes and corners are drained, the capillary pressure increases approaching the threshold capillary pressure, corresponding a decrease in the pressure gradient decrease over the corner. Hence, it is expected to see higher fluid velocities at the initial condition and very low flow rates at the final stage. It is observed that at the final stages of the corner drainage, although the fluid velocity approaches zero, it still maintains a minimum non-zero value. This

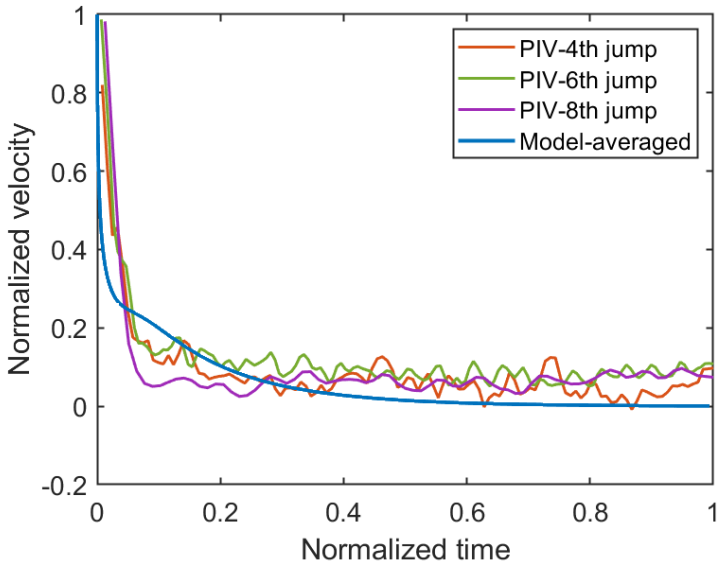

Figure 5.13: The comparison of the experimental fluid velocity and numerical results. PIV measurements are for successive pores in the micro-channel (i.e. for successive Haines jumps). Experimental velocity and time are normalized with measured initial velocity and the duration of waiting time. Experiments correspond to very slow drainage at $log\,Ca = -6.2$.

is attributed to the fact that when the capillary pressure increases across the interface, the interface is able to move and invade tighter parts of the constriction. This interface movement slowly drains the fluid occupying those regions and causes higher rates than what is expected to be the input of the corners. It is noteworthy to mention that μ-PIV method gives the average velocity between each two frames. In this regard, the reported values from the model are averaged over the same time stages from the experiments.

In Hoogland et al. [57], two flow regions are defined for slow drainage conditions: a region with transient state and Haines jumps pore invasions and the invaded region with retained wetting phase at corners and in clusters. It has been experimentally observed that the retained wetting phase reduces in size or disappears even for clusters that seem totally disconnected [88, 57], showing conductivity of fluid through corners. Moura et al. [88] observed that there is a zone adjacent to the front, named active zone, that has a higher probability that retained fluid is drained through the corner and film flows. This is in accordance with our pore-scale observations, where the residual fluid at corners in the vicinity of the front with abrupt pore invasions shows a dynamic behavior and participates in the drainage process.

Or and Assouline [92] and Hoogland et al. [58] by using similar equations sets, known as the foam drainage equation, predicted water retention behind the front.

They were able to predict comparable flow rates with experiments by performing a set of pore network simulations. Although the focus of their study is characterizing the volume of retained fluid and drainage dynamics at a larger scale, they draw some conclusions that can be interpreted in our setting. Or and Assouline [92] studied the corner drainage dynamics as a result of a hydraulic head drop at the tip meniscus under gravity. They optimized parameters such as the hydraulic head drop and the number of conductive corners to fit the results to analytical solution of Nachabe [89]. They observed that the value of the hydraulic head parameter is related to the invasion entry values. Here, we observe and characterize the correlation between corner flow dynamics and the pore throat threshold pressure at the pore-scale adjacent to the front. The dynamics of corner flow is much slower than the fluid drainage through capillaries [57]. As a result, at low flow rates, the front behavior consists of abrupt displacements, controlled by fluid flow through pores, and tremendous slow movements, waiting times, that are controlled by corner flows. Additionally, as is shown here and in other studies [92], the corner conductive capacity is directly correlated with corners cross-sections and drastically decreases with a corner cross-section decrease. This may illustrate why in Moura et al. [88] fluid clusters farthest from the interface participate less in the drainage since the already drained corner network that connects them to the front are much less conductive than near front corners.

5.4.3 Corner flow dynamics during the pore invasion

Now that we have delineated the dynamics behind the waiting times, as a part of capillary dominated pore invasion, we will focus on dynamics of corner flows during the invasion. The corner water-solid contact line of the wetting fluid at pores adjacent to where the invasion happens is measured, see Fig. 5.14. Results show that the width of wetting fluid in corners, l_{sw}, grow up to 30%, corresponding to 69% volume grow, as a result of back flow of wetting fluid through corners of porous media, Fig. 5.14. Values are presented from the moment just before the invasion takes place and during the time that the interface reaches the next constriction and waits until the next pore invasion begins. Measured values are normalized by dividing by the initial value. It reveals that by invasion of the interface to the next pore space and sudden decrease of capillary pressure the corner fluid-solid contact line increases by 20% in average (44% volume increase). This phenomena is not restricted to the pore adjacent to the invasion. By considering one pore farther from the invasion position, Fig. 5.15, it is evident that the grow in wetting width occurs with a time delay and lower relative increase (10% in average).

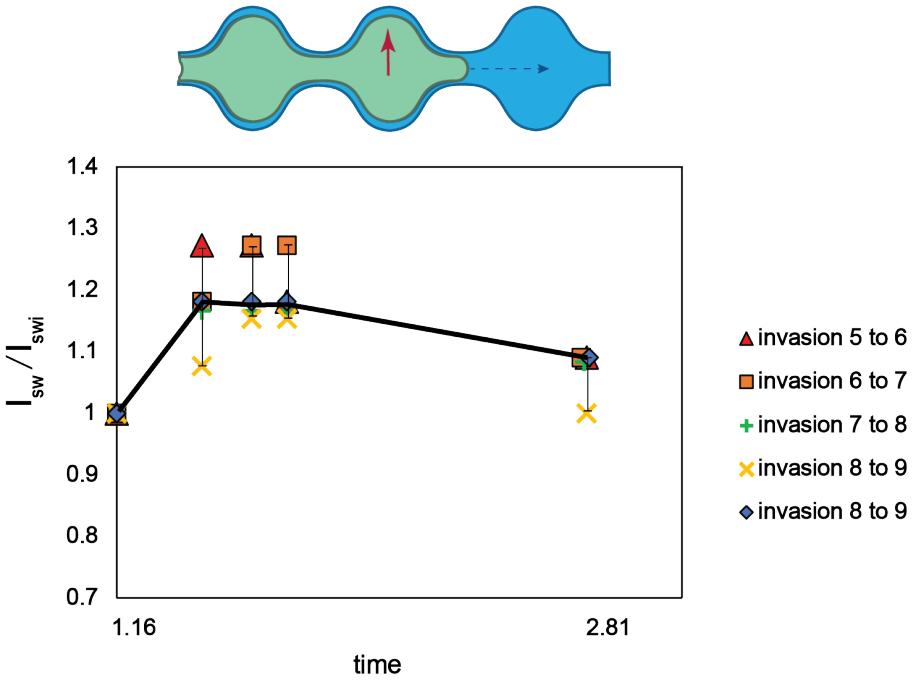

Figure 5.14: Measured corner fluid-solid contact line (l_{sw}) at the pore adjacent to the invasion (at the widest part of the pore for $\log Ca = -5$). Measured values are normalized by the initial value. Time is coordinated by initiating right before the Haines jumps and in ms units (values are presented by a logarithmic axis).

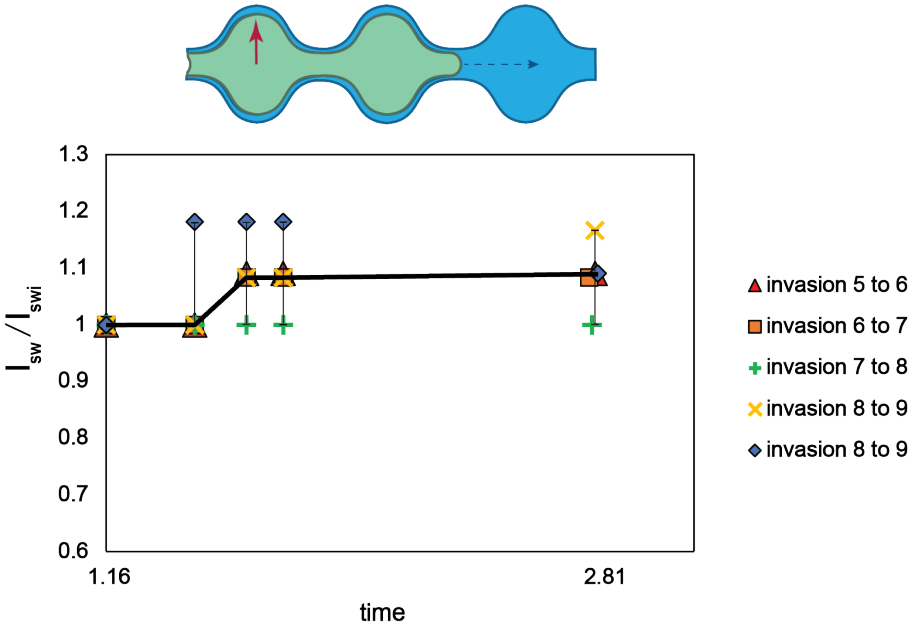

Figure 5.15: The measured corner fluid-solid contact line at widest part of the pore for pores which are one pore apart from the invaded throat at $\log Ca = -5$. l_{sw} is normalized and time is set as Fig. 5.14. The increase in the measured amounts occurs with a delay respect to the pore adjacent to the invaded pore.

Here we attempt to understand the mechanism of the observed back flow during the pore invasion by Haines jumps. If we consider the interface, pinning at the throat, right before it jumps into the next pore, a capillary pressure such as $P^t_{c(throat)}$ (capillary pressure of the interface at the throat at time t, see Fig. 5.10) exists over the interface and is equal to the capillary pressure over the arc meniscus at corners of porous media with specific curvature and radius. At the time $t+\Delta t$, the interface retains a lower capillary pressure as a characteristic behavior of Haines jumps, when the tip meniscus enters wider parts by invading the next pore. For an infinitesimal displacement of interface, since a constant pressure boundary condition is applied for invading phase, the non-wetting phase pressure over the interface is assumed to be constant; one can write:

$$\begin{cases} P^{t+\Delta t}_{c(throat)} < P^t_{c(throat)} \\ P_c = P_{nw} - P_w \\ P_{nw} = cte. \end{cases} \tag{5.20}$$

Eq. (5.20) results in,

$$P^t_{w(throat)} < P^{t+\Delta t}_{w(throat)}. \tag{5.21}$$

At $t+\Delta t$ the curvature of the interface at corners with distance of Δx is the same as curvature of interface at t. Hence, one can write:

$$P^{t+\Delta t}_{c(throat-\Delta x)} = P^t_{c(throat-\Delta x)} = P^t_{c(throat)}. \tag{5.22}$$

By applying the definition of capillary pressure ($P_c = P_{nw} - P_w$) one can conclude:

$$P^{t+\Delta t}_{w(throat-\Delta x)} = P^t_{w(throat)}. \tag{5.23}$$

Considering Eq. (5.17) and Eq. (5.23) one can conclude:

$$P^{t+\Delta t}_{w(throat-\Delta x)} < P^{t+\Delta t}_{w(throat)}. \tag{5.24}$$

This pressure gradient at corners and body of wetting fluid after jump leads to a flow from the body of the wetting fluid toward corners and increases residual wetting profile to satisfy lower capillary pressure condition during the jump by reduction of interface curvature at corners. These dynamics of interface are specially of interest when the geometry of the porous media has smaller throats comparing to pore body size and an increase in corner residual wetting fluid may result in connectivity of these corner fluids that leads to discontinuity of the invading phase. Blocking the invaded channel in this manner and occupying the pore with a bubble is known as snap-off [109]. Existence of these dynamics at corners shows that it may lead to snap-

off. Although here we highlighted the effect of abrupt pore invasions on corners, a systematic study of the influence of these high-energy interfacial releases is required.

5.5 Conclusions

Dynamics of pore invasion by Haines jumps mechanism is studied. Residual corner fluids were observed to have dynamic behavior during waiting times. While the interface is pinning at the constriction before the invasion occurs, a continuous flow from corners toward body of the fluid exist. It is observed the dynamics of this flow has an important effect on reaching the invasion threshold pressure and the definition of waiting times. Numerical results show a close resemblance with experiments, explaining dynamics of corner flows connected with Haines jumps. The model gives a relationship to evaluate the waiting times for the studied configuration. It is observed that the waiting time depends on corner geometry, fluid viscosity, interfacial tension, and the fluid distribution. We also present that by sudden decrease of capillary pressure at the interface, a characteristic of Haines jumps, a pressure gradient between body of the fluid and corner fluids causes backward flow through corners to the drained sections.

5.6 Perspective

Here we studied dynamics of pore invasions at the capillary flow regime in close relation with corner flows. There are still rooms for further research to improve our understanding of the physics of the problem.

- We believe wetting film and Haines jumps dynamics depend on the geometry of the porous media, specially on the pore-throat ratio and corner angles. By changing the geometry, different pore invasion and corner flow dynamics can be studied. Besides, as these phenomena are very fast, having a faster camera and better resolution provides the chance to study dynamics of a single pore invasion.

- Roof [109] reports a limit for pore throat to pore body ratio that below which snap-off will occur. Although we are below the Roof's limit, in none of our experiments snap-off was observed. The relation between pore morphology and snap-off is suggested as one future step.

- The pore-level physics of snap-off and corner flow are related to both constant curvature and no-curvature-driven-flux boundary conditions [67]. However, a systematic study for definition of the boundary condition improves our understanding of the physics of the problem and will help us future up-scaling of these dynamics.
- The effect of gravity is not negligible in real field. A comprehensive study of the gravitational impacts on corner flows is proposed for next steps.
- Here we were able to estimate the waiting time for a simplified configuration. Following a similar methodology for a more complex configuration elucidates pore invasion dynamics in a more complex porous media. Besides, integration of the predicted waiting time in current up-scaled models will improve our prediction of the front dynamics.

Chapter 6

Reactive transport behavior of carbonate rocks in presence of impurities in injected CO2

6.1 Introduction

Geological carbon capture and storage (CCS) is one of the most promising CO_2 mitigation methods as a part of the long-term plan for the reduction of atmospheric carbon. CCS consists of capturing the CO_2 from emission points, such as fossil fuel power plants, transporting it to the injection sites, and storing it in underground reservoirs, e.g., depleted petroleum reservoirs, saline aquifers, and deep un-mineable coal seams [82]. Among these, deep saline aquifers have the largest storage capacity [12] and have gained tremendous attention.

CO_2 storage in deep geological aquifers leads to several flow and reactive transport mechanisms at different scales (time and length-scales). The main CO_2 storage mechanisms are structural trapping, capillary trapping (0-10 years), dissolution into the resident brine (0-1000 years), and mineralization (100-million years) [45, 13]. The mineralization mechanism operates over very long-term time scales and does not participate significantly in the CO_2 storage during the injection period, Fig. 6.1. However, it is the most stable and the safest storage mechanism [82, 13]. Once CO_2 dissolves in the aqueous phase, the acidified brine finds a new equilibrium by reacting with the reservoir and caprock minerals [32, 139]. Mineral precipitation may result from subsequent ion release into the solution by the dissolution of existing solid phase [7, 32]. In some cases the precipitation of secondary minerals exceeds the dissolution of rock minerals and intergranular cementations, leading to petrophysical alterations such as porosity and permeability reduction. It increases the chance of having a more

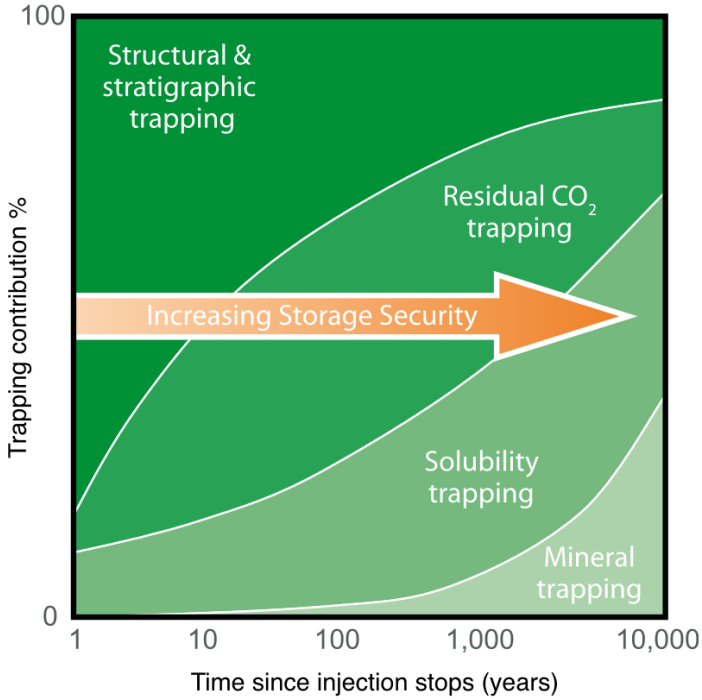

Figure 6.1: A schematic representation of the different storage mechanisms of CO_2 in geological reservoir and reserve stability with time, taken from [82]

integrated caprock. On the contrary, higher dissolution rates presumably increase the porosity and may form new pathways that increase permeability or increase leakage probability. Therefore, a comprehensive understanding of petrophysical and physicochemical alterations by geochemical reactions is needed.

During the CO_2 preparation process for underground injection, it is estimated that CO_2 impurity separation and gas compression comprises around 75% of the total CCS cost [65]. Contaminants in the injected CO_2 gas will tarnish the capture, transport, and injection operations [7]. Most frequent reactive impurities found in the captured CO_2 are SO_x, NO_x, H_2S, and O_2 [133, 7]. The presence of gas impurities impacts the CO_2 solubility in the aqueous phase, the chemical equilibrium, and the rate and type of mineral precipitation and dissolution [144]. Hence, the efficiency and safety of the CO_2 storage are affected by the existence of impurities [129]. Being able to inject pure CO_2 into deep aquifers is one way to reduce the sequestration costs [65, 133]. Therefore, a thorough study and risk analysis of impurities' impact on the reservoir is necessary.

Many experimental and numerical works have targetted the effect of impurities, especially SO_2, in terms of porosity and permeability changes and secondary minerals precipitation [133]. Due to the complexity of reservoir rocks, the variety of brine compositions, different flow conditions, and different initial petrophysical properties of samples, conclusions vary from one study to another [105, 21, 20]. Moreover,

the kinetics of mineral dissolution and precipitation is fundamentally dependent on the available reactive surface area [127] or the concentration of reactive surface sites [56, 153]. It is generally not directly measurable and is currently estimated by measuring geometrical mineral surface area, mineral adsorption methods, or empirical laws. However, the reactive surface area may vary from estimations [91, 75]. Furthermore, it is practically challenging to define how the nucleation occurs during precipitation, while an initial surface area is needed to define the kinetics of mineral precipitation. In addition, there is still discussion on the pore size dependency of the mineral precipitations. Some models consider no pore size dependency for salt precipitation [22]. Others have predicted theoretically that tiny pores are preferred for mineral precipitations [55]. Nevertheless, Emmanuel et al. [37] observed quartz precipitation in smaller pores is inhibited due to interfacial energy of small pores that increases solubility. This controversy arises from the fact that several other factors such as precipitation composition, solution condition, and flow condition in porous media affect the precipitation of different systems [124]. One other point is that there are only a few near-equilibrium experiments that allow accurate characterization of kinetic parameters, and there are uncertainties in the reported values [93, 153, 79]. So far, the definition of pore-scale parameters describing the induced geochemical mechanisms is lacking for understanding the systems mineralogy evolution. In this regard, a well-controlled repeatable experiment with uniform mineralogy is essential to study the geochemical behavior of the system and access to more accurate kinetic parameters.

During the CO_2 sequestration process, the displacement shows diverse behaviors as it gets farther from the injection well. Fluid is being injected into the reservoir, and as the front moves away from the injection point, more surface area is invaded, and the front velocity decreases. Different front behaviors and flow regimes as a function of flow properties are discussed in previous chapters, Chapter 1, Chapter 4, and elsewhere [72, 142]. During the invasion process and, especially once the injection is stopped, the CO_2 plume moves upward due to buoyancy effects. It proceeds until the caprock blocks the plume path and CO_2 is trapped under the reservoir structure. In all the mentioned sequestration stages, there are situations that the interface between fluids is in a pseudo steady condition. Zhang et al. [152] discuss that in viscous flow regime, although several branches formed during the invasion, a preferential flow path takes over other paths, and stagnant zones were created. Leaving large stagnant bodies of wetting fluid is the capillary flow regime characteristic. While the CO_2 plume migrates by gravity in a structural reservoir or is being washed away by an open aquifer, a part of the CO_2 remains as irreducible saturation, surrounded by the aqueous phase (brine) [82]. Moreover, when the reservoir gas cap is fully established,

it forms an interface between the brine and the trapped gas. During these periods, the sequestrated gas will dissolve into the brine and react with surroundings toward a more stable condition, see Fig. 6.1. However, a comprehensive understanding of dissolution across the interface and a precise measurement of reactive species transport at pore-scale is missing.

Recent progress in microfabrication and surface functionalization methods brought new insight into the characterization of reactive fluid flow through porous media. Various methods have been developed to control surface composition, and porous media geometry for studying reactive systems, e.g., direct etching and patterning of the natural rock [119, 102], functionalization of the surface with rock minerals [120, 6], crystal injection into microfluidic devices [100], using thin sections of rocks in between two slabs [116] and mineral growth inside chips [141]. In addition, by coupling microfluidics monitoring systems with spectroscopy methods, such as Raman spectroscopy, pore-scale details, and real-time characterization of the chemical composition of the porous system is achieved [100].

In this chapter, we aim to bring new light in induced mechanisms during reactive transports by investigating the pore-scale effects of SO_2 impurities on the CO_2 sequestration process and mineral composition in carbonate reservoirs by real-time Raman spectroscopy monitoring of the surface-modified microfluidic chip. For this purpose, we designed and developed a novel micromodel that allows us precise monitoring of a calcite system. In what follows, we go through details of our experimental setup, the design and preparation of microfluidic devices, and the methodology used for calcite growth in the porous media. Then, basics of reactions during sequestration in carbonate rocks are explained. Finally, results on the dynamics of mineral dissolution and precipitation are presented. We close this chapter by conclusion and give some perspectives for future works.

6.2 Materials and methods

In this section, we explain our experimental setup. First, we go through our porous media design for microfluidics experiments. Then, we note the process of the microchip preparation. Next, we shortly present the protocol to grow a thick layer of calcite on our structure wall. Finally, our characterization method and details of our experiments are presented.

6.2.1 Porous media design

Here we target to investigate a condition corresponding to the interaction between CO_2 phase and the brine across an established interface with slow dynamics when the CO_2 is capillary-trapped or has migrated under the reservoir structure. In this configuration, the dissolved CO_2 is transported mainly by diffusion in the system. Assuming the gravity effects are negligible, by putting the gaseous phase in contact with the aqueous phase in the porous media, we will explore the geochemical behavior of the system and porous media alterations in our microfluidic device. For this purpose, a microfluidic chip is designed to form a stable fluid-fluid interface. CO_2 is able to dissolve in the aqueous phase and trigger a chain of reactions. An overall pattern of the microfluidic device structure is found in Fig. 6.2. The injection points in inlets and outlets are specified at the beginning of each channel. Two capillaries (1&5) are designed to deliver reactive solutions to the porous media. channel 3 is designed for gas injection, and 2^{nd} and 3^{rd} capillaries deliver a fresh aqueous phase before experiments start (more information in Section 6.2.5). The porous system is designed as homogeneously distributed 40 microns circular pillars with a 20 microns spacing in between. The designed porous system, inlets, and outlets have an homogeneous etching depth about 40 μm. A 3D illustration of the porous media is shown in Fig. 6.3.

6.2.2 Microfluidic device preparation

PDMS microfluidic devices are permeable to gases. Geo-material microchips are short in replicability; once a sample has reacted and deformed, it is impossible to perform the same experiment again. Silicon and glass wafers have shown excellent compatibility with reactive transports, gaseous phases in the system and Raman spectroscopy. However, glass micromodels lack the resolution and control over etched cross-section form compared to silicon-glass microchips. In this study, we apply and adapt a methodology for the preparation of silicon-wafer microfluidic chips to perform replicable transport experiments.

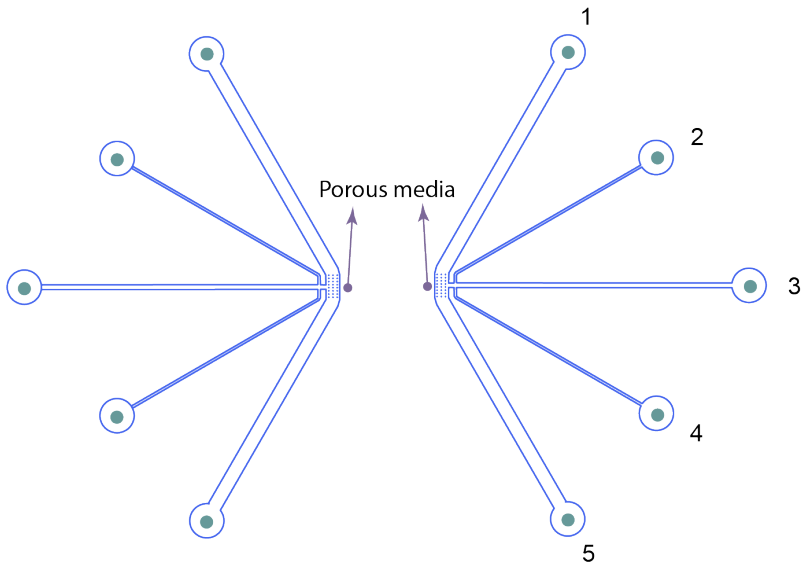

Figure 6.2: The structure and design of the microchips. Two designs are etched on one wafer.

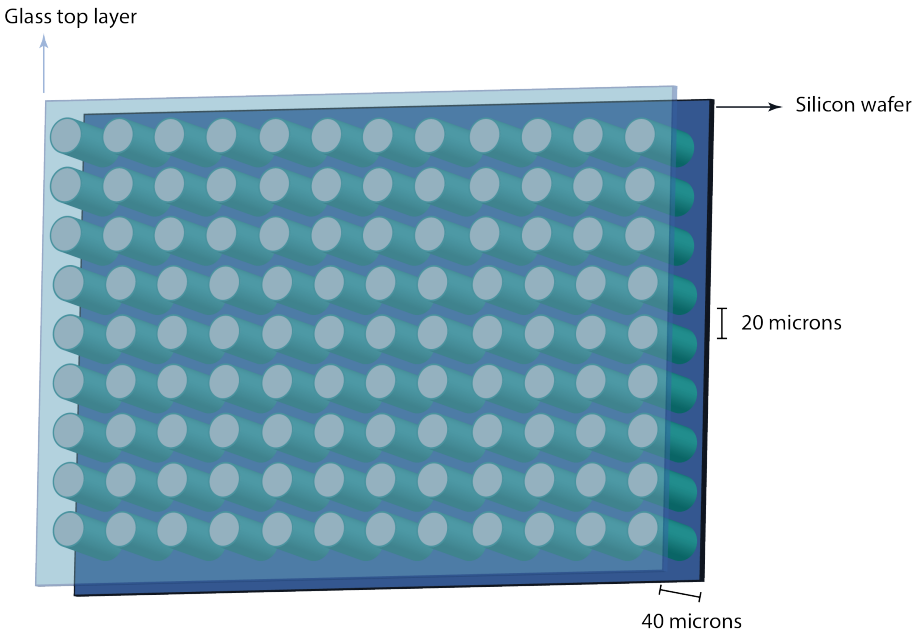

Figure 6.3: A 3D illustration of the porous media.

Having precisely-located injection spots in the micromodel improves the sealing of the experimental setup substantially and reduces the leakage probability. The deep Reactive Ion Etching (DRIE) process has been well known for more than three decades. Cryogenic DRIE is known to etch high aspect ratio features in silicon with smooth sidewalls [136] and has been applied frequently for silicon microfluidic chips substrate preparation. Recently, it has been shown that STiGer, a time-multiplexed cryogenic process, is able to etch through the silicon wafer with vertical and smooth walls [136]. We adopt this process to prepare high-precision silicon microchips with precisely defined injection points. The overall workflow of the silicon-glass microfluidic device is illustrated in Fig. 6.4. This process has been developed in collaboration with GREMI (Groupe de Recherches sur l'Energétique des Milieux Ionisés).

For the first step, a 5-micron layer of SiO_2 is deposited on the backside of a double-sided silicon wafer, using Plasma Enhanced Chemical Vapor Deposition (PECVD), which is a process by which thin films of various materials are deposited on a substrate, Fig. 6.4a. Then, patterns corresponding to the injection points are projected on the backside of the wafer by following the SU-8 deposition method presented in Section 1.4.1, Fig. 6.4b. Then, the wafer goes through the Corial etching of SiO_2 and the silicon dioxide layer is removed from the surface of injection points, Fig. 6.4c. Next, the remaining SU-8 photoresist is removed from the wafer by a Piranha bath (a highly corrosive oxidating solution, prepared by mixing H_2SO_4 and H_2O_2 3:1 volume ratio), Fig. 6.4d. Then, designed microfluidic patterns are reflected on the top-side of the silicon substrate using S1813, and capillaries are etched, with the process detailed in Section 2.1.3, Fig. 6.4e-f. For the next step, the STiGer process is applied to etch through the wafers from the backside of the substrate, see Fig. 6.4g and a top-view of the wafer in Fig. 6.4h. Finally, a borosilicate glass wafer is bonded on top of the substrate, Fig. 6.4i.

6.2.3 Calcite growth in capillaries

Now that a micromodel compatible with our experimental configuration is prepared, we go through the adapted method for making a calcite environment. Wang et al. [141] introduced a novel technique for growing a thin layer of calcium carbonate ($CaCO_3$) in micromodels. With this method, all surfaces of the micromodel is covered with 1-2 μm of nano-crystal calcite. Here, we shortly summarize the methodology of calcite precipitation. First, micromodels are cleaned with Piranha solution, and then 1M sodium hydroxide aqueous solution is injected through capillaries (1 and 3) for 30 minutes at 0.1 $\frac{mL}{min}$ and followed by rinsing with DI water. After, 2 mL N-(trimethoxysilylpropyl)ethylenediaminetriacetate (silane coupling agent, Gelest, 35% in water) is well mixed and stirred with 20 mL 1:1 mixed solution of chloroform and water. Then, the pH value is adjusted to $\approx$ 1.5 with hydrochloric acid. The chloroform

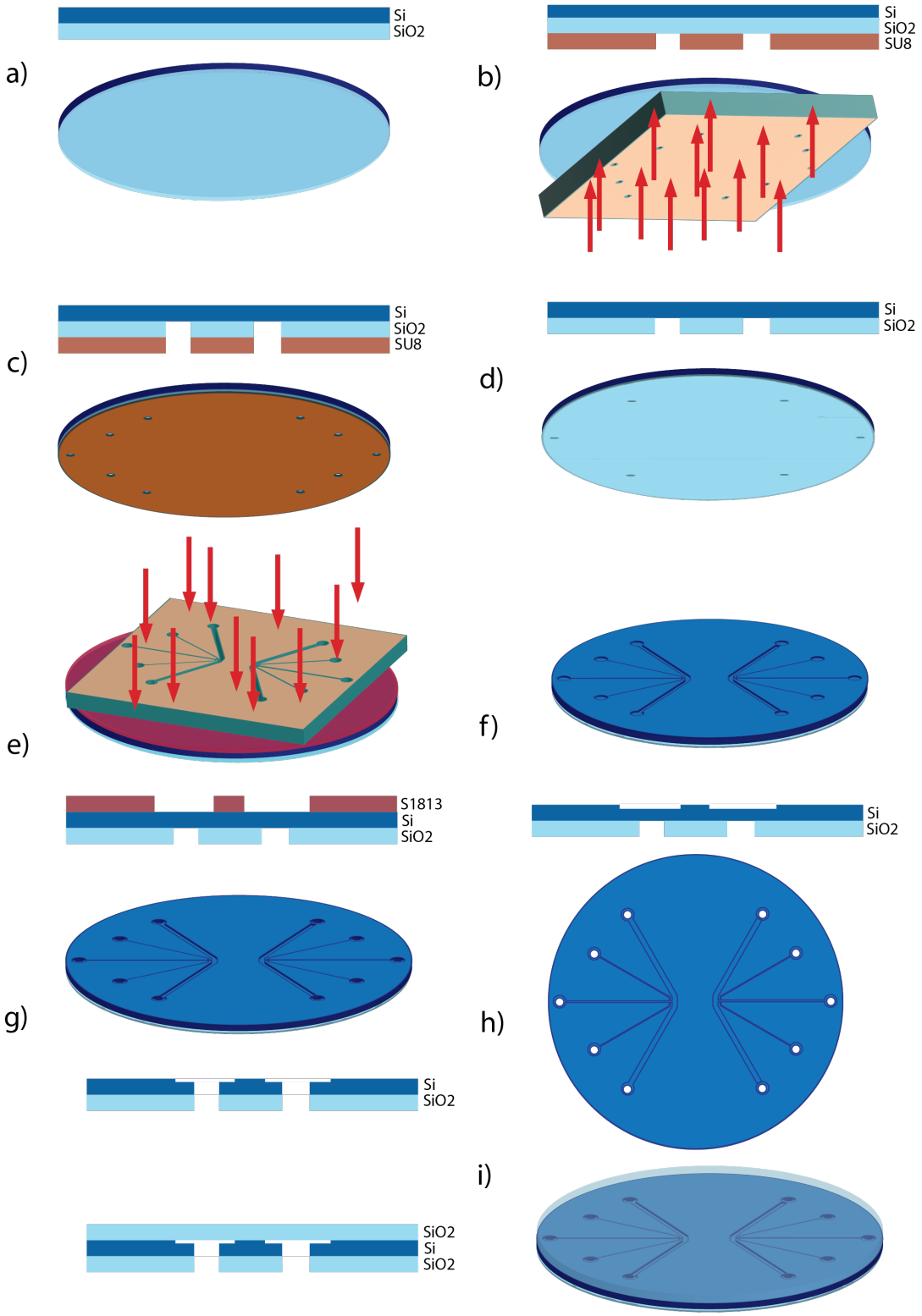

Figure 6.4: The process of the silicon-glass microfluidic device preparation with precise injection positions. Process is ordered as (a) SiO_2 deposition, (b) SU-8 photolithography, (c) SiO_2 Corial etching, (d) SU-8 removal, (e) S1813 photolithography, (f) Front side etching, (g) Back-side STiGer process, (h) prepared wafer and (i) glass bonding. In the illustrated profiles at each stage, the thickness of different layers are not in realistic scale, for a more comprehensive illustration.

phase is injected into channels for 5 mins at 0.1 $\frac{mL}{min}$ and let the fluid remain in the micromodel for 15 mins. The micromodel is then blown dry. This process is repeated 3-5 times, and the micromodel is rinsed with ethanol and 0.05M $CaCl_2$ and dried at 60°C. At the end of this stage, the surface is functionalized and is ready to host calcite crystals.

For growing calcite inside micromodels, a 0.05M $CaCl_2$ solution is pumped through the channels at 0.1 $\frac{mL}{min}$ for 2 mins, and allowed to rest for 10 mins before blowing air into capillaries. Then, a 0.05M Na_2CO_3 solution is pumped through the micromodel at 0.1 $\frac{mL}{min}$ for 2 mins, and is air-dried after remaining there for 10 mins. The alternative injection of $CaCl_2$ and Na_2CO_3 is repeated for 5 to 20 times to gain different $CaCO_3$ layer thickness, Eq. (6.1).

$$CaCl_{2(aq)} + Na_2CO_{3(aq)} \rightleftharpoons CaCO_{3(s)} + 2\,NaCl_{(aq)} \tag{6.1}$$

Finally, the micromodel is rinsed with water and dried at 60°C in air. Fig. 6.5 shows a schematic of our porous media after calcite precipitation and experimental results of Wang et al. [141].

6.2.4 Characterization method

Vibrational spectroscopy methods are nondestructive characterization methods that provide information on the system chemistry and local structures. Raman spectroscopy is an optical scattering technique that considers scattered light from a material excited with a monochromatic light. When an incident photon with a defined wavelength, λ_0, excites a molecule, the vibration level of the molecule changes to a virtual state. If the molecule turn back to the previous energy level, it emits a photon with the same wavelength as the incident photon. This is known as the Rayleigh scattering or elastic behavior. Nevertheless, if the excited molecule reaches a higher vibrational energy level, a photon with a higher wavelength, λ_s, and lower energy will be emitted (red-shift). On the other hand, if the molecule reaches a lower energy state, the emitted light will pick some energy (blue-shift). These behaviors are known as inelastic light scattering and is more a function of material composition and structure rather than the incident wavelength.

Raman spectroscopy is traditionally reported in units of wavenumbers (cm^{-1}) to measure the energy shift of the Raman bands relative to the laser. The Raman shift in this frame reads as

$$Raman\,shift = 10^7 \left(\frac{1}{\lambda_0(nm)} - \frac{1}{\lambda_s(nm)} \right). \tag{6.2}$$

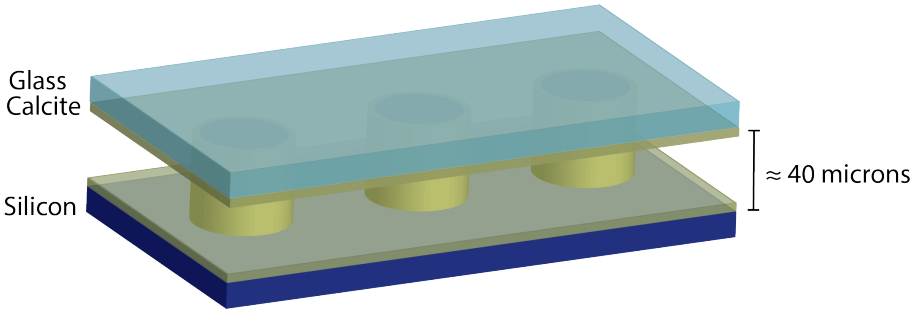

(a)

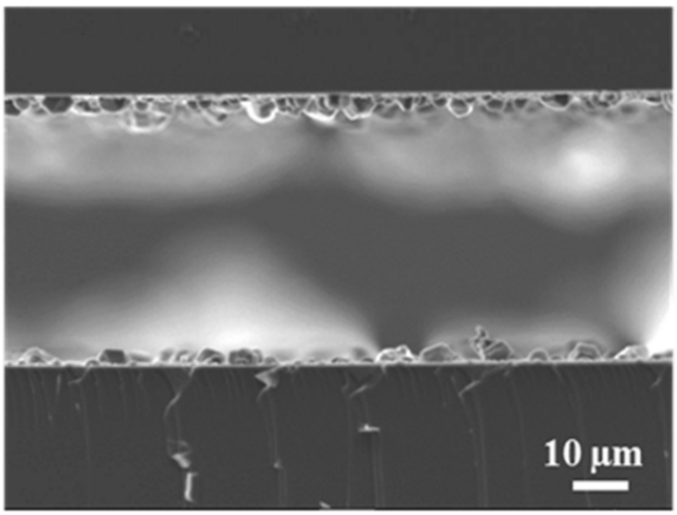

(b)

Figure 6.5: (a) A 3D illustration of the calcite precipitation in our micromodels. (b) SEM image of the coating calcite nano-crystals, taken from Wang et al. [141].

Table 6.1: The composition of applied gas mixtures.

Gas mixture	CO_2 content (mole%)	SO_2 content (mole%)
1	98	2
2	99	1
3	99.5	0.5
4	100	0

Raman bands with lower wavelengths than the laser line, higher energy, are referred to as Anti-Stokes, and the scattered lights with lower energies are known as Stokes lines.

One of the applications of Raman spectroscopy is mineral identification. Its specific arrangement of Raman bands determines the type of the mineral. Recently, it has been used in other microfluidic studies to distinguish the chemical composition [100]. In this research, we benefit from a Raman spectroscopy method to characterize our micromodel chemical composition in real-time.

6.2.5 Experimental setup

An Raman spectrometer (Andor, Shamrock 500i) equiped with a CCD camera (Andor, Newton) and a 532 nm green laser (Coherent, Genesis MX SLM) are coupled with an upright microscope (Eclipse microscope, Nikon) to perform micro-Raman spectrometry. The microscope is equipped with an automated stage that enables accurate mapping through the micromodel. For optical observations, the microscope is also synced with a camera (Andor Neo, sCMOS 5.50 Megapixel). We use a syringe pump (Harvard Apparatus Pump 11 Elite) to control the fluid injection rates. A PTFE (Polytetrafluoroethylene) sample holder and tubing set are applied to resist a highly acidic environment and gas leakage. A gas cylinder with a pressure regulation system is used to control the gaseous phase pressure in the system. Three different gas compositions are used to quantify the role of SO_2 impurities, see Table 6.1.

Before each experiment, the porous media is saturated with degassed DI water. Then, capillaries 1 and 5 (see Fig. 6.2) are closed, and the gas inlet (3^{rd}) is pressurized to move to the system toward the porous section. The pressure is controlled so that it does not invade the porous section. Meanwhile, a slow flow rate is set through the 2^{nd} and 4^{th} channel to prevent mixing between acidified water during the displacement. Finally, the flow is set to zero, and we let the gas interact with the aqueous phase through the pinned interface at pore throats. The composition of the fluid is characterized constantly at different sections of the porous media using Raman spectroscopy. A thorough 3D analysis of the system is applied at the end and the beginning of the experiment to characterize the mineralogy alterations.

This section summarizes our experimental setup, micromodel geometry, microchip preparation method, and mineral growth in the porous system. In what follows, fundamental concepts of the reactions and present numerical simulation results with PHREEQC will be presented. We close our discussion with a conclusion and perspective for future works.

6.3 Geochemical modelling

This section goes through fundamental chemical reactions that are prompted by the introduction of dissolved gas into the defined system. Then, the general concept of mineral reaction kinetics is noted. Finally, PHREEQC is introduced as the geochemical tool for studying our system to assess current models results and compare them with experiments.

6.3.1 Chemical reactions

The injected gas dissolves into the aqueous phase and lowers the pH. CO_2 forms carbonic acid and then dissociates to bicarbonate and a proton and then to carbonate anion, see Eqs. (6.3) to (6.6),

$$CO_{2(g)} + H_2O \rightleftharpoons CO_{2(aq)} + H_2O, \tag{6.3}$$

$$CO_{2(aq)} + H_2O \rightleftharpoons H_2CO_3, \tag{6.4}$$

$$H_2CO_3 \rightleftharpoons HCO_3^- + H^+, \tag{6.5}$$

$$HCO_3^- \rightleftharpoons CO_3^{2-} + H^+. \tag{6.6}$$

$SO_{2(g)}$ dissolves into the water and forms sulfuric acid. Sulfuric acid will dissociate into bisulfate, and sulfate anions depending on the thermodynamic condition:

$$SO_2 + H_2O \rightleftharpoons H_2SO_4, \tag{6.7}$$

$$H_2SO_4 \rightleftharpoons HSO_4^- + H^+, \tag{6.8}$$

$$HSO_4^- \rightleftharpoons SO_4^{2-} + H^+. \tag{6.9}$$

SO_2 is around 30 times more soluble than CO_2 and will substantially affect the chemical equilibrium upon the injection [133]. For example, existence of SO_2 in the system leads to very low pH values and decreases the CO_2 solubility [7]. Hence, the effect of CO_2 and SO_2 on the system must be studied together.

When the pH decreases, calcite minerals will dissolve into the aqueous phase. In Eq. (6.10), it is observed that the higher the H^+ concentration is, the more calcite will dissolve to consume the H^+ and produce Ca^{2+} ion and HCO_3^- cations to bring back the equilibrium,

$$\underset{\text{Calcite}}{CaCO_{3(s)}} + H^+_{(aq)} \rightleftharpoons Ca^{2+}_{(aq)} + HCO^-_{3\,(aq)}. \tag{6.10}$$

Products of Eq. (6.10) react with sulfate ions (produced by dissolution of other minerals, dissolution of SO_2, or existing in the aquifer) and will produce gypsum,

$$Ca^{2+} + SO_4^{2-} + 2\,H_2O \rightleftharpoons CaSO_4 \cdot 2\,H_2O. \tag{6.11}$$

6.3.2 Kinetics

The general format of the reaction rate law was proposed by Lasaga [69]. For a system without any inhibitor or catalyst, it usually reads as

$$r_n = S_A k_n |1 - \Omega_n^p|^q, \tag{6.12}$$

where subscript n stands for a specific mechanism of reaction and r_n, k_n, A_n, Ω, p and q are respectively mineral dissolution or precipitation rate, rate constant, specific reactive surface area per kg water, saturation ratio, and empirical parameters [7, 153]. If for a mineral several mechanisms are active, the net reaction rate will be the sum of each individual rate,

$$r_{net} = \sum_n r_n. \tag{6.13}$$

Palandri and Kharaka [93] divided reaction rates in H^+, OH^- and neutral promoted mechanisms and normally rate equations consist of the net behavior of the system based on these three mechanisms. The rate constant for each of these mechanisms is written as

$$r_H = A_H a_{H^+}^{n_H} e^{\frac{-E_{a,H}}{RT}}, \tag{6.14}$$

$$r_w = A_w e^{\frac{-E_{a,w}}{RT}}, \tag{6.15}$$

and

$$r_{OH} = A_{OH} a_{H^+}^{n_{OH}} e^{\frac{-E_{a,OH}}{RT}}, \tag{6.16}$$

where A_{OH}, A_w, and A_H are Arrhenius pre-exponential factors for each mechanism ($mol.m^{-2}.s^{-1}$), $E_{a,H}$, $E_{a,w}$, and $E_{a,OH}$ are the apparent reaction activation energy of each mechanism ($J.mol^{-1}$), n_H, and n_{OH} are reaction orders, R is the universal gas constant (8.31446 $J.mol^{-1}.K^{-1}$), and T is the temperature (K). These kinetic parameters are summarized for each reaction in Table 6.2. There are other mechanisms

Table 6.2: Mineral phases and kinetic parameters used in this study.

Calcite		Gypsum	
Parameter	Value	Parameter	Value
$A_H\ (mol.m^{-2}.s^{-1})$	-	$A_H\ (mol.m^{-2}.s^{-1})$	-
$E_{a,H}\ (J.mol^{-1})$	-	$E_{a,H}\ (J.mol^{-1})$	-
n_H	-	n_H	-
$A_w\ (mol.m^{-2}.s^{-1})$	6.59×10^{4}	$A_w\ (mol.m^{-2}.s^{-1})$	1.64×10^{-3}
$E_{a,w}\ (J.mol^{-1})$	6.6×10^{4}	$E_{a,w}\ (J.mol^{-1})$	0
n_w	-	n_w	-
$A_{HCO_3^-}\ (mol.m^{-2}.s^{-1})$	1.04×10^{9}	$A_{OH}\ (mol.m^{-2}.s^{-1})$	-
$E_{a,HCO_3^-}\ (J.mol^{-1})$	67	$E_{a,OH}\ (J.mol^{-1})$	-
$n_{HCO_3^-}$	1.6	n_{OH}	-

that can influence the reaction rate. Taking dissolution of carbonate minerals as an example, the rate of the reaction highly depends on the CO_2 partial pressure [98].

The surface area of reactants varies as the reaction proceeds. Here we assume the minerals are spherical or cubic and the reaction occurs homogeneously all over the mineral. Then, the surface area during the reaction reads as

$$S_A = S_{A_0}\left(\frac{m}{m_0}\right)^{\frac{2}{3}}, \tag{6.17}$$

where S_{A_0} is the initial surface area of the mineral.

For a multi-component system finding the equilibrium state composition based on various reactions equilibrium constants or calculating the state of kinetic reactions is very complex. In what follows, PHREEQC is presented as a numerical tool to simulate our system chemistry.

6.3.3 PHREEQC

PHREEQC is a computer program designed to perform a wide range of aqueous geochemical calculations. Several aqueous models are built into it, and using any of these aqueous models, PHREEQC computes of speciation, saturation-index, batch-reaction, and one-dimensional transport, including aqueous, mineral, gas, solid-solution, kinetically controlled reactions, mixing of solutions, and pressure and temperature changes [94]. In this study, we calculate the equilibrium conditions, chemical speciations, and reaction kinetics using PHREEQC. Besides, we perform a series of 1D transport-kinetics implemented simulations to track the aqueous composition and mineralogy alterations for time and position. In the next section, simulation results are presented.

6.4 Results and discussion

First, we explore a batch reaction system to see how a system of calcite in contact with acidified aqueous phase evolves over time. Simulations are performed using PHREEQC. We use the THERMODDEM thermodynamic data set from BRGM and, for kinetics calculations, the reported library of kinetic equations in Zhang et al. [153], Palandri and Kharaka [93] and Marty et al. [79] are applied, which include about 100 mineral phases. Simulations are performed under isothermal ($T = 25°C$) and isobaric ($P = 60\,mbar$) condition. Each component's partial pressure is calculated based on the total gas pressure and the gas mixture composition. Thermodynamic equilibrium is assumed at the gas-water interface to calculate the gaseous phase dissolution using PHREEQC.

First, the aqueous and the gaseous phases are equilibrated. Due to the presence of SO_2 and its high solubility, the pH reduces drastically (≈ -0.48). Then, a kinetic reaction is considered for the solution and the calcite mineral. The evolution of the system for dissolved calcite and precipitated gypsum is plotted over time, see Fig. 6.6. We observe that the calcite dissolves at a high rate in the beginning. As time passes and the mineral surface area reduces, the mineral dissolution slows down. Finally, all the calcite is fully dissolved in the solution. It takes some time for the system to satisfy the required species concentration and prerequisite condition to form gypsum crystals. This is why no gypsum is observed in the system at the initial times, Fig. 6.6. However, it quickly catches up with the calcite dissolution rate after its initiation. Due to the excess of sulfur dioxide in the system and the fact that gypsum keeps a near-zero saturation index during the reaction, it seems that the calcite dissolution rate limits the reaction. In other words, the calcite reactive surface area plays a significant role in controlling the reaction.

Gypsum has a higher molar volume compared to calcite (74.31, compared to 36.94 m^3/mol). The total solid volume in the system is calculated using the molar volume of each mineral, see Fig. 6.7. In the beginning, no gypsum is forming, and calcite is dissolved in the system, the total solid volume decreases. It roughly shows a porosity increase at the beginning of the reaction. However, since precipitation begins, the total solid volume increases. It may be inferred that gypsum decreases porosity drastically afterward and may block some pores. Nevertheless, these results correspond to batch reactions, and the effect of gypsum nucleation on the solid surface and reduction of the reactive surface area is ignored here. Besides, the solution is considered well-mixed in a batch reaction, while in natural porous media, solutes must advect or diffuse through porous media to react. In the next part, a diffusive transport system is considered to

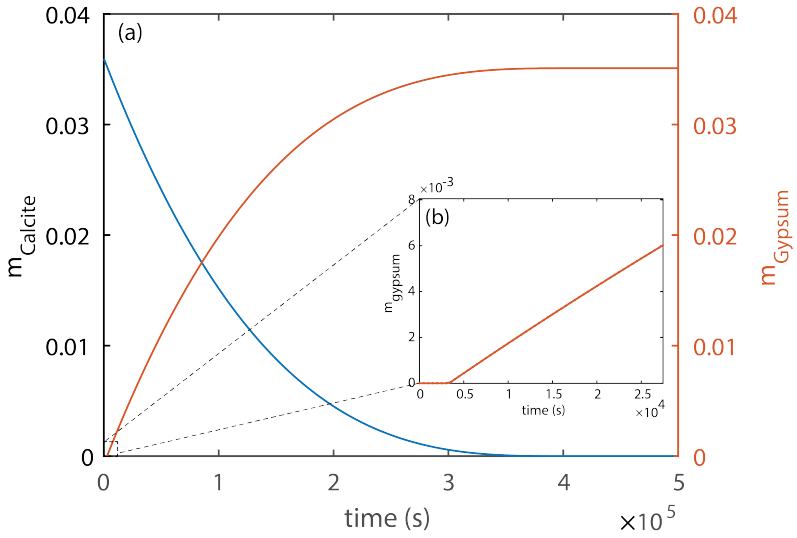

Figure 6.6: (a) The solution composition evolution in a batch reaction of calcite with acidified aqueous phase at equilibrium with CO_2-SO_2 99:1 molar mixture. (b) Moles of precipitated gypsum at initial times of the batch reaction.

study the kinetics of the reaction in a dynamic system.

A reactive transport modeling is performed using 1D transport option of PHREEQC. PHREEQC numerically solves the solute mass balance, expressed as

$$\frac{\partial C}{\partial t} = -v\frac{\partial C}{\partial x} + D_L\frac{\partial^2 C}{\partial x^2} - \frac{\partial q}{\partial t}, \tag{6.18}$$

where C is the solution concentration (mol/kg_w), t is time (s), v is flow velocity (m/s), x is distance (m), D_L is hydrodynamic dispersion coefficient (m^2/s), and q is the concentration in the solid phase (mol/kg) related to interaction between the solid phase and the solution [94]. Here we only consider the diffusion and the equation simplifies into

$$\frac{\partial C}{\partial t} = D_L\frac{\partial^2 C}{\partial x^2}. \tag{6.19}$$

A constant concentration boundary condition with the concentration of the equilibrated water and gas mixture is applied at the inlet ($C_{inlet} = C_{acidifiedaquifer}$), and a closed boundary condition is considered at the end of the column ($\frac{\partial C}{\partial x} = 0$), see Fig. 6.8. The transport with kinetic reactions is solved for hundred consecutive cells, making a conceptualized 1D reactive system. Each cell initiates with $25.5 \times 10^{-3}\,kg$ of water and $3.6 \times 10^{-2}\,mol$ calcite. This system corresponds to our experiments with a volumetrically augmented system due to numerical limitations of PHREEQC in micro-volume calculations and adaptation to microfluidic systems. The PHREEQC code is available in Appendix A.5.

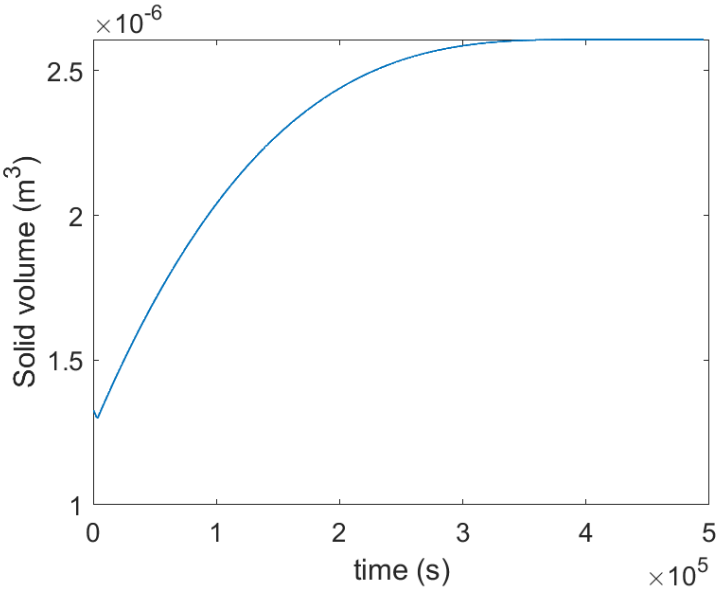

Figure 6.7: The calculated total solid volume in the simulated kinetic batch reaction.

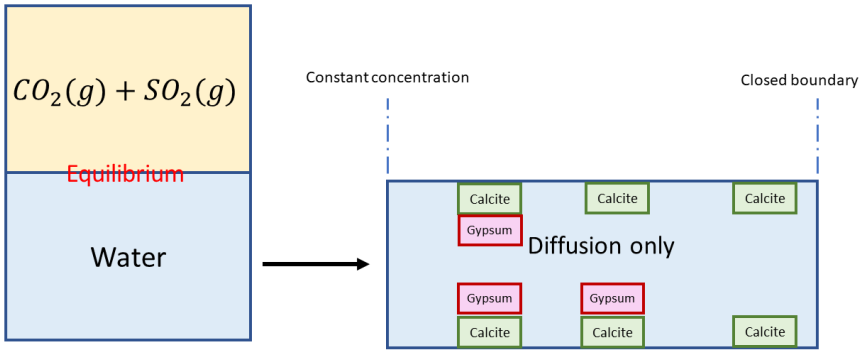

Figure 6.8: A schematic representation of the conceptualized 1D simulation in PHREEQC.

Here we show the results for two cases. In the first set, the gas contains pure CO_2, while the second set corresponds to a SO_2 impure gas mixture. In the beginning, the calcite interacts with the surrounding aqueous phase, and the system pH increases by carbonic anions. Meanwhile, the low pH solution diffuses from the inlet and gradually reduces the pH for both cases, Fig. 6.9. However, pH is substantially lower in the second case due to the existence of sulfur species. This reaction is happening in a very low Pe, Eq. (1.5), and reaction rates are higher than diffusion rate, high Da_{II}, Eq. (1.6), leading to the expectation of having a compact dissolution [121, 30]. Simulations show that as the solution is acidified, calcite is consumed completely, which is in line with the expectations [114], see Fig. 6.10. It is important to point out that since the pH has dropped faster through the system in the second case, the calcite dissolution propagates faster respectively. One reason is, of course, diffusion of sulfur ions even ahead of the dissolution front due to the delay that exists between the kinetics of calcite dissolution and gypsum precipitation, Fig. 6.11. It is also highlighted with calcium concentration data, Fig. 6.12. As the pH decreases, the calcium ion concentration rises. However, it drops drastically as time passes at the inlet. This points commencing of gypsum precipitation in the system in the second case. Fresh sulfur atoms are provided from the inlet and react with the available aqueous calcium, forming gypsum Fig. 6.13. This may reduce pore sizes in porous media since the new phase occupies more space, resulting in lower diffusion rates that are not considered here. In the worst-case scenario, it may even lead to pore isolation. Nonetheless, after the cession of gypsum precipitation due to lack of Ca, SO_2 and CO_2 are still being dissolved from the inlet and will modify the aqueous phase. Besides, due to the existing chemical gradient between cells, other species will also diffuse in between cells. This results in alteration of current thermodynamic state in gypsum precipitated regions and reverse reaction in Eq. (6.11). Consequently, gypsum begins to dissolve and increases the porosity. The evolution of total solid volume has been calculated for the simulated 1D column with time, Fig. 6.14. Values have been normalized by the initial solid volume in the system. In case one, as the dissolution of calcite is the dominant reaction, the results confirm the total dissolution of calcite. However, for the second case, results show an initial increase in the solid phase volume (decrease in porosity), while a decrease in the total solid volume happens afterward at the inlet as the gypsum dissolves again. More precisely, just behind the dissolution front, the solid volume decreases as well, reflecting the delay between the kinetics of calcite dissolution and gypsum formation, see Fig. 6.14, 115.66 days after injection. Later on that secondary mineral forms, solid volume increases again. This is in line with experimental observations of Noiriel et al. [91] and Thaysen et al. [133], where, respectively, a higher porosity increase and total consumption of a limestone column at the inlet is observed by injection of an acidic brine.

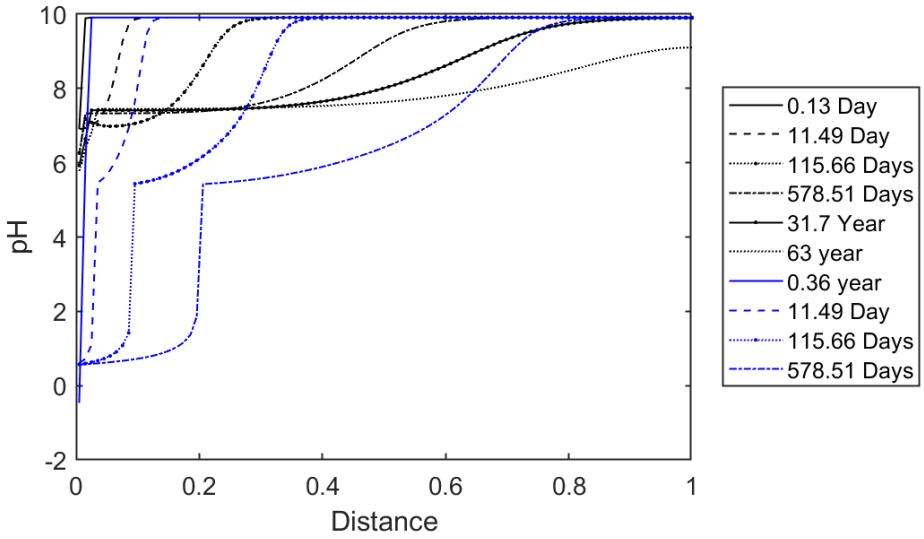

Figure 6.9: Results of simulations using PHREEQC representing pH during the simulated time. Distance values are normalized using the total length. Black graphs correspond to case one, when only CO_2 is injected. The blue line corresponds to existance of SO_2 impurities.

Although here we are able to characterize and distinguish the main chemical mechanisms in the system, results must be interpreted carefully. Although diffusion and transport effects are taken into account, a well-mixed solution is considered in each cell. Besides, all the surface areas of the minerals are considered available for reaction. However, phenomena such as secondary mineral precipitations might make some reactive sites inaccessible. Our reactive microfluidic system is designed to shed light on these small-scale phenomena.

6.5 Conclusion and Perspective

In this chapter, we presented a novel micromodel design and preparation method that paves the way for micron-scale reactive transport analysis and the definition of precise kinetic parameters. The effect of sulfur impurities on mineralization mechanisms is studied in a calcite system using PHREEQC simulations. Results show that the existence of sulfur species drastically reduces the system pH and increases the calcite dissolution rate, resulting in a more aggressive and compact corrosion at near interface areas. However, as the secondary phase, gypsum precipitated behind the dissolution front and changed the total solid volume. Here, it is assumed that there is a uniform dissolution-precipitation over the minerals. However, to validate the effect of gypsum nucleation in the system, experimental studies must be compared to the defined system. The presented experimental system potentially sheds light on the mechanisms

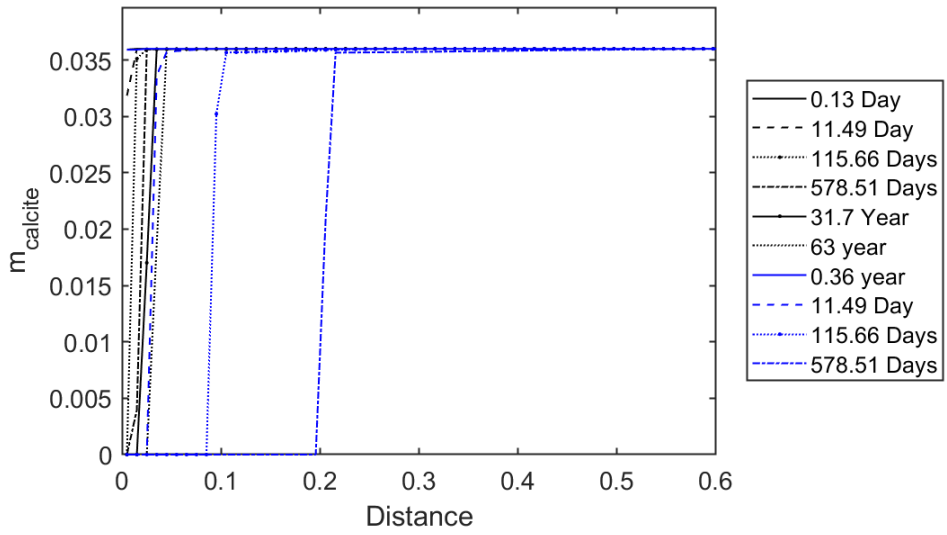

Figure 6.10: The evolution of calcite mineral (moles) through the simulated 1D column. The distance is normalized by the total length. Black and blue are respectively representing pure CO_2 and CO_2+SO_2 mixture.

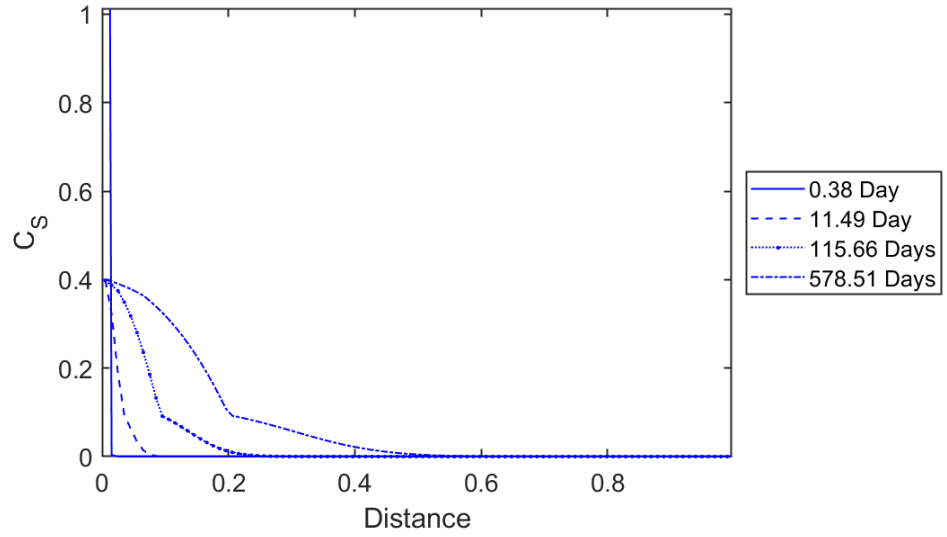

Figure 6.11: Total S molality through the simulated 1D column.

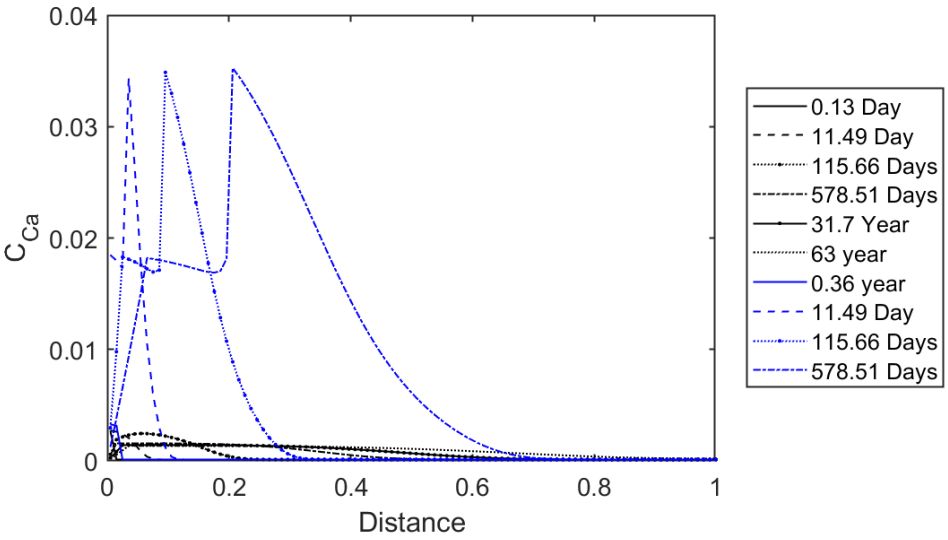

Figure 6.12: Total Ca molality through the simulated 1D column. Black and blue data respectively correspond to first and second case studies.

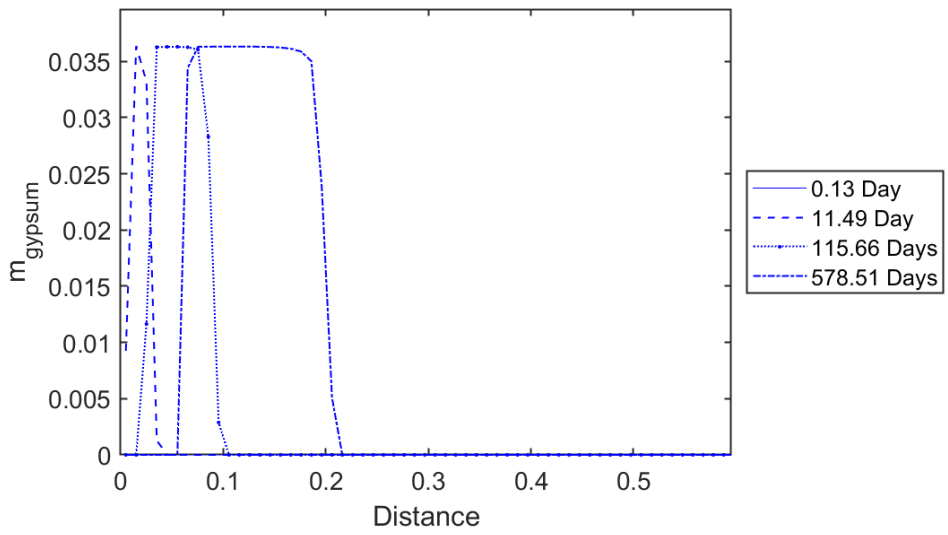

Figure 6.13: The evolution of gypsum with respect to the distance from the inlet for various times.

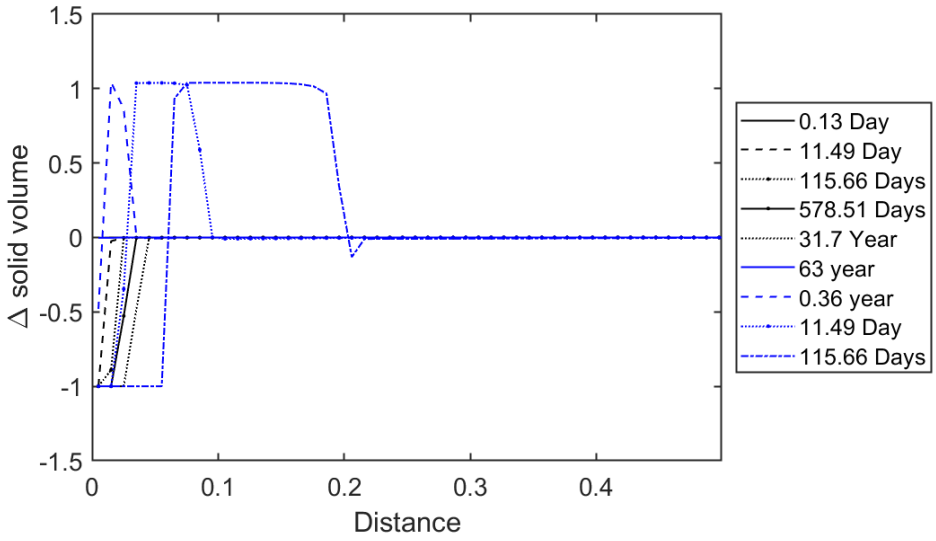

Figure 6.14: The total solid volume changes as a function of distance from the inlet for various times. Black and blue data respectively correspond to first and second case studies.

that are triggered by CO_2 and SO_2 introduction in the system. We have worked on the micromodel and setup preparation, yet we have not been able to conduct any experiments. This part remains to be done.

Chapter 7

Summary and perspective

7.1 Summary

CO_2 sequestration in geological reservoirs has gained attention as a reliable mitigation method to reduce atmospheric CO_2. It is a challenging task involving multiphase reactive flow processes spreading over vast time and length scales. Understanding physical and chemical mechanisms induced by CO_2 sequestration is a prerequisite for obtaining a successful secure and permanent CO_2 storage in subsurface formations. Due to the lower viscosity of CO_2 compared to the brine, the displacement tends to become unstable, and a ramified displacement front develops. The distribution of CO_2 and the displacement patterns depend on fluid, rock, and flow properties. The global fluid displacement front behavior is composed of a series of pore invasions that build up the overall displacement behavior. However, the link between pore invasion mechanisms, the prevailing balance between fundamental forces, and global front behavior was vague. Moreover, the injected CO_2 reacts with the brine and upsets the thermodynamic equilibrium. CO_2 dissolution sets off a cascade of events that modify porous media petrophysical and physicochemical properties through induced dissolution and precipitation kinetics. Pore-scale parameters defining the induced mechanisms had yet to be defined for understanding mineral trapping in the reservoir. Two primary goals were set during this Ph.D.; first, to investigate triggered pore invasion mechanisms in different flow regimes and to quantify the impact of pore-scale events on front behavior and interfacial dynamics. Second, to explore the kinetics of calcite dissolution, the evolution of the reactive surface area, and monitor the alteration of porous media to quantify the effect of SO_2 impurities on CO_2 storage.

We designed and performed precise μ-scale experiments using micromodels, i.e., a transparent replica of porous media network made in synthetic materials. The experimental setup consists of a microscope coupled with a high-resolution camera to visualize the flow and a Raman spectrograph to monitor reaction processes at the

pore-scale. We developed a generic theoretical model based on Navier-Stokes volume averaging that takes into account inertia, viscous, and capillary forces and allows us to assess and predict invasion processes and front behavior.

We examined various flow rates, fluid pairs, and wettability conditions in a series of drainage studies. The fundamental flow regimes of immiscible displacement are identified, and fundamental pore invasion mechanisms and related interface dynamics are captured. The contribution of viscous, capillary, and inertia forces on interface and pore invasion dynamics also are addressed. Due to viscous forces dominancy and inertia effects, the viscous flow regime is characterized by pores that are invaded successively with a continuous interface displacement. At the capillary flow regime, we showed that the invasion condition is determined by threshold capillary pressure. Haines jumps are the predominant pore invasion mechanism in this condition. Pore by pore invasion and a front with mixed capillary and viscous flow regime characteristics describe the crossover flow regime. The differences between distinct pore invasion methods are observed on a single-pore scale. The interface does not find enough time to expand in the pore space in the viscous flow regime, and a body of wetting fluid persists at the pore space curvatures. However, for the capillary flow regime, the interface expands laterally, and only corner wetting fluid and films are retained in drained pores. The results of our model match those of the experiments. In addition, we numerically explored a wide range of conditions to predict flow regime transitions.

We investigated the dynamics of waiting times and corner flows for the capillary flow regime. By applying the micro-PIV technique and measuring the profile of corner fluids, it was revealed that there is a dynamic behavior in corner fluids, while the interface seems pinned and static in the pore throat. Our results suggest a continuous flow in the body of the wetting fluid during pinning. The dynamics of the corner flow are found to have a significant impact on attaining the invasion threshold pressure and defining waiting times. We can anticipate the waiting time and corner flow velocity using theoretical developments.

Finally, a novel silicon-glass micromodels preparation method and design are proposed to study reactive transport for a system of pure CO_2 and a mixture of CO_2 and SO_2. Micromodels are designed to grow micron-scale calcite minerals on its surface, providing a controlled composition and a well-defined geometry, resembling carbonate rocks. Raman spectroscopy technique will help monitor and characterize the evolution of the aqueous phase composition, reactive surface area, and kinetics of reactions. A geochemical model is proposed to predict the behavior of our experiments. It is observed that SO_2 drastically reduces the system's pH and accelerates calcite dissolution. However, as the secondary phase, gypsum precipitates behind the dissolution front and changes the systems porosity.

7.2 Conclusion

In conclusion, this study sets out to investigate micro-scale physical and chemical mechanisms induced by CO_2 storage in geological reservoirs. The results will serve to optimize the process of CO_2 sequestration in geological reservoirs. This study highlighted the relationship between pore-scale mechanisms and the front dynamics. We elucidate the displacement behaviors for different reservoir conditions, from close to far from the injection well. Based on dimensionless numbers, representative of flow conditions, we can predict how CO_2 is distributed. Moreover, we point out that pore invasion traces and residual wetting phase configurations at individual-pore scales are different for each flow pattern. This indicates that the interaction between phases and physicochemical couplings is entirely different in each region of the reservoir. We improve our understanding of fluid-solid interactions and the evolution of porous media petrophysical and physicochemical properties at different flow conditions. It will help to optimize CO_2 sequestration injection cycles and estimate injectivity of wells as a function of time.

Besides, the interfacial dynamics indicated in this study at slow drainage conditions modify the dissolution rates compared to the static condition that classically is assumed at the fluid-fluid interface. It may increase the chance of capillary fingerings in the caprocks and accelerate wettability alterations, resulting in a decrease in capillary trapping and reduction of reservoir storage security.

One other significant finding emerging from this study is that corner flows have a controlling role in the dynamics of low flow rates displacements. These findings support the idea that although the flow is capillary-dominated, there is a region behind the front, where slow viscous drainage through corners controls the dynamics. The findings reported here shed new light on displacement in a capillary flow regime that current transport models fail to predict thoroughly. These results are transferable to pore network models and will improve the modeling of displacement under capillary-dominated conditions.

In addition, the presented experimental setup paves the way for an accurate study of kinetic parameters and minerals nucleation. It helps to define pore-scale parameters describing the induced mechanisms in mineral trapping. Additionally, it enables us to perform risk analysis on allowed injected impurities – The outcome assists in improving reservoir capacity estimation and security evaluation.

7.3 Perspective

Here we investigated pore-scale mechanisms involved in CO_2 sequestration in underground storage. Although we brought new light into the physics and chemistry behind

the sequestration process, there is still room for further investigations. Here we raise some questions and ideas that may motivate future research.

Here, we evaluated key variables during drainage in a model porous media and isolated events to study them individually. Natural porous media, however, is composed of various pore shapes, sizes, and connectivity distributions. Now that we have the fundamental knowledge about front dynamics, studying different pore morphologies, connectivity, and heterogeneity degrees will bring us one step closer to understanding the continuum scale. However, it remains a challenge to integrate these findings in Darcy scale models. Besides, although the model was able to predict the overall front behavior and interface dynamics, it still shows a limitation in precisely matching the time scale. As we have observed experimentally, there are some small-scale phenomena such as viscous slip and coupling at the fluid-fluid interface or corner flow that we neglect during the derivation of the model. The viscous coupling between phases and accounting for dynamics of corner flows will improve the model predictivity.

In this study we investigated pore invasion mechanisms in drainage transports. One important and interesting setting is imbibition in porous media. We assume precursor films play a key role in definition of the pore invasion mechanisms and propose studying the pore invasion mechanisms in a similar system at controlled porous media structure, wettability, and flow rates during imbibition condition.

Here, we highlighted that corner flow has a controlling role in the dynamics of capillary-dominated pore invasions. Upscaling of corner flow dynamics for continuum scale remains yet to be studied. Application of the results in pore network models seems the first approach. Additionally, although our geometry fulfills Roof's conditions for snap-off, no throat films coalescent are observed during our experiments. We surmise that the morphology of pores and pore-throat geometrical transitions have an important influence on the snap-off occurrence and needs to be discovered.

In this study, we presented a novel micromodel preparation to perform micron-scale reactive transport analysis and kinetic parameters. We highlighted the basic geochemical mechanisms for calcite minerals. However, field application of results needs a thorough study of various mineral configurations and brine compositions. Understanding the nucleation in a confined environment is essential to predict secondary minerals deposition and growth. Moreover, the study of caprock minerals in a similar configuration sheds light on the evolution of caprock integrity and storage safety.

Bibliography

[1] Addae-Mensah, K. A., S. Retterer, S. R. Opalenik, D. Thomas, N. V. Lavrik, and J. P. Wikswo (2009). Cryogenic etching of silicon: an alternative method for fabrication of vertical microcantilever master molds. *Journal of microelectromechanical systems 19*(1), 64–74.

[2] Akbarabadi, M. and M. Piri (2013). Relative permeability hysteresis and capillary trapping characteristics of supercritical co2/brine systems: An experimental study at reservoir conditions. *Advances in Water Resources 52*, 190–206.

[3] Aker, E., K. J. Måløy, A. Hansen, and S. Basak (2000). Burst dynamics during drainage displacements in porous media: Simulations and experiments. *EPL (Europhysics Letters) 51*(1), 55.

[4] Al-Housseiny, T. T., J. Hernandez, and H. A. Stone (2014). Preferential flow penetration in a network of identical channels. *Physics of Fluids 26*(4), 042110.

[5] Alaskar, M., K. Li, and R. Horne (2013). Influence of particle size on its transport in discrete fractures: pore-scale visualization using micromodels. In *Proceedings of the Thirty-Eighth Workshop on Geothermal Reservoir Engineering, Stanford, CA, USA*, pp. 11–13.

[6] Alzahid, Y. A., P. Mostaghimi, A. Gerami, A. Singh, K. Privat, T. Amirian, and R. T. Armstrong (2018, 12). Functionalisation of Polydimethylsiloxane (PDMS)-Microfluidic Devices coated with Rock Minerals. *Scientific Reports 8*(1), 15518.

[7] André, L., M. Azaroual, C. Bernstone, and A. Wittek (2015). Modeling the geochemical impact of an injection of CO2 and associated reactive impurities (SO2 and O2) into a saline reservoir. *Transport in Porous Media 108*(1), 185–205.

[8] Armstrong, R. T. and S. Berg (2013). Interfacial velocities and capillary pressure gradients during Haines jumps. *Physical Review E - Statistical, Nonlinear, and Soft Matter Physics 88*(4), 043010.

[9] Armstrong, R. T., N. Evseev, D. Koroteev, and S. Berg (2015). Modeling the velocity field during haines jumps in porous media. *Advances in Water Resources 77*, 57–68.

[10] Aryana, S. A. and A. R. Kovscek (2012, 12). Experiments and analysis of drainage displacement processes relevant to carbon dioxide injection. *Phys. Rev. E 86*, 066310.

[11] Aussillous, P. and D. Quéré (2000). Quick deposition of a fluid on the wall of a tube. *Physics of fluids 12*(10), 2367–2371.

[12] Bachu, S. (2008). Co2 storage in geological media: Role, means, status and barriers to deployment. *Progress in Energy and Combustion Science 34*(2), 254–273.

[13] Bachu, S. (2015). Review of co2 storage efficiency in deep saline aquifers. *International Journal of Greenhouse Gas Control 40*, 188–202.

[14] Bakhshian, S., H. S. Rabbani, S. A. Hosseini, and N. Shokri (2020). New insights into complex interactions between heterogeneity and wettability influencing two-phase flow in porous media. *Geophysical Research Letters 47*(14), e2020GL088187.

[15] Bauer, D., S. Youssef, M. Fleury, S. Bekri, E. Rosenberg, and O. Vizika (2012). Improving the estimations of petrophysical transport behavior of carbonate rocks using a dual pore network approach combined with computed microtomography. *Transport in porous media 94*(2), 505–524.

[16] Benner, F. C., W. W. Riches, F. Bartell, et al. (1938). Nature and importance of surface forces in production of petroleum. In *Drilling and Production Practice 1938*. American Petroleum Institute.

[17] Berg, S., H. Ott, S. A. Klapp, A. Schwing, R. Neiteler, N. Brussee, A. Makurat, L. Leu, F. Enzmann, J.-O. Schwarz, et al. (2013). Real-time 3d imaging of haines jumps in porous media flow. *Proceedings of the National Academy of Sciences 110*(10), 3755–3759.

[18] Blois, G., J. M. Barros, and K. T. Christensen (2015). A microscopic particle image velocimetry method for studying the dynamics of immiscible liquid–liquid interactions in a porous micromodel. *Microfluidics and Nanofluidics 18*(5-6), 1391–1406.

[19] Blunt, M. J. (2017). *Primary Drainage*, pp. 73–114. Cambridge University Press.

[20] Bolourinejad, P. and R. Herber (2015a). Chemical effects of sulfur dioxide co-injection with carbon dioxide on the reservoir and caprock mineralogy and permeability in depleted gas fields. *Applied Geochemistry 59*, 11–22.

[21] Bolourinejad, P. and R. Herber (2015b). Experimental investigation of porosity and permeability variations in reservoirs and caprock following co-injection of sulfur dioxide and hydrogen sulfide with carbon dioxide. *Journal of Petroleum Science and Engineering 129*, 137–144.

[22] Borgia, A., K. Pruess, T. J. Kneafsey, C. M. Oldenburg, and L. Pan (2012). Numerical simulation of salt precipitation in the fractures of a co2-enhanced geothermal system. *Geothermics 44*, 13–22.

[23] Bretherton, F. P. (1961). The motion of long bubbles in tubes. *Journal of Fluid Mechanics 10*(2), 166–188.

[24] Brown, C. A., R. G. Compton, and C. A. Narramore (1993). The kinetics of calcite dissolution/precipitation. *Journal of colloid and interface science 160*(2), 372–379.

[25] Buckley, S. E., M. Leverett, et al. (1942). Mechanism of fluid displacement in sands. *Transactions of the AIME 146*(01), 107–116.

[26] Chatzis, I. and F. Dullien (1983). Dynamic immiscible displacement mechanisms in pore doublets: theory versus experiment. *Journal of Colloid and Interface Science 91*(1), 199–222.

[27] Cox, B. (1962). On driving a viscous fluid out of a tube. *Journal of Fluid Mechanics 14*(1), 81–96.

[28] Daccord, G. (1987). Chemical dissolution of a porous medium by a reactive fluid. *Physical review letters 58*(5), 479.

[29] Daccord, G. and R. Lenormand (1987). Fractal patterns from chemical dissolution. *Nature 325*(6099), 41–43.

[30] Daccord, G., O. Lietard, and R. Lenormand (1993). Chemical dissolution of a porous medium by a reactive fluid—ii. convection vs reaction, behavior diagram. *Chemical engineering science 48*(1), 179–186.

[31] Davidson, J. M., D. Nielsen, and J. Biggar (1966). The dependence of soil water uptake and release upon the applied pressure increment. *Soil Science Society of America Journal 30*(3), 298–304.

[32] Dávila, G., J. Cama, L. Luquot, J. M. Soler, and C. Ayora (2017). Experimental and modeling study of the interaction between a crushed marl caprock and co2-rich solutions under different pressure and temperature conditions. *Chemical Geology 448*, 26–42.

[33] De Wit, A. (2016). Chemo-hydrodynamic patterns in porous media. *Philosophical Transactions of the Royal Society A: Mathematical, Physical and Engineering Sciences 374*(2078), 20150419.

[34] Dong, M. and I. Chatzis (1995). The imbibition and flow of a wetting liquid along the corners of a square capillary tube. *Journal of colloid and interface science 172*(2), 278–288.

[35] Dullien, F. A. (2012). *Porous media: fluid transport and pore structure*. Academic press.

[36] Dussart, R., T. Tillocher, P. Lefaucheux, and M. Boufnichel (2014, 03). Plasma cryogenic etching of silicon: From the early days to today's advanced technologies. *Journal of Physics D: Applied Physics 47*, 123001.

[37] Emmanuel, S., J. J. Ague, and O. Walderhaug (2010). Interfacial energy effects and the evolution of pore size distributions during quartz precipitation in sandstone. *Geochimica et Cosmochimica Acta 74*(12), 3539–3552.

[38] Fairbrother, F. and A. E. Stubbs (1935). 119. studies in electro-endosmosis. part vi. the "bubble-tube" method of measurement. *Journal of the Chemical Society (Resumed)*, 527–529.

[39] Fatt, I. et al. (1956). The network model of porous media. *Transactions of the AIME 207*(01), 144–181.

[40] Feder, J. (2013). *Fractals*. Springer Science & Business Media.

[41] Ferrari, A. and I. Lunati (2014). Inertial effects during irreversible meniscus reconfiguration in angular pores. *Advances in water resources 74*, 1–13.

[42] Fredd, C. N. and H. S. Fogler (1998). Influence of transport and reaction on wormhole formation in porous media. *AIChE journal 44*(9), 1933–1949.

[43] Friend, J. and L. Yeo (2010). Fabrication of microfluidic devices using polydimethylsiloxane. *Biomicrofluidics 4*(2), 026502.

[44] Gerami, A., Y. Alzahid, P. Mostaghimi, N. Kashaninejad, F. Kazemifar, T. Amirian, N. Mosavat, M. E. Warkiani, and R. T. Armstrong (2019). Microfluidics for porous systems: fabrication, microscopy and applications. *Transport in Porous Media 130*(1), 277–304.

[45] Gershenzon, N. I., R. W. Ritzi Jr, D. F. Dominic, E. Mehnert, and R. T. Okwen (2016). Comparison of co2 trapping in highly heterogeneous reservoirs with brooks-corey and van genuchten type capillary pressure curves. *Advances in Water Resources 96*, 225–236.

[46] Golfier, F., C. Zarcone, B. Bazin, R. Lenormand, D. Lasseux, and M. Quintard (2002). On the ability of a darcy-scale model to capture wormhole formation during the dissolution of a porous medium. *Journal of fluid Mechanics 457*, 213.

[47] Gravesen, P., J. Branebjerg, and O. S. Jensen (1993). Microfluidics-a review. *Journal of micromechanics and microengineering 3*(4), 168.

[48] Gray, W. G. (1975). A derivation of the equations for multi-phase transport. *Chemical Engineering Science 30*(2), 229–233.

[49] Gray, W. G. and S. M. Hassanizadeh (1991). Unsaturated flow theory including interfacial phenomena. *Water Resources Research 27*(8), 1855–1863.

[50] Guo, H., Y. Huang, Y. Chen, and Q. Zhou (2016). Quantitative raman spectroscopic measurements of co2 solubility in nacl solution from (273.15 to 473.15) k at p=(10.0, 20.0, 30.0, and 40.0) mpa. *Journal of Chemical & Engineering Data 61*(1), 466–474.

[51] Gupta, S. P. and R. A. Greenkorn (1974). An experimental study of immiscible displacement with an unfavorable mobility ratio in porous media. *Water Resources Research 10*(2), 371–374.

[52] Haeberle, S. and R. Zengerle (2007). Microfluidic platforms for lab-on-a-chip applications. *Lab on a Chip 7*(9), 1094–1110.

[53] Haines, W. B. (1930). Studies in the physical properties of soil. v. the hysteresis effect in capillary properties, and the modes of moisture distribution associated therewith. *The Journal of Agricultural Science 20*(1), 97–116.

[54] Hassanizadeh, S. M. and W. G. Gray (1993). Toward an improved description of the physics of two-phase flow. *Advances in Water Resources 16*(1), 53–67.

[55] Hedges, L. O. and S. Whitelam (2012). Patterning a surface so as to speed nucleation from solution. *Soft Matter 8*(33), 8624–8635.

[56] Helgeson, H. C., W. M. Murphy, and P. Aagaard (1984). Thermodynamic and kinetic constraints on reaction rates among minerals and aqueous solutions. ii. rate constants, effective surface area, and the hydrolysis of feldspar. *Geochimica et Cosmochimica Acta 48*(12), 2405–2432.

[57] Hoogland, F., P. Lehmann, R. Mokso, and D. Or (2016). Drainage mechanisms in porous media: From piston-like invasion to formation of corner flow networks. *Water Resources Research 52*(11), 8413–8436.

[58] Hoogland, F., P. Lehmann, and D. Or (2016). Drainage dynamics controlled by corner flow: Application of the foam drainage equation. *Water Resources Research 52*(11), 8402–8412.

[59] Iliescu, C., H. Taylor, M. Avram, J. Miao, and S. Franssila (2012). A practical guide for the fabrication of microfluidic devices using glass and silicon. *Biomicrofluidics 6*(1), 016505.

[60] Jahanshahi, A., P. Salvo, and J. Vanfleteren (2013). Pdms selective bonding for the fabrication of biocompatible all polymer nc microvalves. *Journal of microelectromechanical systems 22*(6), 1354–1360.

[61] Karadimitriou, N. and S. Hassanizadeh (2012, 08). A review of micromodels and their use in two-phase flow studies. *Vadose Zone Journal 11*, 0.

[62] Karadimitriou, N., M. Musterd, P. Kleingeld, M. Kreutzer, S. Hassanizadeh, and V. Joekar-Niasar (2013). On the fabrication of pdms micromodels by rapid prototyping, and their use in two-phase flow studies. *Water Resources Research 49*(4), 2056–2067.

[63] Kawata, S., T. Ichimura, A. Taguchi, and Y. Kumamoto (2017). Nano-raman scattering microscopy: resolution and enhancement. *Chemical reviews 117*(7), 4983–5001.

[64] Kazemifar, F., G. Blois, D. C. Kyritsis, and K. T. Christensen (2015). A methodology for velocity field measurement in multiphase high-pressure flow of co2 and water in micromodels. *Water Resources Research 51*(4), 3017–3029.

[65] Knauss, K. G., J. W. Johnson, and C. I. Steefel (2005). Evaluation of the impact of co2, co-contaminant gas, aqueous fluid and reservoir rock interactions on the geologic sequestration of co2. *Chemical geology 217*(3-4), 339–350.

[66] Koehler, S. A., S. Hilgenfeldt, and H. Stone (2004). Foam drainage on the microscale: I. modeling flow through single plateau borders. *Journal of colloid and interface science 276*(2), 420–438.

[67] Kovscek, A. and C. Radke (1996). Gas bubble snap-off under pressure-driven flow in constricted noncircular capillaries. *Colloids and Surfaces A: Physicochemical and Engineering Aspects 117*(1-2), 55–76.

[68] Krevor, S. C. M., R. Pini, L. Zuo, and S. M. Benson (2012). Relative permeability and trapping of co2 and water in sandstone rocks at reservoir conditions. *Water Resources Research 48*(2), 0.

[69] Lasaga, A. C. (1998). *Kinetic theory in the earth sciences*, Volume 811. JSTOR.

[70] Legait, B. (1983). Laminar flow of two phases through a capillary tube with variable square cross-section. *Journal of colloid and interface science 96*(1), 28–38.

[71] Lenormand, R. (1990). Liquids in porous media. *Journal of Physics: Condensed Matter 2*(S), SA79.

[72] Lenormand, R., E. Touboul, and C. Zarcone (1988). Numerical models and experiments on immiscible displacements in porous media. *Journal of fluid mechanics 189*, 165–187.

[73] Lenormand, R., C. Zarcone, and A. Sarr (1983, 10). Mechanisms of the displacement of one fluid by another in a network of capillary ducts. *Journal of Fluid Mechanics 135*, 337–353.

[74] Lu, C., L. J. Lee, and Y.-J. Juang (2008). Packaging of microfluidic chips via interstitial bonding technique. *Electrophoresis 29*(7), 1407–1414.

[75] Luquot, L. and P. Gouze (2009). Experimental determination of porosity and permeability changes induced by injection of co2 into carbonate rocks. *Chemical Geology 265*(1-2), 148–159.

[76] Magnini, M. and O. Matar (2020). Morphology of long gas bubbles propagating in square capillaries. *International Journal of Multiphase Flow 129*, 103353.

[77] Måløy, K. J., L. Furuberg, J. Feder, and T. Jøssang (1992). Dynamics of slow drainage in porous media. *Physical review letters 68*(14), 2161.

[78] marquis de Laplace, P. S. (1799). *Traité de mécanique céleste*, Volume 1. Crapelet.

[79] Marty, N. C., F. Claret, A. Lassin, J. Tremosa, P. Blanc, B. Madé, E. Giffaut, B. Cochepin, and C. Tournassat (2015). A database of dissolution and precipitation rates for clay-rocks minerals. *Applied Geochemistry 55*, 108–118.

[80] Meakin, P. and A. M. Tartakovsky (2009). Modeling and simulation of pore-scale multiphase fluid flow and reactive transport in fractured and porous media. *Reviews of Geophysics 47*(3), 0.

[81] Meinhart, C. D., S. T. Wereley, and J. G. Santiago (1999). Piv measurements of a microchannel flow. *Experiments in fluids 27*(5), 414–419.

[82] Metz, B., O. Davidson, H. De Coninck, M. Loos, and L. Meyer (2005). *IPCC special report on carbon dioxide capture and storage*. Cambridge: Cambridge University Press.

[83] Moebius, F. and D. Or (2012). Interfacial jumps and pressure bursts during fluid displacement in interacting irregular capillaries. *Journal of colloid and interface science 377*(1), 406–415.

[84] Moebius, F. and D. Or (2014). Inertial forces affect fluid front displacement dynamics in a pore-throat network model. *Physical Review E 90*(2), 023019.

[85] Mohammadi, S., D. Van Slyke, and B. Ganong (1989). Steam-foam pilot project in dome-tumbador, midway-sunset field. *SPE reservoir engineering 4*(01), 7–16.

[86] Moore, T., R. Slobod, et al. (1955). Displacement of oil by water-effect of wettability, rate, and viscosity on recovery. In *Fall meeting of the petroleum branch of AIME*. Society of Petroleum Engineers.

[87] Morrow, N. R. (1970). Physics and thermodynamics of capillary action in porous media. *Industrial & Engineering Chemistry 62*(6), 32–56.

[88] Moura, M., E. G. Flekkøy, K. J. Måløy, G. Schäfer, and R. Toussaint (2019). Connectivity enhancement due to film flow in porous media. *Physical Review Fluids 4*(9), 094102.

[89] Nachabe, M. (1998). Refining the definition of field capacity in the literature. *Journal of irrigation and drainage engineering 124*(4), 230–232.

[90] Naghavi, B. and T. C. Kibbey (2014). An experimental study of the factors influencing apparent wetting phase residual saturation in dynamically drained porous media. *Transport in porous media 101*(1), 149–160.

[91] Noiriel, C., L. Luquot, B. Madé, L. Raimbault, P. Gouze, and J. van der Lee (2009). Changes in reactive surface area during limestone dissolution: An experimental and modelling study. *Chemical Geology 265*(1-2), 160–170.

[92] Or, D. and S. Assouline (2013). The foam drainage equation for unsaturated flow in porous media. *Water Resources Research 49*(10), 6258–6265.

[93] Palandri, J. L. and Y. K. Kharaka (2004). A compilation of rate parameters of water-mineral interaction kinetics for application to geochemical modeling. Technical report, Geological Survey Menlo Park CA.

[94] Parkhurst, D. L., C. Appelo, et al. (2013). Description of input and examples for phreeqc version 3—a computer program for speciation, batch-reaction, one-dimensional transport, and inverse geochemical calculations. *US geological survey techniques and methods 6*(A43), 497.

[95] Perrin, J.-C. and S. Benson (2010). An experimental study on the influence of sub-core scale heterogeneities on co 2 distribution in reservoir rocks. *Transport in porous media 82*(1), 93–109.

[96] Peters, C. A. (2009). Accessibilities of reactive minerals in consolidated sedimentary rock: An imaging study of three sandstones. *Chemical Geology 265*(1-2), 198–208.

[97] Peters, E. J. and D. L. Flock (1981, 04). The Onset of Instability During Two-Phase Immiscible Displacement in Porous Media. *Society of Petroleum Engineers Journal 21*(02), 249–258.

[98] Plummer, L., T. Wigley, and D. Parkhurst (1978). The kinetics of calcite dissolution in co 2-water systems at 5 degrees to 60 degrees c and 0.0 to 1.0 atm co 2. *American journal of science 278*(2), 179–216.

[99] Poonoosamy, J., M. Klinkenberg, G. Deissmann, F. Brandt, D. Bosbach, U. Mäder, and G. Kosakowski (2020). Effects of solution supersaturation on barite precipitation in porous media and consequences on permeability: Experiments and modelling. *Geochimica et Cosmochimica Acta 270*, 43–60.

[100] Poonoosamy, J., C. Soulaine, A. Burmeister, G. Deissmann, D. Bosbach, and S. Roman (2020). Microfluidic flow-through reactor and 3d raman imaging for in situ assessment of mineral reactivity in porous and fractured porous media. *Lab on a Chip 20*(14), 2562–2571.

[101] Poonoosamy, J., C. Wanner, P. Alt Epping, J. Águila, J. Samper, L. Montenegro, M. Xie, D. Su, K. Mayer, U. Mäder, et al. (2021). Benchmarking of reactive transport codes for 2d simulations with mineral dissolution–precipitation reactions and feedback on transport parameters. *Computational geosciences 25*(4), 1337–1358.

[102] Porter, M. L., J. Jiménez-Martínez, R. Martinez, Q. McCulloch, J. W. Carey, and H. S. Viswanathan (2015). Geo-material microfluidics at reservoir conditions for subsurface energy resource applications. *Lab on a Chip 15*(20), 4044–4053.

[103] Ransohoff, T. and C. Radke (1988). Laminar flow of a wetting liquid along the corners of a predominantly gas-occupied noncircular pore. *Journal of colloid and interface science 121*(2), 392–401.

[104] Ravera, F., E. Santini, G. Loglio, M. Ferrari, and L. Liggieri (2006). Effect of nanoparticles on the interfacial properties of liquid/liquid and liquid/air surface layers. *The Journal of Physical Chemistry B 110*(39), 19543–19551.

[105] Renard, S., J. Sterpenich, J. Pironon, P. Chiquet, and A. Randi (2014). Geochemical effects of an oxycombustion stream containing so2 and o2 on carbonate rocks in the context of co2 storage. *Chemical Geology 382*, 140–152.

[106] Roman, S., S. Lorthois, P. Duru, and F. Risso (2012). Velocimetry of red blood cells in microvessels by the dual-slit method: effect of velocity gradients. *Microvascular Research 84*(3), 249–261.

[107] Roman, S., C. Soulaine, M. A. AlSaud, A. Kovscek, and H. Tchelepi (2016). Particle velocimetry analysis of immiscible two-phase flow in micromodels. *Advances in Water Resources 95*, 199–211.

[108] Roman, S., C. Soulaine, and A. R. Kovscek (2020). Pore-scale visualization and characterization of viscous dissipation in porous media. *Journal of Colloid and Interface Science 558*, 269–279.

[109] Roof, J. (1970). Snap-off of oil droplets in water-wet pores. *Society of Petroleum Engineers Journal 10*(01), 85–90.

[110] Rose, W. (2000). Myths about later-day extensions of darcy's law. *Journal of Petroleum Science and Engineering 26*(1-4), 187–198.

[111] Rose, W., P. A. Witherspoon Jr, et al. (1956). Studies of waterflood performance ii. trapping oil in a pore doublet. *Circular no. 224*.

[112] Rossen, W. R. (2000). Snap-off in constricted tubes and porous media. *Colloids and Surfaces A: Physicochemical and Engineering Aspects 166*(1-3), 101–107.

[113] Saffman, P. G. and G. I. Taylor (1958). The penetration of a fluid into a porous medium or hele-shaw cell containing a more viscous liquid. *Proceedings of the Royal Society of London. Series A. Mathematical and Physical Sciences 245*(1242), 312–329.

[114] Schechter, R. and J. Gidley (1969). The change in pore size distribution from surface reactions in porous media. *AIChE Journal 15*(3), 339–350.

[115] Singh, K., H. Scholl, M. Brinkmann, M. Di Michiel, M. Scheel, S. Herminghaus, and R. Seemann (2017). The role of local instabilities in fluid invasion into permeable media. *Scientific reports 7*, 1–11.

[116] Singh, R., M. Sivaguru, G. A. Fried, B. W. Fouke, R. A. Sanford, M. Carrera, and C. J. Werth (2017). Real rock-microfluidic flow cell: A test bed for real-time in situ analysis of flow, transport, and reaction in a subsurface reactive transport environment. *Journal of contaminant hydrology 204*, 28–39.

[117] Singh, R., H. Yoon, R. A. Sanford, L. Katz, B. W. Fouke, and C. J. Werth (2015). Metabolism-induced caco3 biomineralization during reactive transport in a micromodel: Implications for porosity alteration. *Environmental science & technology 49*(20), 12094–12104.

[118] Siqveland, L. M. and S. Skjaeveland (2014). Derivations of the young–laplace equation. *Unpublished research. https://doi. org/10.13140/RG 2*(4485.5768), 23–30.

[119] Song, W., T. W. de Haas, H. Fadaei, and D. Sinton (2014). Chip-off-the-old-rock: the study of reservoir-relevant geological processes with real-rock micromodels. *Lab on a Chip 14*(22), 4382–4390.

[120] Song, W. and A. R. Kovscek (2015). Functionalization of micromodels with kaolinite for investigation of low salinity oil-recovery processes. *Lab on a Chip 15*(16), 3314–3325.

[121] Soulaine, C., S. Roman, A. Kovscek, and H. A. Tchelepi (2017). Mineral dissolution and wormholing from a pore-scale perspective. *Journal of Fluid Mechanics 827*, 457–483.

[122] Soulaine, C., S. Roman, A. Kovscek, and H. A. Tchelepi (2018). Pore-scale modelling of multiphase reactive flow: application to mineral dissolution with production of CO_2. *Journal of Fluid Mechanics 855*, 616–645.

[123] Spurin, C., T. Bultreys, B. Bijeljic, M. J. Blunt, and S. Krevor (2019). Intermittent fluid connectivity during two-phase flow in a heterogeneous carbonate rock. *Physical Review E 100*(4), 043103.

[124] Stack, A. G. (2015). Precipitation in pores: A geochemical frontier. *Reviews in Mineralogy and Geochemistry 80*(1), 165–190.

[125] Steefel, C. I., S. Molins, and D. Trebotich (2013, 01). Pore Scale Processes Associated with Subsurface CO2 Injection and Sequestration. *Reviews in Mineralogy and Geochemistry 77*(1), 259–303.

[126] Stevenson, J. and A. Gundlach (1986). The application of photolithography to the fabrication of microcircuits. *Journal of Physics E: Scientific Instruments 19*(9), 654.

[127] Stumm, W. (1992). Chemistry of the solid-water interface: processes at the mineral-water and particle-water interface in natural systems.

[128] Szymczak, P. and A. Ladd (2009). Wormhole formation in dissolving fractures. *Journal of Geophysical Research: Solid Earth 114*(B6).

[129] Talman, S. (2015). Subsurface geochemical fate and effects of impurities contained in a co2 stream injected into a deep saline aquifer: What is known. *International Journal of Greenhouse Gas Control 40*, 267–291.

[130] Tan, S. H., N.-T. Nguyen, Y. C. Chua, and T. G. Kang (2010). Oxygen plasma treatment for reducing hydrophobicity of a sealed polydimethylsiloxane microchannel. *Biomicrofluidics 4*(3), 032204.

[131] Tanino, Y., X. Zacarias-Hernandez, and M. Christensen (2018). Oil/water displacement in microfluidic packed beds under weakly water-wetting conditions: competition between precursor film flow and piston-like displacement. *Experiments in Fluids 59*(2), 35.

[132] Taylor, G. (1961). Deposition of a viscous fluid on the wall of a tube. *Journal of fluid mechanics 10*(2), 161–165.

[133] Thaysen, E., J. M. Soler, M. Boone, V. Cnudde, and J. Cama (2017). Effect of dissolved h2so4 on the interaction between co2-rich brine solutions and limestone, sandstone and marl. *Chemical Geology 450*, 31–43.

[134] Thielicke, W. and R. Sonntag (2021). Particle image velocimetry for matlab: Accuracy and enhanced algorithms in pivlab. *Journal of Open Research Software 9*(1).

[135] Thielicke, W. and E. Stamhuis (2014). Pivlab–towards user-friendly, affordable and accurate digital particle image velocimetry in matlab. *Journal of Open Research Software 2*(1).

[136] Tillocher, T., J. Nos, G. Antoun, P. Lefaucheux, M. Boufnichel, and R. Dussart (2021). Comparison between bosch and stiger processes for deep silicon etching. *Micromachines 12*(10), 1143.

[137] Trantidou, T., Y. Elani, E. Parsons, and O. Ces (2017). Hydrophilic surface modification of pdms for droplet microfluidics using a simple, quick, and robust method via pva deposition. *Microsystems & nanoengineering 3*(1), 1–9.

[138] Trietsch, S., T. Hankemeier, and H. Van der Linden (2011). Lab-on-a-chip technologies for massive parallel data generation in the life sciences: A review. *Chemometrics and Intelligent Laboratory Systems 108*(1), 64–75.

[139] Tutolo, B. M., A. J. Luhmann, X.-Z. Kong, M. O. Saar, and W. E. Seyfried Jr (2015). Co2 sequestration in feldspar-rich sandstone: coupled evolution of fluid chemistry, mineral reaction rates, and hydrogeochemical properties. *Geochimica et Cosmochimica Acta 160*, 132–154.

[140] Wagner, A. J. (2008). A practical introduction to the lattice boltzmann method. *Adt. notes for Statistical Mechanics 463*, 663.

[141] Wang, W., S. Chang, and A. Gizzatov (2017). Toward reservoir-on-a-chip: fabricating reservoir micromodels by in situ growing calcium carbonate nanocrystals in microfluidic channels. *ACS applied materials & interfaces 9*(34), 29380–29386.

[142] Wang, Y., C. Zhang, N. Wei, M. Oostrom, T. W. Wietsma, X. Li, and A. Bonneville (2013). Experimental study of crossover from capillary to viscous fingering for supercritical co2–water displacement in a homogeneous pore network. *Environmental science & technology 47*(1), 212–218.

[143] Washburn, E. W. (1921). The dynamics of capillary flow. *Physical review 17*(3), 273.

[144] Wilke, F. D., M. Vásquez, T. Wiersberg, R. Naumann, and J. Erzinger (2012). On the interaction of pure and impure supercritical co2 with rock forming minerals in saline aquifers: An experimental geochemical approach. *Applied Geochemistry 27*(8), 1615–1622.

[145] Wong, H., C. Radke, and S. Morris (1995). The motion of long bubbles in polygonal capillaries. part 1. thin films. *Journal of Fluid Mechanics 292*, 71–94.

[146] Wörner, M. (2012). Numerical modeling of multiphase flows in microfluidics and micro process engineering: a review of methods and applications. *Microfluidics and nanofluidics 12*(6), 841–886.

[147] Xie, M., K. U. Mayer, F. Claret, P. Alt-Epping, D. Jacques, C. Steefel, C. Chiaberge, and J. Simunek (2015). Implementation and evaluation of permeability-porosity and tortuosity-porosity relationships linked to mineral dissolution-precipitation. *Computational geosciences 19*(3), 655–671.

[148] Young, T. (1805). Iii. an essay on the cohesion of fluids. *Philosophical transactions of the royal society of London 95*, 65–87.

[149] Zarcone, C. and R. Lenormand (1994). Experimental-determination of viscous coupling during 2-phase flow in porous-media. *Comptes Rendus de L Academie des Sciences serie II 318*(11), 1429–1435.

[150] Zevi, Y., A. Dathe, J. F. McCarthy, B. K. Richards, and T. S. Steenhuis (2005). Distribution of colloid particles onto interfaces in partially saturated sand. *Environmental science & technology 39*(18), 7055–7064.

[151] Zhang, C., M. Oostrom, J. W. Grate, T. W. Wietsma, and M. G. Warner (2011). Liquid co2 displacement of water in a dual-permeability pore network micromodel. *Environmental science & technology 45*(17), 7581–7588.

[152] Zhang, C., M. Oostrom, T. W. Wietsma, J. W. Grate, and M. G. Warner (2011). Influence of viscous and capillary forces on immiscible fluid displacement: Pore-scale experimental study in a water-wet micromodel demonstrating viscous and capillary fingering. *Energy & Fuels 25*(8), 3493–3505.

[153] Zhang, Y., B. Hu, Y. Teng, K. Tu, and C. Zhu (2019). A library of basic scripts of reaction rates for geochemical modeling using phreeqc. *Computers & Geosciences 133*, 104316.

[154] Zhao, B., C. W. MacMinn, and R. Juanes (2016). Wettability control on multiphase flow in patterned microfluidics. *Proceedings of the National Academy of Sciences 113*(37), 10251–10256.

[155] Zhou, D., M. Blunt, and F. Orr Jr (1997). Hydrocarbon drainage along corners of noncircular capillaries. *Journal of colloid and interface science 187*(1), 11–21.

Appendix A

Appendix Title

A.1 Young-Laplace (Y-L) equation

Y-L equation is a mathematical expression describing the relation between capillary pressure, interfacial tension and interface curvature. Young [148] was the first person who describe the relation of these parameters and principles regarding contact of two fluid at interface interface. marquis de Laplace [78] represented all described relations by young in mathematical therms. A comprehensive review of different methods for proofing this equation based on different approaches, such as force equilibrium and minimisation of surface energy, is presented by Siqveland and Skjaeveland [118]. In this section we aim to present Y-L equation parameters in more details.

Appendix A.1 represents Y-L equation as

$$\Delta P = \sigma(\frac{1}{R_1} + \frac{1}{R_2})$$

Where ΔP, σ, R_1 and R_2 respectively represent Pressure difference, interfacial tension and principal radii of curvature. pressure difference is associated with the amount of pressure drop between two sides of the interface in the point that measurement is under taken, Point P, see Fig. A.1.

For measurement of R_1 and R_2, first the normal line to the surface should be found. Then, every two prependicular plans that contain normal line to the interface may be chosen. The radius of curvature of intersection lines of these plans and interface are principal radii of interface curvature (R_1 and R_2). In Fig. A.1, $\overline{PN}$ is the normal line to the interface ($CADB$) and surfaces ABN and CDN are perpendicular to each other and intercept at line $\overline{PN}$. As it is illustrated in this figure, the interception of these surfaces and the interface are curves $\widehat{APB}$ and $\widehat{CPD}$ respectively and R_2 and R_1 are corresponding curvature radii.

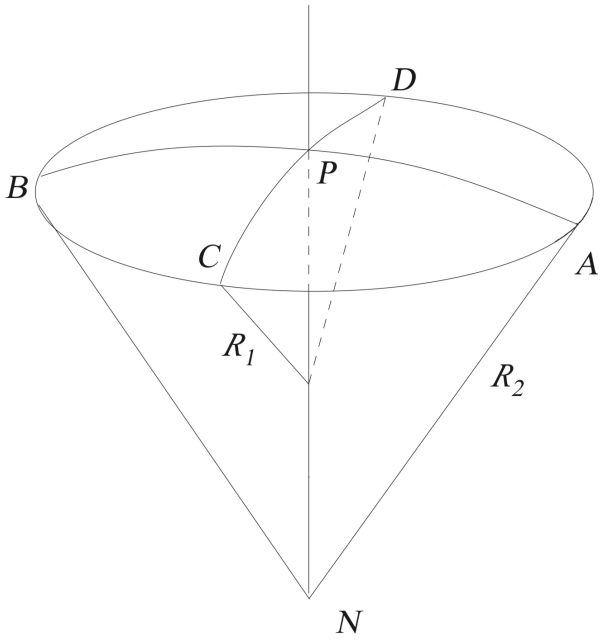

Figure A.1: schematic of interface and representative parameters of Y-L equation [118].

A.2 Master mold preparation using the cryogenic etching method

For microfabrication, a 500 μm thick silicon substrate is used through the process of photolithography. A layer of a positive photoresist[1] (S 1813, Dow chemical company, MICROPOSIT S1800 G2) is distributed homogeneously on the surface of the silicon wafer. For this mean, the wafer is placed on a spin-coater with 3000 rpm [2]speed for 30 s to optimize the deposited photoresist layer (around 1.6 μm). Then, the wafer is placed on a hot plate with a temperature of 115° C for one minute to perform the soft baking. For the next step, the desired patterns are transferred to the wafer by precisely exposing the photoresist layer to ultraviolet light through the positive mask[3]. All the exposed photoresist is removed from the surface by putting the wafer in a developer (MF319) bath for 1.5 minutes and immediately washing the wafer by immersing in water for two minutes. Before the next step, patterns must be checked using a microscope for any deformation during the developing process, and if there is no alteration in patterns, the patterns are fully developed on the wafer. Then, the wafer is ready for the etching process. A plasma cryogenic etching method is used as our etching method. The temperature cools down to -100° C using liquid nitrogen in the ICP reactor (inductively

[1]A positive photoresist is a type of material that, if it is exposed to UV light it is removed using a developer solution, and the part that has not been exposed to UV light remains on the wafer after washing with the developer solution.

[2]Round per minute.

[3]Positive mask or clear-field mask is referred to as a mask when the designed patterns appear dark on the mask and the void space appear clear.

coupled plasma, ALCATEL) to start the cryogenic etching process. The main advantage of this method is the high control on the geometry of the desired patterns along with extremely vertical walls. This process removes layers of the wafer at areas that are not covered with photoresist (see Fig. 2.3) to the desired depth (in our case, $40\,\mu m$) and let the channels remain on the wafer to be used as the master mold for PDMS soft lithography. For this purpose, prior to employment as a master mold, the silicon wafer is coated with a hydrophobic layer, i.e., Teflon, to ease the separation of wafer and PDMS because PDMS is a hydrophilic material and firmly attaches to the mold. More detailed steps of the process and more details on cryogenic etching are presented in [1, 36].

A.3 Master mold preparation using SU-8

The second method that is used for microfabrication is employing SU-8-2025 (Kayaku advanced materials) photoresist in the fabrication process. As the SU-8 is a negative photoresist, a dark-field mask[4] is required for the fabrication process. The photoresist is poured on the wafer, and the wafer is placed in a spin-coater (Fig. 2.4a). In this process, the photoresist remains as patterns and obstacles on the wafer and plays the role of the master mold for making channels in PDMS photolithography. Since the thickness of the photoresist on the wafer is the Depth of the geometries in our experiments, choosing the right spinning speed and duration play a significant role in obtaining the desired thickness of the photoresist on the wafer (in our case, $40\mu m$). For a thickness of $40\,\mu m$, for this SU-8-2025 photoresist, the spinner is set to $500\,rpm$ for 5 seconds with an acceleration of $100\frac{rpm}{s}$ for spreading (Fig. 2.4a) followed by 30 seconds of thickness adjusting with $1700\,rpm$ speed and $300\,\frac{rpm}{s}$ acceleration (Fig. 2.4b). After, the wafer goes under the process of soft baking at the temperature around $65°\,C$ for 5 minutes followed by 15 minutes of 95ºC hot-plate baking (Fig. 2.4c). This step is the most crucial in defining the final geometry resolution. Then, the wafer is exposed to UV light with the hard contact between the UV source and dark-field mask to keep the precision on patterns and dimensions (Fig. 2.4d). Next, the wafer is placed on a hot plate at $65°\,C$ for 1 minute and $95°\,C$ for four additional minutes as a post-exposure baking (Fig. 2.4e). Then the patterns are developed by immersing the wafer in SU-8 developer (1-methoxy-2-propanol acetate, MICROCHEM) for 4.5 minutes (Fig. 2.4f) and then submerging it in water and then in IPA and finally rinsing with water. In the end, the non-exposed parts of the photoresist on the wafer are removed, and the SU-8 on channels remains. Then, to ease the process of soft photolithography, the surface is coated with a hydrophobic layer (PFOCTS, Merck, Sigma-Aldrich) since the PDMS and

[4] A dark-field mask refers to a mask, which designed patterns are clear, and the space between them appears as dark(opaque).

SU-8 are hydrophilic materials and is difficult to detach them. The obtained wafer is ready to be used as a master mold for the preparation of PDMS micromodels (Fig. 2.4g).

A.4 Analytical solution for Theta and Phi functions

In this section, the analytical solution of $\Theta(h^*)$, $\Phi^*(h^*)$ and $\frac{d}{dt^*}\left(A^*(h^*)\dot{h^*}\Theta^*(h^*)\right)$ for a sinusoidal porous media geometry with a constant depth and a rectangular cross section are presented. The dimensionless form of the channel geometry, surface area, and the permeability respectively are

$$r^*(h^*) = \frac{r_p^*+1}{2} - \frac{r_p^*-1}{2}\cos\frac{2\pi h^*}{H^*}, \tag{A.1}$$

$$A^*(h^*) = \frac{2r(h^*)D_0}{\bar{A}}, \tag{A.2}$$

and

$$K^*(h^*) = \frac{\left(\frac{D_0^2}{12}\right)\left(1-6(\frac{2}{\pi})^5\frac{D_0}{2r(h^*)}\right)}{K_c}. \tag{A.3}$$

First we treat $\Theta(h^*)$ function. By definition, we have

$$\Theta^*(h^*) = \Gamma\int_0^{h^*}\frac{1}{A^*(x)}\,dx + \int_{h^*}^{L^*}\frac{1}{A^*(x)}\,dx.$$

substituting dimensionless parameters in the equation, and defining $a = \frac{r_p+r_{th}}{2} = a$, $b = \frac{r_p-r_{th}}{2}$ and $\alpha = \frac{2\pi h_c}{H}$,

$$\Theta^*(h^*) = \frac{\bar{A}}{2D_0}\Gamma\int_0^{h^*}\frac{1}{(a-b\cos\alpha x)}\,dx + \frac{\bar{A}}{2D_0}\int_{h^*}^{L^*}\frac{1}{(a-b\cos\alpha x)}\,dx. \tag{A.4}$$

since $a > b$ for all r_p and r_{th} , the analytical solution of the integral will be

$$\begin{aligned}\Theta(h^*) = \frac{2\bar{A}}{\alpha D_0}\left(\frac{2}{\sqrt{a^2-b^2}}\right)\Bigg[\Bigg[(\Gamma-1)\arctan\left(\sqrt{\frac{a+b}{a-b}}\tan\left(\frac{\alpha}{2}h^*\right)\right)\\ +\arctan\left(\sqrt{\frac{a+b}{a-b}}\tan\left(\frac{\alpha}{2}\right)\right)\Bigg] + \frac{\alpha}{2}\left((\Gamma-1)h^*+1\right)\\ -\left[(\Gamma-1)\arctan\left(\tan\left(\frac{\alpha}{2}h^*\right)\right)+\arctan\left(\tan\left(\frac{\alpha}{2}\right)\right)\right]\Bigg],\end{aligned} \tag{A.5}$$

To calculate the $\Phi^*(h^*)$, by definition we have

$$\Phi^*(h^*) = M\int_0^{h^*}\frac{1}{A^*(x)K^*(x)}\,dx + \int_{h^*}^{L^*}\frac{1}{A^*(x)K^*(x)}\,dx.$$

By substituting the parameters, we have

$$\Phi^*(h^*) = \frac{\bar{A}K_c}{2D_0}\left(M\int_0^{h^*}\frac{1}{A-B\cos\alpha h^*}\,dx+\int_{h^*}^{1}\frac{\bar{A}K_c}{A-B\cos\frac{2\pi Lx}{H}}\,dx\right), \tag{A.6}$$

where $A=\frac{D_0^2}{12}\left(\frac{r_p+r_{th}}{2}\right)-\frac{D_0^3}{2\times2}(\frac{2}{\pi})^5$ and $B=\left(\frac{D_0^2}{12}\right)\left(\frac{r_p-r_{th}}{2}\right)$. The analytical solution of the integral depends on the A and B values.

$|A|>|B|$**:**

$$\begin{aligned}\Phi^*(h^*) = \left(\frac{2\bar{A}K_c}{\alpha D_0}\right)\left(\frac{2}{\sqrt{A^2-B^2}}\right)\Bigg[\Bigg[(M-1)\arctan\left(\sqrt{\frac{A+B}{A-B}}\tan\left(\frac{\alpha h^*}{2}\right)\right)\\ +\arctan\left(\sqrt{\frac{A+B}{A-B}}\tan\left(\frac{\alpha}{2}\right)\right)\Bigg]+\left(\frac{\alpha}{2}\right)\left[(M-1)h^*+1\right]\\ +\left[(M-1)\arctan\left(\tan\left(\frac{\alpha h^*}{2}\right)\right)+\arctan\left(\tan\left(\frac{\alpha}{2}\right)\right)\right]\Bigg].\end{aligned} \tag{A.7}$$

$|A|<|B|$**:**

$$\begin{aligned}\Phi^*(h^*) = \left(\frac{2\bar{A}K_c}{\alpha D_0}\right)\left(\frac{1}{\sqrt{B^2-A^2}}\right)\\ \left[(M-1)\ln\left(\frac{-B+A\cos\alpha h^*+\sqrt{B^2-A^2}\sin\alpha h^*}{A-B\cos\alpha h^*}\right)\right.\\ \left.+\ln\left(\frac{-B+A\cos\alpha+\sqrt{B^2-A^2}\sin\alpha}{A-B\cos\alpha}\right)\right].\end{aligned} \tag{A.8}$$

For calculation of $\frac{d}{dt^*}\left(A^*(h^*)\dot{h^*}\Theta^*(h^*)\right)$ one can write

$$\begin{aligned}\frac{d}{dt^*}\left(A^*(h^*)\dot{h^*}\Theta^*(h^*)\right)=\frac{d}{dt^*}\left(A^*(h^*)\dot{h^*}\right)\Theta^*(h^*)+\frac{d}{dt^*}\left(\Theta^*(h^*)\right)A^*(h^*)\dot{h^*}=\\ \left[\left(a-b\cos\alpha h^*\right)\ddot{h^*}+(b\alpha\sin\alpha)\,\dot{h^*}^2\right]\times\\ \left[\frac{2\bar{A}}{\alpha D_0}\left(\frac{2}{\sqrt{a^2-b^2}}\right)\left[\left[(\Gamma-1)\arctan\left(\sqrt{\frac{a+b}{a-b}}\tan\left(\frac{\alpha h^*}{2}\right)\right)+\arctan\left(\sqrt{\frac{a+b}{a-b}}\tan\left(\frac{\alpha}{2}\right)\right)\right]\right.\right.\\ \left.\left.+\frac{\alpha}{2}\left((\Gamma-1)h^*+1\right)-\left[(\Gamma-1)\arctan\left(\tan\left(\frac{\alpha h^*}{2}\right)\right)+\arctan\left(\tan\left(\frac{\alpha}{2}\right)\right)\right]\right]\\ +\left[\left(\frac{2\bar{A}}{\alpha D_0}\right)\left(\frac{2}{\sqrt{a^2-b^2}}\right)\sqrt{\frac{a+b}{a-b}}\frac{\alpha}{2}(\Gamma-1)(a-b)\dot{h^*}^2\right].\end{aligned} \tag{A.9}$$

A.5 PHREEQC

In this section the developed code for geochemical simulations using PHREEQC is presented.

```
    DATABASE C:/phreeqc/database/PHREEQC_ThermoddemV1.10_15Dec2020.dat
SOLUTION 1-101
-temp 25
-water 25.5e-3
END
 #
RATES

Calcite

# from Marty et al 2015
# pre-exponent coefficient A is calculated from logk using equation A=k/exp(-Ea/RT
# experimental condition range T=10-100C, pH not specified

-start
1 rem unit should be mol,kgw-1 and second-1
2 rem parm(1) is surface area in the unit of m2/kgw
3 rem calculation of surface area can be found in the note
4 rem M is current moles of minerals. M0 is the initial moles of minerals
5 rem parm(2) is a correction factor
10 rem acid solution parameters
11 a1=0
12 E1=0
13 n1=0
20 rem neutral solution parameters
21 a2=6.59E+04
22 E2=66000
30 rem co2 solution parameters
31 a3=1.04E+09
32 E3=67000
33 n2=1.6
36 rem rate=0 if no minerals and undersaturated
40 SR_mineral=SR("calcite")
```

```
41 if (M<0) then goto 200
42 if (M=0 and SR_mineral<1) then goto 200
43 if (M0<=0) then SA=PARM(1) else SA=PARM(1)*(M/M0)^0.67
50 if (SA<=0) then SA=1
60 R=8.31451
75 Rate1=a1*EXP(-E1/R/TK)*ACT("H+")^n1  #acid rate expression
80 Rate2=a2*EXP(-E2/R/TK)               #neutral rate expression
85 Rate3=a3*EXP(-E3/R/TK)*ACT("HCO3-")^n2    #base rate expression
90 Rate=(Rate1+Rate2+Rate3)*(1-Sr_mineral)*SA*parm(2)
100 moles= rate*Time
200 save moles
-end
  #

gypsum
# from Palandri and Kharaka 2004
# experimental condition range T=25C, pH=7
# No activation energy available. Rate only valid at 25C.

-start
1 rem unit should be mol,kgw-1 and second-1
2 rem parm(1) is surface area in the unit of m2/kgw
3 rem calculation of surface area can be found in the note
4 rem M is current moles of minerals. M0 is the initial moles of minerals
5 rem parm(2) is a correction factor
10 rem acid solution parameters
11 a1=0
12 E1=0
13 n1=0
20 rem neutral solution parameters
21 a2=1.64E-03
22 E2=0
30 rem base solution parameters
31 a3=0
32 E3=0
33 n2=0
36 rem rate=0 if no minerals and undersaturated
40 SR_mineral=SR("gypsum")
41 if (M<0) then goto 200
```

```
42 if (M=0 and SR_mineral<1) then goto 200
43 if (M0<=0) then SA=PARM(1) else SA=PARM(1)*(M/M0)^0.67
50 if (SA<=0) then SA=1
60 R=8.31451
75 Rate1=a1*EXP(-E1/R/TK)*ACT("H+")^n1  #acid rate expression
80 Rate2=a2*EXP(-E2/R/TK)               #neutral rate expression
85 Rate3=a3*EXP(-E3/R/TK)*ACT("H+")^n2    #base rate expression
90 Rate=(Rate1+Rate2+Rate3)*(1-Sr_mineral)*SA*parm(2)
100 moles= rate*Time
200 save moles
-end
 #
KINETICS 1-101
Calcite
-m 3.6e-2
-m0 3.6e-2
-parms 5 0.3
Gypsum
-m 0
-m0 0# initial moles of the kinetic reactant
-parms 1 1
INCREMENTAL_REACTIONS true
END

SOLUTION 0
-temp 25
-water 0.25
END

USE SOLUTION 0
EQUILIBRIUM_PHASES 1
CO2(g) -1.4 10
SO2(g) -3.4 0.1
SAVE SOLUTION 0
COPY SOLUTION 0 101
END

SELECTED_OUTPUT
-file 1D_simulation_results.txt
```

```
-simulation true
-solution true
-distance true
-time true
-pH true
-percent_error true
-saturation_indices Calcite Gypsum
-kinetic_reactants Calcite Gypsum
-totals S Ca
-molalities CO2 HCO3- CO3-2
-activities CO2 HCO3- CO3-2


TRANSPORT
-cells 100
-lengths 100*0.01
-initial_time 0
-shifts 5000000
-time_step 100 second 10
-flow_direction diffusion_only
-dispersivities 100*0
-boundary_conditions constant closed
-print_cells 1 20 50 70
-print_frequency 5000000
-punch_cells 1-100
-punch_frequency 3
Copy solution 100 101
END
```

Mahdi MANSOURI-BOROUJENI

Etude des mécanismes physiques et chimiques induits par le stockage du CO_2 dans les aquifères salins profonds à l'aide des outils de la microfluidique

Résumé :

Le stockage de CO_2 (CS) dans les réservoirs géologiques est envisagé pour réduire le CO_2 atmosphérique. Le CO_2 est capté, purifié, transporté et injecté dans un réservoir géologique profond recouvert d'une roche couverture imperméable. Un stockage sûr et permanent du CO_2 dépend en grande partie de notre compréhension des mécanismes physiques et chimiques induits par le CS. Des études à petite échelle sont nécessaires pour le comportement du CO_2 à l'échelle du réservoir. L'objectif de cette thèse est d'utiliser des réplicas de roches à l'échelle du micromètre pour cibler les mécanismes fondamentaux (i) du déplacement du CO_2, (ii) de l'évolution géochimique du réservoir. Nous avons caractérisé expérimentalement et numériquement les mécanismes à l'origine des différents régimes d'écoulements du CO_2. De plus, nous avons observé que les impuretés présentes dans le CO_2 augmentent considérablement la dissolution des carbonates et produisent du gypse entraînant des altérations pétrophysiques.

Mots clés : Écoulement multiphasique, Stockage du CO_2, Physique à l'échelle des pores, Pore-doublet, Mécanismes d'invasion des pores.

A microfluidic study of the physical and chemical mechanisms induced by CO_2 injection in deep saline aquifers

Summary :

CO_2 sequestration (CS) in geological reservoirs is targeting reduction of atmospheric CO_2. CO_2 is captured, purified, transported and injected into a deep geological reservoir covered by an impermeable caprock. The success of a secure and permanent storage of CO_2 in subsurface formations depends largely on our understanding of physical and chemical mechanisms induced by CS. Small-scale studies are needed to serve as pieces of the big puzzle of reservoir-scale CS behavior. The aim of this PhD is to use micron-scale replicas of reservoirs to target fundamental mechanisms of (i) CO_2-brine displacement, (ii) the geochemical reservoir evolution in the presence of impurities. We characterized experimentally and numerically the micron-scale mechanisms behind CO_2 and brine displacement. Moreover, we observed that impurities drastically increase carbonate dissolution and produces gypsum resulting in petrophysical alterations. These results will serve to optimize the injection process for CS.

Keywords: Multiphase flow, CO_2 storage, Pore-scale physics, Pore-doublet, Pore invasion mechanisms.

Institut des Sciences de la Terre d'Orléans (ISTO)
1A rue de la Férollerie,
Orléans, France